Bifunctional chemical tools for the conditional control of targeted protein degradation

Author

CYRILLE STEPHANE KOUNDE

Supervisors

PROF. EDWARD TATE
DR. JOHN HARLING (GlaxoSmithKline)
DR. MARCEL MUELBAIER (GlaxoSmithKline)

Department of Chemistry
IMPERIAL COLLEGE LONDON

Thesis submitted in partial fulfilment of the requirements for the degree of DOCTOR OF PHILOSOPHY and the DIPLOMA OF IMPERIAL COLLEGE LONDON
13th Jan 2023

Declarations

Copyright declaration

Declaration of originality

I, CYRILLE STEPHANE KOUNDE, declare that all of the work recorded herein is my own, and was produced during my candidature for a DOCTOR OF PHILOSOPHY at IMPERIAL COLLEGE LONDON. I certify that, to the best of my knowledge, my thesis does not infringe upon anyone's copyright nor violate any proprietary rights and that any ideas, techniques, quotations, or any other material from the work of other people included in my thesis, published or otherwise, are fully acknowledged in accordance with the standard referencing practices and written permission from the copyright owner(s) to include such material(s) in my thesis has been obtained. Any work or materials that are derived from others, or are the result of collaboration with others, have been attributed appropriately.

License

Abstract

The ubiquitin-proteasome system (UPS) is a key pathway involved in protein homeostasis via the regulation of intracellular protein levels. The application of proximity-induced biology to the UPS has given birth to proteolysis targeting chimeras (PROTACs), which are bifunctional molecules able to co-opt an E3 ligase for the ubiquitination and proteasome-dependent degradation of a selected protein. Targeted protein degradation (TPD) with PROTACs is now established as a disruptive modality both in chemical biology and drug discovery as it allows the efficient knockdown of an intracellular protein with a small molecule in a catalytic manner. With their unique mode of action and modular synthesis, PROTACs are being developed as therapeutics for various human diseases.

In order to enable discrete control over PROTACs function, our first investigation used light as a precision tool for the spatiotemporal activation of caged and photoswitchable degraders. The design, synthesis, photochemistry, and cellular activity of novel light-activated PROTACs is reported. Furthermore, with the ambition to apply such tools *in vivo*, non-conventional light sources were explored to activate the degraders and overcome the limitations of ultraviolet and visible light. In a second approach, variation in intracellular oxygen concentration was used as a means to selectively activate PROTACs. Incorporation of a bioreductive unit on a degrader followed by testing in a hypoxic environment is presented.

In summary, this thesis describes our investigation towards the conditional control of TPD with newly designed bifunctional degraders which may help better study and tackle disease-relevant proteins.

Acknowledgements

I would like to thank my supervisor Professor Ed Tate for giving me the opportunity to join his group and explore such an exciting topic as protein degradation. With the vibrant discussions about the science, the experiments, and the new ideas around my research, I have often been pushed out of my comfort zone. Working in the Tate group has truly made me a better researcher and the skills I have gained will continue to serve me as I carry on with my career in industry.

I am grateful to my industrial supervisors John D. Harling and Marcel Muelbaier who have always been available to follow my progress and supported some of my "out of the box" ideas. I acknowledge the support from GlaxoSmithKline Research and Development Ltd and the Engineering and Physical Sciences Research Council (EPSRC) Grant EP/R512540/1 for my research.

I would like to thank many of the past and present members of the Tate group who made my 4-year journey enjoyable, especially Roxani Nikoloudaki, Milon Mondal, María Maneiro Rey, Simeon Draganov and Leran Zhang. Thanks also to many of the Tate group members who provided me with some help for my experiments including Masha Shchepinova, Dan Conole, Qisi Zhang, Andrea Goya Grocin and Charlie Saunders. Thanks to the lab managers, Jennie Hutton, Ravi Singh, and Edward Bartlett who created a pleasant atmosphere in the laboratory.

Many of the results generated in this thesis have come through the dedication of Imperial College staff members who went the extra mile to accommodate my requests. This includes Andrew Coulson, Lisa Haigh, and Peter Haycock.

The diligent proofreading of the thesis was done by Janine Gray and Jana Volaric who have significantly help in improving the quality of the final manuscript.

I would like to thank the various labs which have provided help, equipment, or feedback to run some of the experiments: the Fuchter goup, Dr Beata Wojciak-Stothard, Prof. Peter Parker, Prof. Eric Aboagye, Dr Marta Costa Braga, Dr Kuldip Nijran and Chloe Bowen.

My tenacity and motivation have been held in check by my spouse, Phattharanan Kounde who sacrificed time and energy in our household so that I can focus on my research. My Sunflower, thanks for always walking with me. Success is not mine but ours.

Finally, my physical, emotional, and mental health have been maintained by my spiritual shield, my father in heaven, Abba, and his son, the Christ, who gave me the strength to get to the finish line.

Publications arising from the thesis

Kounde, C. S., Shchepinova, M. M., Saunders, C. N., Muelbaier, M., Rackham, M. D., Harling, J. D., & Tate, E. W. (2020). A caged E3 ligase ligand for PROTAC-mediated protein degradation with light. *Chemical Communications*, *56*(41), 5532-5535.

Maneiro, M., Forte, N., Shchepinova, M. M., Kounde, C. S., Chudasama, V., Baker, J. R., & Tate, E. W. (2020). Antibody–PROTAC conjugates enable HER2-dependent targeted protein degradation of BRD4. *ACS chemical biology*, *15*(6), 1306-1312.

Kounde, C. S., & Tate, E. W. (2020). Photoactive Bifunctional Degraders: Precision Tools To Regulate Protein Stability: Miniperspective. *Journal of Medicinal Chemistry*, *63*(24), 15483-15493.

Maneiro, M., De Vita, E., Conole, D., Kounde, C. S., Zhang, Q., & Tate, E. W. (2021). PROTACs, molecular glues and bifunctionals from bench to bedside: Unlocking the clinical potential of catalytic drugs. *Progress in medicinal chemistry*, *60*, 67-190.

Zhang, Q., Kounde, C. S., Mondal, M., Greenfield, J. L., Baker, J. R., Kotelnikov, S., ... & Tate, E. W. (2022). Light-mediated multi-target protein degradation using arylazopyrazole photoswitchable PROTACs (AP-PROTACs). *Chemical Communications*, *58*(78), 10933-10936.

Table of contents

Contents

List of figures

Chapter 3

Chapter 4

List of tables

List of schemes

List of appendices

Appendix 2.1 Characteristics of the box "Scoot"

Appendix 2.2 LC-MS profile after uncaging of PROTAC **12**

Appendix 2.3 Caged PROTAC **12** stability in DMSO

Appendix 2.4 BRD4 Tm determination

Appendix 2.5 Predicted photon yield per decay for various radioisotopes

Appendix 2.6 UV chromatogram after incubation of **12** with ^{90}Y spheres

Appendix 2.7 Estimation of the number of photons needed to uncage PROTAC **12** using ^{90}Y

Appendix 3.1 LC-MS profile after irradiating PROTAC **31** at 365 nm

Appendix 3.2 UV-Vis spectrum of **40** after irradiation at 365 nm

Appendix 3.3 Equation used to calculate the PSS ratio of **40** by UV-vis

Appendix 3.4 Timecourse experiments to evaluate the stability of the *Z* isomer of **34** and **42**

Appendix 3.5 Dose response curves computed from western blots analysis of BRD4 after treatment with photoswitchable PROTACs

Appendix 3.6 Immunoblots of BRD4 in HeLa cells after timecourse experiment with **40**

Appendix 3.7 Effect of 50 nM and 500 nM PROTAC **42** on mchBRD4 levels

Appendix 3.8 Proteasome-dependency experiment with 40 and Bortezomib

Abbreviations

ACN	Acetonitrile
^{18}FDG	Fluorodeoxyglucose
AcOH	Acetic acid
ADDP	1,1'-(Azodicarbonyl)dipiperidine
AID	Auxin inducible degron
AR	Androgen receptor
AUC	Area under the curve
B-LID	Blue light inducible degron
Boc	tert-Butyloxycarbonyl
BRD4	Bromodomain-containing protein 4
BRET	Bioluminescence resonance energy transfer
CETSA	Cellular thermal shift assay
cIAP	Cellular Inhibitor of Apoptosis Protein
CRBN	Cereblon
CRISPR	Clustered regularly interspaced short palindromic repeats
Cys	Cysteine
DBU	1,8-diazabicyclo[5.4.0]undec-7-ene
DC_{50}	Concentration at which 50% degradation is achieved
DCM	Dichloromethane
DEACM	Diethylamino coumarin
DIAD	Diisopropyl azodicarboxylate
DIPEA	N,N-Diisopropylethylamine
DMAP	4-Dimethylaminopyridine
Dmax	Concentration at which the maximale degradation is observed
DMEM	Dulbecco's Modified Eagle Medium
DMF	Dimethylformamide
DMNB	4,5-dimethoxy-2-nitrobenzyl
DMSO	Dimethylsulfoxide
DNA	Deoxyribonucleic acid
DUB	Deubiquitinase
ER	Estrogen receptor
EtOH	Ethanol
FCS	Fetal calf Serum
Fmoc	Fluorenylmethyloxycarbonyl
Fmoc-O-Su	9-Fluorenylmethoxycarbonyl-N-hydroxysuccinimide
GFP	Green fluorescent protein
HATU	Hexafluorophosphate Azabenzotriazole Tetramethyl Uronium
HCC	Hepatocellulo carcinoma
HECT	Homologous to the E6AP carboxyl terminus
HEK293	Human embryonic kidney cells

HIF	Hypoxia-inducible factor
HRE	Hypoxia response element
HRMS	High-resolution mass spectrometry
IMiDs	Immunomodulatory imide drugs
LC-MS	liquid chromatography-mass spectrometry
LED	light-emitting diode
LiHMDS	Lithium bis(trimethylsilyl)amide
LOV2	Light oxygen voltage sensing protein
Lys	Lysine
LYTAC	Lysosome-targeting chimeras
m/z	Mass to charge ratio
M6PR	Mannose 6-phosphate receptor
mchBRD4	mCherry Bromodomain-containing protein 4
mchBTK	mCherry Bruton's tyrosine kinase
MeNPOC	3,4-(methylenedioxy)-6-nitrophenylethoxycarbonyl
MeNPOM	α-methyl-(6-nitropiperonyloxymethyl)
MeOH	Methanol
min	Minutes
mRNA	Messenger ribonucleic acid
MS	Mass spectrometry
NaHMDS	Sodium bis(trimethylsilyl)amide
NTR	Nitroreductase
NVOC	6-nitroveratryloxycarbonyl
ODC	ornithine decarboxylase
PBS	Phosphate buffer saline
Pd/C	Palladium on carbon
PDT	Photodynamic therapy
PEG	Polyethylene glycol
PET	Positron emission tomography
PHOTAC	Photochemically targeting chimeras
PNB	para-nitrobenzyl
POI	Protein of interest
PPh3	Triphenylphosphine
PPh3PO	Triphenylphosphine oxide
PPIs	Protein-protein interactions
PROTAC	Proteolysis targeting chimeras
PSS	Photostationary state
PSTs	Photostatins
PTMs	Post-translational modifications
RBR	RING-between-RING
RFP	Red fluorescent protein
RING	Really Interesting New Gene
RIPA	Radioimmunoprecipitation assay buffer
ROS	Reactive oxygen species

RT	Room temparature
SAR	Structure activity relationship
SCF complex	Skp, Cullin, F-box containing complex
SEM	Standard error of the mean
SIRT	Selective internal radiation therapy
tBuOK	Potassium tert-butoxide
TFA	Trifluoroacetic acid
THF	Tetrahydrofuran
TLC	Thin layer chromatography
Tm	Melting temperature
TMSCl	Trimethylsilyl chloride
TPD	Targeted protein degradation
UPS	Ubiquitin proteasome system
UV-Vis	Ultraviolet-visible
VHL	Von hippel Lindau
YFP	Yellow fluorescent protein

Chapter 1 | Introduction

1.1 The Ubiquitin proteasome system

Proteostasis or protein homeostasis is defined as the dynamic regulation of the proteome within the cells to maintain healthy function.[1,2] Indeed, protein levels in the cellular environment are governed by pre-and post-translational processes which keep the right balance between protein synthesis, folding and degradation[3] (**Figure 1.1**). Protein degradation which stands as one pillar of the proteostasis network is executed mainly by the ubiquitin proteasome system (UPS) and in part by the lysosomal degradation pathway.[4] While the former deals mainly with the degradation of individual proteins (aberrant, misfolded, or no longer required proteins), the latter degrades mostly protein aggregates and defective organelles.[5] In 2004, Aaron Ciechanover, Avram Hershko and Irwin Rose were jointly awarded the Nobel Prize in Chemistry for their discovery of ubiquitin-mediated protein degradation. Their work revealed that the UPS is split in between a tagging process which requires ubiquitin and a degradation process performed in a small cellular machinery called the proteasome.[6]
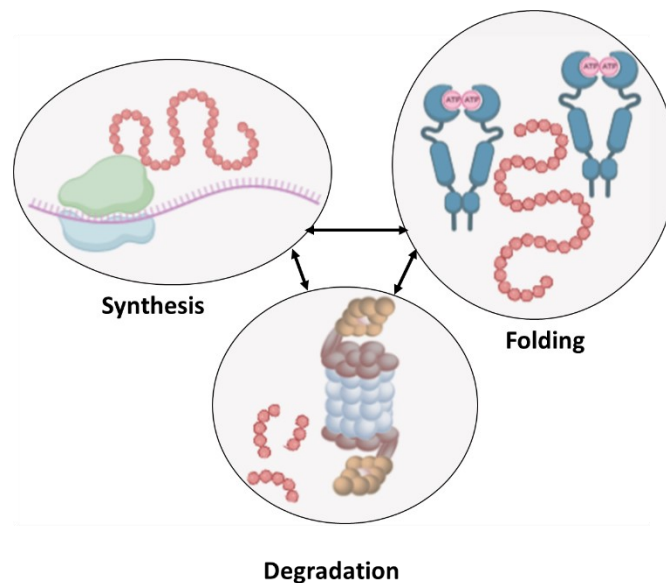
Figure 1.1 Protein homeostasis.

Ubiquitin is a 76-amino acid long regulatory protein highly conserved and widely expressed in most eukaryotic tissues.[7] Attachment of ubiquitin to substrate proteins is performed in three steps. First, the terminal glycine residue of ubiquitin is linked to ubiquitin-activating enzyme E1 via a thioester bond. In a second step, ubiquitin is transferred to an active-site cysteine residue of a ubiquitin-conjugating enzyme E2. In a third step, mediated by a ubiquitin-protein ligase E3, ubiquitin is attached to a lysine residue of substrate protein via an isopeptide bond[8] (**Figure 1.2**). Cysteine, threonine, and serine side chains from the substrate protein can also be labelled with ubiquitin. In humans, 2 E1s, 40 E2s and about 600 E3s are known.[9] E3 ligases are a diverse set of
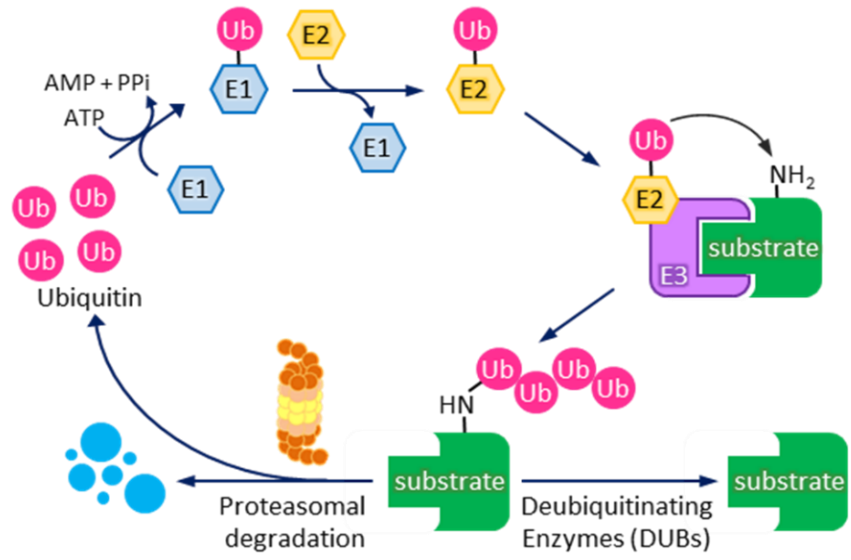
Figure 1.2 Protein ubiquitination via the cascade E1, E2 and E3 enzymes. Image reproduced with permission.[10]

multiunit enzymes divided into three classes (RING E3s, HECT E3s, RBR E3s) which differ in their structural domains and mode of ubiquitin transfer.[11] Besides, the culling-RING ligases (CRLs) have been the most exploited in the field of TPD. It should be noted that the ubiquitination process can be undone by deubiquitinase enzymes (DUBs) which are also crucial in homeostasis as their action stabilizes protein levels.[12] The ubiquitin sequence contains 7 lysine residues which can be further tagged with ubiquitin itself and through mono and polyubiquitination, the tagging process controls the fate of the substrate protein. A degradation outcome is mainly initiated by polyubiquitination on lysine 48 (K48) while other cellular processes can be modulated by diverse ubiquitination pattern stemming from ubiquitin[13] (**Figure 1.3**).
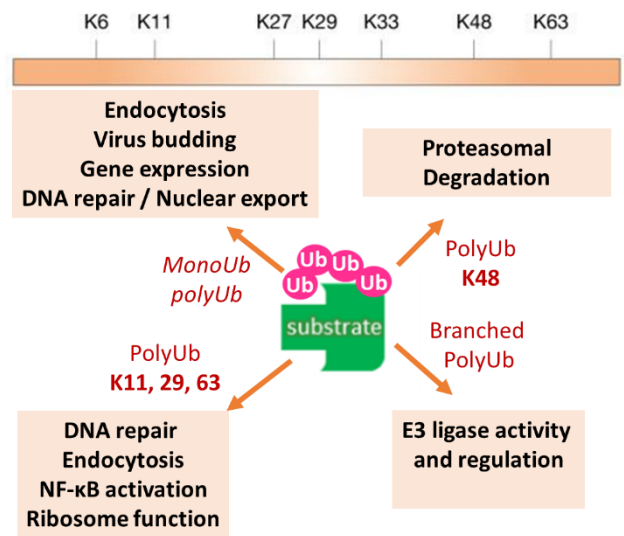
Figure 1.3 Ubiquitin tagging pattern and biological pathways.

Once the substrate proteins have been polyubiquitinated, they are shuttled to the proteasome for degradation. The proteasome is a sophisticated structure made of a core particle (20S) and 2 regulatory particles (19S).[14] The regulatory particle contains a lid and a base involved in the binding, deubiquitination, unfolding and translocation of the substrate proteins into the hydrolytic chamber of the proteasome (**Figure 1.4**).
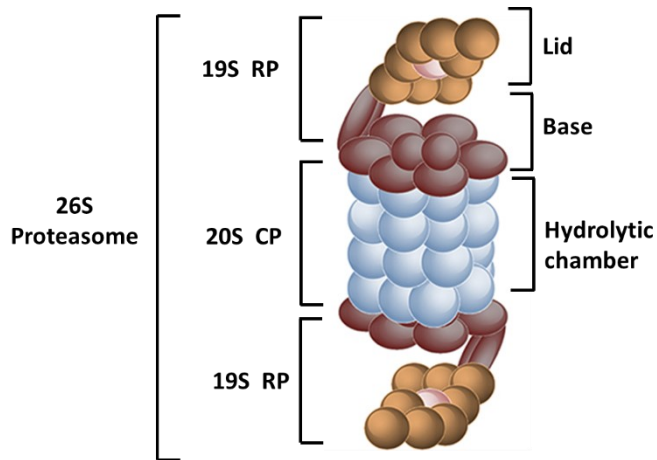
Figure 1.4 Proteasome structure

The proteins are then digested in the core particle by peptidases which trim them into small peptides and amino acids which can be recycled for protein synthesis.

Because of the importance of the UPS as a major degradation pathway, its dysregulation is often associated with multiple human pathologies.[1,2,15] Defaults in certain E3 ligases (e.g., parkin) or DUBs (e.g., UCHL1) are linked to neurodegenerative diseases such as Parkinson's or Alzheimer's disease.[16,17] Moreover, cellular mechanisms such as the regulation of growth signaling pathways, DNA replication and repair, as well as cytokinesis are in part controlled by the UPS. As a consequence, mutation of UPS genes contributes to the development and progression of certain cancers.[18] The implication of the UPS in several human disorders makes it a relevant pathway to tackle in drug discovery and attempt to disrupt or restore the function of components of the UPS are still being investigated both preclinically and clinically.[19,20]

1.2 Targeted protein degradation

1.2.1 Birth of proximity induced degradation

Two decades after the groundwork done by Ciechanover and others to decipher the mode of action of the UPS, a peculiar idea emerged about artificially modulating protein levels by controlling the ubiquitination step. In 1999, Kenten et al. from the biotech company Proteinix described in a patent application a peptidic "element" that would bring into close proximity a protein of interest (POI) and the ubiquitination system.[21] The purpose of the so called "element" was to allow the transfer of ubiquitin onto the POI (**Figure 1.5**).
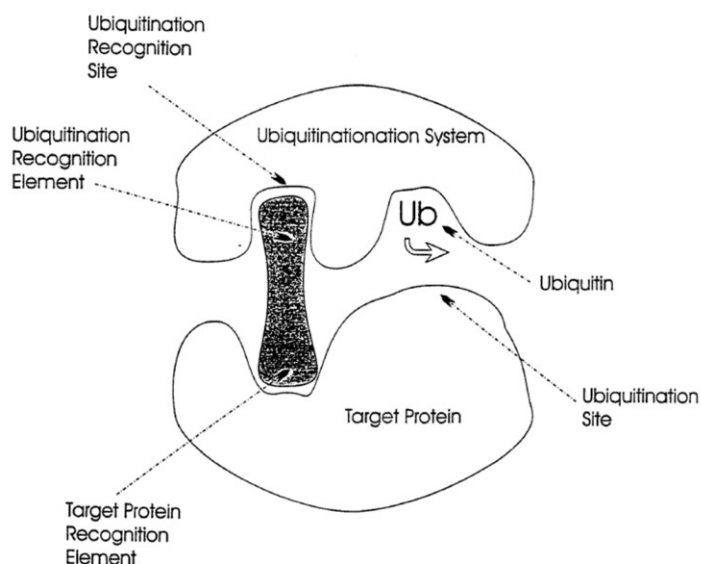
Figure 1.5 Initial proximity-induced degradation concept from Proteinix. Image reproduced with permission. [21]

Kenten and co-workers further suggested that degradation of the POI would be beneficial to treat various cancers and viral infections. In the same patent was cited the work from Gosink and Vierstra, who engineered E2 constructs fused to a peptide designed to recognize a defined POI. Using *in-vitro* cell-free assays, they were able to show that their E2 "Chimeras" could ubiquitinate and degrade their POI.[22] Expanding on the initial patent from Proteinix, Sakamoto, Crews and Deshaies introduced in 2001 the concept of targeted protein degradation (TPD) by designing a molecule coined a proteolysis targeting chimera (PROTAC)[23] (**Figure 1.6**).
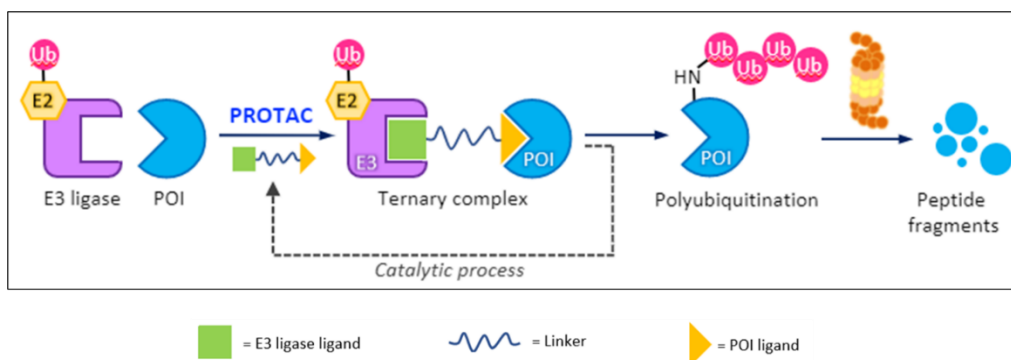
Figure 1.6 PROTACs mode of action. Image reproduced with permission.[10]

The bifunctional molecule was made of a warhead (a methionine aminopeptidase (MetAP2) inhibitor known as ovalicin), a short aliphatic linker and a peptide able to recruit a ubiquitin ligase SCF$^{\beta\text{-TRCP}}$. The designed PROTAC enabled the ubiquitination and degradation of MetAP2 in xenopus extracts and established the first experimental proof of concept for TPD with small a molecule as a POI binder[23] (**Figure 1.7**).
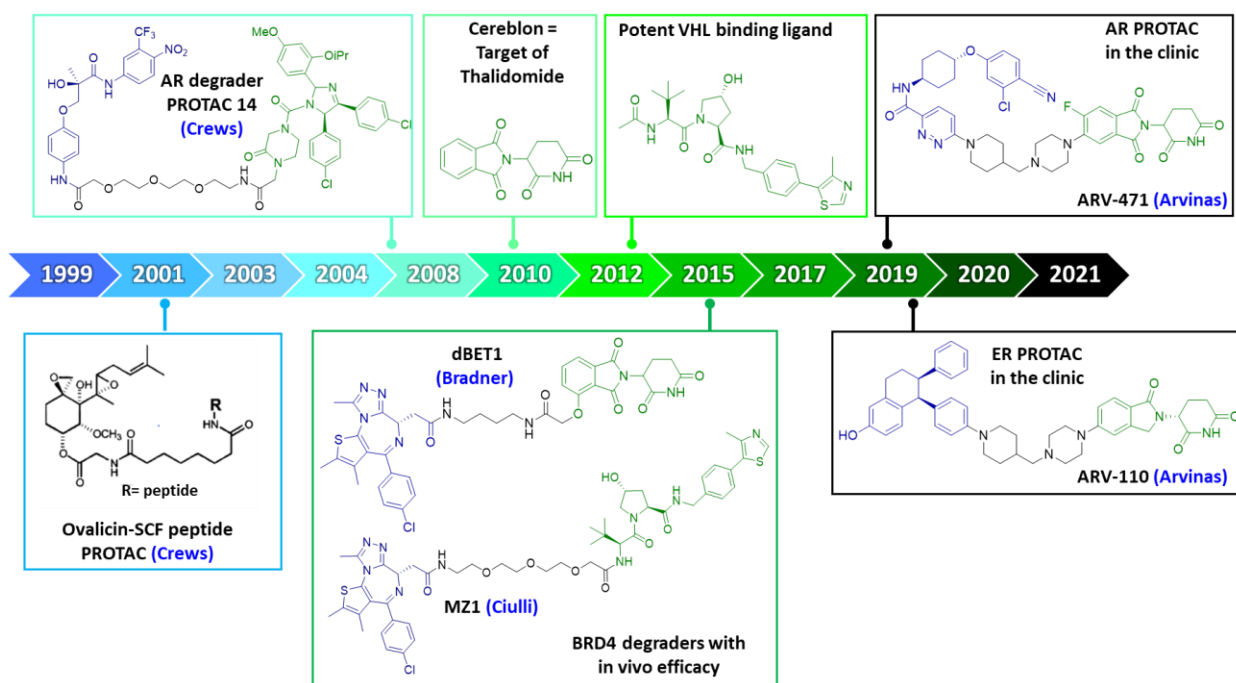
Figure 1.7 PROTACs development: from peptidic PROTACs to small-molecule PROTACs in the clinic. Image adapted with permission.[10]

A few years later, the same research group achieved the degradation of the androgen receptor and FKBP12 (both fused to green fluorescent protein, GFP), by recruiting Von Hippel Lindau tumor suppressor (VHL).[24] A short hydroxyproline-containing peptide derived from hypoxia-inducible factor 1α (HIF1α) was used to recruit VHL E3 ligase. Because of the peptidic nature of the VHL-recruiting motif, Crews' lab resorted to a polyarginine cell-penetrating sequence to aid the PROTAC enter the cells. Nonetheless, successful depletion of their POIs was observed by western blot analysis and fluorescence microscopy.

The first entire small molecule-based PROTAC made of a non-steroidal androgen receptor ligand (POI binder) and a MDM2 E3 recruiter known as nutlin was eventually published by Crews' lab in 2008.[25] Degradation of the androgen receptor was observed at 10 µM in HeLa cells (**Figure 1.7**). In 2010, the E3 ligase Cul4-cereblon was identified as the cellular target of the immunomodulatory imide drug (IMiD) thalidomide[26] and in 2012, Ciulli's lab reported tight binders of the VHL E3 ligase.[27] These two developments in the E3 ligase field culminated in the discovery of PROTAC **MZ1** and **dBET1**, potent degraders of the bromodomain proteins (BRDs)[28,29] (**cf. section 2.1.3**). The first *in vivo* efficacy data with a PROTAC were also generated with **dBET1** on a murine xenograft model of human leukemia cells where it proved to be efficacious.[29] Those *in vitro* and *in vivo* proof-of-concept studies stimulated more research around TPD both in academia and in industry.[30] In 2019, the biotech company Arvinas progressed into the clinic two degraders ARV-110 and ARV-471, for the treatment of metastatic castration-resistant prostate cancer (mCRPC) and estrogen positive, HER negative breast cancer, respectively.[31,32]

1.2.2 Proteolysis targeting chimeras

1.2.2.1 Main features of PROTACs

PROTACs represent a disruptive modality both in the field of chemical biology and drug discovery.[33–35] In comparison with more time-consuming genetic strategies such as RNA interference or CRISPR-cas9 used to knockdown or knockout a protein, PROTACs provide a straightforward alternative to study a protein function or pathway and validate a target.[36]

By inducing degradation, it has been demonstrated that PROTACs annihilates all functions of a protein including scaffolding functions.[37] As such, degraders constitute an excellent tool to fully understand the role of a protein. Addressing the non-enzymatic function of a POI can also be of therapeutic value as described by Crews' lab efforts to address the non-kinase related function of focal adhesion kinase (FAK).[38]

The mode of action of PROTACs is often described as "event-driven" as opposed to "occupancy-driven". Indeed, for a PROTAC to be efficacious, the formation of a ternary complex between the POI, the PROTAC and the E3 ligase is the main "event" that should take place[39] (**Figure 1.8**). This concept is different from traditional small molecule inhibitors which have to maintain binding to the POI often at high concentrations to show efficacy.

After ubiquitination of the POI, the PROTAC can dissociate from the ternary complex and binds to another molecule of POI to start another cycle. This process implies that PROTACs act catalytically and sub-stoichiometric amount of degraders are sufficient to deplete a POI.[40] From a drug discovery perspective, this feature of PROTACs can translate into low doses required to reach efficacy and to a higher therapeutic index (optimized dose range between efficacy and

toxicity).[34,41,42] Due to this three-component mode of action, increase in PROTAC concentrations can reach an optimum where high ternary complex formation occurs. Beyond that optimum, binary
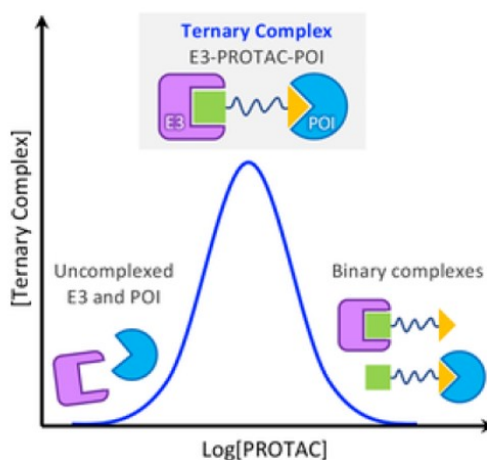
Figure 1.8 Ternary complex formation. Image reproduced with permission.[10]

interactions may prevail and less degradation will be observed. This has been described as the "hook effect".[39,43]

Another key aspect of the bifunctional degrader modality is the long-lasting efficacy observed as compared with small molecules inhibitors. As the POI is cleared from the cell, its rate of resynthesis becomes the rate-determining step for the duration of action of the degrader. Mares et al. have described RIPK2 degraders which maintained efficacy in absence of measured drug levels 72 h after initial dosing. This feature of PROTACs (decoupled pharmacokinetics versus pharmacodynamics) can be beneficial to reduce drug regimen and adjust drug dosages.[44]

An interesting finding about PROTACs is also the fact that a strong binding affinity from the warhead does not always correlate with a better degradation outcome. This observation raised the hypothesis that weak binders may be appropriate as POI ligands to build PROTACs. In the case of proteins labelled as "undruggable" (i.e., challenging targets lacking a well-defined ligand binding or enzyme active site), PROTACs are viewed as a great opportunity as low affinity binders may be more accessible to identify than inhibitors.[45,46]

Due to the plasticity of the ternary complex formation in the PROTAC mode of action, differential protein substrate specificity can occur while using the same warhead. Crews' and Gray's lab have shown that a promiscuous kinase warhead can degrade only part of the initial kinase pool the warhead has an affinity for.[47,48] The selectivity observed in those experiments was imparted to the nature of the protein-protein interactions (PPIs) occurring during ternary complex formation. Such PPIs can be leveraged to achieve selective degradation of unique protein isoform. As an example, by changing the orientation of the recruited VHL E3 ligase (via a new chemical attachment point on the VHL ligand), Smith et al. selectively degraded the mitogen-activated protein kinase p38α over p38δ.[49]

Finally, we note that PROTACs have been able to degrade proteins forming part of complexes. Farnaby et al. developed a degrader (ACBI1) against proteins of the BAF chromatin remodeling complex, SMARCA2 and SMARCA4.[50] Interestingly, not only ACBI1 induced the degradation

of the SMARCA targets it was designed for, but it also depleted two other BAF components ACTLA6 and PHF10.

A summary of PROTAC keys features is given in **Table 1.1** and underlines the transformative nature of these new molecules for both chemical biology and drug discovery.

Table 1.1 PROTACs main characteristics

Characteristics	Comments
Facile synthesis	Modular chemistry, not genetically engineered
Event-driven	Brief encounter between POI and E3 ligase during ternary complex formation triggers ubiquitination then degradation
Catalytic	PROTAC reused for multiple cycles of degradation
Degradative	Elimination of the target and all its function (including scaffolding functions)
Decoupled PK and PD	Long duration of action, remains efficacious after the PROTAC has been eliminated
Strong POI binder not required	Potential to tackle "undruggable" proteins
Isoform-selective degradation	Degradation of unique protein isoforms without modifying the warhead

1.2.2.2 Design and testing

The current design of PROTAC is still empirical. Considering a target for which a warhead is already available, a typical strategy would consist of combining various E3 ligands and linkers in a modular fashion to create a small library of PROTACs. The most widely used E3 ligands are pictured in **Figure 1.9**.
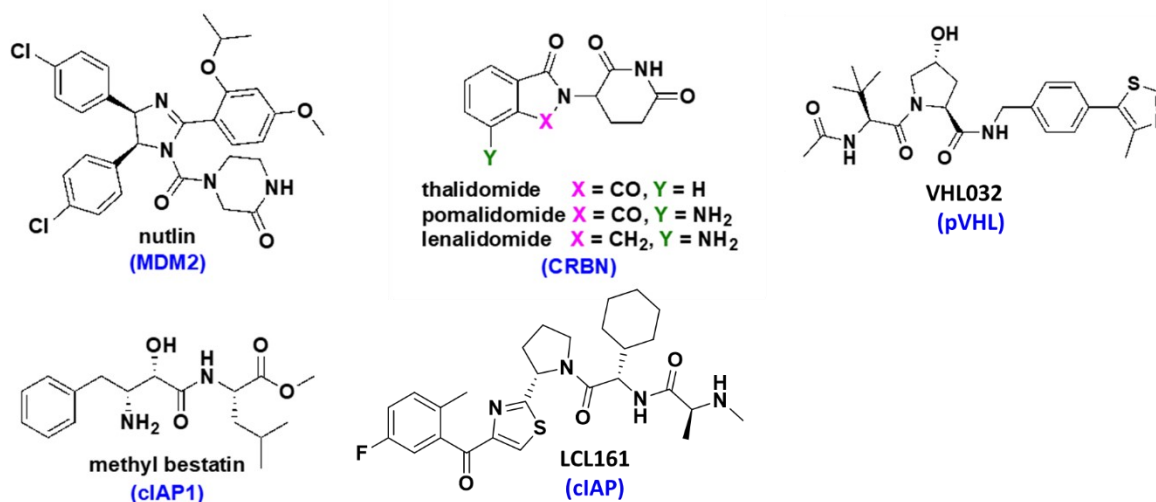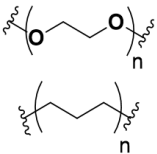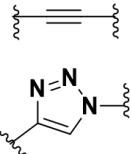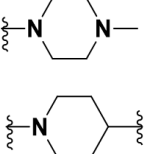
Figure 1.9 Main E3 ligase ligands used in TPD. Image adapted with permission.[10]

Together, IMiDs (thalidomide, pomalidomide, lenalidomide) and the VHL ligand are incorporated in more than 80% of the degraders reported to date.[10,51] The recruiters of cellular inhibitor of apoptosis Protein 1 (cIAP1) have been used extensively by Naito's group in molecules named specific and non-genetic inhibitor of apoptosis protein [IAP]-dependent Protein Erasers (SNIPERs).[52–54] However, since cIAP inhibitors tend to induce cIAP depletion, such ligands remain less attractive than the IMiDs or the VHL ligand. Finally, the use of nutlin ligands which recruit MDM2 remains rare.[55,56]

Since the binders for the POI and the E3 ligase are often already optimized, the last portion of a PROTAC amenable for investigation is the linker which plays an important role in both the pharmacokinetics and pharmacodynamics characteristics of a degrader.[57–60] The most common type of linkers used in PROTACs design is provided in **Table 1.2**.

Table 1.2 Most common linkers used in PROTACs design.

PEG and alkyl	Alkyne and triazole	Piperazine and piperidine

Polyethylene glycol (PEG) chains tend to be favored as they bring flexibility and polarity to the degrader.[57] Various lengths of alkyl chains are easy to source commercially, hence they are incorporated in many degraders. A trend towards rigidification has also been observed with linkers such as alkynes, piperidines and piperazines.[61,62] With less rotatable bonds, fewer ternary complexes poses are possible and this may lead to a preferred complex with greater ubiquitination efficiency. Permeability can also be positively affected with a less flexible degrader. As for triazoles, the ease of click chemistry such as Huisgen copper-catalyzed azide-alkyne cycloaddition, has encouraged their inclusion into linkers.[63]

Regarding the linker length, a study from Zorba et al. found that short linkers incorporated in their bifunctional (with less than 5 PEG units) were detrimental for degradation of Bruton's tyrosine kinase (BTK) while longer linkers were more favored.[64] By studying ternary complex formation using a TR-FRET assay, it was shown that PROTACs with short linkers were not forming good ternary complexes while degraders with more than 5 PEG units would. Since every pair of POI and E3 ligase behave differently, general rules for linker design have not yet been clearly laid out and the results from Zorba's and coworkers do not always apply.

In order to move towards rational design of PROTACs, the Ciulli group extensively used a combination of biophysical assays (e.g., surface plasmon resonance (SPR), isothermal titration calorimetry, ITC) and ternary complex crystal structures to establish binding cooperativity as a key parameter to focus on for PROTAC optimization.[65] Cooperativity α, is defined as the influence of the initial binary event (e.g., between the PROTAC and the POI) on the binding affinity for the third component of the ternary system (here, the E3 ligase). Numerically, it is obtained by the ratio between the dissociation constants of the binary and tertiary systems ($\alpha = K_d^{\text{binary}}/K_d^{\text{tertiary}}$). When α >1, there is positive cooperativity, and the first binary interaction facilitates the ternary complex formation. Inversely, when α <1, there is negative cooperativity. In their study of PROTAC **MZ1**,

Ciulli's lab found that complexes with positive cooperativity ($\alpha > 22$) caused more efficient degradation than complexes with negative cooperativity ($\alpha < 1$).[65] However, the study from Zorba et al. on BTK had an opposite outcome. Their PROTAC with the highest cooperativity was not the best degrader.[64] Considering that most binding studies are conducted in cell-free systems which cannot fully recapitulate the complexity of the intracellular environment, there are some limitations to the predictability of an approach purely based on biophysical measurements.

Although X-rays of ternary complexes have been used to optimize a few degraders,[66,67] the method is limited by the fact that only one ternary complex is captured among all possible complexes that can be formed. As such, an optimization campaign may be biased towards only one X-ray pose. Nonetheless, accumulation of structural data on PROTACs will help better understand the dynamics at play and improve the design strategies.[68]

After PROTACs have been designed and synthesized, testing in an endogenous and relevant system should take place. A great number of publications present western blots data to report on endogenous protein levels. Although this semiquantitative technique is not complicated to set up, it has a low throughput, and it is time consuming. As research on TPD has rapidly expanded, novel assays complementary to western blots have emerged such as fluorescence and luminescence-based reporter assays.[69] Of note is the HiBiT assay developed by Promega[70] (**Figure 1.10**). It consists of a nanoluciferase enzyme split into a HiBiT peptide and a LgBiT core, the two parts being complementary (with picomolar affinity). Besides, the POI is tagged with HiBiT using CRISPR-Cas9 in cells stably expressing LgBiT. The signal emitted by the reconstituted nanoluciferase in cells is meant to decrease if the HiBiT-tagged POI is degraded by a PROTAC. This system enables high throughput and quantitative assessment of novel degraders.
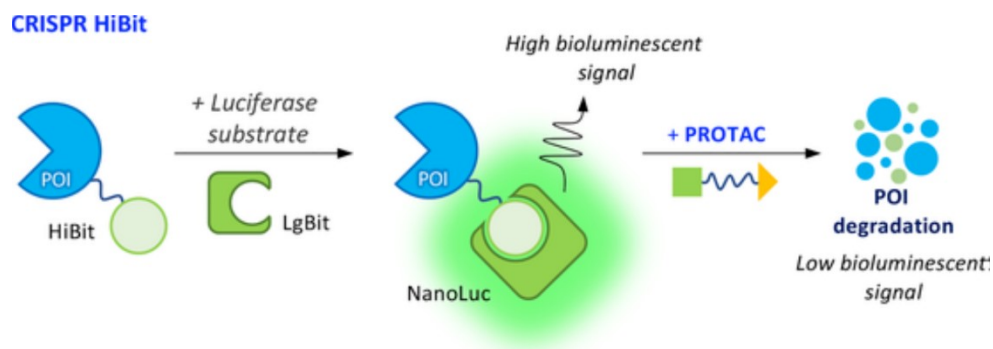
Figure 1.10 HiBiT system from Promega. Image reproduced with permission.[10]

The main parameters extracted from a protein degradation assay are the concentration at which 50% degradation is achieved (DC_{50}) and the maximal degradation level obtained (Dmax).[70]

1.2.3 Molecular glues

Alongside the increasing research done on PROTACs, more light has also been brought on molecular glues.[71–73] Structurally and mechanistically, the two entities differ. While PROTACs are tripartite compounds made of a POI binder, a linker and an E3 ligase recruiter, molecule glues are linker-free monofunctional molecules having an initial low affinity for their binding partners. The mode of action of molecular glues is quite unique as it involves the reprogramming of PPIs between two binding partners to ensure a tight ternary complex leading to degradation[74] (**Figure 1.11 A**). It has been discovered that IMiDs act as glues by binding to cereblon and by inducing the recruitment of neosubstrates (such IKZF1, IKZF3, GSTP1, SALL4) for ubiquitination and subsequent degradation. This peculiar mechanism is thought to involve a change of conformation of cereblon, and exposure of a cryptic moiety not present prior to the binding of IMIDs.[75–77]
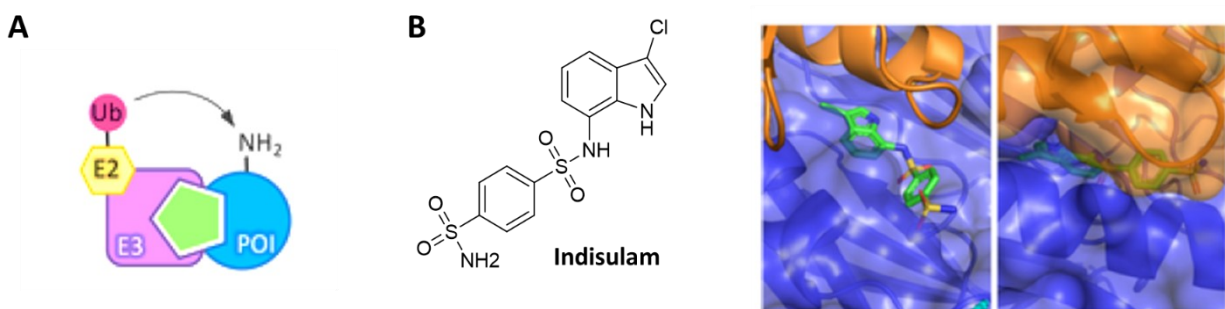
Figure 1.11 Molecular glues mode of action (A) schematic representation of the tight binding induced by a glue. (B) Snapshots of the crystal structure of the human DDB1-DDA1-DCAF15 E3 ubiquitin ligase (blue) in complex with RBM39 (orange) and Indisulam (green) (PDB: 6SJ7). Image adapted with permission.[10]

Auxin is an example of molecular glue from the plant realm,[78] but the discovery of such compounds remains serendipitous. For instance, indisulam is an anticancer drug for which the mode of action was unveiled recently (**Figure 1.11 B**). Indisulam induces the degradation of the splicing factor RBM39 by recruiting the E3 ligase DCFA15 despite having no measurable affinity for RBM39.[79]

Overall, thanks to a reasonable molecular weight and favorable physicochemical properties, molecular glues maintain a high level of attractiveness for medicinal chemists. Research towards rational identification of glues in underway despite the challenges the discovery of this class of molecules brings.[80]

1.2.4 Scope of Targeted protein degradation

With targeted protein degradation being widely deployed in academic settings and in industry, the number of targets amenable for degradation is consistently rising. At the time the data was compiled for this thesis, a total of 83 human and 2 viral target proteins had been successfully knocked down by a peptidic or small molecule-based PROTACs (**Table 1.3**).

Table 1.3 Summary of proteins degraded by small molecule and peptide-based PROTACs. Table adapted with permission.[10]

Target	Target class	Therapeutic area[a]	Reference
ADRA1A	GPCR	ONC	81
AHR	Transcription factor	ONC	82
AKT1/2/3	Kinase	ONC	83
ALK	RTK	ONC	84–86
AR	NHR	ONC	87–90
AURKA/B	Kinase	ONC	91
BCL2	Antiapoptotic protein	ONC	92
BCL6	Transcription factor	ONC	93
Bcl-xL	Antiapoptotic protein	ONC	94
BCR-ABL	Kinase	ONC	95–97
BLK	Kinase	ONC	98
BRAF	Kinase	ONC	99
BRAF (V600E)	Kinase	ONC	100
BRD2/3/4	Epigenetic target	ONC	101–105
BRD7	Epigenetic target	ONC	106
BRD9	Epigenetic target	ONC	106,107
BTK	Kinase	ONC	108,109
BTK (C481S)	Kinase	ONC	108
c-ABL	Kinase	ONC	97
CDC20	Kinase	ONC	110
CDK2	Kinase	ONC	111,112
CDK4	Kinase	ONC	113
CDK5	Kinase	ONC	112
CDK6	Kinase	ONC	114
CDK8	Kinase	ONC	115
CDK9	Kinase	ONC	111,116
c-IAP (BIRC2)	E3 ligase	ONC	117
CK2	Kinase	ONC	118
CRABPI/II	Carrier protein	ONC	117,119
CRBN	E3 ligase	ONC/IA	120–122
CREPT (RPRD1B)	Transcription modulator	ONC	123
EED (PRC2 complex)	Transcription factor	ONC	124,125
EGFR	RTK	ONC	126
EGFR (L858R/T790M)	RTK	ONC	127,128
ER	NHR	ONC	129–131
ERK1/2 (MAPK3/1)	Kinase	ONC	132
ERRα	NHR	ONC	133,134
FAK (PTK2)	Kinase	ONC	135,136

FAK2 (PTK2B)	Kinase	ONC	[137]
FKBP12	Immunophilin	CNS/IA	[101,138,139]
FLT3	RTK	ONC	[140]
FRS2	RTK effector	ONC	[141]
GSPT1	Translation factor	ONC	[142,143]
HDAC1/2/3	Epigenetic target	ONC	[144]
HDAC6	Epigenetic target	ONC	[145,146]
HER2	RTK	ONC	[126]
HGFR (c-Met)	RTK	ONC	[126]
HMGCR	Oxidoreductase	CVD	[147]
HTT	Scaffolding protein	CNS	[148]
IRAK4	Kinase	IA	[149]
JAK1/2	Kinase	ONC	[150]
KRAS (G12C)	Hydrolase	ONC	[151]
LRRK2	Kinase	ONC/CNS	[152]
MAPK11 (p38β)	Kinase	ONC	[153]
MAPK13 (p38δ)	Kinase	ONC/IA	[154]
MAPK14 (p38α)	Kinase	ONC/IA	[153,154]
MCL1	Antiapoptotic protein	ONC	[92]
MDM2	E3 ligase	ONC	[155,156]
MetAP2	Peptidase	ONC	[157]
NS3/4A	HCV protease	ID	[158]
PARP1	Glycosyltransferase	ONC	[159,160]
PCAF/GCN5 (KAT2B)	Epigenetic target	ONC/IA	[161]
PDE4	Hydrolase	IA	[131]
PI3K	Kinase	ONC	[162]
PIR	Transcription coregulator	ONC	[163]
PLK1	Kinase	ONC	[164]
RAR	Transcription factor	ONC	[165]
RIPK2	Kinase	IA	[134]
Rpn13 (ADRM1)	Ubiquitin receptor	ONC	[166]
SGK3	Kinase	ONC	[167]
SHP2 (PTPN11)	Phosphatase	ONC	[168]
SIRT2	Epigenetic target	ONC	[169]
SLC91A	Carrier protein	ONC	[170]
SMAD3	Transcription modulator	ONC/FBR	[171]
SMARCA2/4	Transcription factor	ONC	[172]
SNCA (α-Synuclein)	Synapse control	CNS	[173]
STAT3	Transcription factor	ONC	[174]
TACC3	Motor spindle protein	ONC	[175]
Tau	Microtubule stabilisation	CNS	[176]
TBK1	Kinase	ONC	[177]
TRIM24	Transcription factor	ONC	[178]

TrkC	RTK	ONC	179
VHL	E3 ligase	BLD	180
WEE1	Kinase	ONC	181
X-Protein	HBV viral protein	ID	182

BLD: Blood disorders; CNS: Central nervous system diseases; CVD: cardiovascular diseases; FBR: Fibrotic diseases; IA: Inflammation and autoimmune diseases; ID: Infectious diseases; ONC: Oncology

A closer look at therapeutic areas highlights that the field of oncology has greatly benefited from the research community focus on degraders. With reported DC_{50} values often below 100 nM and along with *in vivo* proof-of-concept, degraders aimed at nuclear hormone receptors, kinases and transcription factors have shown great promise[42,183] (**Figure 1.12 A**).
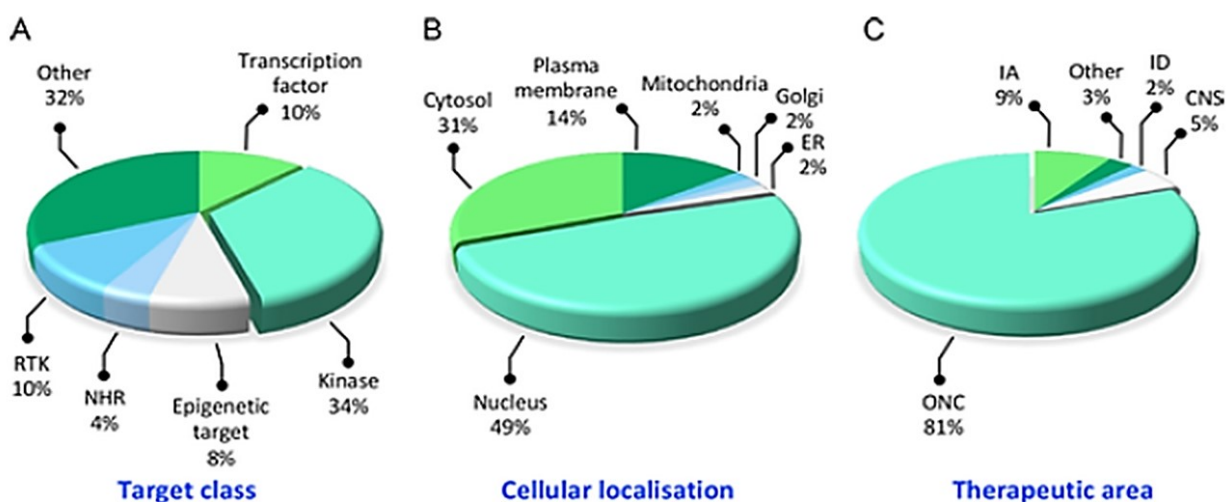
Figure 1.12 Proteins degraded by PROTACs according to (A) target class (B) cellular localization and (C) therapeutic area. NHR, Nuclear hormone receptor; RTK, Receptor-tyrosine kinase; ER, Endoplasmic reticulum; CNS, Central nervous system diseases; IA, Inflammation, and autoimmune diseases; ID, Infectious diseases; ONC, Oncology. "Other" in "Target class" = enzymes other than kinase. Image adapted with permission.[10]

The broad intracellular expression profile of the E3 ligases cereblon and VHL in various cell lines has permitted the degradation of nuclear and cytosolic proteins (**Figure 1.12 B**). Besides cancer-related targets, proteins involved in the central nervous system (e.g., LRRK2) and autoimmune diseases (IRAK4, RIPK2) have also been pursued for various indications[184] (**Figure 1.12 C**).

After a first rewarding decade of exciting research leading to clinical compounds, a new era is being uncovered in the TPD field on various fronts. First, the limitations due to the small number of E3 ligases recruited is being addressed.[51] Identifying novel E3 ligands would increase the number of POI-E3 combinations to discover a potential degrader. Furthermore, recruiting E3 ligases with diverse expression levels or localization would lead to highly selective degraders.

The Nomura and Cravatt group have pioneered the use of chemoproteomics approaches to discover covalent E3 ligands. Through their efforts, three new E3 ligases (DCAF16, RNF114 and RNF4) have been added to the list of recruitable E3s[185–187] (**Figure 1.13**).

Compound or covalent fragment	**KB02**	**Nimbolide**	**CCW16**
E3 ligase recruited	DCAF16	RNF114	RNF4
Protein degraded	BRD4	BRD4	BRD4
	FKBP12	BCR-ABL	
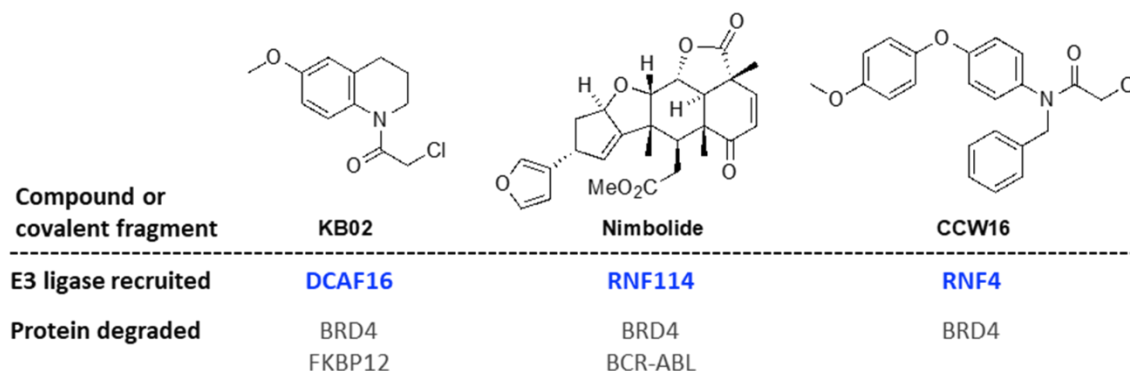
Figure 1.13 New covalent E3 ligands. Image reproduced with permission.[10]

Secondly, another avenue for targeted degradation via the lysosome has been opened by the research work from Bertozzi's lab who has developed lysosome targeting chimeras (LYTACs).[188]Those antibody-polysaccharides conjugates enable the degradation of extracellular and membrane-bound proteins by engaging the mannose-6-phosphate receptor (M6PR). Internalization of the POI is achieved after binding of the polysaccharide moiety to M6PR. The LYTAC technology is now being developed as a therapeutic modality. Following on from Bertozzi's approach, other groups are investigating degradation via the autophagy pathway.[189–191] Thirdly, TPD has revealed that molecule induced proximity can be a powerful mean to interfere with intracellular biological processes. Ubiquitination is now viewed as one post-translational modification (PTM) among others and the field is now broadly open to develop new tools to hijack other known PTMs (e.g. (de)phosphorylation, deubiquitination, acetylation, etc.) for therapeutic purposes.[192–194]

1.2.5 Current limitations of targeted protein degradation

The existing limitations associated with PROTACs relate to their physicochemical properties, their toxicity and resistance profile.
Being tripartite compounds, the molecular weight of PROTACs often reach close to 1 kDa. In addition, the presence of multiple hydrogen bond donors often imparts them with poor permeability while high lipophilicity and high number of rotatable bonds tend to affect their solubility.[195] Since oral dosing is a major delivery route for therapeutics and is also considered for PROTACs, their physicochemical properties represent an optimization challenge for medicinal chemists.[196,197] Identifying warheads and E3 ligands with properties already aligned with Lipinski's rules would be a key aspect in obtaining developable compounds. The two clinical stage degraders from Arvinas incorporates the smaller IMIDs E3 ligands including a piperazinomethyl

piperidine linker which may significantly improve the overall pharmacokinetic profile of those compounds.[198]

Several PROTACs have demonstrated the ability to degrade the mutated protein in resistant cancers thanks to a unique mode of action which does not rely on strong binding from the warhead. Whether the resistance from the cancer is caused by point mutation or overexpression of the inhibited protein, PROTACs have been utilized in vitro and in vivo where small molecules inhibitors were ineffective.[199–202] As an example, Crew's lab reported PROTAC **SJF-068**, as a degrader of several mutated forms of the kinase BRAF, including those resulting from treatment with the BRAF inhibitor vemurafenib[203] (**Figure 1.14**).
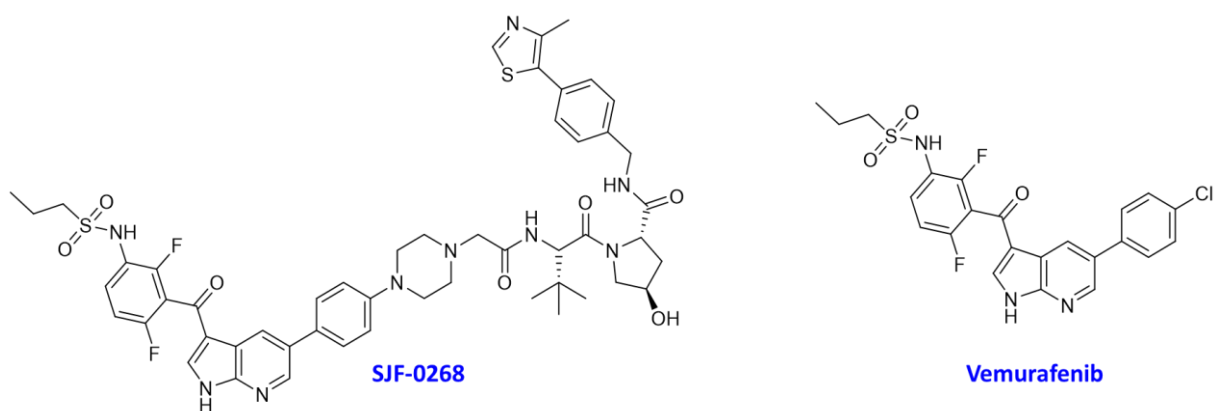
Figure 1.14 BRAF degrader and its warhead vemurafenib.

Another striking case is the degradation of the mutated form of BTK (C481S) with PROTAC **MT-802** which has overcome the lack of cysteine residue necessary for the inhibitor ibrutinib to be efficacious[204] (**cf. section 3.2.3**).

Despite the benefits brought by PROTACs to overcome resistance developed by cancer cells, PROTACs themselves can also induce resistance. In most instances, the PROTAC-mediated resistance observed affected a component of the UPS, notably the E3 ligase.[205] Ottis et al. showed that loss of function from the UPS component was the main resistance mechanism for both VHL- and cereblon-based BRD4 degraders.[206]

In a recent report, Kurimchak et al. found that cancer cells developed resistance to PROTACs targeting the GTPase KRAS via overexpression of the drug efflux protein pump MDR1.[207] With regards to UPS-derived resistance, expanding the number of E3 ligases which can be recruited for TPD would help in designing combination therapies from structurally diverse PROTACs.

As more degraders move towards the clinic, toxicological information is being collected first in preclinical studies while human data will come gradually.[208] Potential findings will either come from on- or off-targets effects. Thanks to the specificity carried by the PROTAC warhead, degradation of a unique target can often be achieved. However, when using IMiDs ligands as E3 recruiter, degradation of secondary targets should be monitored. Concurrent degradation of additional targets has been observed with PROTACs bearing thalidomide or lenalidomide in their structure.[77,209]

In such cases, large scale proteomics analysis is useful to identify such collateral degradation events and ultimately may help in explaining in vivo findings.[210] If the POI intended for degradation is ubiquitously expressed, then knockdown of that target protein may lead to unwanted on-target effects. It is common that the protein to be addressed in the "disease" state is also required in the "healthy" state. Thus, means to achieve selectivity may need to be developed.

Although PROTACs have shown promising results in terms of duration of action (i.e., maintenance of the pharmacodynamic effect after the PROTAC has been cleared), a prolonged knockdown of a protein being slowly resynthesized could lead to on-target side effects.[208,211] Being able to restrict or limit the efficacy of the degraders may be beneficial to control those unwanted outcomes.

1.3 Research objectives

1.3.1 Conditional control of targeted protein degradation

For targeted protein degradation to realize its full potential as therapeutics, some of the limitations mentioned above will have to be addressed, in particular those related to tissue specificity. In parallel to the work presented in this thesis, some research has been carried out by the Tate group and others to develop degraders with enhanced selectivity profile[212] (i.e., with degradation of the POI only in the intended tissue and nowhere else). For instance, by conjugating a BRD4 degrader to the antibody trastuzumab (Herceptin®), the Tate and Baker groups have shown specific degradation of BRD4 only in HER2 positive breast cancer cell lines (SK-BR3) while leaving BRD4 levels unaffected in HER2 negative cells (MCF-7)[213] (**Figure 1.15**).
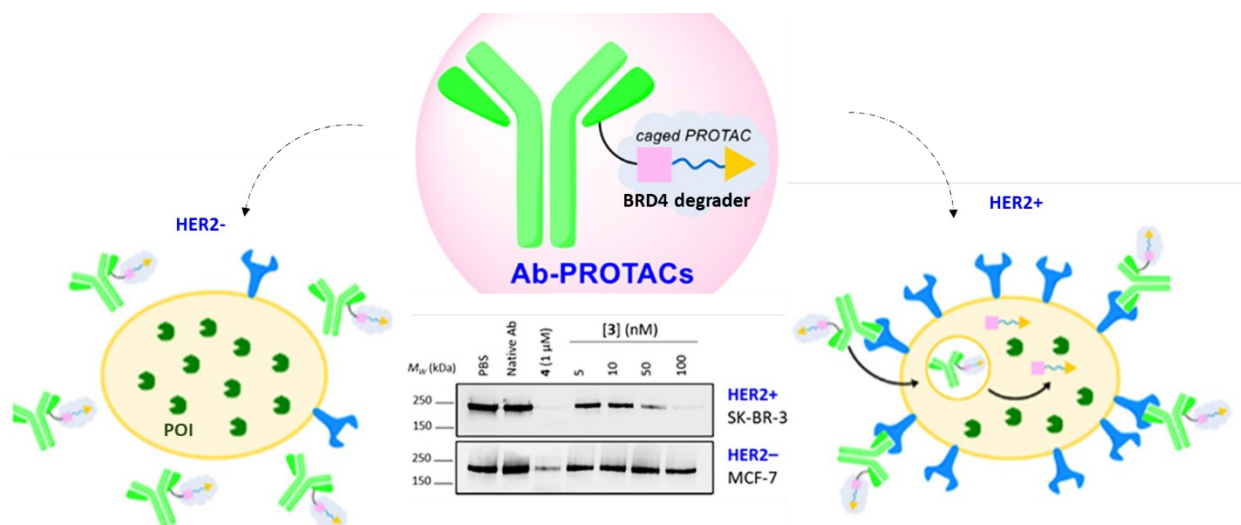
Figure 1.15 Ab-PROTAC from the Tate and Baker research groups. Degradation occurs only in HER2+ cell line leaving BRD4 unaffected in HER2- cells. Image adapted with permission.[213]

Similarly, by exploiting the overexpression of the folate 1 receptor (FOL1R) in certain cancer cells, the Jin and Wei groups developed IMiD- and VHL-based degraders conjugated to folic acid to accomplish FOL1R-dependent internalization and degradation of their POI.[214,215]

In both cases (antibody conjugates and folic acid conjugates), the receptors on the cell surface were successfully utilized to attain tissue selectivity although the activation of the degrader was dependent on an intracellular hydrolytic step. With the goal of maintaining tissue specificity and having a more precise spatiotemporal control of degraders' activity, we envisioned the design of novel PROTACs as therapeutics which are (de)activated by an intra- or extracellular stimulus. The triggering mechanism of (de)activation should render the PROTAC activity conditional on the presence or absence of the stimulus.

From a chemical biology perspective, having degraders with a greater level of control in space and in time would also allow precise study of a protein function and its related pathway.

1.3.2 Harnessing extra- and intracellular stimuli

To achieve spatiotemporal control of bifunctional degraders' activity, we first turned to light as an extracellular stimulus which operates in time and space and has been used as a reliable strategy to achieve precise control of many cellular functions with exquisite resolution.[216] In addition to being noninvasive, the intensity, wavelength, and exposure time from the light source can be accurately adjusted.[217] The combination of PROTACs with light should offer an excellent spatiotemporal control over protein knockdown and in the case of a disease-relevant protein, may lead to some applications in the field of photopharmacology via localized activation in the desired tissue only.[218,219] Two designs were considered for the light-activated degraders, namely caged degraders described in **Chapter 2** which are irreversibly activated and photoswitchable degraders which should offer a reversible on/off mechanism and are described in **Chapter 3**.

Intracellular methods were also considered to achieve conditional control of PROTACs activity. Here, we suggest leveraging on unique pre-existing conditions within the cell to activate a degrader. Differences between cancer cells and healthy cells are often detected at the level of the cellular membrane due to the expression of distinct receptors.[220] In addition, the biochemistry occurring in those two cell types is also unique and characteristics such as glucose consumption, activity of metabolic enzymes, pH of the cytosol or oxygen levels are dissimilar in healthy cells versus cancer cells.[221] The latter component which separates the normoxic state (i.e., healthy cells with atmospheric oxygen supply) and hypoxic state (cancer cells with low oxygen levels) has been utilized to design drugs with an oxygen level-dependent mechanism.[222,223] Thus, it is proposed that TPD with a PROTAC sensitive to intracellular oxygen levels would constitute a novel, selective and conditional way of controlling protein degradation (**Chapter 4**).

1.3.3 Objectives of the research work

The research work presented in this thesis summarizes the investigation towards the conditional control of newly designed protein degraders with the purpose of knocking down a protein with a high level of spatiotemporal control. The objectives of the research were:

-the design and synthesis of caged, photoswitchable, and hypoxia-sensitive PROTACs.

-the evaluation of light as an external stimulus to enable the control of PROTACs activity.

-the evaluation of oxygen level as an intracellular stimulus to modulate the activity of PROTACs.

Bifunctional degraders have been given diverse names and acronyms in the literature. In this thesis, the original term "PROTAC" and the term "degrader" will be used as synonyms. For the light-controlled PROTACs described from the research we have conducted and from the published work from others, the terms "caged [degrader/PROTAC]" and "(photo)switchable [degrader/PROTAC]" will be used for consistency and clarity. Some of the acronyms given to light-activated PROTACs are listed in **Table 1.4**.

Table 1.4. Acronyms given to light activated PROTACs.

Given acronyms	Full name	reference
AzoPROTACs	Azobenzene-proteolysis targeting chimeras	[224]
PHOTACs	PHOtochemically TArgeting Chimeras	[225]
PhotoPROTACs	Photoswitchable PROTACs	[226]
AP-PROTACs	Arylazopyrazole photoswitchable PROTACs	[227]
Pc-PROTACs	Photo-caged PROTACs	[228]
Opto-PROTACs	Optically activated PROTACs	[229]

Chapter 2 | Caged degraders

2.1 Light-mediated protein degradation

2.1.1 From optogenetic to caged molecules

The spatiotemporal control of cellular protein concentration with light can be engineered in principle at the DNA, mRNA, or protein level.[230,231] Light-activated transcription factors and RNA-binding modules have been described for such an endeavor.[232,233] However, a delay between the light-triggered event and the effect on protein stability often results in sub-optimal temporal resolution. As an alternative, the development of light-sensitive tools acting directly at the protein level (i.e., after transcription and translation) has proven to be a robust and preferable option to regulate intracellular protein concentration.[234,235] The earliest example of light-mediated control of protein abundance combined the use of the cell degradation machinery (the UPS) and a protein borrowed from the plant realm, the light oxygen voltage sensing protein (LOV2).[236]

LOV2 acts as a sensor which promotes phototropism in plants and fungi via its blue light- sensitive flavin chromophore.[237] The change of conformation triggered by exposure of LOV2 to blue light via a photochemical reaction has been exploited to reduce intracellular protein concentration. In 2013, Renicke et al. developed a construct in which their target protein (red fluorescent protein, RFP) was fused to a LOV2 domain.[238] A 37-amino acid long peptide from ornithine decarboxylase (ODC), which is recognized as a degradation signal by the proteasome, was furthermore attached to the LOV2 domain (**Figure 2.1**). In absence of light, the ODC degron was masked due to the folding of LOV2. Exposure to blue light revealed the degron through unfolding of LOV2 and led to the degradation of the whole construct in *Saccharomyces cerevisiae*.
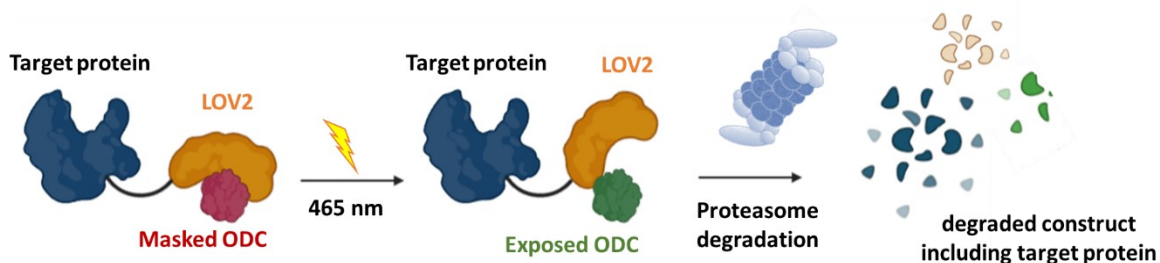
Figure 2.1 Light induced protein degradation with LOV2 and ODC degron. Upon irradiation with blue light (465 nm), a change of conformation of LOV2 allows the ODC degron to be exposed and triggers proteasomal degradation.

In a similar approach, Bonger et al. developed the blue-light inducible degron (B-LID) which consists of a fusion construct between a cryptic tetrapeptide degron (Arg-Arg-Arg-Gly) and LOV2.[239] B-LID was linked to their target protein (yellow fluorescent protein (YFP) or mCherry) (**Figure 2.2**). Both in Zebrafish and mammalian cells, reduction in fluorescence intensity for YFP and mCherry was only achieved after irradiation with blue light (465 nm). The data obtained confirmed the unfolding of LOV2 to expose the tetrapeptide sequence and trigger degradation.

Those two proofs of concept studies served as a catalyst to further investigate light-mediated protein degradation.
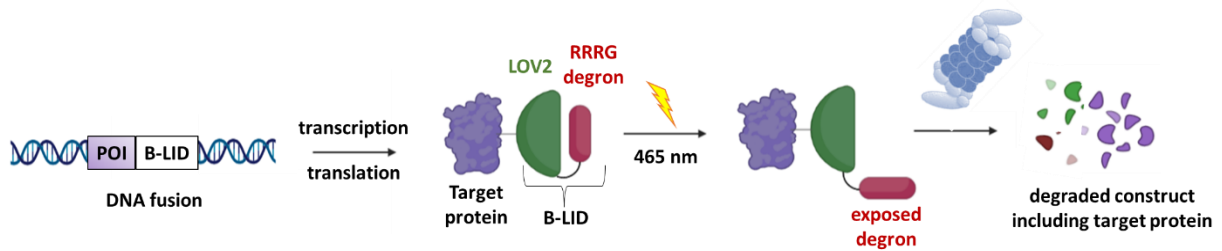
Figure 2.2 Light-induced protein degradation with B-LID system. Upon irradiation with blue light (465 nm), a change of conformation of LOV2 exposed the tetrapeptide degron allowing for recognition by the proteasome and subsequent degradation of the target protein.

With the desire to simplify and broaden the scope of the previous methods, Delacour et al. developed a small molecule photo-triggered system in mammalian cells using the plant hormone auxin.[240] An artificial SCF E3 ligase (Skp1/Cul1/F-box) was engineered by expressing the auxin-binding protein TIR-1 in HEK293 cells. In parallel, an auxin inducible degron sequence (AID) was fused to a protein of interest (eGFP) (**Figure 2.3**). Recognition between the AID and the E3 ligase TIR1 box, mediated by auxin, was prevented by attaching a caging group to the plant hormone. Within this system, eGFP degradation (observed both by Western blot and fluorescence microscopy) could only be obtained after cells had been irradiated at 365 nm or 405 nm. Rapid uncaging of auxin resulted in proximity-driven ubiquitination of AID by the E3 and subsequent proteasomal degradation of eGFP.
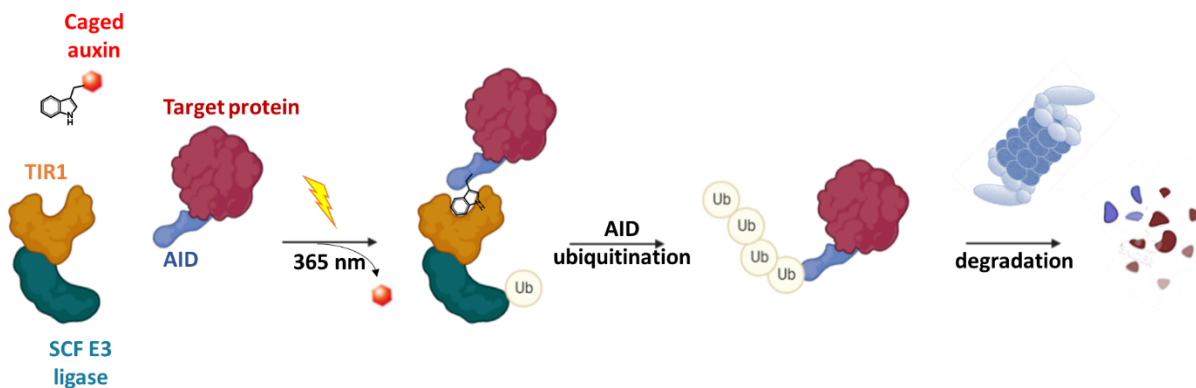
Figure 2.3 Light-induced protein degradation with caged auxin. Upon irradiation with UV light (365 nm), auxin loses its caging group and brings into close proximity the auxin inducible degron (AID) and the SCF E3 ligase. Subsequent ubiquitination of the AID is triggered, followed by degradation of the fused construct AID-target protein.

A summary of the methods described to accomplish light-triggered protein degradation is presented in **Table 2.1**.

Table 2.1 Light-mediated protein degradation approaches

Target Protein	Light triggered system	Degron sequence	Irradiation time*/ time to degradation
Red fluorescent protein (RFP)	Light oxygen voltage protein (LOV2)[238]	Murine ornithine decarboxylase (ODC	1 h / few hours
Yellow fluorescent protein (YFP) and mCherry	Light oxygen voltage protein (LOV2)[239]	Tetrapeptide (RRRG)	1-2 h / 2 h
eGFP	Caged auxin[240]	Auxin inducible degron (AID)	2- 8 min / 20 min

*Irradiation time = average length of time the system is irradiated for; time to degradation = average length of time it takes to observe degradation

While optogenetic methods are potentially applicable to any protein, generation of the optimal construct can be a lengthy process. In the examples mentioned above, both the irradiation time and temporal resolution exceeded hours despite LOV2 kinetics of activation being on a timescale of microseconds. Achieving the control of protein degradation in a few steps, without genetic engineering and with high spatiotemporal resolution is the ambition we set to reach using bifunctional degraders. The research work from Delacour et al. paved the way towards spatiotemporal control of protein stability uniquely by means of small molecules. In the same manner, our proposed approach relies on the use of a caging strategy but applied to PROTACs in order to control protein stability with high precision.

2.1.2 Caged PROTAC design

In this section, the investigation towards the control of a degrader's activity with light using a photosensitive appendage is described. Upon irradiation with UV light, we aimed to achieve the irreversible release of an active degrader which will ultimately trigger the disposal of a protein in the proteasome (**Figure 2.4**)
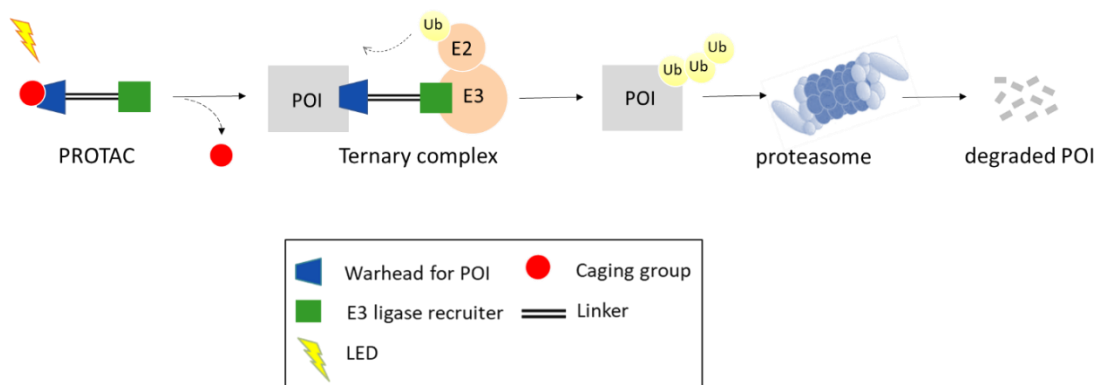
Figure 2.4 Caged PROTAC concept

The design of a caged degrader requires prior knowledge of the structure-activity relationship (SAR) of each individual component of the PROTAC. Key functional groups or binding interactions between the warhead and the protein of interest, or between the E3 ligand and its respective ligase can be leveraged to build a caged degrader.

Besides the structural design aspects, other key properties required for a caged degrader include a reasonable permeability and intracellular stability along with the ability to quickly release the PROTAC in high yield following photolysis. The three methods to generate a caged degrader - attachment to the E3 ligand, to the POI warhead or on the linker are described in the subsequent sections (**Figure 2.5**).
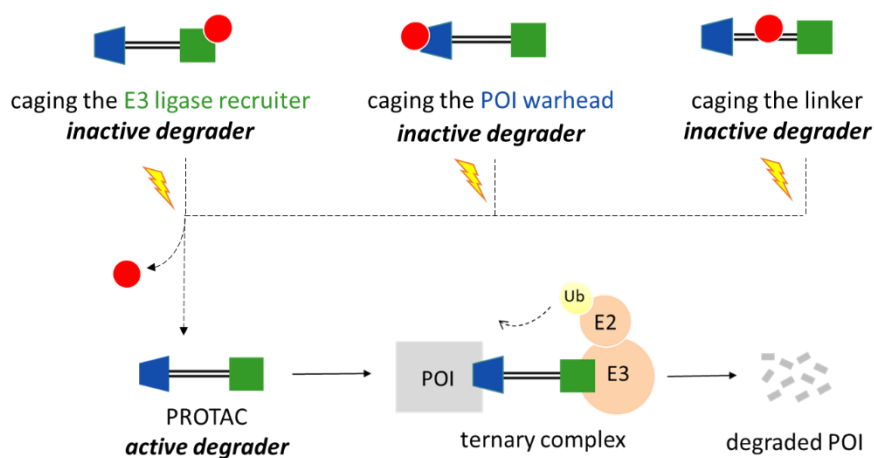
Figure 2.5 Various caged PROTAC design

2.1.2.1 Caging the E3 ligase ligand

It was hypothesized that caged derivatives of widely used E3 ligands would provide useful tools for the light-dependent degradation of a broad range of targets. Cereblon and VHL recruiting ligands are included in more than 80% of reported PROTACs and thus were deemed suitable starting points for a proof-of-concept caged E3 ligand. The structural information available for cereblon and VHL E3 ligases with their respective ligands was used to design our caged degraders.[241,242] For IMiDs derivatives such as thalidomide, interaction with cereblon was inhibited by functionalizing the NH- of the glutarimide group with a suitable caging moiety (**Figure 2.6 A**). This blocking strategy has often been used to generate the negative control of cereblon-recruiting degraders via N-methylation of the imide portion.[243] For VHL ligands, the design of our caged degraders relied on the modification of the key hydroxyl group required for binding to VHL E3 ligase[27,244] (**Figure 2.6 B**). The absolute configuration of the hydroxyproline ((*4R*)-configuration) was kept the same while performing the caging chemistry so that binding to VHL would be maintained.
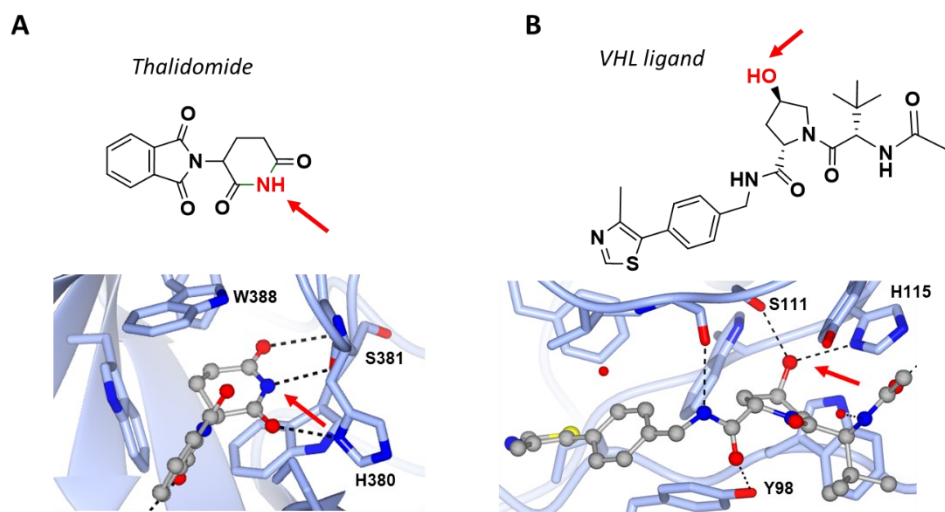
Figure 2.6 Caging the E3 ligand. Caging group attachment points are identified by red arrows. **(A)** Crystal structure of thalidomide bound to DDB1-CRBN E3 ubiquitin ligase (PDB code 4CI1)[241]. **(B)** Crystal structure of VHL ligand bound to pVHL:EloB:EloC complex (PDB code 4W9H)[242]. Interactions with key amino acids are shown in dotted line.

It is important to note that caging of the E3 binding moiety of a PROTAC leaves the warhead free to interact with the target protein. As such, a caged bifunctional degrader can remain a good binder and inhibitor of the protein of interest. Thus, it is essential to characterize the biological effect of the caged degrader prior to irradiation to fully understand the impact of the uncaging step towards the biological outcome.

2.1.2.2 Caging the warhead

A caged degrader can also be obtained by functionalizing the warhead (i.e., the POI binding motif) of a bifunctional molecule. In this design, the caged degrader remains inactive before irradiation due to lack of target engagement (**Figure 2.5**). An example of this strategy was reported during the course of our investigation and is discussed in subsequent paragraphs[228] (**cf. section 2.4**). With the caging group attached on the warhead, the E3 ligand is free to interact with its E3 partner. Cellular effects arising from this remaining interaction may or may not be significant. Cereblon recruiting degraders have shown some level of promiscuity since they have been reported to reduce the levels of proteins unrelated to the initial targeted POI.[77,245] Thus, monitoring off-targets effects resulting from the binding of neo-substrates to cereblon is recommended for IMiDs-based degraders. On the contrary, a caged degrader with a free VHL ligand may be less promiscuous since there is little precedent of modulation of secondary targets resulting from cell treatment with VHL-based PROTACs.

2.1.2.3 Caging the linker
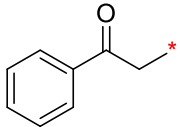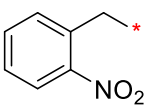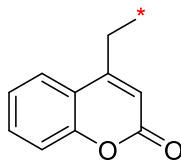
The linker of a PROTAC plays a crucial role in allowing the formation of the ternary complex needed for the ubiquitination step. In cases where chemical modification of the E3 ligand or the warhead is not feasible, an alternative approach may exploit the linker as a caging site (**Figure 2.5**). With the provision that structural data of the ternary complex is available, the design of a

caged linker may be attempted to inhibit the binding to the E3 ligase, the POI or prevent ternary complex formation via unfavorable steric or electronic interactions. Although the inactivation of a PROTAC by caging the linker might be achievable, multiple iterations of synthesis may be necessary to find an optimal inactive caged degrader. Hence, alteration of the warhead or the E3 ligand offers a faster option to identify a caged bifunctional.

2.1.2.4 Caging groups

In 2013, Klán et al. thoroughly described the various caging groups which are used both in chemistry and biology applications.[246] Three classes of caging groups - arylcarbonyl, nitroaryl and coumarin derivatives dominate the photoprotecting groups (PPG) field (**Table 2.2**).

Table 2.2 Most used photoprotecting group classes

Name	Arylcarbonyl	Nitroaryl	Coumarin
Structure			
Max absorption*	300-400 nm		

*The range provided is where the maximum absorption is often observed for this groups. Absorption outside of the range (<300 nm and >400 nm can also take place).

Selection of the appropriate PPG will depend on the application being pursued. Overall, some of the main characteristics to taken into consideration are:
-a strong absorption at a relevant wavelength λ for biological applications. Usually, $\lambda > 300$ nm is preferred.
-a good efficiency of release for the parent molecule relative to the number of photons needed (defined as the quantum yield).
-a high chemical stability prior to irradiation.
-the released by-products must poorly absorb at the uncaging wavelength λ and be biologically inert.

The 3 PPG classes described above fulfill most of these criteria although we note that the nature of the substituents around the core structure, the type of solvent in which the uncaging reaction is conducted as well as the PH of the uncaging solution can influence the absorption maximum and/or the quantum yield. For our application in the field of protein degradation, we turned to the nitrobenzyl group since there are substantial examples in the literature detailing both the benefits and limitations of such groups.[246,247] Initial examples used a simple nitrobenzyl linked via the heteroatom of functional groups such as alcohols, amines, carboxylic acids, or phosphates.

The cleavage mechanism involves the formation of a benzylic radical which rearranges into a benzisoxaline that eventually releases the leaving group and a nitrosobenzaldehyde by-product[248] (**Scheme 2.1**).
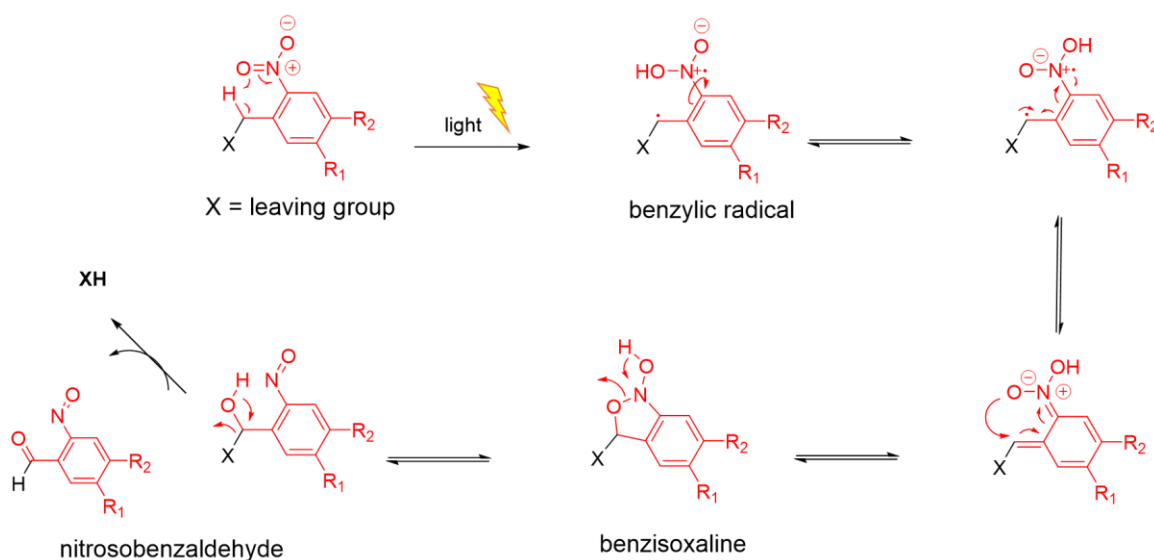
Scheme 2.1 Photocleavage mechanism with a nitrobenzyl caging group.

As nitrosobenzaldehyde can cause interference with the uncaging light and unwanted reactivity in the biological system, efforts have been made to generate an improved version of the simple nitrobenzyl derivative[246] (**Figure 2.7**). Two additional methoxy groups (in DMNB and NVOC) increase the absorbance to greater than 350 nm and up to 420 nm in some cases. Introduction of a methyl group at the benzylic position (MeNPOM, MeNPOC) generates a less reactive ketone after
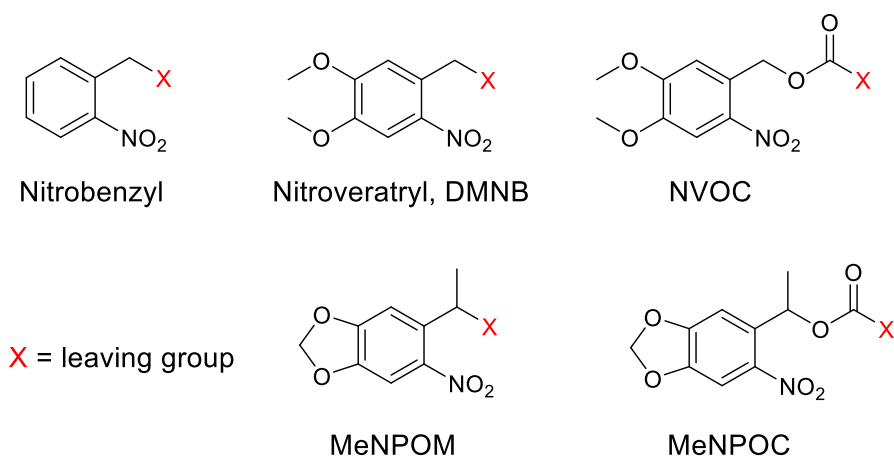
Figure 2.7 Nitrobenzyl photoprotecting groups. DMNB = 4,5-dimethoxy-2-nitrobenzyl ; NVOC = 6-nitroveratryloxycarbonyl; MeNPOM = α-methyl-(6-nitropiperonyloxymethyl) MeNPOC = 3,4-(methylenedioxy)-6-nitrophenylethoxycarbonyl.

irradiation instead of an aldehyde. In this research, we focused our attention on the DMNB group as building blocks were readily accessible for the caging chemistry. The various publications on light activated degradation via a caging strategy have made use of the same DMNB photoprotecting group[249] (cf. **section 2.4**).

2.1.3 BRD4: a target for proof of concept

2.1.3.1 BRD4 and oncology

Bromodomain protein 4 (BRD4) was chosen as a model protein to validate our light-dependent protein degradation approach. BRD4 is part of the bromodomain and extra terminal family (BET) which comprises BRD2, BRD3, BRD4 and BRDT. Those proteins act as epigenetic readers as they recognize and bind to acetylated lysines on histones to regulate chromatin remodeling and transcription[250] (**Figure 2.8**).
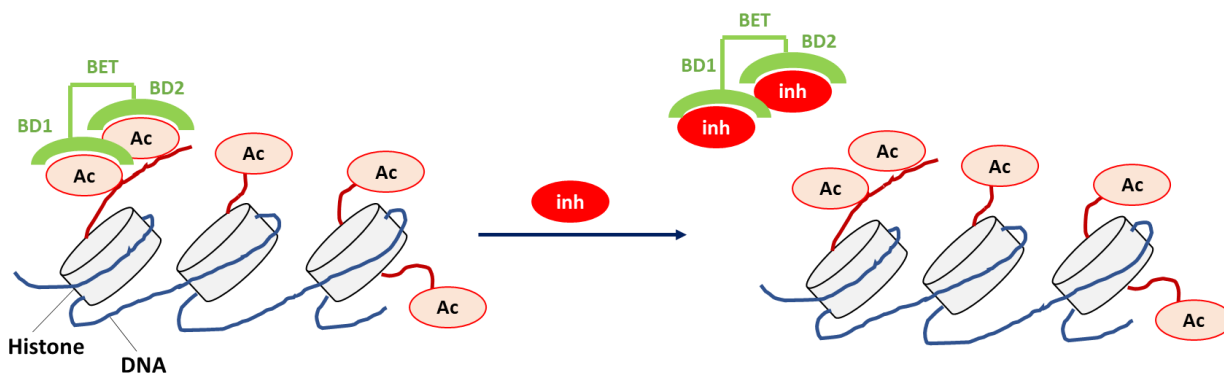
Figure 2.8 Bromodomain protein function and inhibition. BET = Bromodomain and extra terminal; BD1 and BD2 = bromodomain 1 and 2; Ac = Acetyl groups on histones. Inh = BET inhibitor which works by preventing binding of BET to acetylated lysines on histones.

BRD4 gene is located on chromosome 19 and the gene product is a 152 kDa protein which is located mainly in the nucleus due to its chromatin binding function. Two alternatively spliced transcripts have been described leading to a long isoform (residues 1-1362) and a short isoform (residues 1-722) which are ubiquitously expressed in various tissues. The role of each isoform is not fully understood but BRD4 functions as a master transcription regulator and is involved in the early stage of embryonic development.[251] Besides embryogenesis, BRD4 directly and indirectly regulates the expression of several cancer-associated genes such as c-MYC, BRAF, KRAS and PIM2.[252,253] For this reason, BRD4 has been pursued as an oncology target with several BRD4 inhibitors currently investigated in the clinic.[254] Non-transcriptional functions of BRD4 have also been reported where BRD4 is proposed to control DNA damage checkpoint activation and repair as well as telomere maintenance.[255]

2.1.3.2 BRD4 degraders

BRD4 was among the first target proteins investigated in TPD. Three seminal publications validated proximity induced degradation with small molecules by connecting a BRD4 inhibitor to either VHL ligand VH032 or to an IMiD scaffold.[28,29,256] The compounds **MZ1**, **dBET1** and **ARV-825** are now regularly used as positive control in TPD experiments (**Figure 2.9**). Rapid and sustained degradation of BRD4 (up to 48 h) has been achieved at low nanomolar concentration with those degraders. Compound **MZ1** also demonstrated partial selectivity for BRD4 versus BRD2 and BRD3. In addition, degradation of BRD4 has shown a stronger effect on cell proliferation in comparison with inhibition alone. Finally, BRD4 degraders have demonstrated *in vivo* efficacy in various models of blood cancers.[257]

Compound	MZ1
DC50	100 nM
Cell line	HeLa
Molecular weight	1002.64
E3 recruited	VHL
Selectivity	BRD4>BRD2/BRD3

Compound	ARV-825
DC50	1 nM
Cell line	Namalwa, CA-46
Molecular weight	923.44
E3 recruited	Cereblon
Selectivity	Not selective

Compound	dBET1
DC50	430 nM
Cell line	MV4-11
Molecular weight	785.27
E3 recruited	Cereblon
Selectivity	Not selective
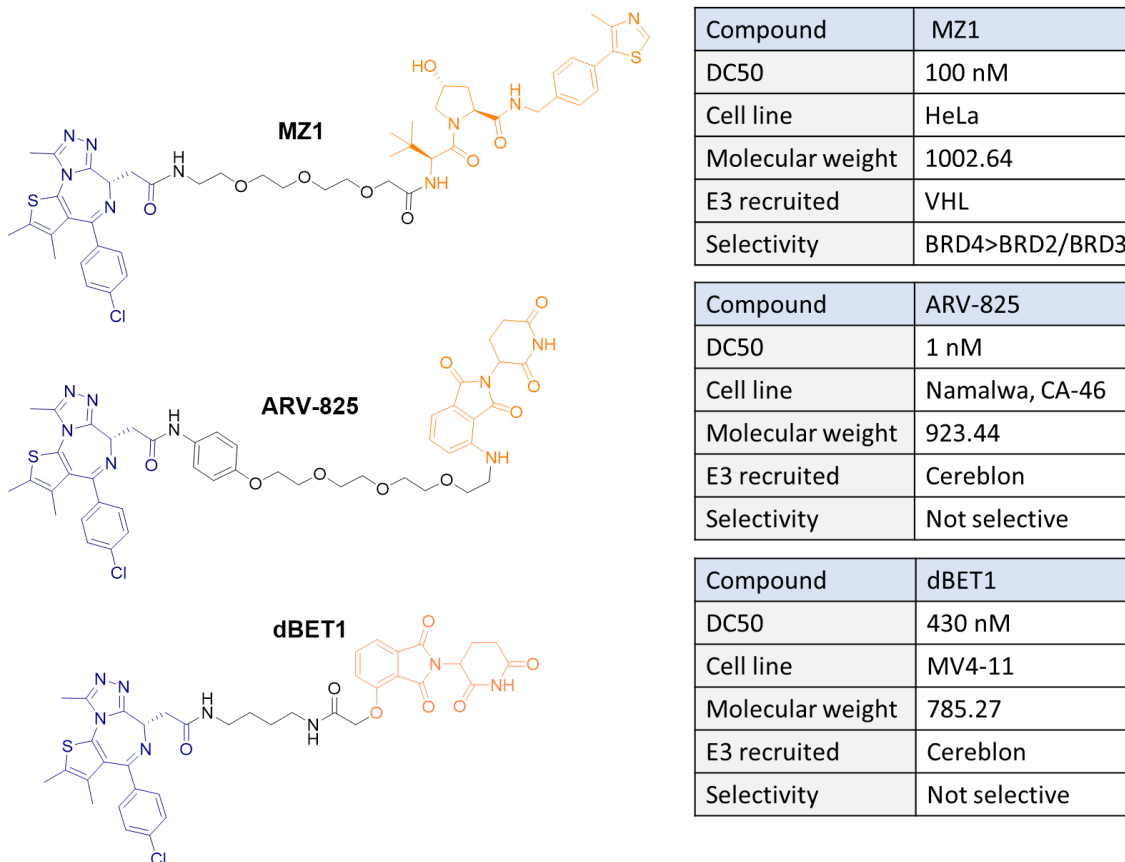
Figure 2.9 Examples of reported BRD4 degraders

2.1.3.3 BRD4 and proof of concept studies in Targeted protein degradation

BRD4's half-life has been experimentally evaluated to be around 18 h.[258] This relatively long half-life is considered a benefit for the investigation of a new degradation tool or platform as a positive degradation signal may be more difficult to capture for a protein with a rapid turnover. Due to the availability of a number of BRD4 chemical warheads and well-characterized structure-activity relationships (SAR),[259] design and synthesis of a new degradation tool for initial validation can

often be straightforward with. **Table 2.3** gives a non-exhaustive list of novel TDP strategies which have been validated with BRD4 as a model target.

Table 2.3 Protein degradation approaches validated with BRD4. The inhibitor **JQ1** has commonly been used to synthesize a BET degrader

TDP strategy	Description	Inhibitor used	E3 ligase used
dTAG system[260]	expression of FKBP12^{F36V} in-frame with BRD4 or any other POI as a new chemical knockdown platform	AP1867, synthetic FKBP12^{F36V}-directed ligand	cereblon
PHOTAC[225]	PROTACs incorporating a photoswitchable unit	JQ1, BET inhibitor	cereblon
Antibody-PROTAC[213,261]	Adduct between a PROTAC and an antibody for targeted delivery	JQ1, BET inhibitor	VHL
Folate-PROTAC[215]	Adduct between a PROTAC and Folic acid for targeted delivery	JQ1, BET inhibitor	VHL
Covalent E3 recruiters[262–264]	Identification of new E3 ligase via covalent chemoproteomics approach	JQ1, BET inhibitor	DCAF16 RNF114 RNF4

.
In the research we have conducted around light-activated and hypoxia-activated degraders, we likewise developed BRD4-targeting tools compounds for our proof of concept.

2.2 Results and discussion: chemistry and *in vitro* experiments

2.2.1 Results with caged cereblon ligand

2.2.1.1 N-benzyl linkage with DMNB hydroxythalidomide

The initial attempt to obtain a caged degrader was derived from the bifunctional degrader **dBET1** reported in 2015 by Bradner's lab[29] (**Figure 2.9**). It was hypothesized that the glutarimide moiety of **dBET1** could be caged with 4,5-dimethoxy-2-nitrobenzyl (DMNB) via *N*-alkylation resulting in an inactive degrader. The synthetic route to access the caged hydroxythalidomide E3 ligand is shown in **scheme 2.2**.
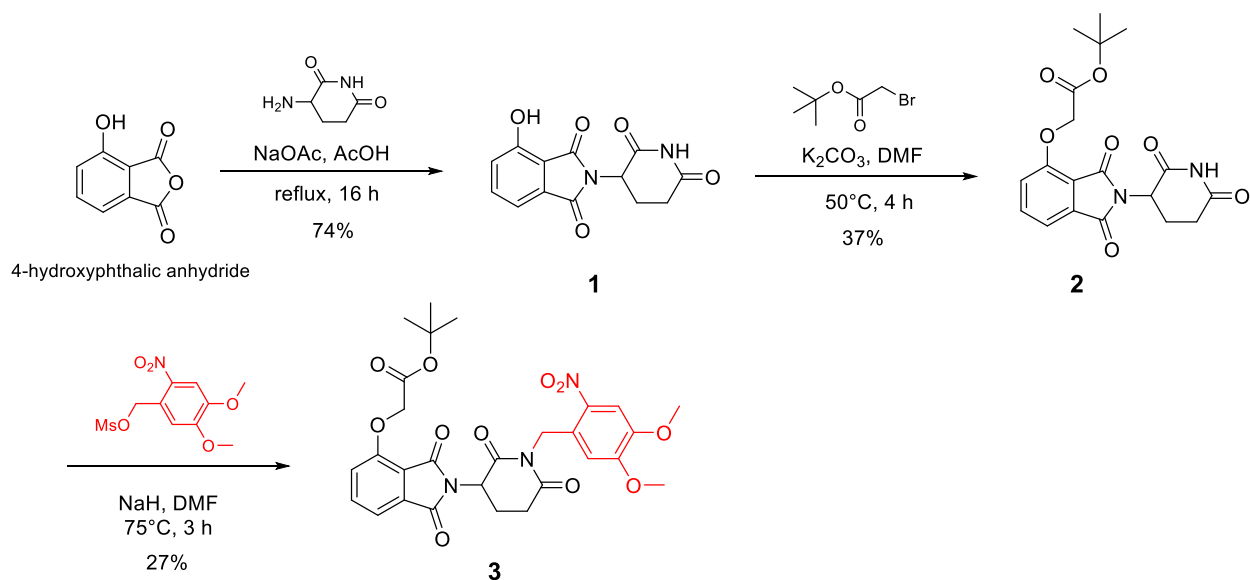
Scheme 2.2 Synthesis of N-caged hydroxythalidomide

Condensation between 4-hydroxyphthalic anhydride and 3-aminopiperidine-2,6-dione yielded 4-hydroxythalidomide **1**. Next, O-alkylation with tert-Butyl bromoacetate led to protected intermediate **2** which was eventually *N*-alkylated with mesylated 4,5-dimethoxy-2-nitrobenzyl alcohol to give the caged thalidomide derivative **3**.

2.2.1.2 Photochemistry of N-linked DMNB hydroxythalidomide

The DMNB thalidomide intermediate **3** was assessed for its ability to release the parent glutarimide motif upon irradiation with UV light. The irradiation set up was made up of a LED light centered at 365 nm and affixed to a handmade metallic box built by a former PhD researcher from the Tate lab, Dr Charlie Saunders (**Figure 2.10 A**). Measurements of the power delivered from the box gave a lower limit of 25 mW/cm^2 when the sample was positioned 80 mm away from the LED and an upper limit of 85 mW/cm^2 when the sample was 53 mm away from the LED (**Appendix 2.1**). The DMNB group is usually cleaved at 365 nm[246] and the UV-Vis spectrum of compound **3** recorded at room temperature in acetonitrile shows good absorption within the range 300-380 nm (**Figure 2.10 C**). Nonetheless, continuous irradiation of compound **3** for 10 mins in deuterated chloroform from 80 mm did not lead to compound **2** (**Figure 2.10 B**). A partly aqueous solution (acetonitrile/water 1:1) was also used to facilitate uncaging since the release of the NH- glutarimide occurs via proton exchange (**Scheme 2.1**). However, cleavage of the DMNB group was still not achieved in this mixed aqueous medium (**Figure 2.10 B**). A color changed was noticeable upon irradiation for much longer time (up to 50 mins, **Figure 2.10 D**) but ^{1}H NMR confirmed retention of the DMNB cage (**Figure 2.11**). Bringing the sample closer to the LED source (<35 mm) was also ineffective. At this stage, shorter and more energetic wavelengths were considered, and we investigated the use of UVA and UVB radiations in a Luzchem oven (**Figure 2.10 E**). Unfortunately, irradiation with light bulbs centered at 350 nm (UVA) and 315 nm (UVB) did not produce any uncaging.
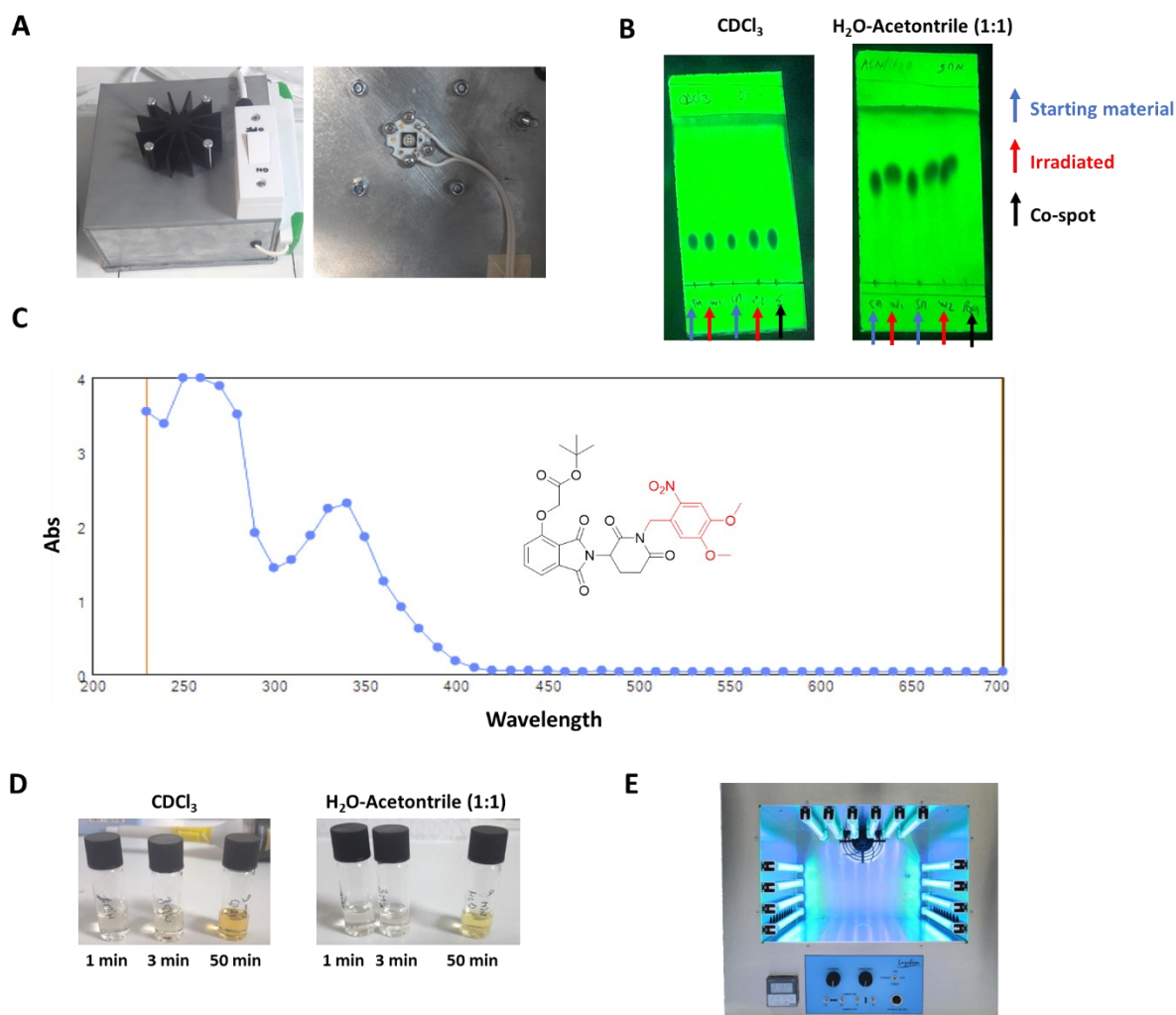
Figure 2.10 Photocleavage attempt of compound **3**. (A) Scoot box used for irradiation of our caged molecule. It was affixed with a 365 nm LED and a small sample placed underneath. (B) TLCs of uncaging experiments in deuterated chloroform and water-acetonitrile. Small aliquots of compound **3** were irradiated for 10 mins at 365 nm to check for the release of compound **2**. (C) UV-Vis spectrum of compound **3** (100 μM) recorded at room temperature in acetonitrile. (D) A color change was observed after irradiation at 365 nm for up to 50 mins in deuterated chloroform and water-acetonitrile but cleavage of the DMNB group did not occur. (E) Luzchem oven (inside view) used to irradiate compound **3** with UVA and UVB. Image reproduced with permission from LuzChem Research Inc.

The results obtained with our DMNB hydroxythalidomide **3** are in contrast with a recent report from Liu et al. who have demonstrated that thalidomide caged with the exact same DMNB group can be released upon irradiation at 365 nm.[229] The reason why uncaging could not be achieved in our case remains unclear. Liu's example is further discussed in **section 2.4**.
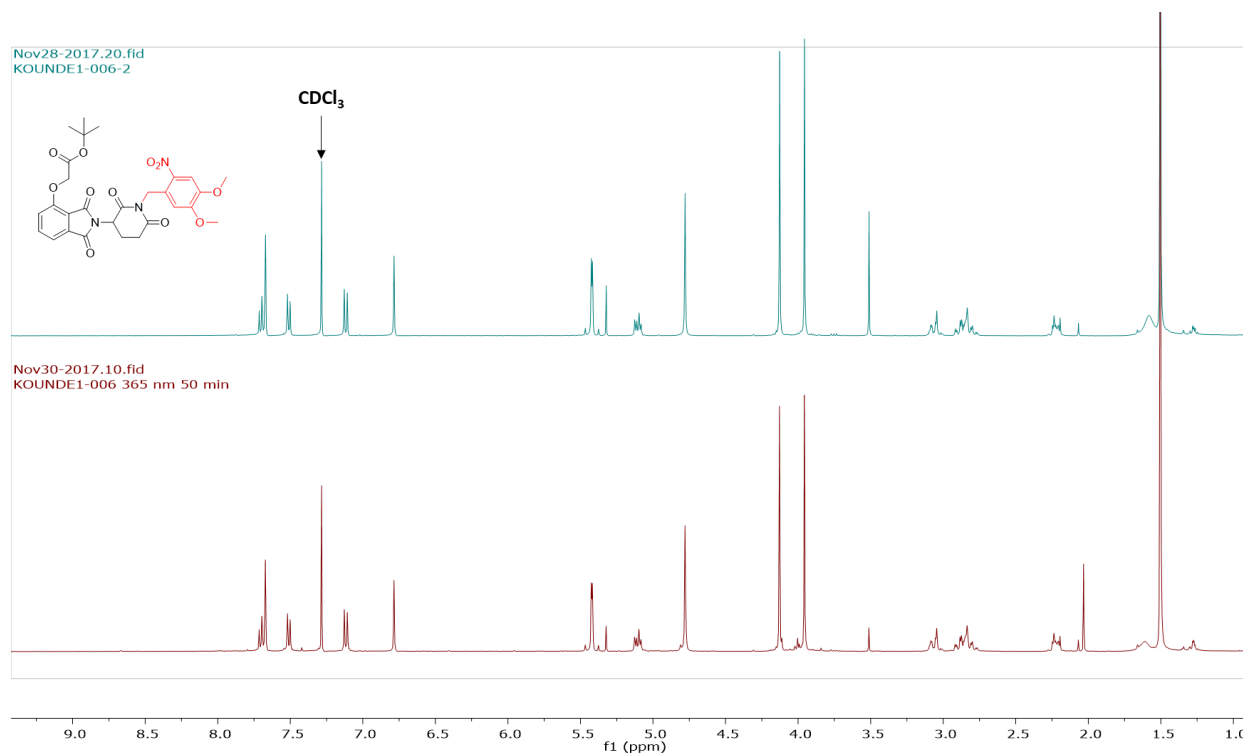
Figure 2.11 ^{1}H NMR of compound **3** before and after a 50-min irradiation at 365 nm. 3 mg of **3** was dissolved in deuterated chloroform and irradiated in a vial for up to 50 min. ^{1}H NMR was run directly after irradiation was stopped.

2.2.1.3 Alternative design: carbamate and N-methylether

C-N bond photolysis when the nitrogen is directly attached to a nitroveratryl group via N-benzyl linkage has been reported.[246] However, caging of molecules containing a free NH using a nitrobenzyl cage is frequently done through a carbamate or a methyl ether functionality. The cleavage process is understood to be assisted by the release of carbon dioxide in the case of a carbamate. For the N-methyl ether, formation of an amino alcohol species which then collapses to release the free amine facilitates the uncaging process (**Scheme 2.3**). Thus, we attempted to cage compound **2** with the commercially available 6-nitroveratryl chloroformate (NVOC-chloride). A summary of the conditions attempted is shown in **Scheme 2.4**. The combination of sodium hydride to deprotonate the glutarimide and DMAP to activate the chloroformate led to identifiable new spots by TLC but all of the basic conditions tested produced insufficient conversion to isolate the desired carbamate **4** in desired purity.
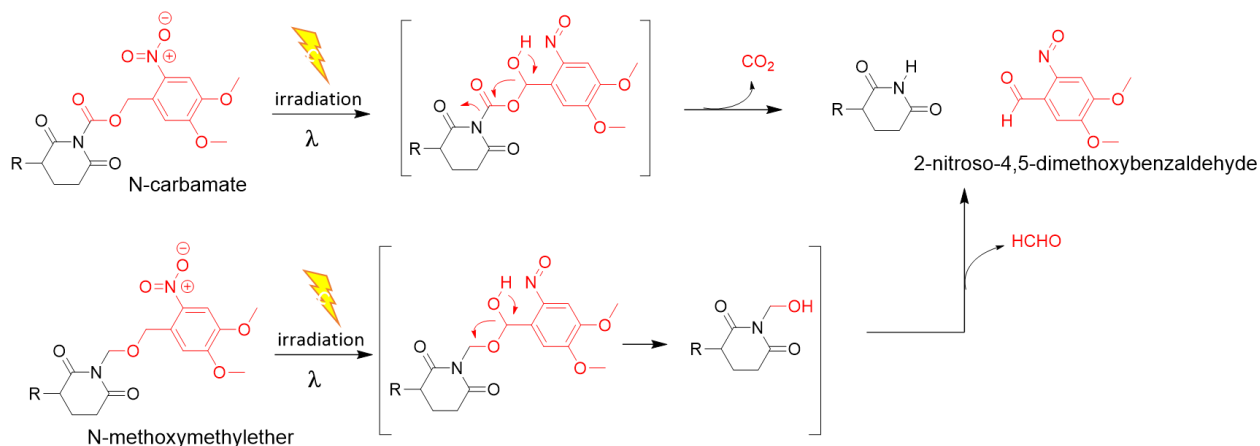
Scheme 2.3 Proposed photocleavage of glutarimide N-carbamate and N-methoxymethyl derivative
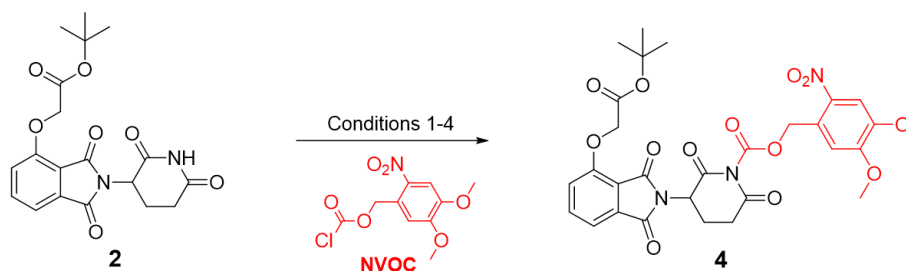
Reaction	Conditions	Results after Flash chromatography	Isolated product yield (%)
#1	Et₃N, DMF, RT, 16 h	Starting material recovered	0
#2	NaH, THF, RT, 2 h then 1 h at 50˚C	Starting material and nitrobenzyl alcohol	0
#3	NaH, DMF, 75˚C, 16 h	Trace amount of product mixed with nitrobenzyl alcohol	0
#4	NaH, DMF, RT, DMAP, 65˚C	Product peak along with some nitrobenzyl alcohol	14*

* Purity < 50%

Scheme 2.4 Acylation attempt of compound **2**

After our unsuccessful attempt with NVOC, we turned to the N-methylether linkage. 6-Nitropiperonyloxymethyl group (NPOM) has been established as a useful photocaging unit for aromatic N-heterocycles by Dieters' lab.[265] In their report, NPOM was introduced via alkylation from a synthetically made NPOM chloride intermediate (**Scheme 2.5 A**).
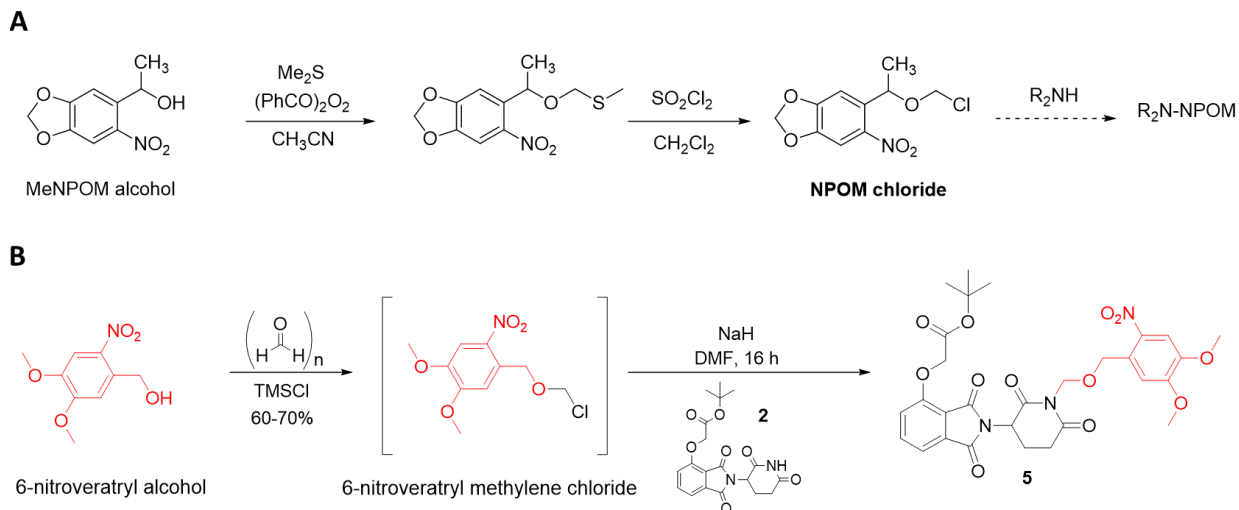
Scheme 2.5 N-methylether linkage synthesis. (A) Route devised by Dieters et al. to access NPOM chloride via formation of a thioether which is then cleaved with sulfuryl chloride (B) 6-nitroveratrol was converted to the methylene chloride which was then reacted with compound **2**.

We devised a simple route to turn the commercial 6-nitroveratryl alcohol into its methylene chloride derivative using TMSCl**.** The crude material was directly used for alkylation of **2** since oxymethylene chloride compounds are known for their instability (**Scheme 2.5 B**). Although the desired caged product **5** was identified by LC-MS and TLC, it was not successful isolated due to the number of side products generated. Efforts to synthesize a caged IMiD were stopped at this point in favour for the VHL ligand.

2.2.2 Results with caged VHL ligand

2.2.2.1 Carbonate linkage: synthesis and photochemistry

A key binding motif of VHL ligands is a hydroxyproline which makes hydrogen bond interactions with two residues (Ser 111, His 115) within the VHL E3 ligase.[244] Our strategy to build a caged VHL ligand relied on the functionalization of the hydroxyproline to prevent binding to VHL E3 ligase. An alcohol moiety is commonly caged with a nitroaryl group via a carbonate as the chemistry can be performed using commercially available nitroaryl chloroformates. Similarly to the carbamate linker of the nitrobenzyl cage, photolysis of the carbonate is assisted by the release of carbon dioxide.

After protecting the free amine of our VHL ligand **6** with a Boc group, acylation of compound **7** was attempted under various basic conditions (**Scheme 2.6**). With triethylamine and sodium hydride, the starting material was recovered mainly with no sign of product observed. When the base was changed to lithium hexamethyldisilazide (LiHMDS), some caged product **8** was identified and isolated. However, the poor recovery was insufficient to obtain full characterization of the desired product. Photolysis of carbonate **8** was still attempted and release of the parent VHL ligand was confirmed by LC-MS and TLC (**Figure 2.12**) with about 50% uncaging achieved after irradiation for 8 mins at 365 nm.

Scheme 2.6 O-acylation of VHL ligand with nitroveratryl chloroformate
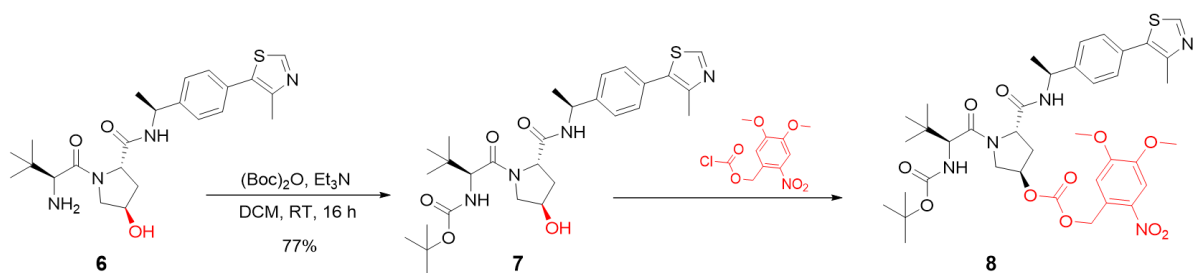
Acylation with chloroformate	Conditions	Isolated product yield (%)
#1	Et$_3$N, DMAP, DCM, RT	0
#2	NaH, DMF, RT or heated	0
#3	CDI then DMNB alcohol	0
#4	LiHMDS, THF, -78°C to 0°C	10-15
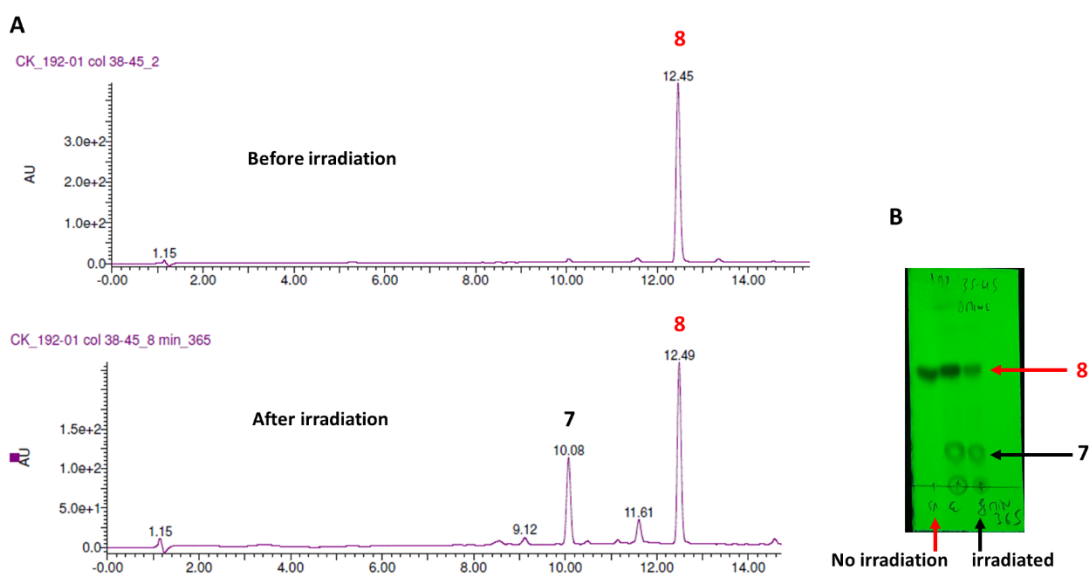
Figure 2.12 Uncaging of O-acylated compound **8**. (A) LC-MS chromatogram of compound **8** (100 μM) before and after an 8-min irradiation in acetonitrile/water (3:1). About 50% uncaging was achieved. (B) TLC of the irradiation experiment showing more polar compound **7** formed.

Although uncaging was observed, the low yield arising from the O-acylation of **7** meant we decided to use alternative linkages to the carbonate, such as an ether.

2.2.2.2 Ether linkage: synthesis and photochemistry

To generate another caged VHL ligand with a benzyl ether linkage, we investigated the O-alkylation of the hydroxyproline with DMNB bromide or DMNB alcohol activated as a mesylate. Neither sodium hydride nor LiHMDS generated the caged VHL ligand. Further search into the patent literature led us to an example of direct O-alkylation of an hydroxyproline. In their 2008 patent application, Enanta pharmaceuticals described a biphasic system made of 50% aqueous sodium hydroxide and dichloromethane supplemented with a phase transfer catalyst, tetrabutylammonium iodide (TBAI) to achieve O-alkylation of macrocyclic HCV protease inhibitors.[266] Using these conditions, we successfully caged the VHL ligand **7** in 53% yield, in a single step, without the need to prepare an activated caging reagent. A brief discussion about caging chemistry is further presented in **section 2.4**.

Photolysis of benzyl ether **9** at 365 nm led to the release of the parent VHL ligand **7** observed both by LC-MS and TLC (**Figure 2.13**) with complete uncaging of the VHL ligand accomplished after a 10-min irradiation.
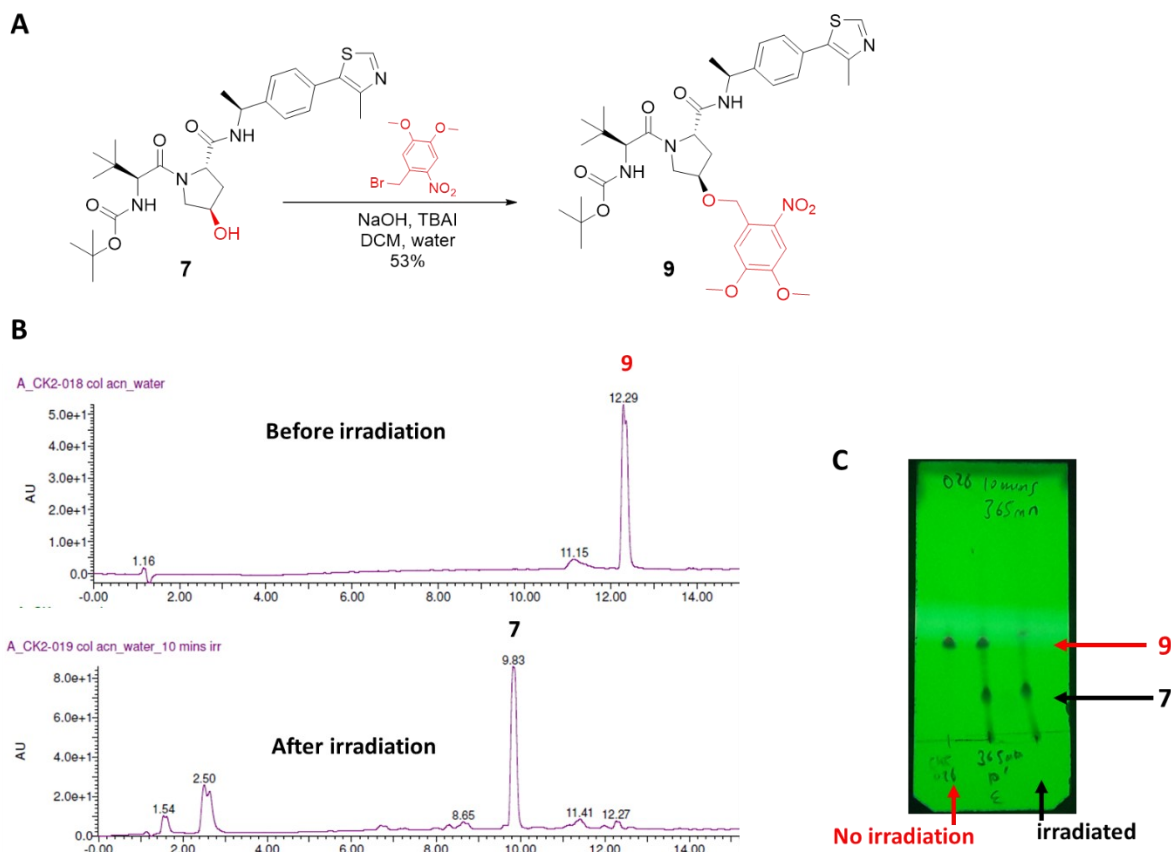
Figure 2.13 Synthesis and uncaging of O-alkylated compound **9**. (A) LC-MS chromatogram of compound **9** (100 μM) before and after a 10-min irradiation in acetonitrile/water (3:1). Complete uncaging was achieved. (C) TLC of the irradiation experiment showing more polar compound **7** formed.

2.2.2.3 Caged BRD4 degrader: full synthesis and photochemistry

The improved synthetic route and successful photochemistry led us to incorporate our novel DMNB caged VHL ligand **9** into a BRD4-targeting PROTAC with **MZ1** as a template to build our caged degrader. The synthetic route to access the final caged bifunctional molecule **12** is described in **Scheme 2.7**. After Boc deprotection of compound **9**, an amide coupling was conducted with a PEG3 azide carboxylate linker. The resulting compound **10** which bears a terminal azide and a nitrobenzyl caging group underwent a Staudinger reduction to give the amine **11** which was eventually coupled to **JQ1** carboxylate.
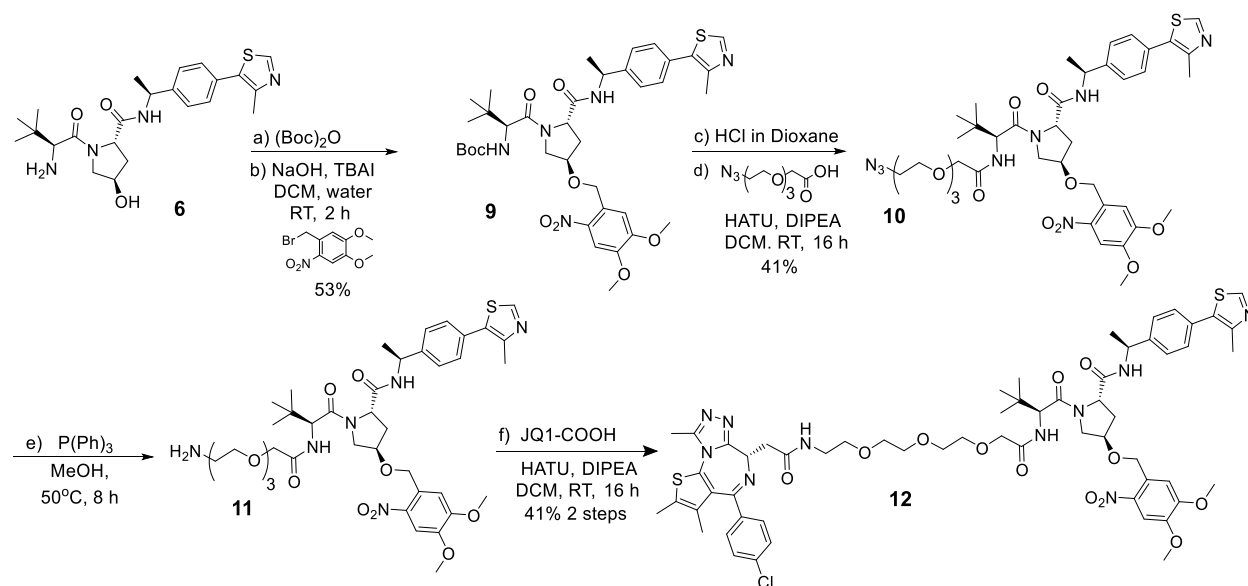
Scheme 2.7 Synthesis of caged degrader **12**

The UV spectrum of the caged degrader showed an expected absorption in the range 350 - 380 nm (**Figure 2.14 A**). A 50 μM aqueous solution of **12** showed complete and clean uncaging after irradiation for 3 minutes and more than 50% uncaging was observed by LC-MS following a short 60-second irradiation (**Figure 2.14 B, appendix 2.2**). Rapid uncaging upon irradiation was a desirable feature for the use of the caged PROTAC *in cellulo* as exposure of cells to UV light could be kept to a minimum. Compound **12** was also shown to be stable in organic solvent when protected from light as no trace of uncaged material was observed after 5 days (**Appendix 2.3**). Thus, PROTAC **12** was deemed suitable for experiments in cells.
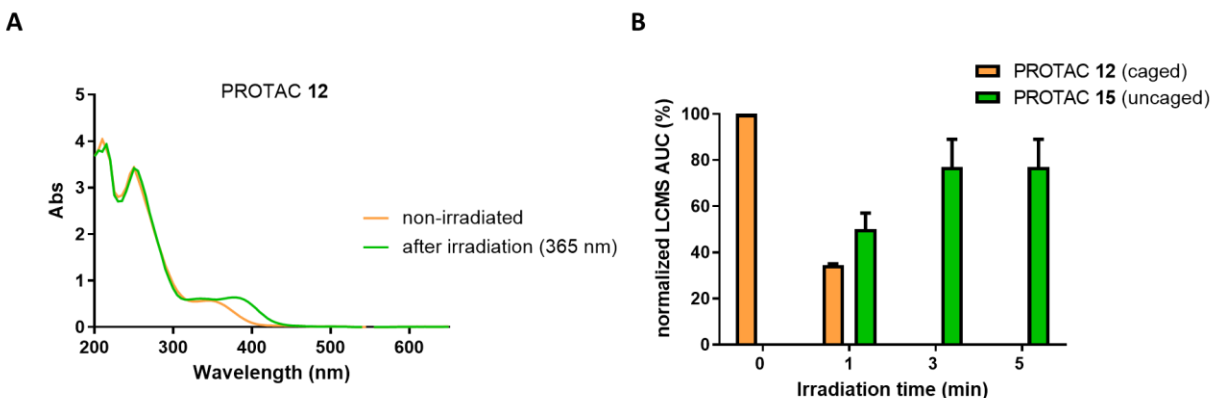
Figure 2.14 Photocharacterization of compound **12**. (A) UV-Vis spectrum of caged PROTAC **12** (200 μM in ACN). Spectrum was recorded before and after a three-minute irradiation time at 365 nm under a 25 mW LED. (B) Uncaging of PROTAC **12** following irradiation with a 25 mW 365 nm LED. A 50 μM solution of **12** in acetonitrile–water (1 : 1) was irradiated for 1-, 3- or 5-min. LC-MS area under the curve (AUC) was extracted from the chromatogram full UV spectrum.

2.2.4.4 Uncaged BRD4 degrader synthesis

In addition to the caged degrader **12**, the PROTAC **15** which is released after irradiation was also synthesized for comparison. This differs from PROTAC **MZ1** only by an extra methyl group present on the benzylic position of the benzylamine of the VHL ligand. The 3-step synthesis began with an amide coupling between amine **6** and the PEG3 azide carboxylate linker. Reduction of the azide **13** was conducted via hydrogenation to yield the primary amine **14** which was finally coupled to **JQ1** carboxylate to yield compound **15** (**Scheme 2.8**).
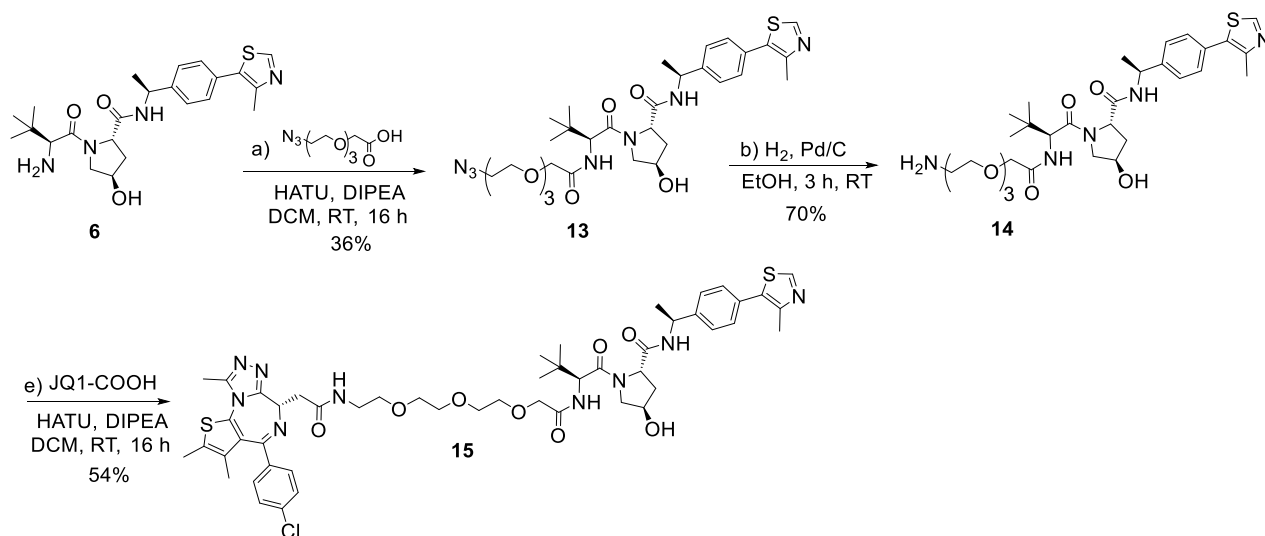
Scheme 2.8 Synthesis of PROTAC **15**.

We note that one single chemical transformation would be advantageous to turn any final VHL-based PROTAC into its caged counterpart. Thus, we also attempted the direct caging of parent compound **15** with DMNB bromide under the same phase transfer catalysis conditions (as shown in **Figure 2.13**). However, the caged molecule **12** was recovered in low yield (14%). Caging of the VHL ligand in a sequential step was a better route to access our caged final PROTAC **12**.

2.2.4.5 Biological testing of the caged BRD4 degrader

PROTAC **12** and **15** were thus tested to validate our caging approach and to confirm the mode of action of our photoactivatable degrader in a cellular environment. Moreover, to monitor BRD4 degradation upon activation via uncaging, we employed live-cell fluorescence microscopy. HeLa cells were chosen due to high endogenous BRD4 expression levels and simple culture procedures.

2.2.4.5.1 Assessment of the parent degrader

Besides our parent PROTAC **15**, GlaxoSmithKline provided with us with another VHL-based PROTAC **16** as a positive control (**Figure 2.15 A**). Treatment of HeLa cells for 24 h with **15** and **16** led to significant degradation of BRD4 at 100 nM (28% and 44% degradation, respectively) and complete depletion of BRD4 at 1 μM and above. This initial result confirmed that uncaged novel analogue **15** was an effective degrader of BRD4. Additionally, we also assessed the depletion of c-Myc protein levels as described with previously reported BRD4 degraders such as **dBET1** and **MZ1**.[28,29] Accordingly, treatment of HeLa cells for 24 h with parent PROTAC **15** led to c-Myc levels reduction at concentrations above 1 μM (**Figure 2.15 B**) validating a known mode of action for this class of degraders.
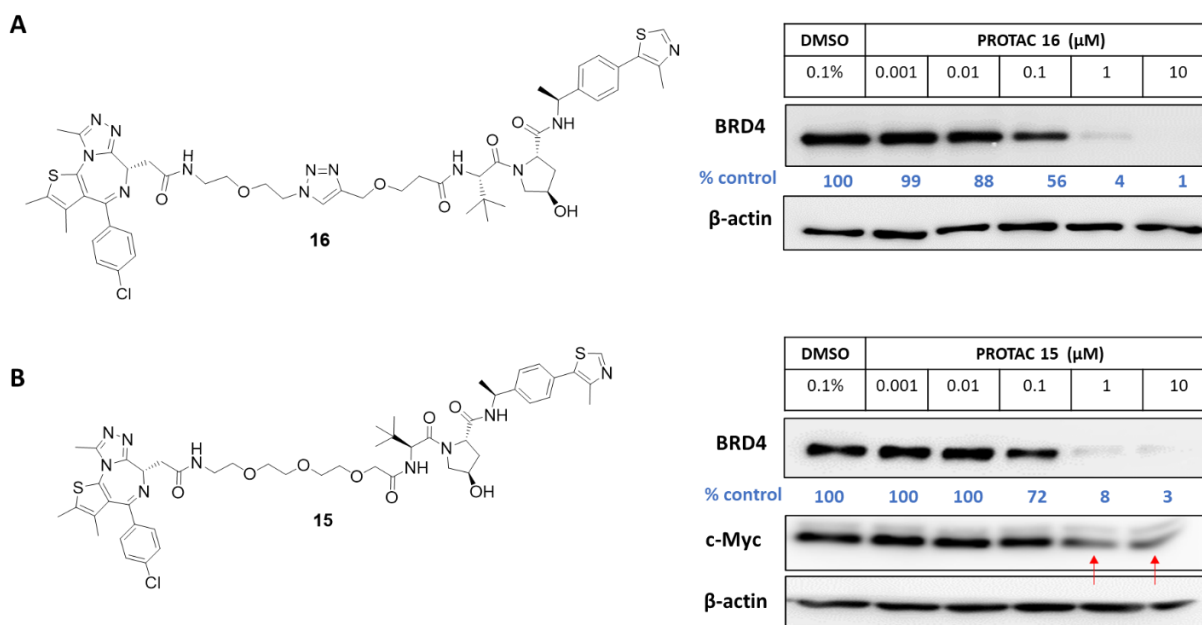
Figure 2.15 BDR4 degradation profile with uncaged compound **15** and control **16**. (A) Structure of control compound **16** provided by GSK. HeLa cells were treated with PROTAC **16** or uncaged PROTAC **15** for 24 h. Cells were lysed, and lysates collected for Western blot analysis. (B) Structure and Western blot analysis for PROTAC **15**.

2.2.4.5.2 Caged degrader: concentration and irradiation time experiments

With the degradation activity of uncaged parent PROTAC **15** confirmed, the caged degrader **12** was tested at various concentrations (from 10 nM to 10 µM) in HeLa cells under irradiating and non-irradiating conditions. After incubation with compound **12** for 90 mins to allow for sufficient cell penetration, irradiation at 365 nm for 5 mins was conducted before returning the cells into the incubator for another 6 h. Western blot analysis of the lysates showed dose-dependent depletion of BRD4 only upon irradiation (**Figure 2.16 A**).
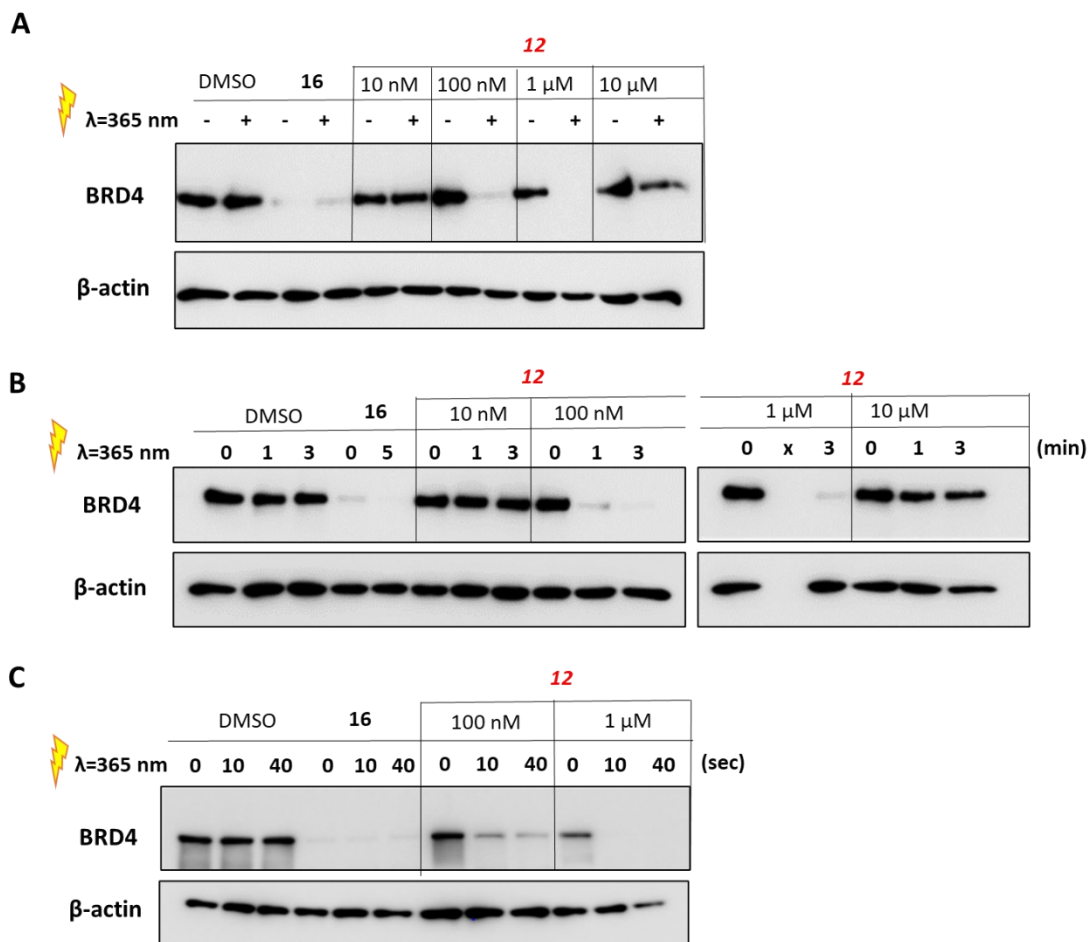
Figure 2.16 BDR4 degradation profile with caged compound **12.** (A) Effect of concentration. HeLa cells were incubated with DMSO, PROTAC **16**, or caged PROTAC **12** for 1 h 30 min then irradiated for 5 min at 365 nm. After 6 h, lysates were collected for Western blot analysis. (B) Effect of irradiation time. After 1 h 30 min incubation, HeLa cells were irradiated for 1 min or 3 min at 365 nm. Western blot analysis was performed 6 h post-irradiation. (C) After 1 h 30 min incubation, HeLa cells were irradiated for 10 or 40 sec at 365 nm. Western blot analysis was performed 6 h post-irradiation.

Significant knockdown of BRD4 was seen at 0.1 µM and 1 µM while at 10 µM, degradation was less pronounced. Two hypotheses were proposed to account for this; first, compound **12** binds and stabilizes BRD4 prior to uncaging, resulting in increased BRD4 levels before the release of the PROTAC upon irradiation. Accumulation of BRD4 upon treatment with BRD4 inhibitors has literature precedent.[267] Another possible explanation for a weaker degradation at 10 µM could be the hook effect (vide supra). With higher concentration of **12**, binary interactions between the caged PROTAC and BRD4 may prevail over ternary complex formation after irradiation. We note nonetheless that the hook effect was not observed with the parent degrader **15** at 10 µM.

With this first positive result, the caging approach was validated, and we next investigated the impact of the irradiation time on BRD4 degradation profile. From the initial five-minute irradiation, the exposure of the cells to UV light for photouncaging was reduced to three and one minute(s). In both cases, BRD4 could be completely depleted at 0.1 and 1 µM after a 6 h incubation (**Figure 2.16 B**) with the same weaker degradation profile observed at 10 µM. We thus reduced the irradiation to 40 and 10 seconds only. Gratifyingly, under such short exposure time to UV light, BRD4 degradation was achieved in a dose-dependent manner at both 0.1 and 1 µM (**Figure 2.16 C**). This suggests that at these concentrations, the amount of uncaged material made available after 10 seconds of irradiation, is sufficient for degradation to take place even though the active degrader might not be released quantitatively. The catalytic nature of the TPD is likely to contribute to the observed activity.

2.2.4.5.3 Caged degrader: timepoint experiments

To determine the onset of degradation after irradiation, we conducted timepoint experiments with control compound **16**, parent degrader **15** and caged degrader **12** at 1 µM.

Preliminary experiments indicated that **16** and parent molecule **15** have a different BRD4 degradation rate. While **16** took 4 h to reach 90% degradation of BRD4, 1 h only was sufficient for **15** to reach the same outcome (**Figure 2.17 A**). A difference in permeability between the two PROTACs may explain our observation (cf. **section 2.2.4.5.4**). After a 2 h pre-incubation then a 60-second irradiation, the timepoint experiment for the caged compound **12** was initiated. BRD4 was degraded by 84% in just one hour after irradiation which is a comparable degradation rate as the parent compound **15**. The prompt depletion of BRD4 after a short UV light exposure suggests that the photouncaging step is relatively fast in the cellular environment and does not constitute a rate-limiting step in the caging approach. We further confirmed the fast onset of BRD4 degradation by **12** could be replicated using different concentrations and irradiation times (**Figure 2.17 B**).

A

B
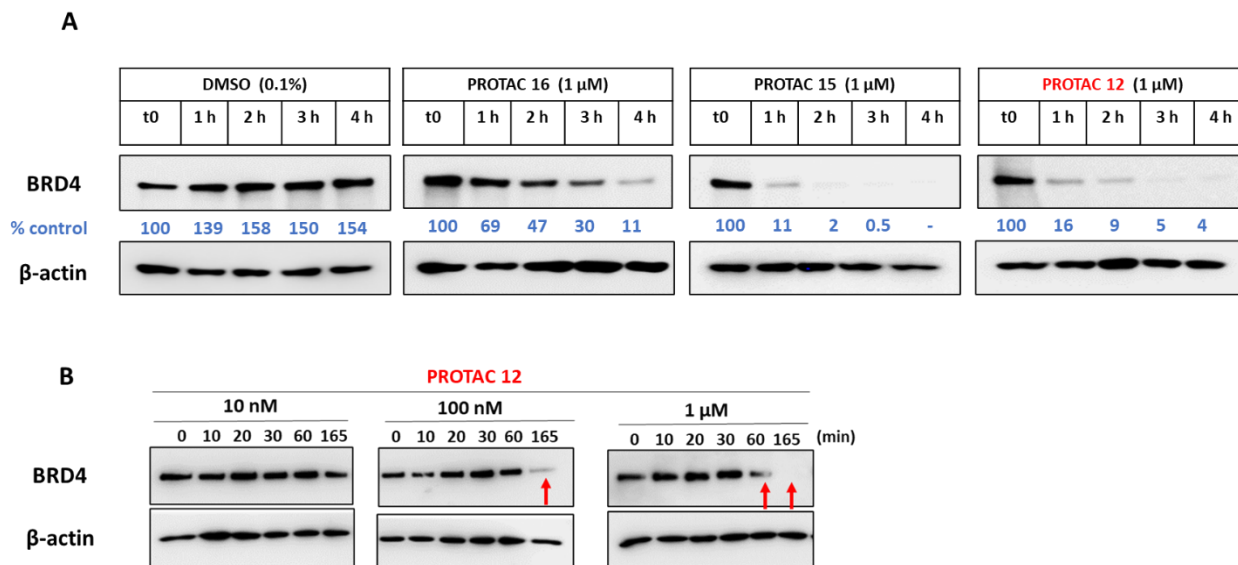
Figure 2.17 Timecourse of BRD4 degradation. (A) HeLa cells were lysed at 60-min intervals to evaluate onset of BRD4 degradation following incubation at t0. For PROTAC **12**, t0 represents time after a 2 h pre-incubation followed by irradiation at 365 nm for 3 mins. (B) HeLa cells were incubated with PROTAC **12** for 2 h before a short irradiation at 365 nm for 3 mins. Cell lysis was then conducted at specific timepoints.

2.2.4.5.4 Mode of action: washout experiment

Due to their dual binding structure, bifunctional degraders tend to have a high molecular weight. This characteristic can be a limiting factor for cell permeability. Compound **12** has a DMNB group that brings its molecular weight just above 1.2 kDa, increasing the likelihood that it is poorly permeable.[268] To assess if our caged molecule effectively entered cells and was being uncaged intracellularly, a washout experiment was conducted. HeLa cells were incubated with test compounds for 2 h before the growth medium was replaced. The purpose of this washout step was to remove from the culturing medium any residual test compound which had not entered the cells. Subsequently, cells were briefly irradiated at 365 nm and further incubated for 6 h before final lysis and Western blot analysis. The gels obtained confirmed that the caged degrader **12** had effectively entered the cells within the 2 h treatment as shown by the complete BRD4 degradation following irradiation (**Figure 2.18**). Moreover, the contrast in degradation profile between the parent degrader **15** and control compound **16** was of note. While the former led to robust BRD4 knockdown within 2 h incubation, the latter showed weaker degradation. This data correlated well with the slower degradation seen for **16** in the timecourse experiment (cf. **section 2.2.4.5.3**).
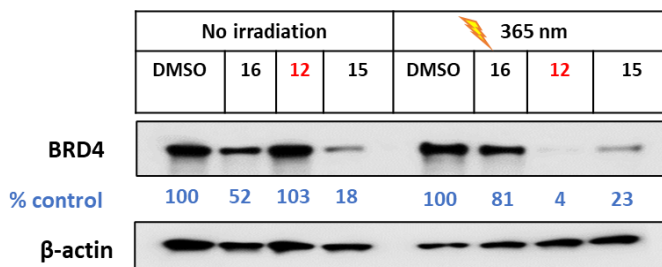
Figure 2.18 Washout experiment. Cells were incubated with DMSO, PROTAC 16, 12 or 15 (1 μM) for 2 h, then washed 3 times with PBS before irradiation to remove residual compound in the cell culture medium. Cells were lysed after 6 h, and lysates collected for Western blot analysis.

2.2.4.5.5 Mode of action: VHL and proteasome dependency

As **12** was a new bifunctional with a novel mode of activation, it was important to confirm that it functioned as a bona fide PROTAC. The dependence on VHL E3 ligase to induce degradation was demonstrated by preincubating HeLa cells with rising concentrations of the ligand **17** (**Figure 2.19 C**). The ability of compound **12** to deplete BRD4 levels after irradiation was severely impaired with competing concentrations of the ligand **17** (**Figure 2.19 A**). Likewise, pre-incubation with 10 μM of the proteasome inhibitor, bortezomib (BTZ), prevented compound **12** from depleting BRD4 levels after UV light exposure (**Figure 2.19 B**). The control **16** and parent compound **15** had a characteristic PROTAC mode of action which was unaffected by the irradiating conditions. Altogether, the collected results confirmed a VHL- and proteasome-dependent mode of action for the caged compound **12**.
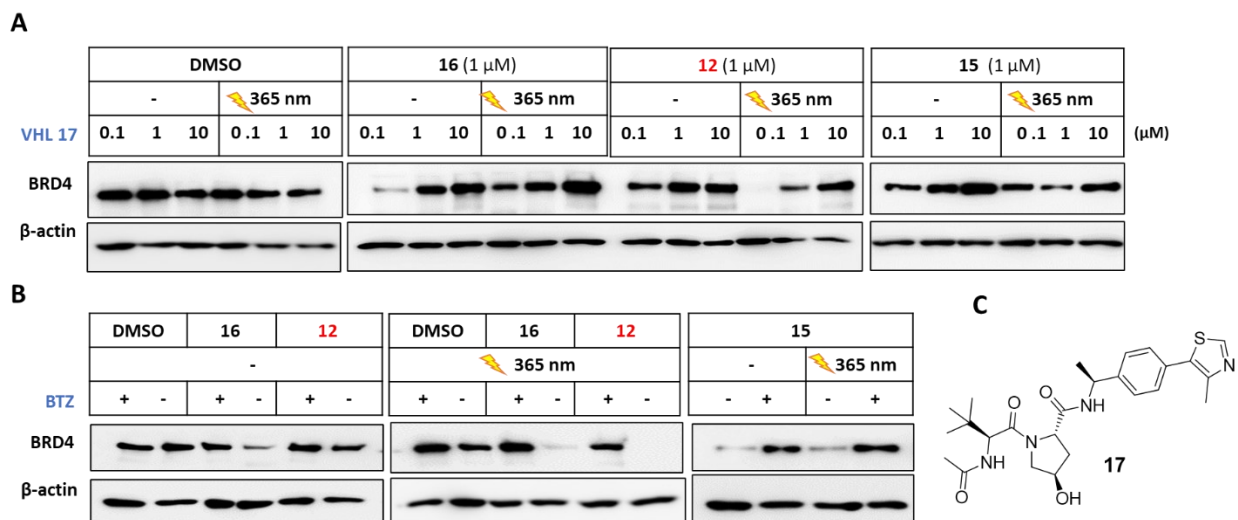
Figure 2.19 Evaluation of caged PROTAC mode of action. (A) VHL-dependency: HeLa cells were pre-incubated with VHL ligand **17** (0.1, 1 and 10 μM) for 2 h, then treated with DMSO vehicle 0.1% (v/v), PROTAC **16**, **12** or **15** (1 μM) for 2 h before irradiation, followed by cell lysis and Western blot analysis. (B) Proteasome-dependency: HeLa cells were pre-incubated with proteasome inhibitor bortezomib (BTZ, 10 μM) for 2 h, then treated with DMSO vehicle 0.1% (v/v), PROTAC **16**, **12** or **15** (1 μM) for 2 h before irradiation followed by cell lysis and Western blot analysis. (C) Structure of ligand **17**.

2.2.4.5.6 Target engagement with BRD4: CETSA experiments

The structure of our caged degrader **12** incorporates the BRD4 inhibitor, JQ1. As the E3 ligase ligand is caged and not JQ1, binding to BRD4 should be maintained for **12** before irradiation. Target engagement assays to measure BRD4 binding had not been previously established in the Tate group. Thus, a simple, label-free method requiring only BRD4 expressing cells and BRD4 targeting antibodies was chosen. Cellular thermal shift assay (CETSA) is a method based on the concept that ligand binding to a protein induces a thermal stabilization resulting in a shift of its denaturation temperature[269] (**Figure 2.20 A**). By quantifying the amount of residual soluble BRD4 in presence and absence of compound after heat treatment, target engagement can be assessed.

We initially determined the melting temperature (Tm) of BRD4 as 44.3°C (**Appendix 2.4**). Using this set temperature, we performed an isothermal dose response for JQ1 and compound **12**. We observed a dose dependent increase in BRD4 band intensity reflecting higher concentration of BRD4 in the soluble fraction, and thus increased stabilization as compared with the DMSO control for both compounds (**Figure 2.20 B**). This confirmed that the caged PROTAC **12** was engaging BRD4 in cells in a similar manner to JQ1.
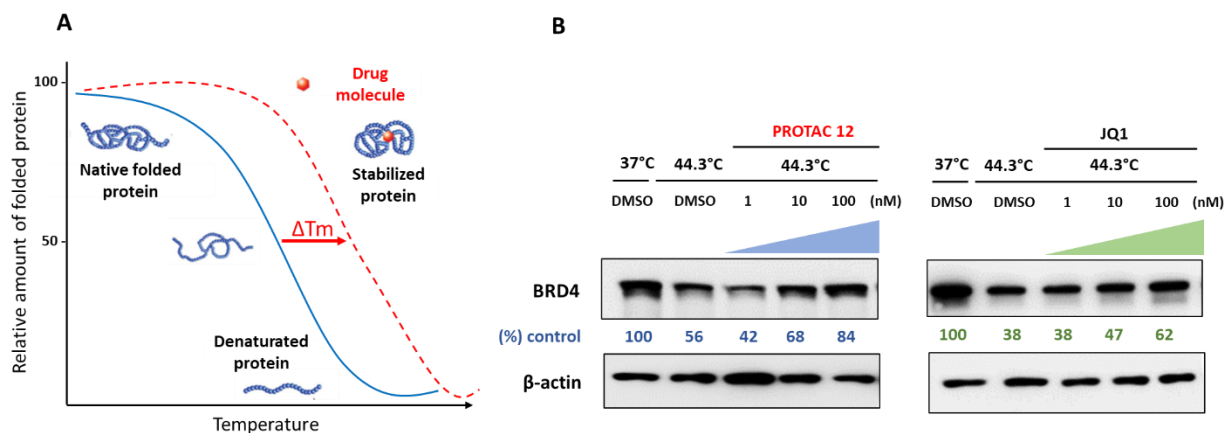
Figure 2.20 Target engagement via CETSA. (A) Cellular Thermal Shift Assay concept. Drug molecule binding results in thermal stabilization of the bound protein leading to a shift of its melting temperature versus the unbound protein (ΔTm) (B) Evaluation of ligand-induced thermal stabilization of BRD4 by CETSA. Hela cells were treated with caged PROTAC **12** or JQ1 for 18 h. After collection of the intact cells, heat treatment was performed at 44.3°C (melting temperature previously obtained) followed by cell lysis. The recovered soluble fractions were analysed by Western blot.

2.2.4.5.7 Effect on cell proliferation: Incucyte experiments

The effect of our caged degrader on cell proliferation was assessed using the Incucyte® S3, a live-cell imaging system which allows automatic image acquisition and analysis of cells in culture. HeLa cells were first monitored after treatment with the intermediate **9** (caged E3 ligand intermediate prior to adding the linker and JQ1, **Figure 2.21**) over six days. The growth curve indicated that the caged E3 ligand alone did not affect cell proliferation as compared with the DMSO control **(Figure 2.21 A).**
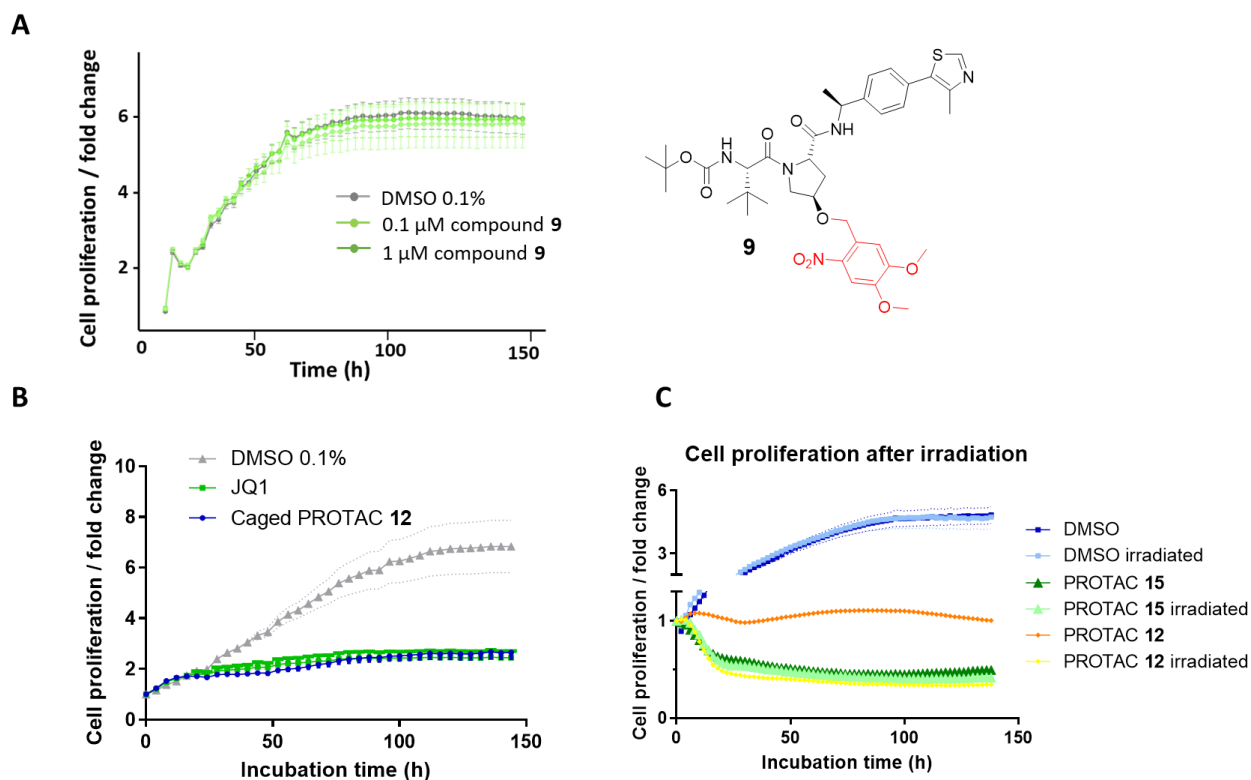
Figure 2.21 Effect of caged degrader on cell growth**.** (A) HeLa cells were treated with DMSO, intermediate **9** (0.1 and 1 μM) without irradiation. Cell count was measured over 6 days, normalized to cell count at t0, and fold changes plotted. (B) HeLa cells were treated with DMSO, JQ1 (1 μM) or caged PROTAC **12** (1 μM) without irradiation. Cell count was measured over 6 days, normalized to cell count at t0, and fold changes plotted. (C) HeLa cells were treated with DMSO, PROTAC **15** (1 μM) or **12** (1 μM) either without initial irradiation or with a 60 second irradiation time. Cell count was followed over 6 days, normalized to cell count at t0, and fold changes plotted.

Uncaging of the DMNB group attached as an ether linkage releases in stoichiometric amount 2-nitroso-4,5-dimethoxybenzaldehyde as a side-product (**Scheme 2.3**). This by-product was not synthesized due to its instability and thus could not be tested for its potential effect on cell growth. Nonetheless, we note that Dieters et al. have demonstrated that their nitrosoketone by-product formed during activation of their caged degrader did not affect BRD4 protein levels after treatment of HEK293T cells.[270] Furthermore, the widespread use of DMNB derivatives as light activated groups to control and study biological systems suggests that potential cellular perturbations generated by the nitroso-released moiety falls within an acceptable level.

With sufficient evidence to suggest that the caged VHL warhead was not inherently toxic to mammalian cells, the entire degrader **12** was evaluated for effect on cell proliferation. Without being irradiated, **12** attenuated cell growth to a similar extent as JQ1 (**Figure 2.21 B**) exhibiting a cytostatic effect. Although the caged degrader **12** was not able to deplete BRD4 levels, it can still interact with BRD4 via its free JQ1 moiety (cf. **section 2.2.4.5.6**, CETSA experiments).

Finally, the parent PROTAC **15** and the caged compound **12** were tested prior and post irradiation. Upon irradiation, compound **12** was cytotoxic, analogous to PROTAC **15**, which exhibits a cytotoxic effect regardless of the irradiation status (**Figure 2.21 C**). In conclusion, these experiments confirm mechanistically that the uncaging of **12** upon irradiation leads to BRD4 depletion and cell growth dysregulation. This also emphasizes the stronger cellular effect of degradation versus inhibition of BRD4.

2.2.4.5.8 Visualizing degradation by live fluorescence microscopy

In addition to Western blots as a readout for our experiments, we also aimed to visualize the depletion of our target protein, BRD4, via live cell fluorescence microscopy. A GFP-BRD4 construct plasmid was generated by Dr Maria Shchepinova, postdoctoral researcher in the Tate group, for transient expression in HEK293 cells. Preliminary experiments were conducted to confirm the ability of compounds **12** and **15** to degrade BRD4 upon irradiation in non-transfected HEK293 cells. As in HeLa cells, 1 μM of compound **12** achieved complete degradation of BRD4 after irradiation for only 60 seconds (**Figure 2.22**). In transfected HEK293 cells, the caged degrader **12** was unable to deplete GFP-tagged BRD4 under non-irradiating conditions. However, robust decrease of fluorescence signal was observed within 2 h of initial irradiation confirming uncaging of **12** and reduction of GFP-BRD4 protein levels (**Figure 2.23**).

DMSO		15		12			
0.1%		1 μM		0.1 μM		1 μM	
-	⚡	-	⚡	-	⚡	-	⚡
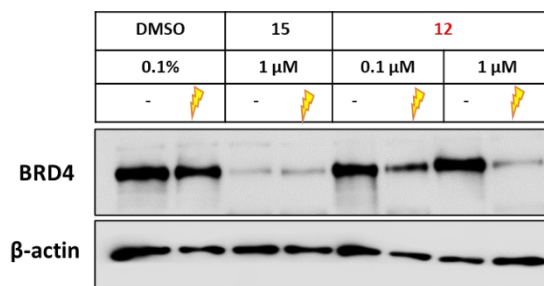
Figure 2.22 Evaluation of caged degrader in HEK293 cells. HEK293 cells were incubated with DMSO, PROTAC **15** or PROTAC **12** for 2 h then irradiated for 1 min. After 24 h, lysates were collected for Western blot analysis.
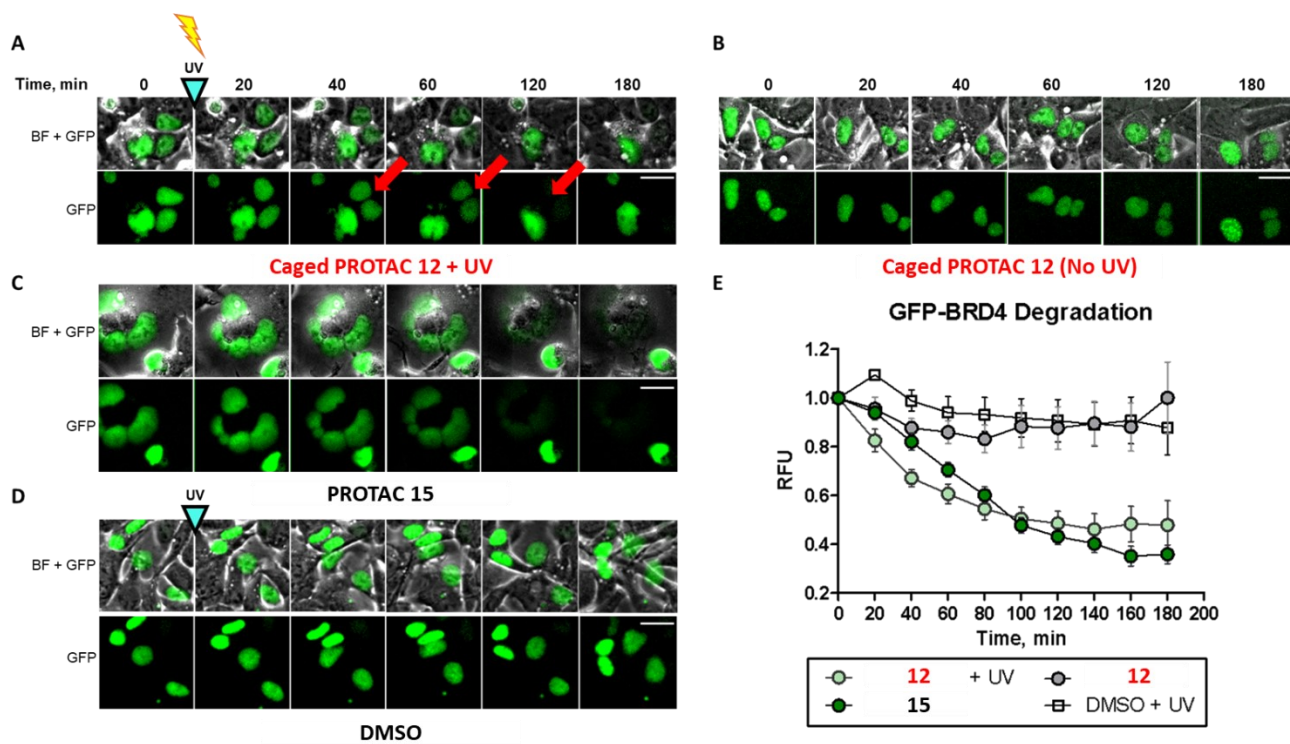
Figure 2.23 Light-induced GFP-BRD4 degradation by caged PROTAC measured by live-cell fluorescence imaging of HEK293 cells transfected with pEGFP-BRD4-C1 plasmid. Cells were incubated with (A) 1 µM PROTAC **12** for 1 h and UV irradiated for 60 seconds, or with (B) 1 µM PROTAC **12** (no irradiation), (C) 1 µM PROTAC **15** (no irradiation) or (D) DMSO vehicle (0.1% v/v), and UV irradiated for 60 seconds. GFP fluorescence was monitored over 3 h, with images taken every 20 min. Scale bar = 20 mm. (E) Quantification of GFP signal degradation over time following PROTAC (1 µM) or DMSO (0.1% v/v) treatment, with or without UV irradiation. Each data point represents background-subtracted time-normalized mean fluorescence from n = 10 single cells, error bars represent SEM.

2.3 Towards *in vivo* application

The most advanced application of light in combination with small molecules in a clinical setting is photodynamic therapy (PDT).[271,272] It relies on the use of photosensitizing chemicals which upon irradiation (λ >600 nm) in the presence of molecular oxygen, generate reactive oxygen species (ROS) causing cellular damages that ultimately lead to cell death (**Figure 2.24**). In PDT, as the light source is only applied where the photosensitizer has diffused, tissue selective toxicity can be accomplished. PDT has been praised as a therapeutic option as it is a non-invasive procedure and offers a good safety profile.[273] It has been successfully applied for the treatment of various skin conditions, esophagus, head, and neck cancers.[274] Recognizing the strong potential of protein degraders as drug molecules, we proposed that caged degraders could be used as a new form of light-mediated therapy. With a promising *in vitro* data using our caged degrader, we hence decided to investigate *in vivo* applications.
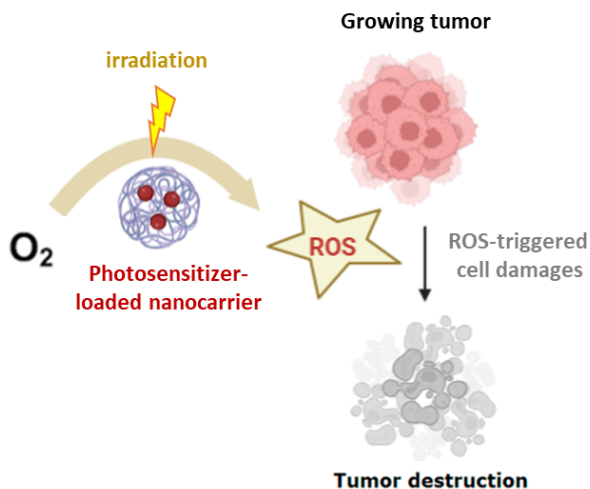
Figure 2.24 Principle of photodynamic therapy (PDT). Activation of photosensitizing chemicals with specific wavelengths of light in presence oxygen (O_2) generates reactive oxygen species (ROS) which can trigger apoptotic and necrotic cell death.

2.3.1 Limitations of caging groups

In principle, delivery of light into a cancerous tissue containing sufficient concentrations of a caged degrader (designed for a specific oncogenic target) could allow a targeted cytotoxic effect only in cells subjected to irradiation. *In vivo* use of photocaged PROTACs has been limited to Zebrafish models which permit UV light delivery without hindrance due to the optical transparency of the fish species. Indeed, Xue et al. demonstrated the effect of UV light on the development of Zebrafish embryos pretreated with caged BRD4 targeting PROTACs.[228] In their study, impairment in the growth of the fish yolk resulting from BRD4 degradation was only seen upon irradiation while non-irradiated embryos also treated with the same caged bifunctionals maintained normal yolk development (**Figure 2.25**).

As most caged degraders incorporate the DMNB group, the activating wavelength used is often limited to 365 nm – the maximal absorbance of DMNB. Unfortunately, such wavelength offers poor tissue penetration, hence restricts the use of UV-activated molecules to *in vitro* experiments only. In order for the caged degrader approach to be useful for *in vivo* applications, unique solutions need to be developed. We thus considered alternative activating wavelengths alongside innovative light delivery methods.
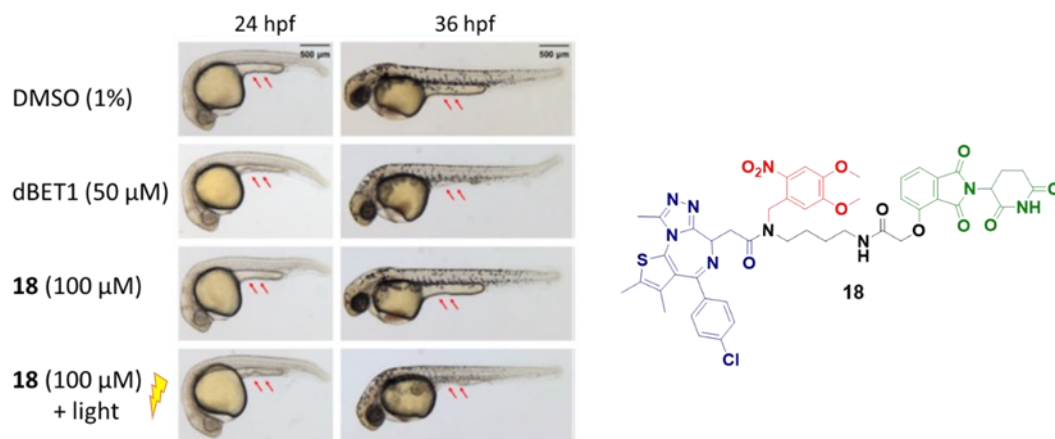
Figure 2.25 Use of photocaged PROTACs in zebrafish. Phenotype of zebrafish embryos treated with dBET1 and caged PROTAC **18** at 24 and 36 h postfertilization (hpf). Non-irradiated embryos treated with **18** developed a full yolk as per the DMSO control while embryos irradiated at 365 nm for 10 min fail to grow a yolk extension in the presence of **18** similarly to dBET1. Image adapted with permission.[228] Copyright 2019 American Chemical Society.

2.3.2 Uncaging in the visible range

As shown in **Figure 2.26**, the tissue depth that can be reached through the skin is dependent on the wavelength of the incident light. When using short wavelengths below 380 nm (UV range), as little as 0.1 mm penetration depth is achieved while above 800 nm (infrared and near-infra red), the subcutaneous tissue can be targeted at a depth of 5 mm.[275] Considering the positive correlation between wavelength and tissue penetration, the activation of our caged PROTAC **12** at a wavelength longer than 365 nm was also proposed. However, the UV spectrum of caged PROTAC **12** showed weak absorbance above 400 nm (visible range) and raised some uncertainty with regards to the ease of photocleavage at longer wavelengths (cf. **Figure 2.14 A**).
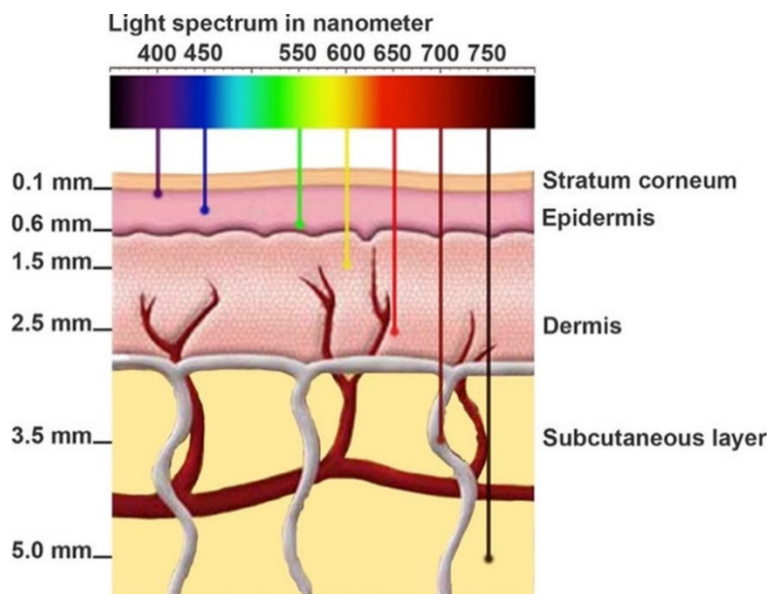
Figure 2.26 Penetration depth of light into tissue according to its wavelength. Image reproduced with permission.[275]

405 nm was selected as an initial uncaging wavelength in the visible range. First, a 50 µM solution of PROTAC **12** in acetonitrile/water was subjected to 1- and 3-min irradiation at 405 nm. Uncaging efficiency was monitored by LC-MS. After 60 seconds, up to 82% of the parent PROTAC was observed with complete uncaging obtained upon irradiation for 180 seconds (**Figure 2.27 A**). This positive result led us to assess in-cell photoactivation and degradation at 405 nm. HeLa cells were incubated with compound **12** for 1 h and 30 mins before being irradiated for 60 seconds at 405 nm. Dose-dependent degradation of BRD4 was visualized by Western blot analysis confirming the release of the parent PROTAC in cells (**Figure 2.27 B**). Since 405 nm is still at the beginning of the visible range, the gain in terms of tissue penetration over 365 nm may be negligible. Although, assessment at longer wavelengths was not performed in our study, we refer the reader to the development of caging groups designed for activation at the higher end of the visible scale. As an example, Zhu lab engineered coumarin-based photocaging groups with uncaging wavelength extending to 600 nm and the added benefit of being orthogonal to UV sensitive photoprotecting group.[276] Besides modifying the caging group structure to achieve *in vivo* activation at a deeper level in tissue, the source of irradiation can be altered. For instance, two-photon excitation with lasers centered in the infrared and near infrared region can allow activation of UV sensitive caging groups.[277–279] That specific strategy was not a point of focus in our research.
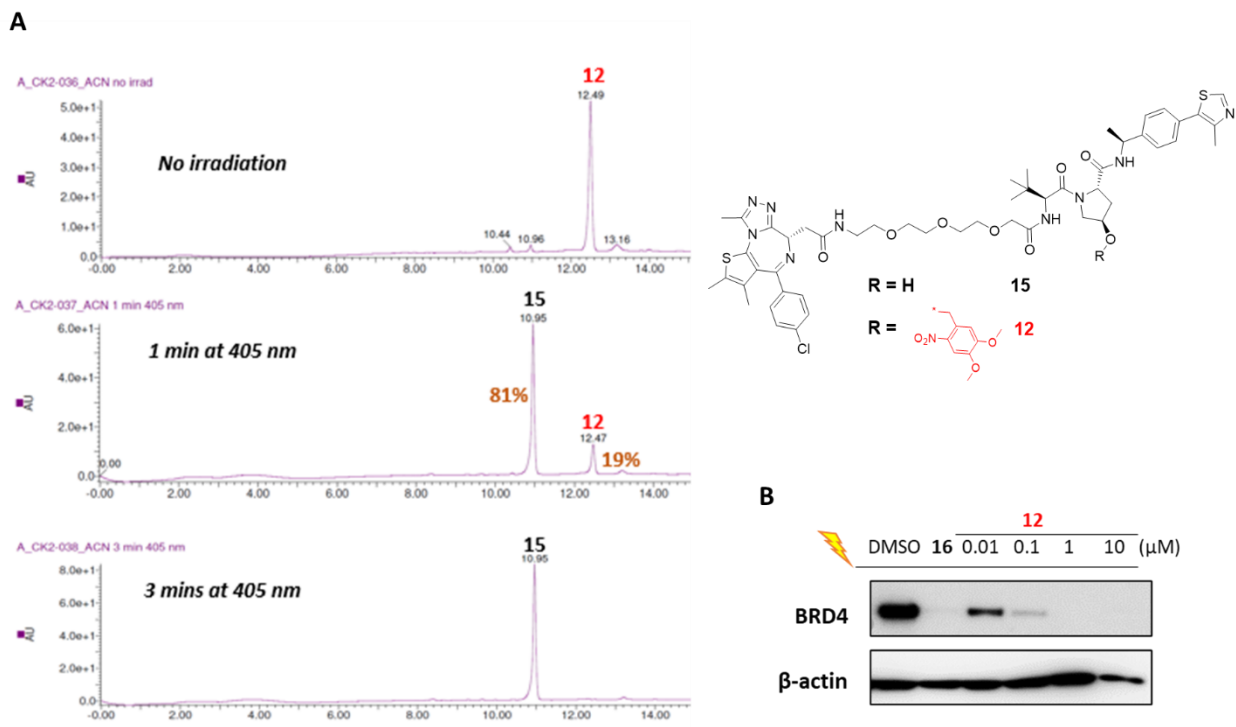
Figure 2.27 Uncaging of compound **12** at 405 nm. (A) LC-MS chromatogram of compound **12** (50 µM) before and after a 1- or 3- min irradiation in acetonitrile/water (3:1). About 80% uncaging was achieved after 60 seconds. (B) HeLa cells were incubated with DMSO, PROTAC **16** or PROTAC **12** for 1 h 30 mins then irradiated for 1 min at 405 nm. After 24 h, lysates were collected for Western blot analysis.

2.3.3 Light delivery *in vivo*

Application of light to uncage a molecule is often done externally (i.e., the light source is outside of the cell), and this represents a limitation to get through cellular layers. Another appealing avenue for such endeavor is the direct delivery of light from within the target tissue for uncaging of a molecule *in vivo*. Our research led us to consider two reported approaches, Upconversion nanoparticles (UCNPs) and Cerenkov radiation.

2.3.3.1 Upconversion nanoparticles

Upconversion is a process by which the excitation of certain material (such are rare-earth metals) with long wavelength photons (near infrared, NIR) leads to the emission of radiations with shorter wavelength (typically in the UV-Vis range) upon relaxation. This phenomenon has been exploited in bioimaging applications with the emergence of nanoparticles doped with lanthanides.[280,281] Upconversion nanoparticles (UCNPs) containing lanthanides can be injected into tissues and allow irradiation with NIR light to a 10 mm depth. For example, the Xing group has exploited the properties of UCNPs to trigger localized bioluminescence in living mice.[282] A caged luciferin molecule was chemically attached to the UCNPs via a nitrobenzyl group and excitation with 980 nm light caused the emission of UV light and subsequent the release of luciferin (**Figure 2.28 A**). Considering this strategy, one could contemplate a similar approach for a caged PROTAC to degrade a cancer target. Injection of an UCNP-caged PROTAC adduct into a cancer tissue followed by NIR-triggered release of the parent PROTAC could be an interesting therapeutic approach (**Figure 2.28 B**). However, this method was beyond the scope of this research, although it remains a promising therapeutic strategy.
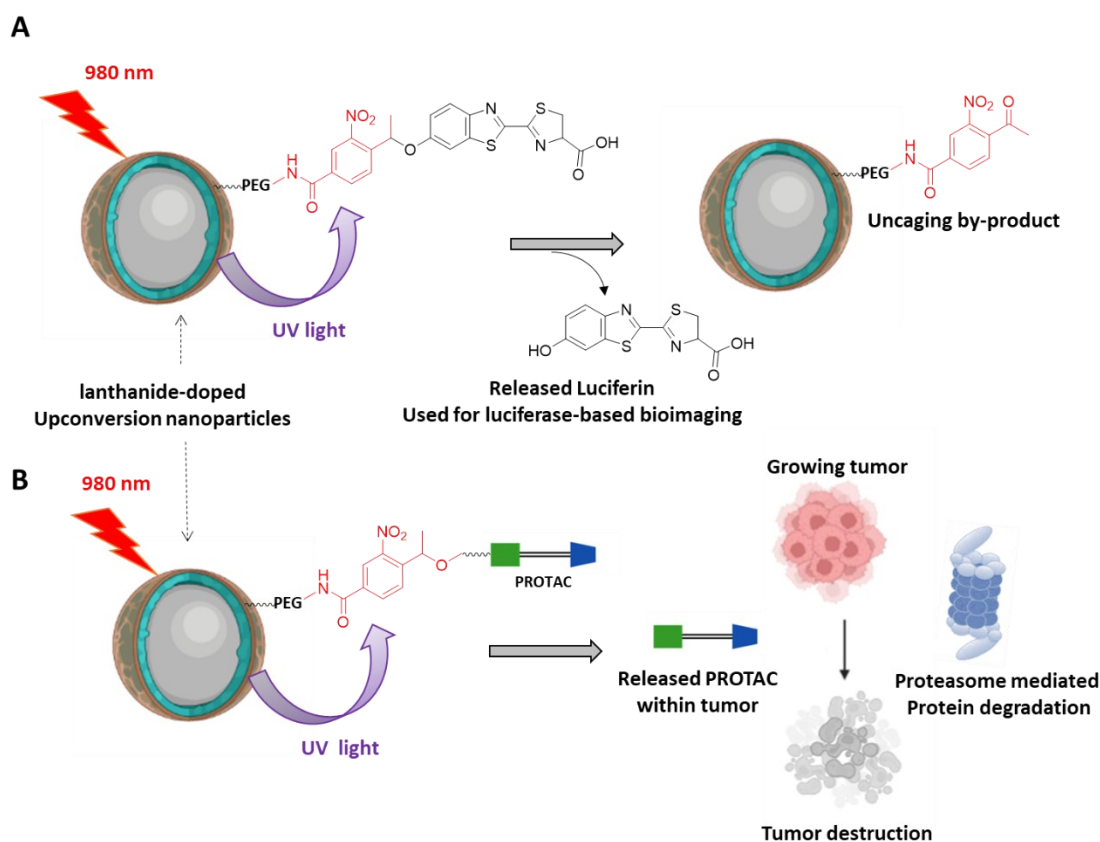
Figure 2.28 Uncaging mediated via upconversion nanoparticle. (A) Caged luciferin was chemically attached to lanthanide-doped nanoparticles. After near-infrared irradiation, the resulting UV allowed the release of luciferin. (B) Upconversion strategy applied to caged PROTAC as a potential follow-up approach.

2.3.3.2 Harnessing Cherenkov radiation

In 2011, Ran et al. reported the release of a caged luciferin "without using light".[283] A 4,5-dimethoxy nitrophenyl ester of luciferin (DMNP-luciferin) was uncaged by a commonly used PET tracer, Fluorodeoxyglucose (^{18}F-FDG). The authors presented data showing that UV-visible light resulting from the decay of ^{18}F-FDG, known as Cherenkov radiation, could be harnessed for the photoactivation of DMNP-luciferin. When a charged particle travels in a medium at a speed greater than the phase velocity of light in that medium, surrounding molecules can be polarized to a high energy (excited) state and relax back to a ground state by emitting light that spans across the UV-visible range. This emission of light was named after the Russian scientist Pavel Cherenkov, who first observed this radiation in 1934[284] (**Figure 2.29**). Cherenkov radiation can emanate from various sources including nuclear reactors, particle accelerators and common radionuclides used in clinical settings. Besides bioimaging, several attempts have been made to utilize Cherenkov radiations for biomedical applications, notably through photouncaging.[285] In a manner similar to Ran et al., we decided to investigate the activation of our photocaged PROTAC **12** with various radionuclides for use of caged PROTACs *in vivo*.
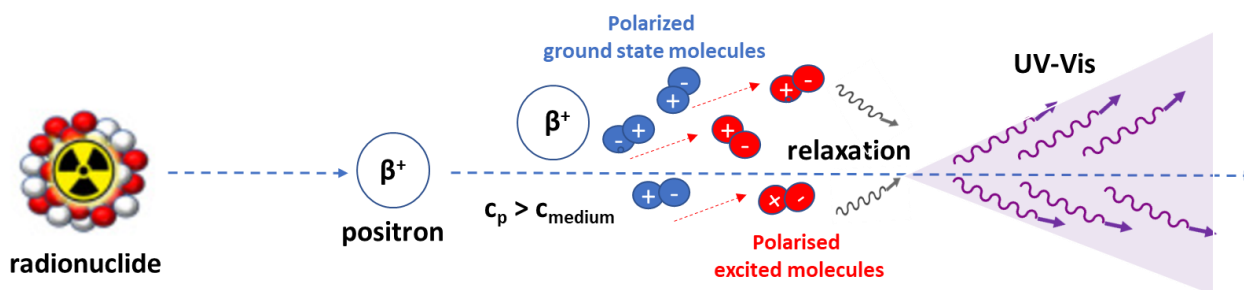
Figure 2.29 Cherenkov radiation principle. Positrons from radionuclides travelling at a speed (c_p) which is greater than the speed of light in that particular medium (c_{medium}) can turn particles into an excited state. Relaxation of those particles to a ground state results into the emission of UV-Vis light.

2.3.3.2.1 Experiments with ^{18}F

Fluorine 18 (^{18}F) is a fluorine radioisotope which decays by emitting positrons. ^{18}F has a half-life of 109 mins and is used to produce radiotracers such ^{18}F-FDG. This tracer is accumulated in certain organs such as the brain and the kidney but also in solid cancers where consumption of glucose tends to be higher than in healthy tissues.[286] For this reason, ^{18}F-FDG is extensively used for imaging tumors in oncology.[287] In order to have access to ^{18}F-FDG, a collaboration was started with the laboratory of Eric Aboagye (Department of Surgery and Cancer – Imperial College London). A postdoctoral student from Prof. Aboagye's lab, Dr. Marta Costa Braga conducted the experiments to test if our caged BRD4 degrader **12** could be activated in cells with ^{18}F-FDG. VHL-positive and VHL-negative renal carcinoma cell lines (RCC-4) were used for the experiments with an initial dose of 20 μCi ^{18}F-FDG (about 20 times less radioactivity than the dose used in the animal study from Ran et al.) since we were working with cells only and not yet *in vivo*. The

experimental set up is describe in **Figure 2.30 A**. RCC4 cells were treated with ^{18}F-FDG for 1 h and after a media change to remove extra cellular ^{18}F-FDG, cells were incubated with 1 μM of either caged PROTAC **12** or parent degrader **15**. Western blot analysis was conducted after 24 h. As expected, the parent degrader **15** achieved complete depletion of BRD4 in VHL-positive cells and not in VHL-negative cells irrespective of the presence or absence of ^{18}F-FDG **(Figure 2.30 B)**.

When the caged degrader **12** and ^{18}F-FDG were combined, BRD4 depletion was not observed in VHL-positive cells indicating that the process of uncaging had not occurred (**Figure 2.30 C**). Lack of BRD4 degradation could have been due to several factors. First, the dose of ^{18}F-FDG (20 μCi) may have been insufficient to trigger the release of the DMNB group. Secondly, since the caged PROTAC was added one hour after the cells had been treated with ^{18}F-FDG, 30% of the initial radioactivity would have been lost due to fast kinetics of decay of ^{18}F-FDG.
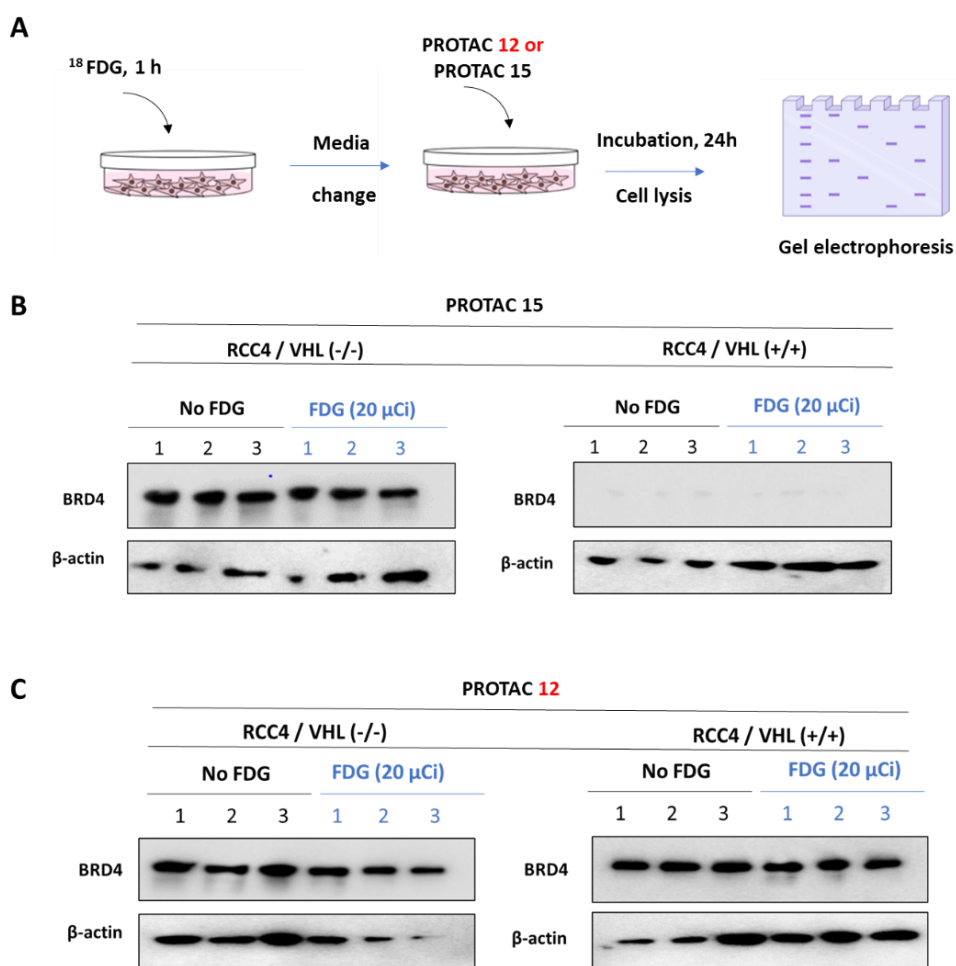
Figure 2.30 Attempt to uncage PROTAC **12** in RCC4 cells with ^{18}FDG. (A) The protocol consists of a preincubation with ^{18}FDG, followed by a change of medium before final treatment with PROTAC (1μM). (B) RCC4 cells (VHL positive or negative) were treated with PROTAC **15** after a pre-incubation with ^{18}FDG or DMSO. Cells were lysed after 24 h and lysates collected for Western blot analysis. (C) RCC4 cells (VHL positive or negative) were treated with PROTAC **12** after a pre-incubation with ^{18}FDG or DMSO. Cells were lysed after 24 h and lysates collected for Western blot analysis.

The uncaging of compound **12** by ^{18}F-FDG was thus investigated *in vitro* prior to further cellular experiments. Compound **12** (100 μM) was incubated with 500 μCi or 1000 μCi of ^{18}F-FDG for 24 h at room temperature in the dark. LC-MS analysis confirms that uncaging did not occur despite a dose of radioactivity twice as high as the dose used by Ran et al (**Figure 2.31**).

In 2011, Cherry's laboratory described the potential of Cherenkov radiation as a new tool for molecular imaging. In the publication, Cerenkov light output from diverse radionuclides was modelled through Monte Carlo simulations and the predicted photon yield per decay (for the wavelength range 400-800 nm) was found to be between 1 and 100 photons. For Fluorine 18 (^{18}F), the estimated number of photons per decay was 1.4 while Phosphorus 32 (^{32}P) and Yttrium 90 (^{90}Y) gave 33 and 57 photons per decay respectively (**Appendix 2.5**). With the knowledge of this information, we then determined to source for ^{32}P and ^{90}Y to attempt the photouncaging of our caged degrader **12**. At this stage, our hypothesis was that a radionuclide which can deliver a higher number of photons per decay than ^{18}F will facilitate uncaging.
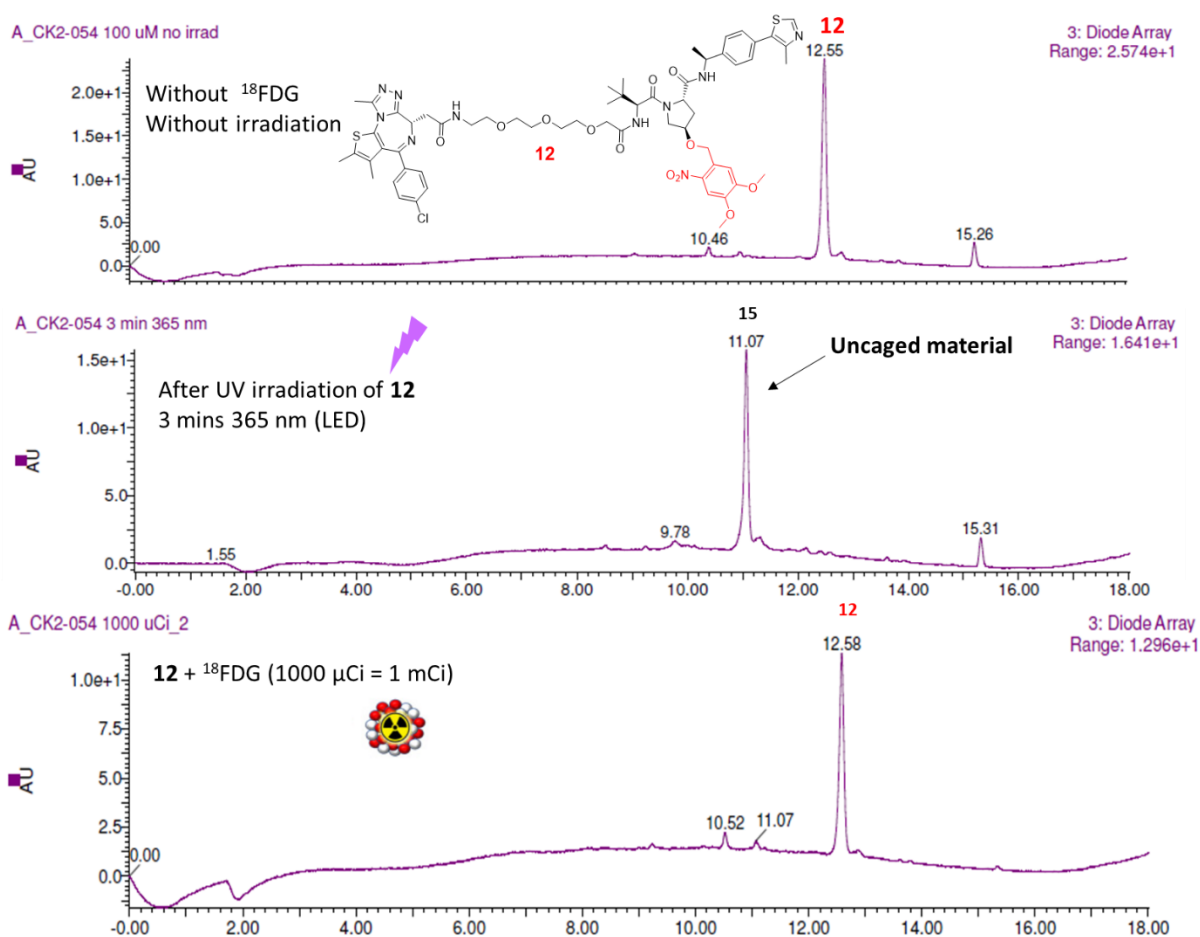
Figure 2.31 Attempt to uncage compound **12** with ^{18}FDG. LC-MS chromatogram of compound **12** (100 μM) without irradiation and without ^{18}FDG in acetonitrile/water (3:1) (top). LC-MS chromatogram of compound **12** after UV irradiation (365 m for 3 mins) (middle). LC-MS chromatogram of compound **12** after incubation with ^{18}FDG (1 mCi) for 24 h in the dark (bottom).

2.3.3.2.2 Experiments with ^{32}P

Phosphorus 32 (^{32}P) is a phosphorus radioisotope which decays by emitting positrons with a half-life of 14 days and is used in medicine, molecular biology, and biochemistry to identify or trace phosphorylated molecules.[288] Because of the high energy β^+ particles emitted by ^{32}P, it has also been investigated as a treatment option in radiation oncology.[289] For our research purpose, ^{32}P was sourced from Peter Parker (Senior Investigator at the Crick Institute). A solution of ^{32}P-labelled sodium orthophosphate in water was added to a 100 µM solution of caged degrader **12**. Various radioactivity doses ranging from 50 µCi to 500 µCi were used while the samples were kept at room temperature for 24 h and protected from light. Because of ^{32}P long half-life (14.26 days) which would require a 4-month waiting time to get cold samples (free from radioactivity), extraction with ethyl acetate was performed to recover any material derived from the caged degrader while the orthophosphate could be washed away in the aqueous layer. Extracted samples were then submitted for LC-MS analysis. Unfortunately, no uncaged PROTAC **15** was detected even at the highest radioactivity dose tested (500 µCi) (**Figure 2.32**). This result led us to look at another radionuclide, Yttrium (^{90}Y) as a more powerful source of Cherenkov radiation.
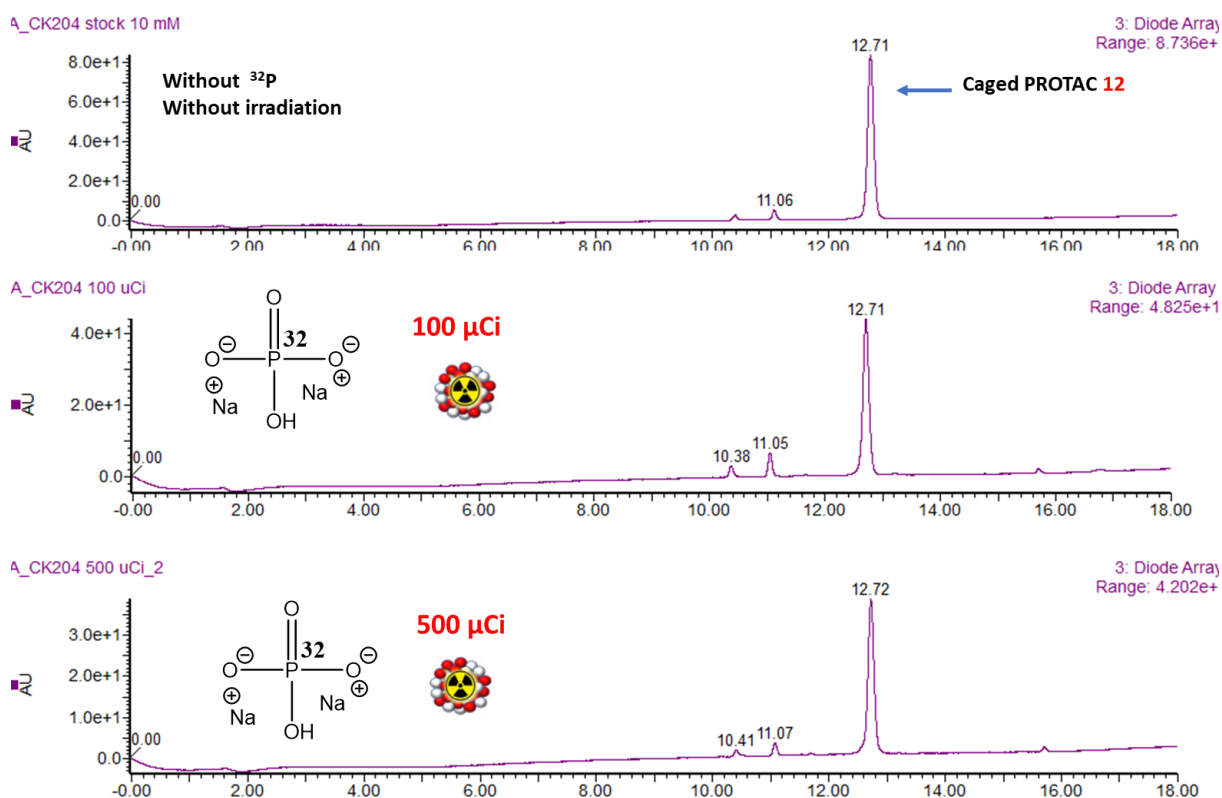
Figure 2.32 Attempt to uncage compound **12** with ^{32}P. LC-MS chromatogram of compound **12** (100 µM) without irradiation and without ^{32}P in acetonitrile/water (3:1) (top). LC-MS chromatogram of compound **12** after incubation with ^{32}P (100 µCi) for 24 h in the dark (middle). LC-MS chromatogram of compound **12** after incubation with ^{32}P (500 µCi) for 24 h in the dark (bottom).

2.3.3.2.3 Experiments with ^{90}Y

Yttrium 90 (^{90}Y) decays by emitting positrons and has a half-life of 64.1 hours. Its main application is in radiation oncology for the treatment of hepatocellular carcinoma (HCC).[290] Hartl et al. have also demonstrated that Cerenkov light from ^{90}Y can be harnessed to activate PDT.[290] Unlike ^{18}F, ^{90}Y is extremely difficult to source because of the limited numbers of manufacturers worldwide. In collaboration with the laboratory of Dr. Kuldip Nijran (Department of Nuclear medicine – Imperial College London), access to ^{90}Y was made possible. After a patient was treated for liver cancer via a radioembolization procedure (radiotherapy in which ^{90}Y tiny beads called SIRT spheres are delivered directly into the liver)[291], the left over ^{90}Y was incubated with our caged PROTAC **12**. A 10 mCi dose of SIRT spheres was used in triplicate and the samples were kept at room temperature protected from light for two months. LC-MS analysis was made difficult as a major solvent front made the signal-to-noise ratio decrease significantly (**Appendix 2.6**).
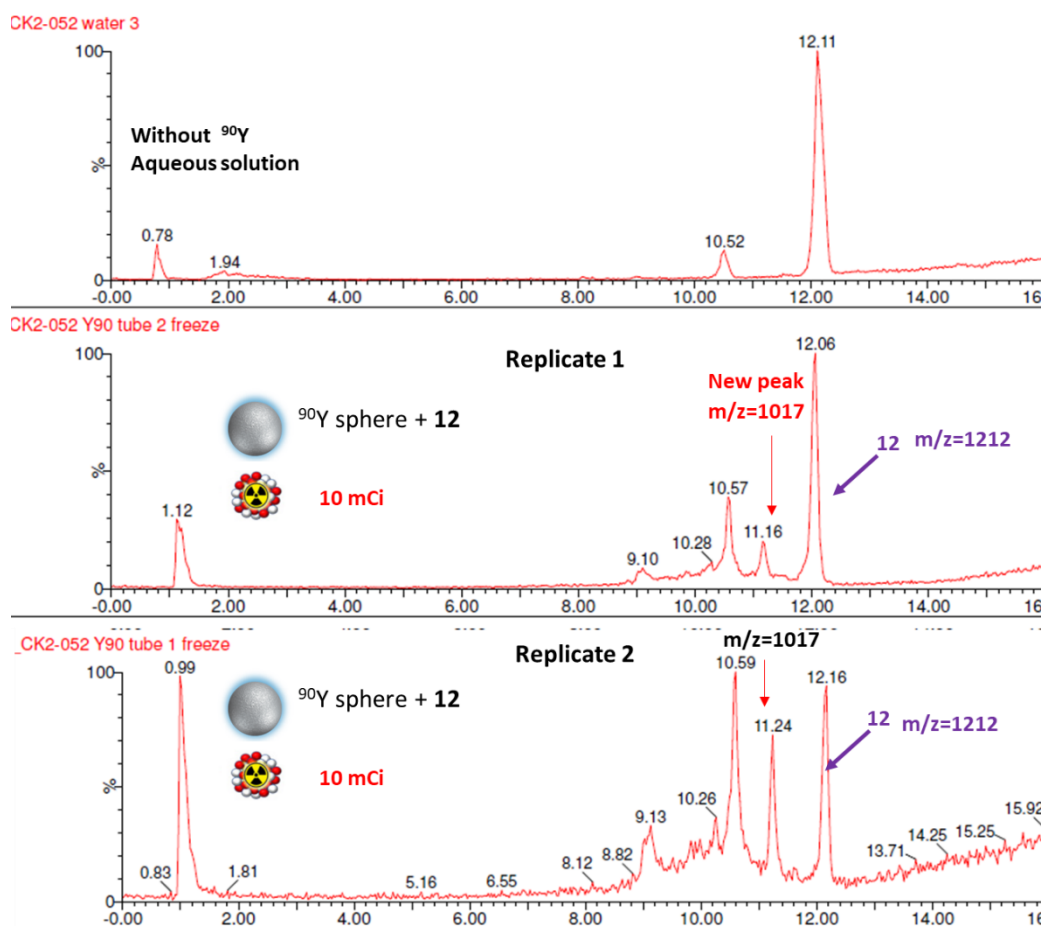
Figure 2.33 Mass chromatogram trace TIC (total ion count) after incubation of **12** with ^{90}Y spheres (10 mCi) for 60 days in the dark. A new peak could be identified with the mass corresponding to the uncaged material m/z=1017 (M+1).

Nonetheless, a new peak bearing the expected mass gave us a qualitative confirmation that uncaging occurred (**Figure 2.33**). The UV chromatogram was not sufficiently resolved to give a quantitative estimation of the level of uncaging. These preliminary results with ^{90}Y, although not significant, partly corroborate our hypothesis that Cerenkov rays as source of light can be used for small-molecule uncaging.[285]

An estimation of the theoretical number of photons which would be required for uncaging our caged molecule with a radionuclide such as ^{90}Y was carried out (**Appendix 2.7**). This approximate calculation reveals that about 50 times more photons would be required from ^{90}Y to achieve the same level of uncaging as a 25 mW 365 nm LED. Of note, the calculation does not take into consideration the two following points:

-the photons from Cerenkov radiation are more distributed in the UV-Visible spectrum (with each individual photon carrying different energy levels) and this uneven distribution can certainly impede the uncaging process

-the photon yield from the radioisotope decreases over time

As a consequence, we conclude that a significantly higher dose of ^{90}Y (~0.5 Ci) would be needed to reach the level of uncaging achieved by 365 nm LED.

2.4 Other reported caged degraders

During this research, several groups concurrently investigated light mediated activation of a bifunctional via a caging strategy.[228,229,270] The publication of multiple research papers using the same approach fully validates the concept and demonstrates its versatility. An analysis of those novel caged degraders has been reviewed in detail.

2.4.1 Caging chemistry

The caging approach used in those publication is largely similar to that attempted in this thesis whereby the most widely used E3 ligase ligands, IMiDs and VHL ligands have been functionalized with a caging group to block interaction with their respective E3 ligase. A brief overview in relation to our work is discussed here. Since crystallographic information is available for both cereblon and VHL proteins with their bound ligand (**Figure 2.7**), the caging groups were attached on the glutarimide NH- to prevent cereblon binding and on the hydroxyl group of VHL to block the interaction with key amino acid residues (cf. **section 2.2.1.1**).
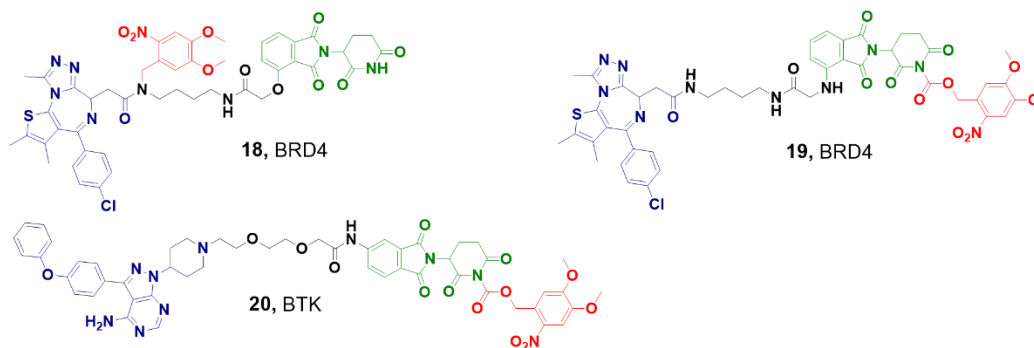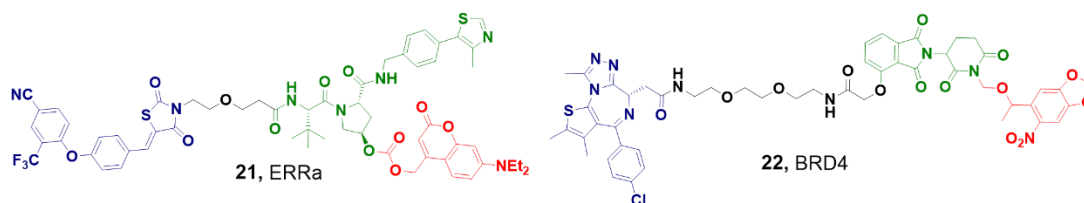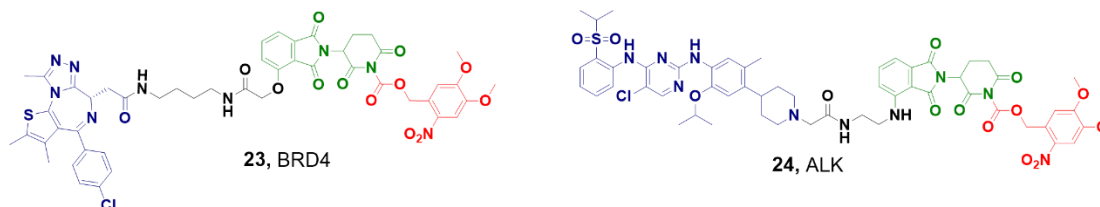
Figure 2.34 Structures of the reported caged PROTACs. Each caged degrader is made of a warhead (depicted in blue), a linker (black), an E3 ligase recruiter (green), and a photocleavable group (red). Compounds **18**, **19**, **22** and **23** were designed to degrade bromodomain-containing protein 4 (BRD4) upon irradiation. Compound X4 was designed to degrade the estrogen-related receptor α (ERRα) upon irradiation. Compounds **20** and **24** were designed to degrade Bruton tyrosine kinase (BTK) and anaplastic lymphoma kinase (ALK), respectively, upon irradiation.

The DMNB group was the most exemplified in those novel caged degraders due to its good absorption at 365 nm and strong precedent in the field of photopharmacology (cf. **section 2.1.2**). The structure of the reported caged degraders is described in **Figure 2.34**.

Apart from compound **18** for which the caging motif is located on the warhead of the POI, the photocaged for all degraders has been placed mainly on the E3 ligase binding part for the reasons explained above. The type of chemistry used to build those compounds is summarized in **Figure 2.35**. The glutarimide moiety usually required a strong base to perform acylation (with NaH or NaHMDS for compounds **19**, **20**, **23** and **24**). Naro et al. also achieved alkylation of the N-glutarimide after synthesizing themselves NPOM chloromethyl ether to obtain **22**. In our case, this type of chemistry did not allow us to access a caged IMiD derivative (cf. **section 2.2.3.3**). For the VHL ligand, successful conditions were developed for O-acylation of the hydroxyl group (compound **21**). Finally, we note that appendage of the cage at a late stage in the chemical synthesis allows in principle for functionalization of multiple PROTACs readily. Such plug and play approach where any degrader can potentially be turned into a light activated PROTAC in one step may prove advantageous.

	compound	caging yield	caging group availability	early or late caging
NaHMDS / DMNB chloroformate	19	27%	commercial	early
	20			late
NaH / DMNB chloroformate	23	47%	commercial	early
	24	34%	commercial	early
DBU / NPOM chloromethylether	22	80%	synthesis required 2 steps	early
DIPEA / DEACM chloroformate	21	59%	synthesis required 3 steps	late
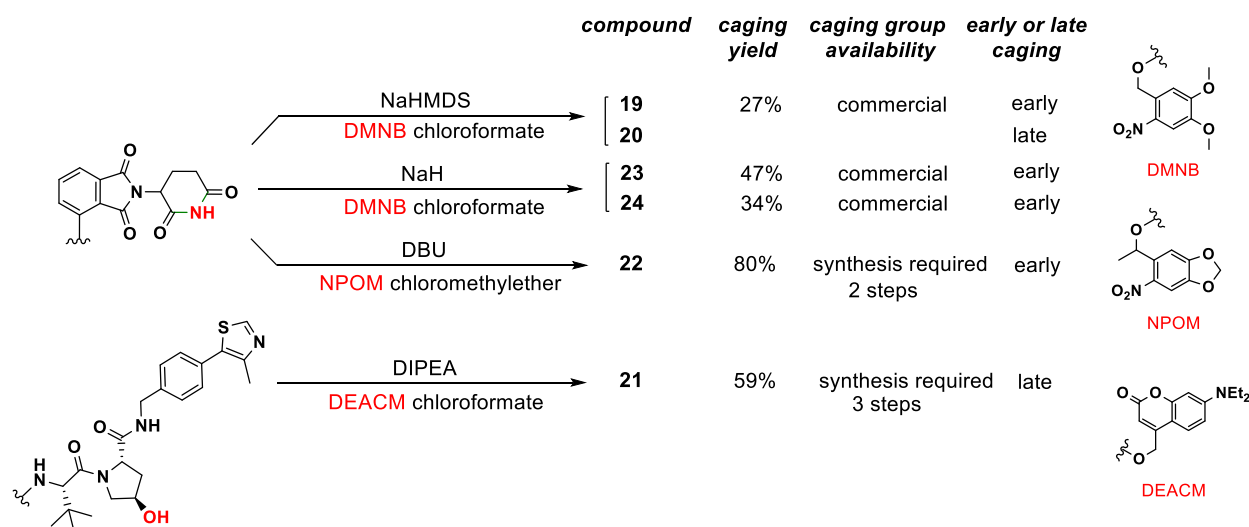
Figure 2.35 Chemical functionalization of E3 ligase ligands with photolabile groups. Varied strategies have been used to introduce the caging groups via acylation or alkylation with most groups installed relatively early in the synthesis as direct chemical modification of the parent PROTAC in the final step was not always feasible. The yield reported represents the yield of the caging step. "Early" caging refers to a synthetic route in which the caging group was not directly attached to the parent PROTAC as opposed to "late" caging. DBU = 1,8-diazabicyclo[5.4.0]undec-7-ene; DEACM = diethylamino coumarin; DIPEA = N,N-diisopropylethylamine; DMNB = 4,5-dimethoxy-2-nitrobenzyl; NaHMDS = sodium bis(trimethylsilyl)- amide; NPOM = 6-nitropiperonyloxymethyl.

2.4.2 Photochemistry

In general, a light source centered at 365 nm was sufficient to obtain at least 50% uncaging in aqueous solution after an 80-second irradiation time for most reported caged compounds. While no hurdle was faced to uncage the VHL-based degraders, we have noted a few contrasting results between various laboratories with regards to glutarimide-based degraders.

As an example, caged PROTACs **19** and **23** depicted in **Figure 2.34** are derived from PROTAC **dBET1** and both carry the exact same caging group. Whereas caged compound **19** failed to deliver any trace of the parent degrader upon irradiation at 365 nm, the caged degrader **23** (opto-dBET1) was reported to successfully photolyzed at 365 nm, although a long irradiation time (>15 mins) was needed to reach adequate level of uncaging.

Likewise, after synthesizing our caged thalidomide intermediate **3** (cf. **section 2.2.3.2**), we were unable to cleave the DMNB group despite using various light sources. In contrast, Li et al. reported the facile conversion of their caged pomalidomide to the parent molecule at 365 nm in acetonitrile. The variability in uncaging efficiency for the glutarimide moiety may be a concern when designing a degrader with a caged IMiD as the E3 ligand. Here, the variations in experimental conditions (solvent, light source type, etc.) may explain some of the contradictory results observed.

2.4.3 Scope of targets investigated via a caged degrader strategy

Light-dependent activation of a caged PROTAC has been validated with bromodomain containing protein 4 (BRD4)[228,292], Estrogen-related receptor alpha (ERRα)[270], Bruton's tyrosine kinase (BTK)[228] and anaplastic lymphoma kinase (ALK)[229] by leveraging on the availability of potent known degraders. In this regard, the caging strategy has proven to be extremely versatile. With a plethora of degraders now available for multiple targets classes, the toolbox of caged degraders can be expanded substantially. The attachment of a caging group on both the VHL and IMiD ligands is established and will facilitate the conversion of a PROTAC into its caged counterpart. Besides using caged E3 ligands, the opportunity to cage the warhead of a degrader remains and the ease of the chemistry will dictate if such option will be exemplified further. In any case, we anticipate that additional examples of caged degraders for diverse target classes will be described in the future.

2.5 Conclusion

Our first investigation on light activated PROTACs led us to validate the caged degrader approach. By using the VHL ligand, we were able to degrade BRD4 conditional on UV light irradiation. As the VHL E3 ligand is widely encountered in the TPD field, we anticipate that our caged E3 motif will enable light-dependent degradation of multiple proteins. Our results along with concurrent publications on caged degraders represent a novel approach within chemical biology and provide useful spatiotemporal tools to study protein function.

In order to overcome the limitation of UV light *in vivo*, we turned to Cerenkov light emitted by radionuclides to achieve uncaging and provide an innovative solution for applications beyond chemical biology. The data we gathered suggest that doses of radiation in the range of 0.5 Ci would be required to observe significant uncaging. Such doses may be incompatible with radiation safety requirements and predefined exposure limits in the clinic. Nonetheless, we remain confident that localized *in vivo* activation of a degrader with light would produce a tissue selective effect and improve the therapeutic index of PROTACs. The disseminated work on caged PROTACs including the research presented here may serve as a strong basis for further investigation for *in vivo* applications.

Chapter 3 | Photoswitchable degraders

3.1 Photoswitchable tools in biology

3.1.1 Spatiotemporal control at a cellular level

The reversible control of cellular functions in a spatiotemporal manner is an endeavor which scientists have been keen to conquer. Among various approaches, photoswitches, light-responsive small organic molecules have been designed to be either incorporated into small molecules (that should exert a biological effect after interacting with a target) or to be directly integrated into macromolecules such as peptides, proteins, or DNA to intrinsically alter their conformation.[293,294] Upon exposure of the photoswitch unit to light, an isomerization is triggered where the shape and properties of the photoswitch change. This isomerization reaction can translate into novel binding interactions, conformational changes of a protein and the inhibition or activation of a receptor or an enzyme.

Key desired characteristics looked for in photoswitches are a high photostationary state ratio (PSS) (defined as the isomers relative proportion after irradiation at a wavelength λ), an acceptable separation in absorption bands between the two isomers, a fast-switching capacity and a good quantum yield (i.e., the efficiency of the photoisomerization event).
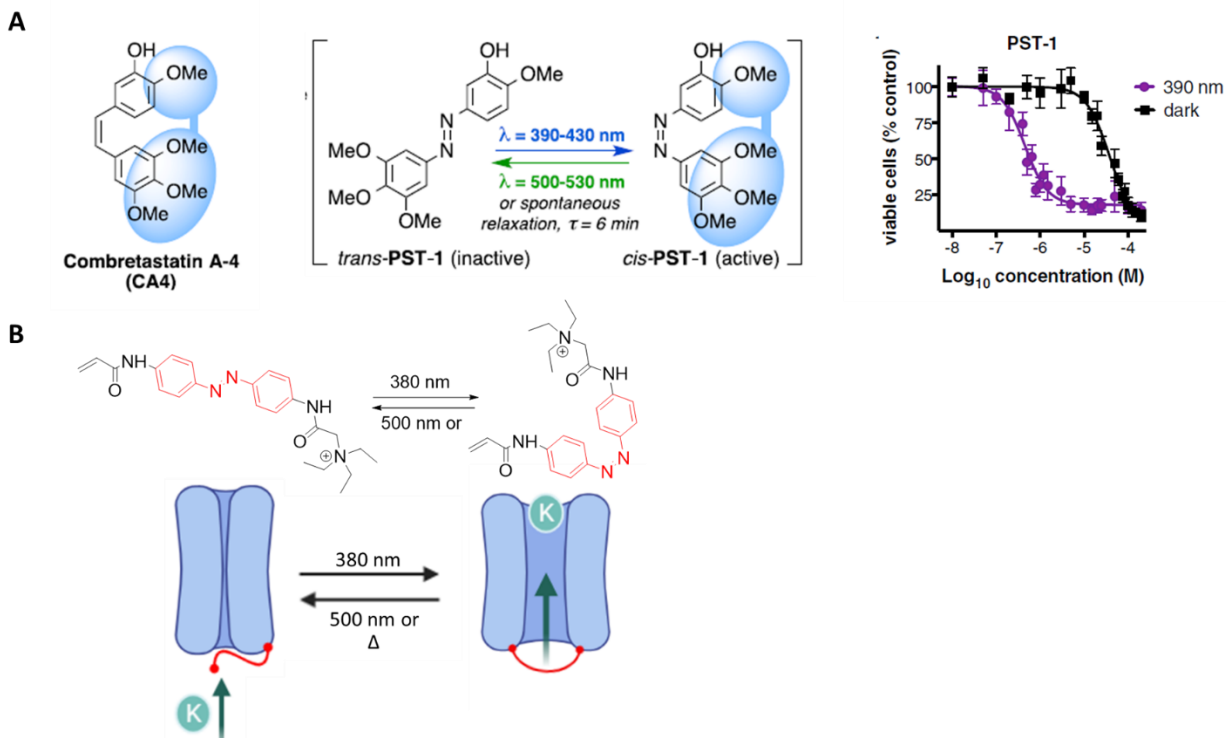
Figure 3.1 Examples of biological applications of azobenzene photoswitches. (A) Structure of Combretastatin A-4 (left). Photostatins (PSTs) derived from Combretastatin A-4 and *trans-cis* isomerization (center). Cell viability dose-response curves for PST-1 under 390 nm irradiation and in the dark (right) reproduced with permission.[295] (B) Structures and photoisomerization of acrylamide-azobenzene-quaternary ammonium photoswitchable potassium channel blockers.

Moreover, thermal stability of the isomers (i.e., long half-life) and compatibility with physiological conditions (solubility, chemical and metabolic stability) are added benefits. Azobenzene derivatives are among the most widely used photoswitches due to their relatively simple synthesis and tunable photochromic properties.[296,297] Some successful applications of azobenzene photoswitches include the optical control of cell division. The Trauner and Thorn-Seshold groups developed photostatins based on a known tubulin polymerization inhibitor, Combretastatin A-4.[295] They have demonstrated that while the *trans* (*E* isomer) was not toxic to cells the *cis* (*Z* isomer) prevented cell division and induced cell death. The toxicity of photostatins could be modulated by keeping the cells treated in the dark (inactive photostatins) or by exposing them to blue light (390-430 nm, active photostatins) (**Figure 3.1 A**). Another noteworthy example includes the restoration of light sensitivity in blind mice using acrylamide-azobenzene-quaternary ammonium photoswitches (AAQ) which interact with voltage gated potassium channels in the animals' retinal neurons (**Figure 3.1 B**).[298] While the *E* isomer of AAQ blocks the channel and increases excitability of the retinal neurons, the *Z* form unblocks the channel allowing a potassium ion flow that reduces excitability. The authors reported that bi-directional control of neuronal firing can be achieved with different wavelengths, namely 380 nm or 500 nm. These two examples emphasize the benefits of photoswitches as powerful biological tools and their potential as light-activated therapeutics. In addition, multiple reviews have described the applications of photoswitches to realize spatiotemporal control of other cellular processes[296,299,300] (transcription, translation, etc.). As part of our goal to develop tool compounds to precisely control protein degradation in space and time, we also turn to photoswitches to generate novel degraders.

3.1.2 Photoswitchable PROTAC concept

The caging approach described in chapter 2 offered an efficient way to irreversibly induce protein degradation starting from an inactive degrader. Here, we hypothesized that the integration of a reversible photoswitchable motif into a bifunctional degrader would provide a subtle way to both trigger and halt protein degradation on demand by using the same molecule. Bearing in mind that the formation of a ternary complex is critical for PROTACs mode of action, we reasoned that conformational changes associated with the photoswitch isomerization would affect both binary and ternary binding interactions. In the optimal case, one isomer only (*Z* or *E*) would trigger efficient protein degradation via favourable interactions while the other isomer would be ineffective or less effective in disrupting the stability of the studied protein (**Figure 3.2**).

The linker connecting the warhead and the E3 ligand is in principle commutable, and its composition and length often dictate the biological outcome of a degrader (**cf. chapter 1**). Consequently, our design involved installing a bis-arylazo-containing motif as the linker in our bifunctional compounds in order to gain the on/off switch capacity.
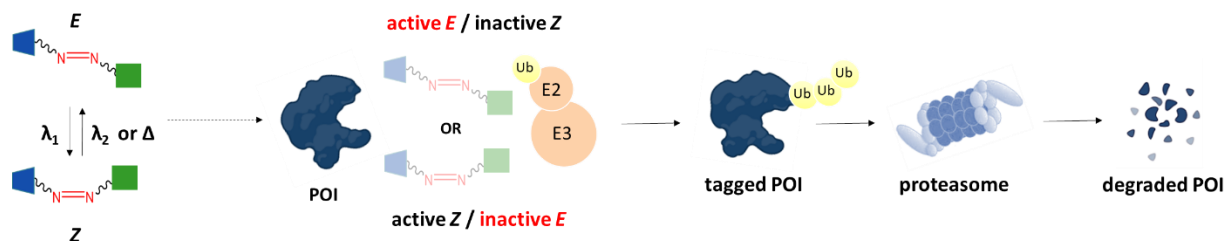
Figure 3.2 Photoswitchable degrader concept. The bis-arylazo motif enables the formation of two geometrical isomers: the Z isomer can be obtained by irradiation of the E isomer with a specific wavelength λ_1, and inversely, the E isomer can be generated from the Z either with another wavelength λ_2 or by thermal relaxation. The difference in conformation between the two isomers affects binding interactions and allows degradation to occur with only one isomer (Z or E) but not the other.

3.1.3 Arylazopyrazole photoswitch

To probe our photoswitchable PROTAC design, we turned to the heteroazoarene photoswitches developed by the Fuchter lab at Imperial College London.[301–303] By replacing one of the phenyl rings (normally present in azobenzene photoswitches) with a 5-membered heterocycle ring such as a pyrazole, Fuchter's lab engineered photoswitches with superior photochemical properties. The azopyrazole chemical system can be quantitatively switched in both directions (E to Z and conversely) thanks to a sufficiently large separation of absorption bands for the two isomers. In addition, the Z isomer can offer an extremely long half-life (up to 1000 days) which compete with the best azobenzene (tetrafluoroazobenzene) developed by the Hecht lab[304] (half-life of 700 days) (**Figure 3.3**).
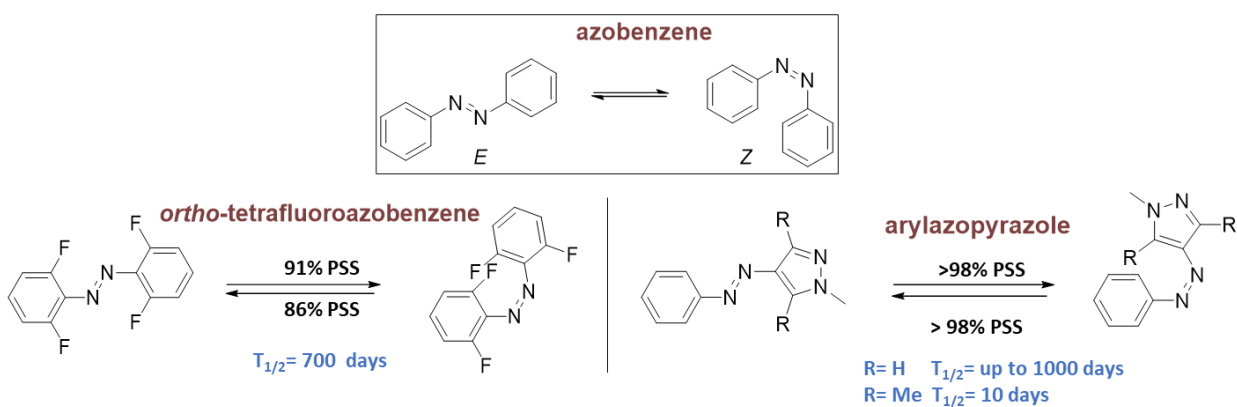
Figure 3.3 Reported photoswitches. The classical azobenzene (top) led to the *ortho*-tetrafluoroazobenzene motif from the Hetcht lab (left). The Fuchter lab substituted a phenyl ring for a pyrazole ring (right).

The photochemical properties of the arylazopyrazole system can be tuned by altering the nature of the substituents on the 5-membered ring, thus its three-dimensional conformation. It was demonstrated that the dimethyl substituted pyrazole adopts a twisted conformation while the non-substituted pyrazole exits as a T-shaped molecule which confers its unique *Z* isomer thermal stability. Furthermore, the azopyrazole photoswitch has shown good fatigue resistance when being irradiated multiple times.[303,304] With regards to physicochemical properties, the polar pyrazole ring imparts the photoswitch with a better solubility profile than the azobenzene, thus with a better prospect for use in drug design.[305] The Fuchter lab has been broadening the biological applications of the azopyrazole photoswitch by designing antibacterial amidohydrolases inhibitors,[306] modulating the activity of the transient receptor potential ankyrin 1 (TRPA1) channel.[307] Switching the azopyrazole under non irradiating conditions (via pH variation or electrochemical reaction) has also been a subject of research from the Fuchter lab.[308] Altogether, the attractive properties of the azopyrazole switch (high PSS ratios and long half-lives) led us to select it for the design of our photoswitchable degraders.

3.2 Results and discussion: chemistry and *in vitro* assessment

3.2.1 Photoswitchable linker

Our initial design for the photoswitchable linker was based on the arylazopyrazole motif described above. The objective was to obtain the functionalized linker **25** with two orthogonal protecting groups (on the ethylamino sidechain and the benzylamine) in order to introduce the E3 ligand and the warhead at a later stage (**Figure 3.4**). The possibility to extend the linker on either side via amide bond formation or reductive amination was also feasible thanks to the two amino groups present in the linker.
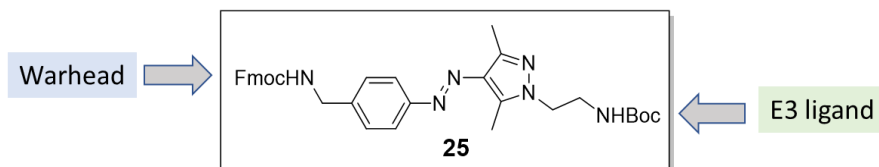
Figure 3.4 Photoswitchable linker design. Attachment of the E3 ligand and the warhead can occur after orthogonal deprotection of one of the amino groups.

3.2.1.1 First synthetic route: pyrazole formation with *N*-Boc-ethylhydrazine

The route attempted to synthesize compound **25** is described in **Scheme 3.1**. *Para*-aminobenzylamine **26** was Fmoc protected and the resulting aniline **27** was converted to a diazonium salt which was subsequently quenched with acetylacetone to give the diketone **28**. Formation of the final pyrazole ring to get to **25** required a condensation with *N*-Boc-ethylhydrazine **29**. However, the synthesis of **29** proved to be very challenging.
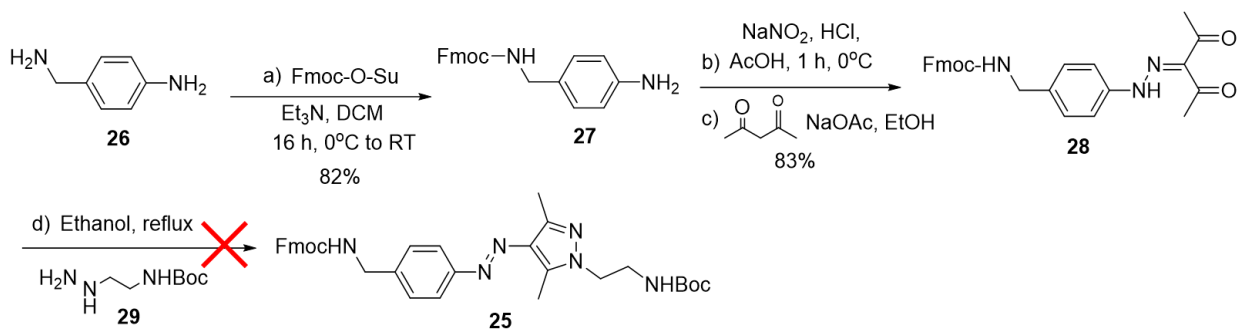
Scheme 3.1 Synthesis of photoswitchable linker **25**.

The various routes attempted to obtain the hydrazine side chain **29** are summarized in **Scheme 3.2.**
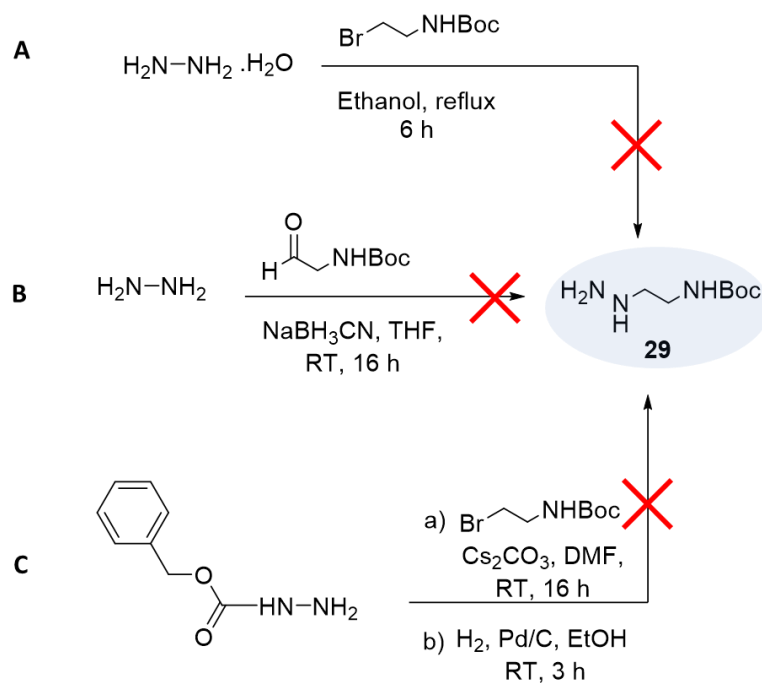
Scheme 3.2 Attempted reactions to synthesize the hydrazine substrate **29**. (A) Route with *N*-*B*oc-ethylbromide. (B) Route with *N*-*B*oc-acetaldehyde. (C) Route with benzyl carbazate.

Alkylation of hydrazine with *N*-*B*oc-ethylbromide gave a complex crude mixture in which the product **29** could not be identified by ^{1}H NMR. Reductive amination with *N*-*B*oc-acetaldehyde equally failed to deliver the desired hydrazine. Alkylation of benzyl carbazate with *N*-*B*oc-ethylbromide gave a low crude yield (10%). Subsequent attempt to cleave off the benzyl carbamate via hydrogenation ended up in the cleavage of the N-N bond. Therefore, an alternative route to **25** was explored.

3.2.1.2 Second synthetic route: pyrazole *N*-alkylation

The alternative pathway involved forming the pyrazole ring first, followed by an *N*-alkylation (**Scheme 3.3**). The pyrazole ring formation conditions are highlighted in **Table 3.1** (step a). In our first attempt, diketone **28** and hydrazine were heated at 80°C for 4 h in a mixture of acetonitrile and acetic acid. Complete disappearance of the starting material was observed by TLC along with the appearance of a new spot which was isolated by flash chromatography. ^{1}H NMR spectroscopy revealed that the isolated material did not correspond to the expected product **30** but rather to the para-amino-Fmoc-protected benzylamine **27**. In our second attempt, acetic acid was replaced with a mixture of ethanol and methanol in which the diketone **28** and hydrazine were heated at 70°C overnight. Unfortunately, the same reaction profile was obtained. In our third attempt, the reaction was monitored closely straight from the start. After 2 h, complete consumption of the starting material was visualized by TLC with formation of the desired product. Continuous heating at 50°C led to the appearance of multiple spots including the previously isolated by-product. It was concluded that a short reaction time was crucial to accomplish the pyrazole ring formation.
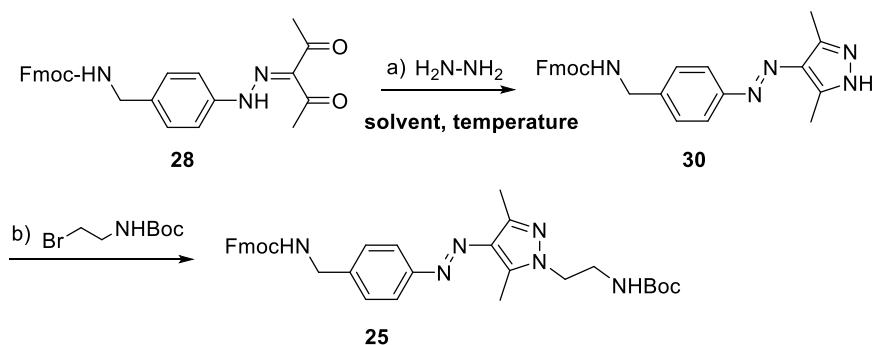
Scheme 3.3 Synthesis of hydrazine sidechain **25** via pyrazole ring formation and *N*-alkylation.

Table 3.1 Formation of pyrazole intermediate **30** (reaction a) and *N*-alkylation (reaction b) to obtain **25**

Reaction	Conditions	outcome	Product yield (%)
a #1	ACN, AcOH, 80°C, 4 h	Starting material consumed New spot (**27**)	0
a #2	EtOH/MeOH, 70°C, 16 h	Starting material consumed New spot (**27**)	0
a #3	EtOH/MeOH, 50°C	2 h: product **30** formed 5 h: several spots including **27**	50%
b #1	tBuOK, THF, RT, 16 h	Fmoc deprotection	0
b #2	Cs$_2$CO$_3$, DMF, RT, 16 h	Fmoc deprotection	0

After obtaining pyrazole **30**, the ultimate step to access the key building block **25** necessitated the alkylation with *N-B*oc-ethyl bromide. Since the dimethylpyrazole moiety in **25** is symmetrical, alkylation on either nitrogen of the ring would lead to the same final molecule.

A set of two basic conditions, namely with potassium tert-butoxide or cesium carbonate were attempted at room temperature (**Table 3.1**) (step b). Besides the slow conversion to the desired alkylated product, Fmoc deprotected material was mainly observed.

In order to circumvent the use of a strong base to deprotonate the pyrazole and keep the Fmoc group in place, a Mitsunobu reaction was also carried out under neutral conditions with n-tributylphosphine and ADDP. Although the Fmoc group remained stable in these conditions, no alkylated product was obtained (**Scheme 3.4**).
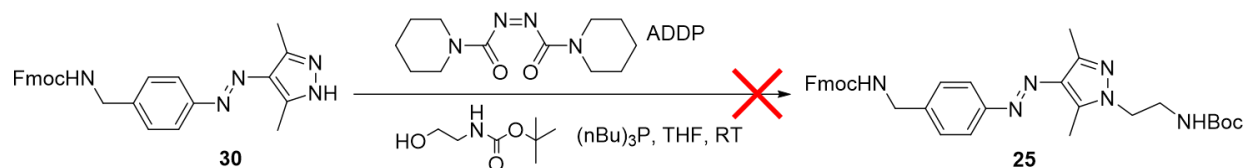
Scheme 3.4 Attempt to synthesize the hydrazine sidechain **25** via Mitsunobu conditions.

3.2.1.3 Third synthetic route: pyrazole formation with 2-hydrazinoethanol

Since the pyrazole ring formation could be achieved with hydrazine to get compound **30**, a search for commercially available pre-functionalized hydrazines was carried out to facilitate the synthesis. Due to the scarcity of such building blocks, the selection remained limited. 2-Hydrazinoethanol was among the few easily accessible hydrazines and was utilized to build a pyrazole ring bearing an ethyl alcohol sidechain **31** that could be further converted to the carboxylic acid **32** (**Scheme 3.5**).
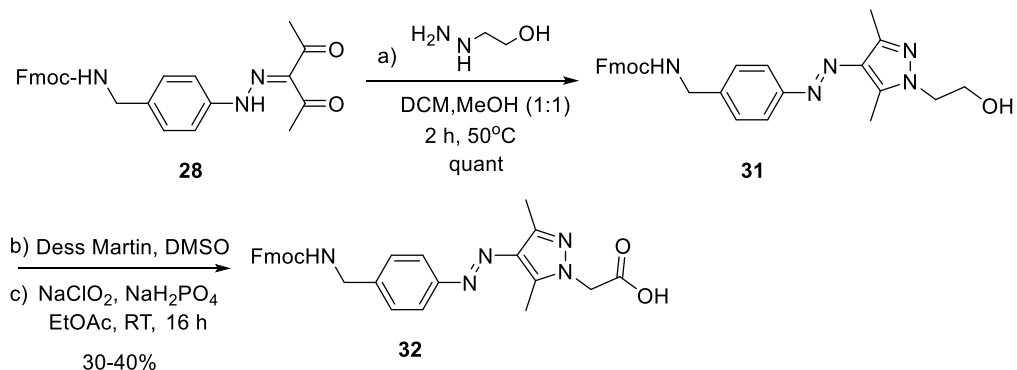
Scheme 3.5 Synthesis of photoswitchable linker **32**

Condensation of 2-hydrazinoethanol with the diketone **28** in DCM and methanol at 50˚C quantitatively produced the primary alcohol **31**. Then a two-step oxidation with Dess-Martin reagent followed by Pinnick oxidation resulted in the formation of carboxylic acid **32**. Isolation of the aldehyde intermediate was also undertaken but the low yields obtained after purification led us to execute the second oxidation immediately after work up of the Dess-Martin reaction.

3.2.1.4 Photocharacterization of the azopyrazole alcohol photoswitch

Since the alcohol **31** could be readily made without purification, we characterized its photoswitching properties by TLC, LC-MS, UV-Vis, and NMR spectroscopy. A solvent system consisting of ethyl acetate and cyclohexane (7:3) was sufficient to observe a decent separation between the *E* and *Z* isomers of **31** by TLC. Pre-irradiation at 365 nm and for 60 seconds of an aliquot of **31** indicated that the *Z* isomer moved slower on the normal phase silica, hence was more polar than its *E* counterpart (**Figure 3.5**).
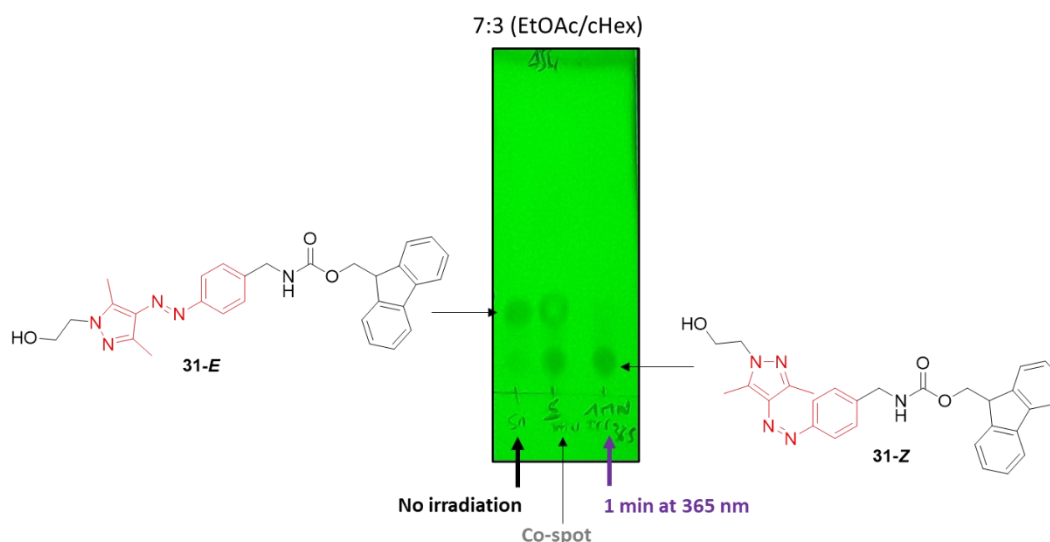
Figure 3.5 Separation of **31** isomers by TLC. An aliquot of **31** in DCM was irradiated for 1 min at 365 nm and compared with a non-irradiated sample.
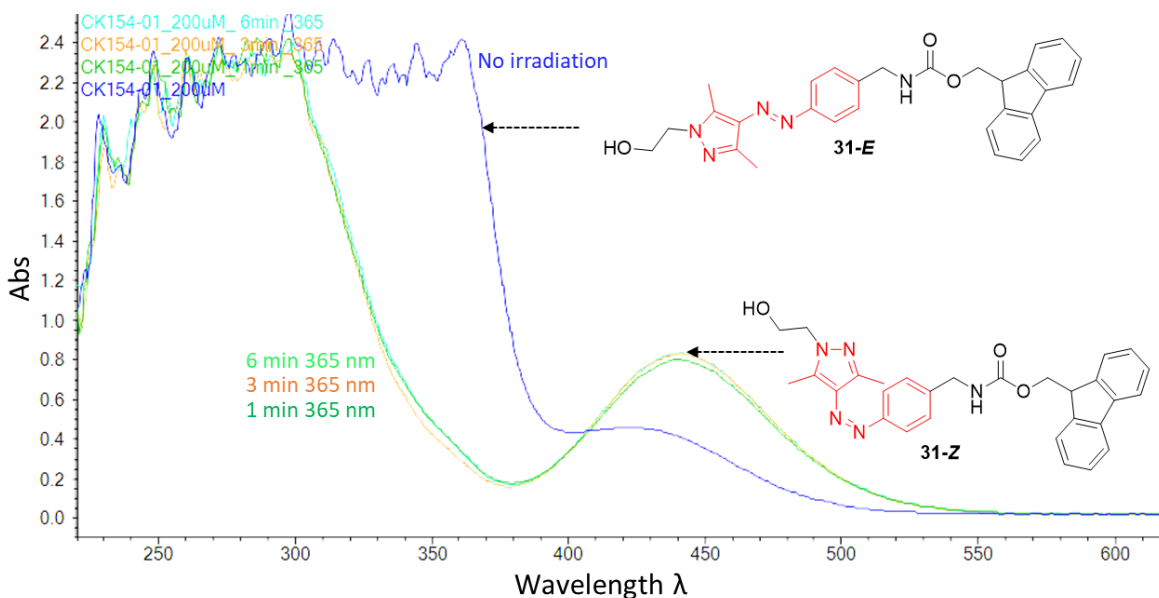
Figure 3.6 Characterization of **31** by UV-Vis. 200 µM solution of **31** in acetonitrile was irradiated for 1, 3 or 6 min. The UV-Vis spectrum was then recorded while minimizing exposure of the sample to ambient light.

Next, the alcohol **31** was characterized by UV-Vis spectroscopy. Aliquots of **31** in acetonitrile (200 µM) were irradiated for 1, 3 or 6 minutes at 365 nm (**Figure 3.6**). Recording of the UV-Vis spectrum of each irradiated aliquot showed a notable shift in absorption maximum. While the *E* isomer showed a high absorption band between 340-380 nm, the *Z* isomer had a strong absorption band between 430-470 nm. The gap in absorption observed at 450 nm between the two isomers was subsequently utilized to switch back from the *Z* to the *E* isomer preferentially by irradiating the system at 457 nm. The photoswitching properties of the alcohol **31** were also assessed by LC-MS. Aliquots of **31** (100 µM) in acetonitrile: water were irradiated for 1 or 6 minutes at 365 nm. LC-MS chromatograms displayed near quantitative obtention of the *Z* isomer (AUC of 98%) after irradiation (**Figure 3.7**).
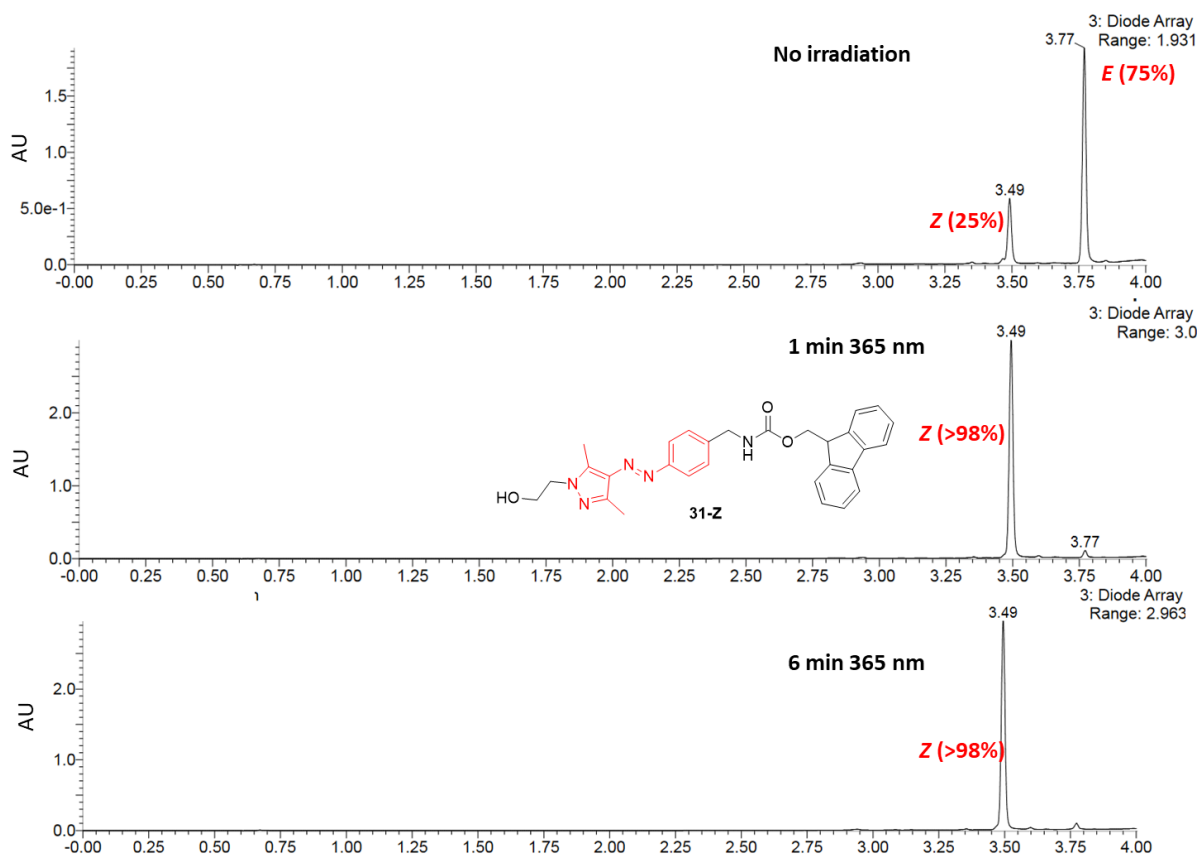
Figure 3.7 Characterization of **31** by LC-MS. 100 μM solution of **31** in acetonitrile–water (1 : 1) was irradiated for 1- or 6 min. Near-quantitative formation of the *Z* isomer was obtained. The Z isomer observed in absence of irradiation is likely the result of visible light switching.

Thermal relaxation of the Z isomer when protected from ambient light at room temperature occurs relatively slowly. Indeed, after 23 h and 43 h, the reversion of the *Z* isomer led to 45% and 56% of the *E* isomer, respectively (**Appendix 3.1**). The half-life of the synthesized degraders was eventually determined using aliquots protected from ambient light in the succeeding experiments.

Finally, the alcohol **31** was also analyzed by ^{1}H NMR spectroscopy and in our first attempt to record a sample immediately after irradiation at 365 nm, amber tubes (which shield and limit the sample exposure to ambient light to avoid back switching) were not used. Sample recording was done as quickly as possible after the initial irradiation in deuterated solvent to limit back switching. The *Z* to *E* ratio of 55:45 was calculated based the differential peaks observed before and after irradiation (**Figure 3.8**).
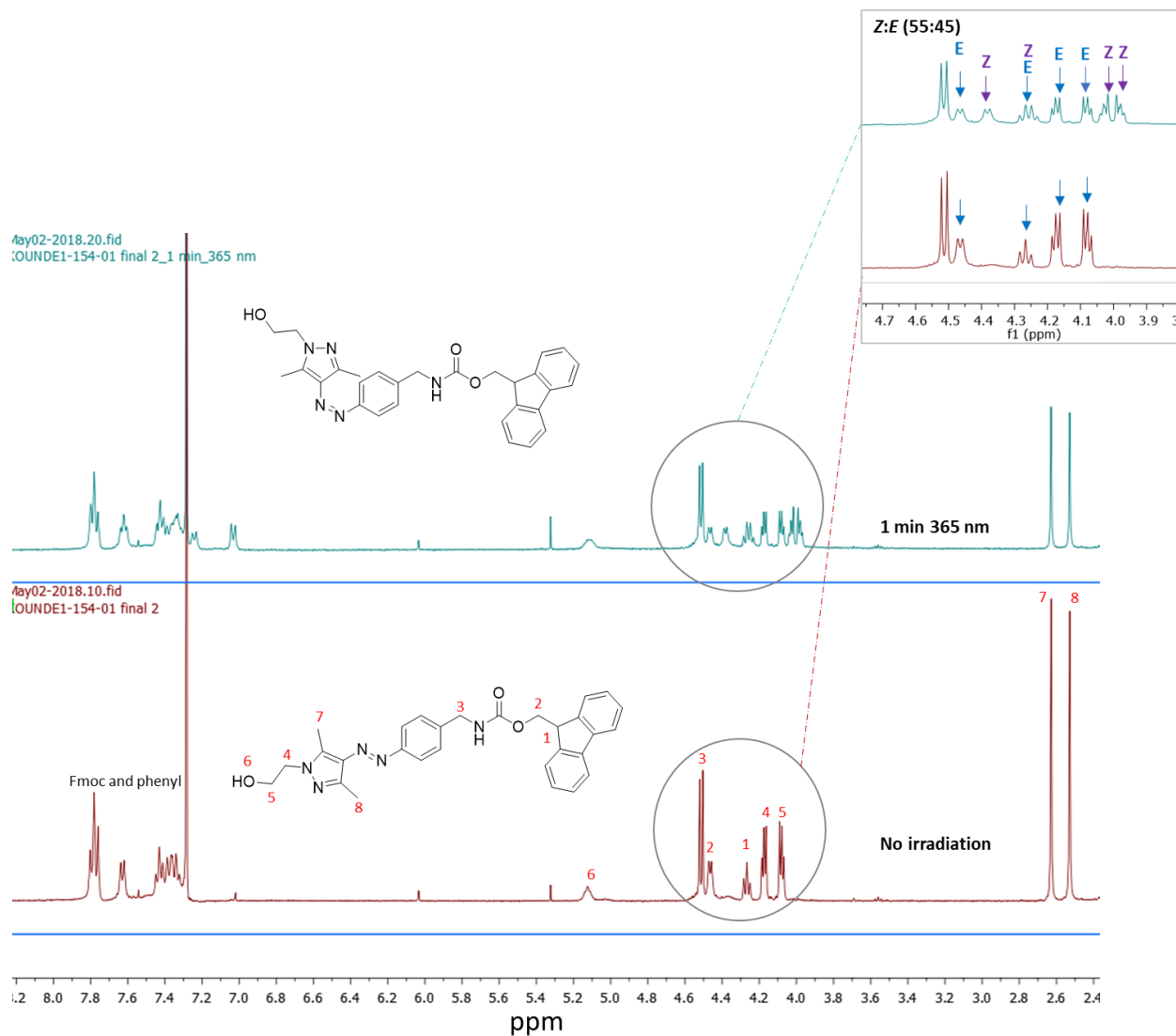
Figure 3.8 Characterization of **31** by ^{1}H NMR. 3 mg of alcohol **31** was dissolved in deuterated chloroform. The solution was irradiated at 365 nm for 1 min then covered with aluminium foil before recording the ^{1}H NMR spectrum.

Here, the suboptimal protection from ambient light and a short irradiation time relative to the concentration of the sample (i.e., the PSS was not reached) may account for the lower ratio observed as compared with the data gathered via LC-MS. Nonetheless, the initial photocharacterization of intermediate **31,** including high PSS based on the LC-MS data, confirmed excellent switching properties for application in protein degraders.

3.2.2 BRD4 photoswitchable degraders

3.2.2.1 VHL-based switchable degraders

The two-step oxidation of alcohol **31** yielded the carboxylic acid **32**. Thanks to our easy access to the warhead **JQ1** and the VHL ligand provided by GlaxoSmithKline Ltd., we managed to synthesize our first BRD4 photoswitchable PROTAC according to **Scheme 3.6**.
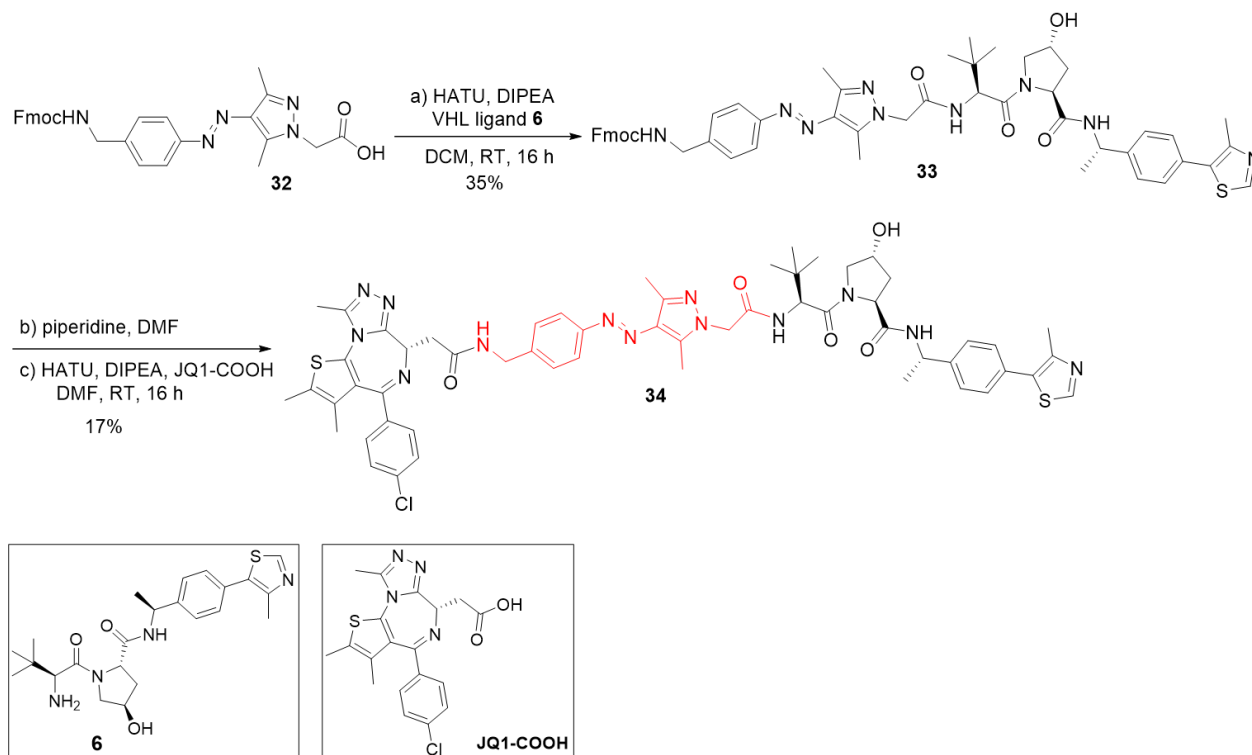
Scheme 3.6 Synthesis of BRD4 photoswitchable PROTAC **34**

The VHL ligand **6** was coupled to the carboxylic acid linker **32**. After isolation of the resulting amide **33**, Fmoc group deprotection followed by a second amide coupling afforded the desired final degrader **34**. The recorded UV spectrum of **34** after irradiation at 365 nm was comparable to the alcohol **31** (noticeable absorption between 340-380 nm) and at 457 nm (where the transition from *Z* to *E* should occur), a negligible difference in absorption was observed (**Figure 3.9 A**). In the case of compound **34**, the PSS ratios obtained by LC-MS after a 3-min irradiation at 365 nm and 457 nm were 90% *Z* and up to 80% *E*, respectively (**Figure 3.9 B**).
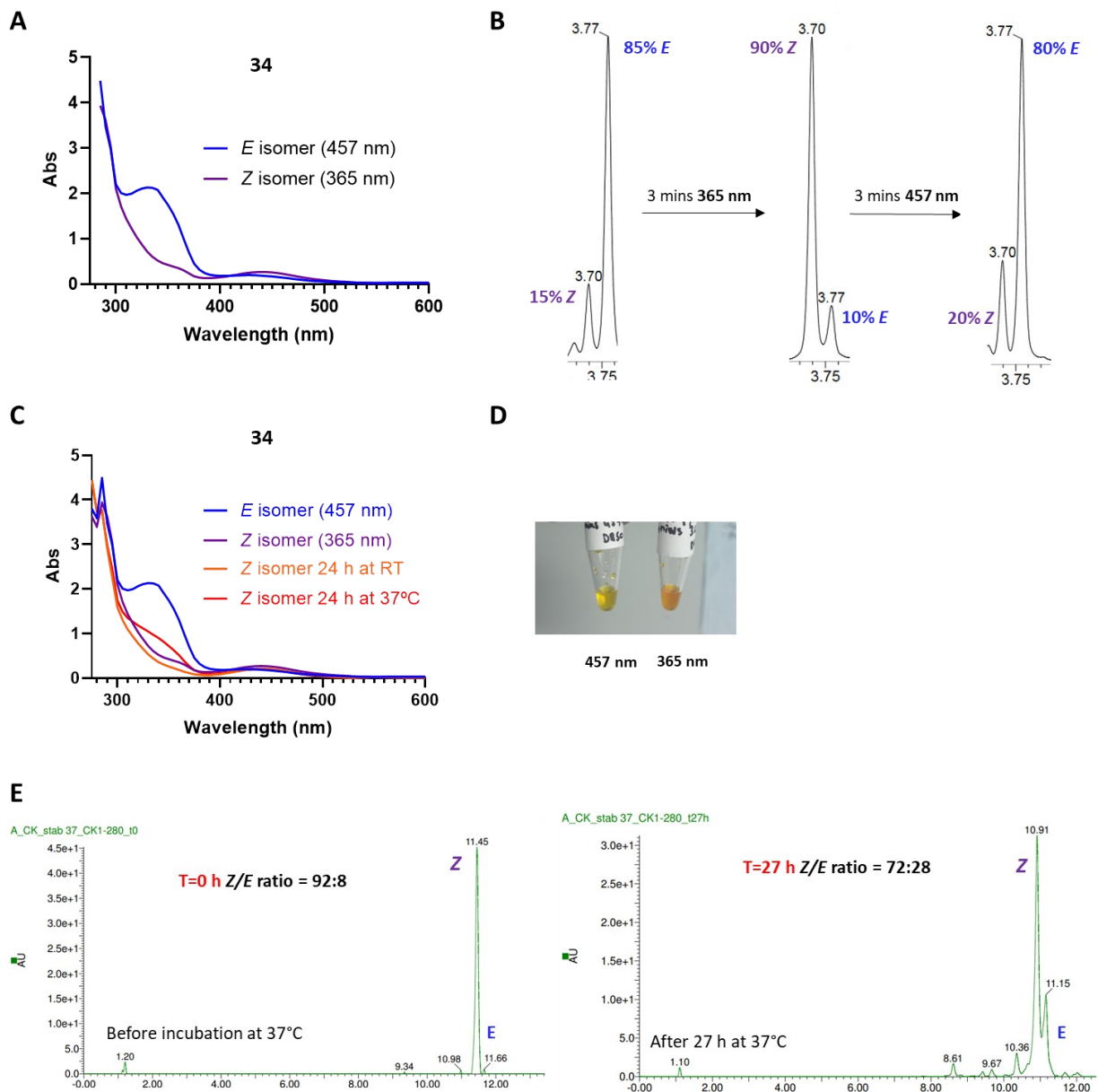
Figure 3.9 Photocharacterization of **34**. (A) UV-Vis spectrum (100 μM in ACN) after irradiation for 3 min at 365 nm or 457 nm. (B) LC-MS chromatogram (100 μM solution) in ACN/water (1 : 1) after irradiation for 3 min at 365 nm or 457 nm. (C) UV-Vis spectrum after keeping the sample for 24 h at room temperature or at 37˚C in the dark following irradiation at 365 nm for 3 mins. (D) Physical aspect of DMSO stock solutions irradiated at 365 nm or 457 nm. (E) LC-MS chromatogram before and after keeping the sample irradiated at 365 nm for 24 h at 37˚C.

Since the photoswitchable degrader would be used in cell culture incubated at 37˚C, we also assessed the stability of the *Z* isomer in aqueous solution at that particular temperature, after irradiation at 365 nm and keeping the sample protected from ambient light. The UV-Vis spectrum showed a good stability of the *Z* isomer at room temperature after 24 h but with a slight hyperchromic shift at 37˚C. This shift indicated partial reversion to the *E* isomer (**Figure 3.9 C**) and was confirmed by LC-MS data where, after 27 h at 37˚C, a 20% reversion was computed from

the chromatogram AUCs (**Figure 3.9 E**). Finally, irradiation of compound **34** DMSO stock solutions at 365 nm and 457 nm resulted in bright orange and yellow colorations, respectively (**Figure 3.9 D**). Overall, **34** showed favorable photoswitching properties alongside good stability of the *Z* isomer.

3.2.2.2 IMiD-based switchable degraders

The synthesis of IMID-based photoswitchable degraders followed a similar route as described above using the carboxylic acid **32**. Three final compounds were made with various linker lengths. For the first compound, the azopyrazole photoswitch was extended by an aminopropyl linker (**Scheme 3.7**).

Scheme 3.7 Synthesis of BRD4 photoswitchable PROTAC **37**. An aminopropyl linker (blue) extends the photoswitch.
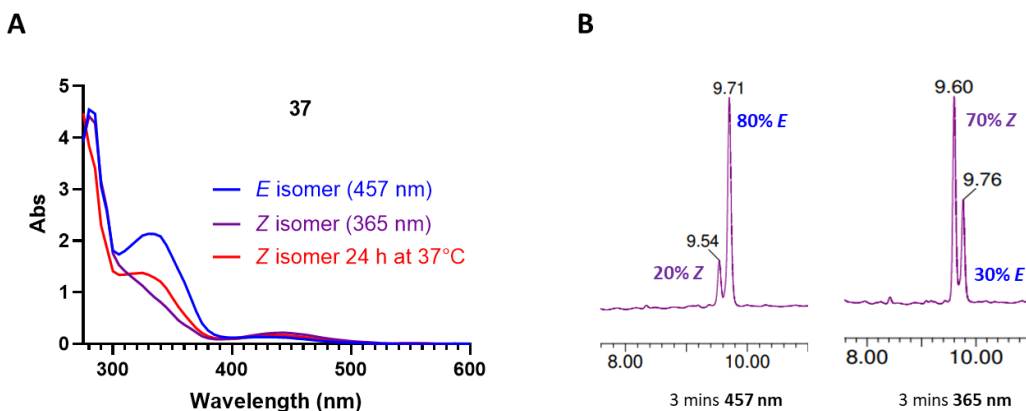
Figure 3.10 Photocharacterization of **37**. (A) UV-Vis spectrum (100 µM in ACN) after irradiation for 3 min at 365 nm or 457 nm plus UV trace after keeping the sample for 24 h at 37°C in the dark following irradiation at 365 nm. (B) LC-MS chromatogram (100 µM solution) in ACN/water (1 : 1) after irradiation for 3 min at 365 nm or 457 nm.

Starting from the hydroxythalidomide *tert*-butyl ester **2**, treatment with TFA followed by a coupling with tert-butyl-(3-aminopropyl)carbamate led to derivative **35**. By using the same sequence (i.e., Boc deprotection and amide coupling), the adduct **36** was obtained. Fmoc group removal and coupling with **JQ1** carboxylic acid afforded the photoswitchable compound **37**. Photocharacterization of **37** by LC-MS led to a PSS ratio of 80% *E* isomer and 70% *Z* after a 3-min irradiation at 457 nm and 365 nm, respectively (**Figure 3.10 B**). Assessment of the stability of the *Z* isomer by UV-Vis at 37°C and for 24 h showed a hyperchromic shift which indicated a partial reversion to the *E* isomer. The extent of the reversion has not been quantified in this case although the UV-Vis spectrum still suggests a prevalence of the *Z* isomer (**Figure 3.10 A**).

The second compound which was synthesized had an additional short ethylamine linker between the azopyrazole photoswitch and the hydroxythalidomide (**Scheme 3.8**)
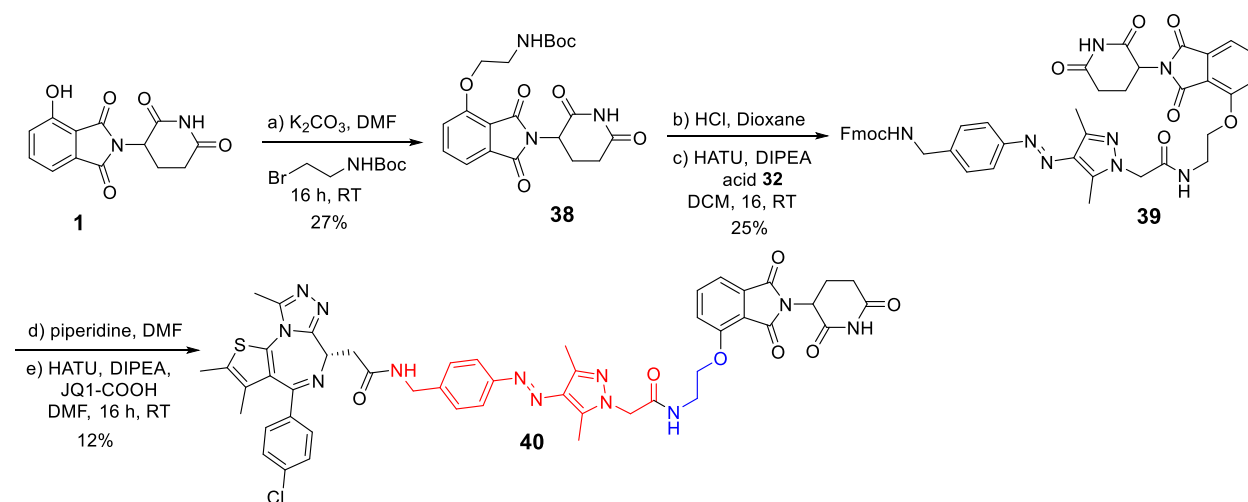
Scheme 3.8 Synthesis of BRD4 photoswitchable PROTAC **40**. An ethylamine linker (blue) extends the photoswitch.

Alkylation of hydroxythalidomide **1** with tert-butyl-(2-bromoethyl)carbamate was unselective and a mixture of mono- and bis-alkylated material was obtained. Column chromatography allowed the isolation of the single alkylated intermediate **38** with sufficient purity to proceed with the subsequent Boc deprotection and coupling with acid **32**. Final Fmoc deprotection of intermediate **39** and attachment to **JQ1** afforded the degrader **40**.

The photoswitching characteristics of **40** assessed at 365 nm and 457 nm resulted in well-defined absorption bands in the initial UV-Vis spectrum (**Appendix 3.2**). Further assessment of the stability of the *Z* isomer for 24 h at room temperature and at 37°C highlighted a noticeable reversion of the *Z* isomer under both conditions, despite the poor baseline recorded in this experiment (**Figure 3.11 A**). This data was also supported by a weak PSS ratio (57% *Z* isomer only) seen by LC-MS after irradiation at 365 nm for 3 minutes (**Figure 3.11 B**).

In order to reconfirm those preliminary data, compound **40** was further analyzed by the Fuchter lab to accurately measure the PSS ratio by UV-Vis using Fischer's method (**Appendix 3.3**). Eventually, values of 85% and 78% were calculated for the PSS ratios at 365 nm and 457 nm, respectively (**Figure 3.11 C**). The lower PSS value observed by LC-MS was arduous to explain since earlier compounds (**34** and **37**) recorded PSS ratio of at least 70% using the same analytical method. The inferior half-life that was initially observed for the *Z* isomer was not further investigated by the Fuchter lab.

Finally, multiple cycles of irradiation at 365 nm and 457 nm did not affect the switching ability of compound **40** which maintained good absorption after 20 cycles between the two wavelengths.
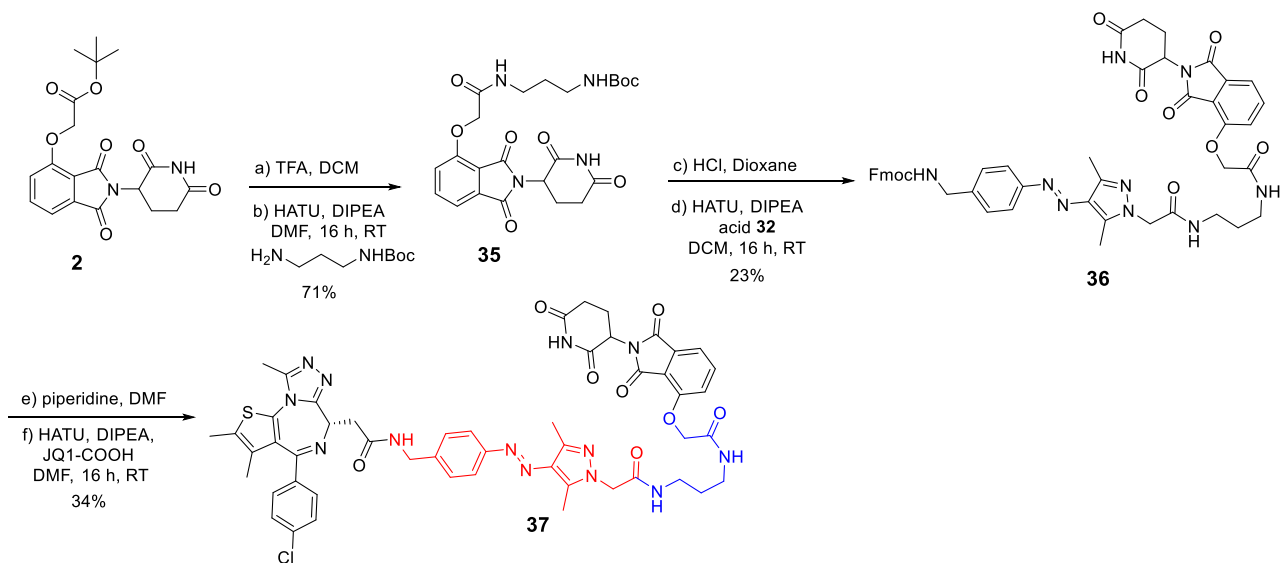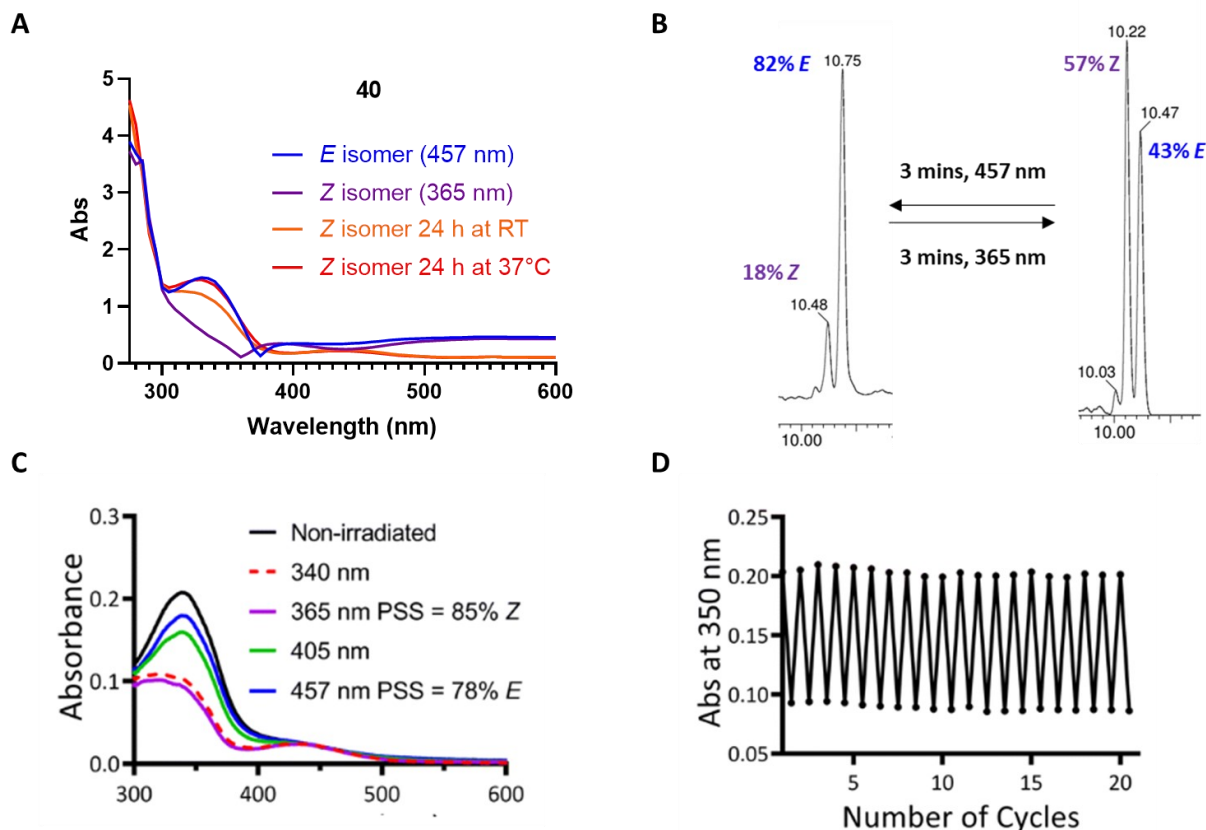

Figure 3.11 Photocharacterization of **40**. (A) UV-Vis spectrum (100 μM in ACN) after irradiation for 3 min at 365 nm or 457 nm plus UV trace after keeping the sample for 24 h at room temperature or 37˚C in the dark following irradiation at 365 nm. (B) LC-MS chromatogram (100 μM solution) in ACN/water (1 : 1) after irradiation for 3 min at 365 nm or 457 nm. (C) UV-Vis spectrum generated by the Fuchter lab to accurately measure the PSS ratio via Fischer's method. (D) Reversible switching of a 25 mM solution in water with 0.25% DMSO following 365 nm or 457 nm irradiation for 20 cycles.

For the last BRD4 photoswitchable degrader exemplified, we first sought to connect pomalidomide via its aniline moiety directly to acid **32** (**Scheme 3.9 A**). Standard amide coupling (with HATU) failed and activation of the carboxylic acid **32** (via acyl chloride formation) proved to be equally unsuccessful. The poor nucleophilicity of the aniline probably renders the amide bond formation more difficult. Using lenalidomide which bears one carbonyl less than pomalidomide, the amide intermediate **41** was obtained in a 25% yield after column chromatography (**Scheme 3.9 B**). Subsequent Fmoc deprotection and coupling with **JQ1** led to the final bifunctional molecule **42**. Photocharacterization of **42** by UV-Vis and LC-MS let to favorable PSS ratios of 76% *E* and 92% *Z* along with a good stability of the *Z* isomer at room temperature for 24 h. As previously noted with the compounds described above, partial loss of the *Z* isomer was also recorded when the compound was kept at 37˚C for 24 h (**Figure 3.12 A and B**).
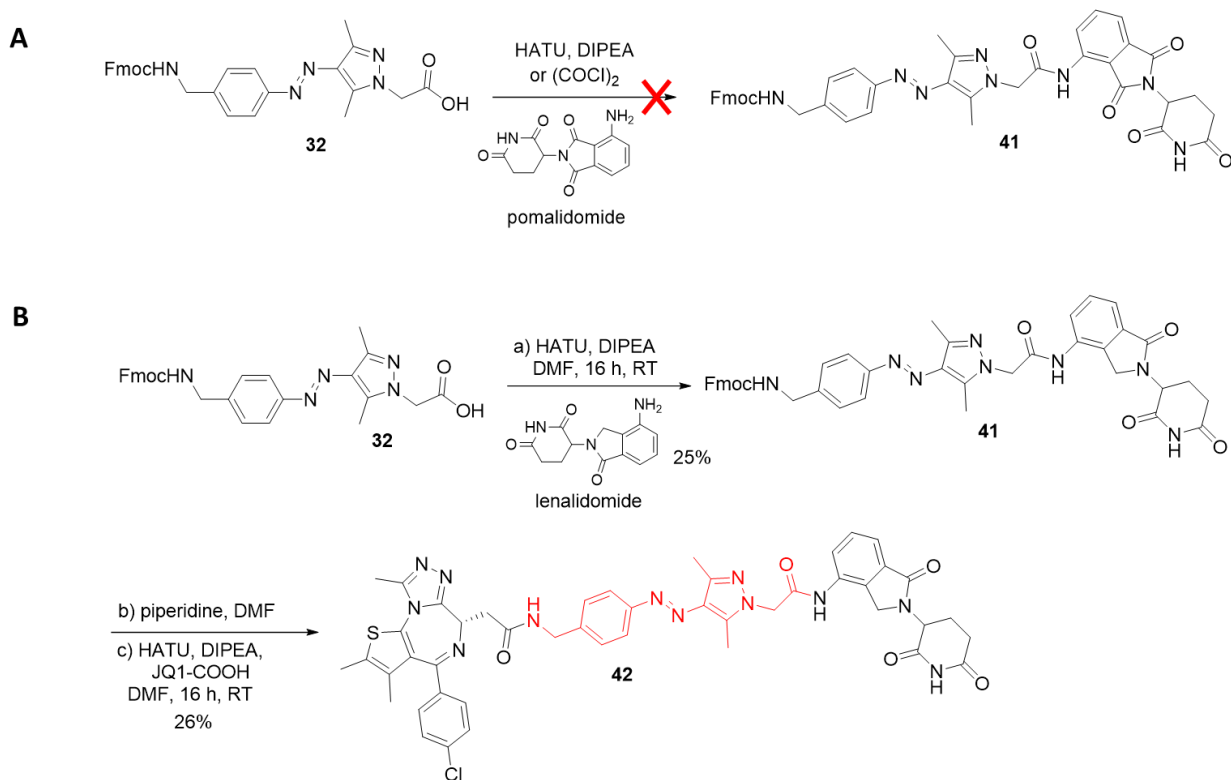
Scheme 3.9 Synthesis of BRD4 photoswitchable PROTAC **42** with direct attachment of lenalidomide to the photo-switch
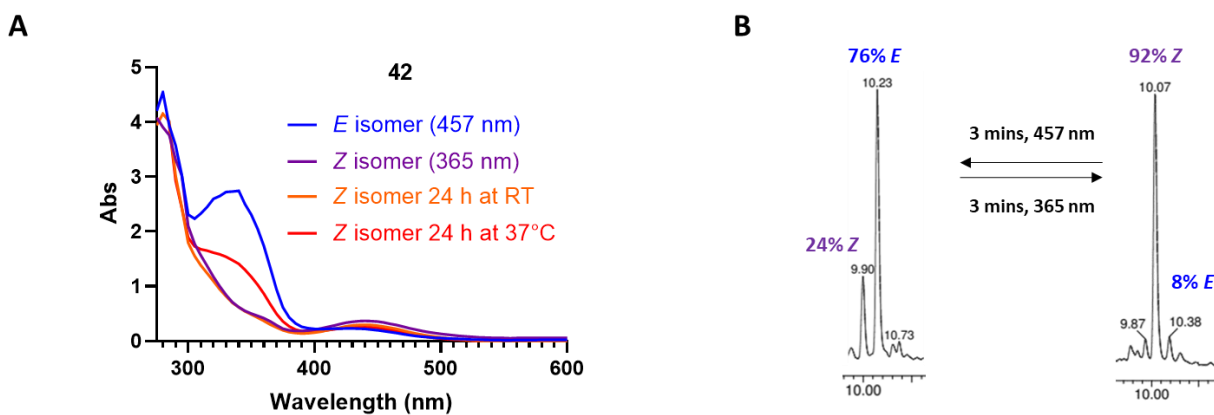
Figure 3.12 Photocharacterization of **42**. (A) UV-Vis spectrum (100 μM in ACN) after irradiation for 3 min at 365 nm or 457 nm plus UV trace after keeping the sample for 24 h at room temperature or 37°C in the dark following irradiation at 365 nm. (B) LC-MS chromatogram (100 μM solution) in ACN/water (1 : 1) after irradiation for 3 min at 365 nm or 457 nm.

Overall, the bifunctional compounds synthesized incorporating the azopyrazole photoswitch in between **JQ1** and the selected E3 ligase ligand retained good photoswitching properties when using 365 nm and 457 nm wavelengths. Each isomer could be obtained in good proportion relative to its counterpart as indicated by the PSS ratios. Timecourse experiments to evaluate the stability of the *Z* isomer under physiological conditions (37°C in an incubator) were also conducted for compounds **34**, **40** and **42** (**Appendix 3.4**). Although thermal reversion occurred, the data gathered showed that the *Z* isomer of **34** had a half-life of more than 24 h, and of at least 5 h for **40** and **42** after irradiation at 365 nm. Despite the impact of the temperature on the stability of the *Z* isomer, the half-lives were still within an acceptable range for our biological evaluation. A summary of the characteristics of each compound is given in **Table 3.2**.

Table 3.2 Characteristics of the photoswitchable compounds synthesized

compound	E3 ligand	PSS 365 nm (*E* to *Z*)	PSS 457 nm (*Z* to *E*)	Half-life 25°C / 37°C
34	VHL	90%	80%	>48 h[b] / >27 h[b]
37	thalidomide	70%	80%	-- / >24 h[a]
40	thalidomide	85%*	78%*	-- / at least 5 h[b]
42	lenalidomide	92%	76%	>24 h[a] / at least 5 h[b]

[a]value based on UV-Vis
[b]values based on LC-MS
*determined by UV-Vis (Fuchter group)

3.2.2.3 Single irradiation

In the first instance and for practical purposes, *in vitro* testing of the photoswitchable compounds was conducted by irradiating the compounds before addition to the cells. HeLa cells were incubated with DMSO 0.1% (v/v), positive control **16** or various concentrations of the test compounds (from 10 nM to 10 µM). Typically, stock solutions of photoswitchable compounds were irradiated at 365 nm or 457 nm for 3 min and dilutions were made (while keeping the samples protecting from light) before treating the cells. After incubation for 24 h, cells were lysed and BRD4 levels were quantified by western blot analysis (**Figure 3.13**).
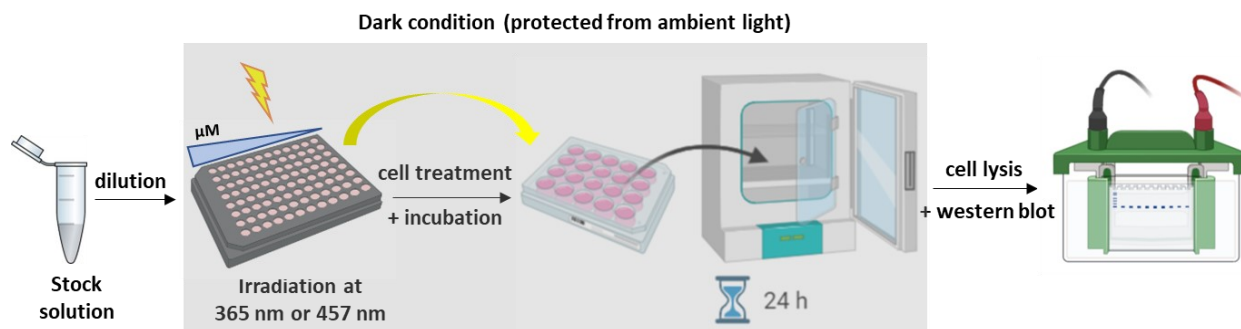
Figure 3.13 *In vitro* testing protocol for the photoswitchable PROTACs. Stock solutions of photoswitchable compounds were used to prepare dilutions in 96-well plates. In the dark (red light used), the plates were irradiated at 365 nm or 457 nm for 3 mins before adding the solutions to the incubation plate containing HeLa cells. After 24 h treatment, cells were lysis and BRD4 content was determined via western blot analysis.
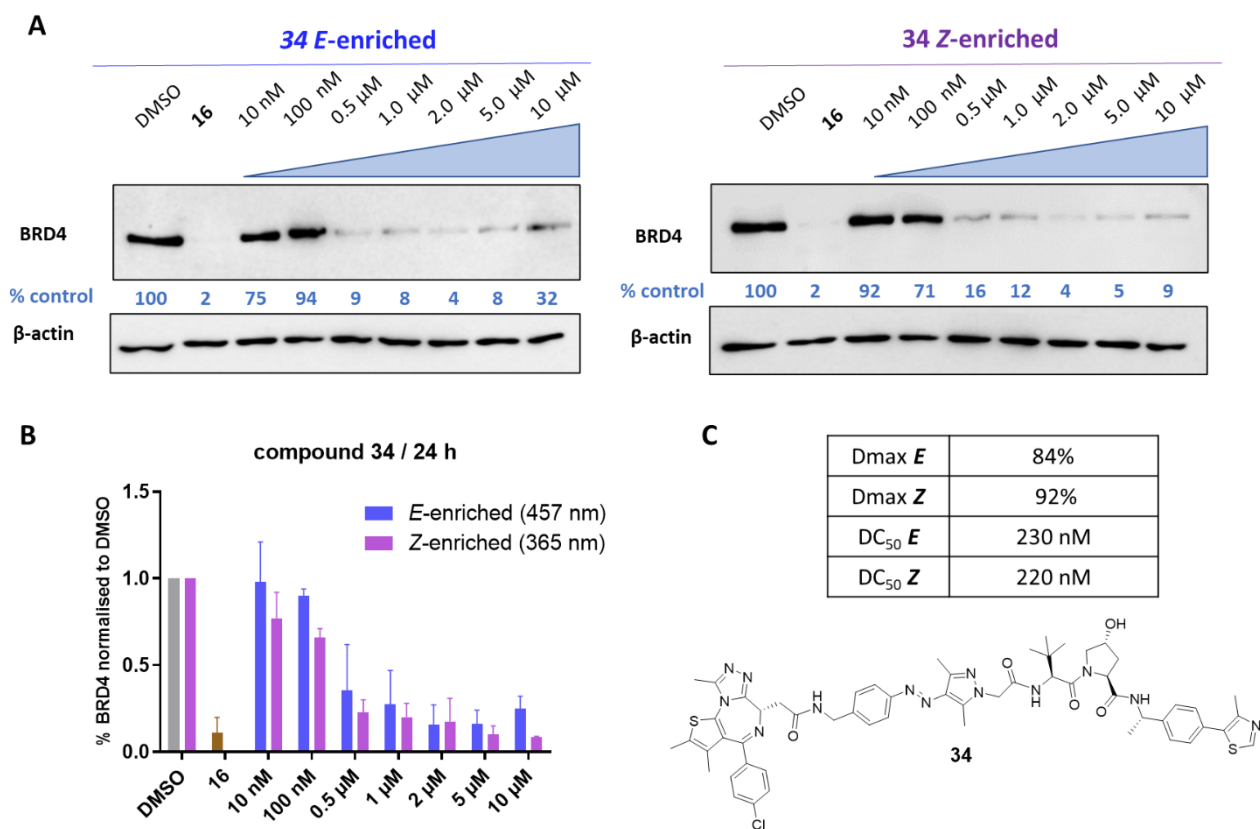
Figure 3.14 *In vitro* testing of photoswitchable PROTAC **34**. (A) Immunoblots and (B) quantification of BRD4 in HeLa cells after 24 h treatment with DMSO control, **16** or **34** irradiated with 457 nm (*E*-enriched) or 365 nm (*Z*-enriched) wavelength. (C) Extracted Dmax and DC_{50} values from duplicates experiments obtained by plotting BRD4 band intensities.

For the VHL degrader **34**, the *E* and *Z*-enriched samples led to similar degradation profiles with Dmax values of 84% and 92%, respectively (**Figure 3.14**). DC_{50} values from duplicate experiments were also calculated by plotting BRD4 band intensities and fitting them into sigmoidal dose response curves (**Appendix 3.5**).

Under the experimental conditions tested, a dose-dependent degradation of BRD4, with no difference between the *E* and *Z* isomer after a 24 h treatment period was observed. A beginning of a hook effect was noted at the highest concentration used (10 µM). With this novel rigid azopyrazole linker, a decent potency level was retained for **34** when compared with the VHL-based degrader **MZ1** and its PEG linker (DC_{50} ~100 nM). This suggests that the azopyrazole linker did not impede ternary complex formation and subsequent ubiquitination of BRD4.

For the first IMiD-based photoswitchable compound **37**, both *E* and *Z*-enriched samples showed favorable dose dependent degradation profile starting from 0.5 µM with Dmax value of 92% and 83%, respectively (**Figure 3.15**). A DC_{50} value of 235 nM was obtained for the *E* isomer while a poor fit into a sigmoidal curve for the *Z* isomer led us to approximate the DC_{50} between 100 and 500 nM. Nonetheless, the *E* isomer displayed a stronger degradation profile. For this novel compound, degradation was validated with thalidomide as an E3 ligase ligand.

Figure 3.15 *In vitro* testing of photoswitchable PROTAC **37**. (A) Immunoblots and (B) quantification of BRD4 in HeLa cells after 24 h treatment with DMSO control or **37** irradiated with 457 nm (E-enriched) or 365 nm (Z-enriched) wavelength. (C) Extracted Dmax and DC50 values from duplicates experiments obtained by plotting BRD4 band intensities.

With the photoswitchable compound **40** bearing a shorter linker to thalidomide than compound **37**, a mixed picture was drawn from the triplicate experiments. While the *Z* isomer attained a better Dmax value of 92% versus 86% for the *E* isomer, a 5-fold difference in DC_{50} values was calculated in favor of the *E* isomer when fitting BRD4 band intensities into a sigmoidal dose response curve. The *E*-enriched sample achieved a DC_{50} of 123 nM against 627 nM for the *Z* isomer (**Figure 3.16**). In order to confirm the superiority of the *E* isomer, a timecourse experiment over a 24 h period was conducted using 0.5 μM and 2 μM **40.** The *E* isomer was confirmed to be a faster degrader in the early hours post-incubation (after 2 h) although a similar degradation endpoint was reached for both isomers (**Appendix 3.6**).
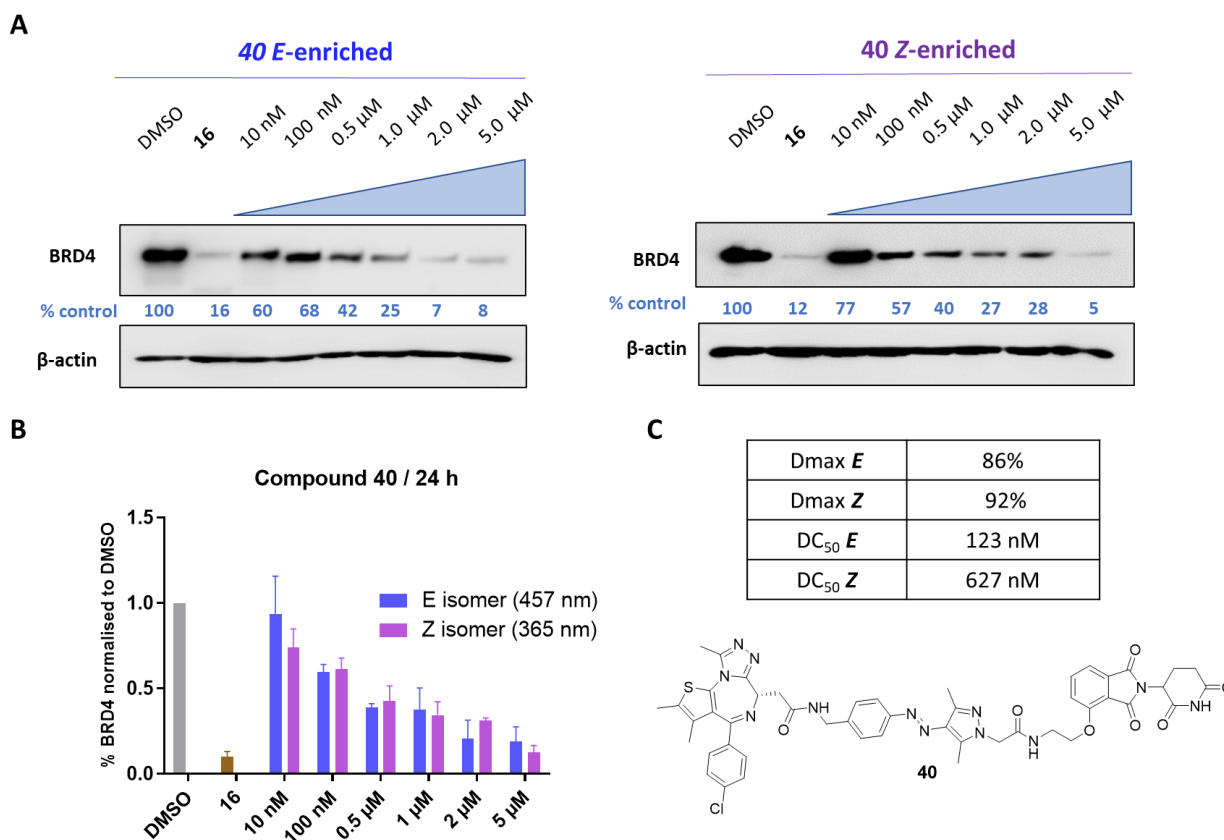
Figure 3.16 *In vitro* testing of photoswitchable PROTAC **40**. (A) Immunoblots and (B) quantification of BRD4 in HeLa cells after 24 h treatment with DMSO control, **16** or **40** irradiated with 457 nm (E-enriched) or 365 nm (Z-enriched) wavelength. (C) Extracted Dmax and DC50 values from triplicates experiments obtained by plotting BRD4 band intensities.

Lastly, the two isomers of the photoswitchable compound **42** made with lenalidomide as an E3 ligase ligand were also able to degrader BRD4. However, a significant hook effect was observed from 2 μM and concentrations above. This hook effect was more pronounced for the *E*-enriched sample which also had a lower average Dmax (53% versus 69% for the Z-enriched sample). In the case of **42**, the more disparate BRD4 band intensities did not allow for an accurate estimation of the DC_{50} values.
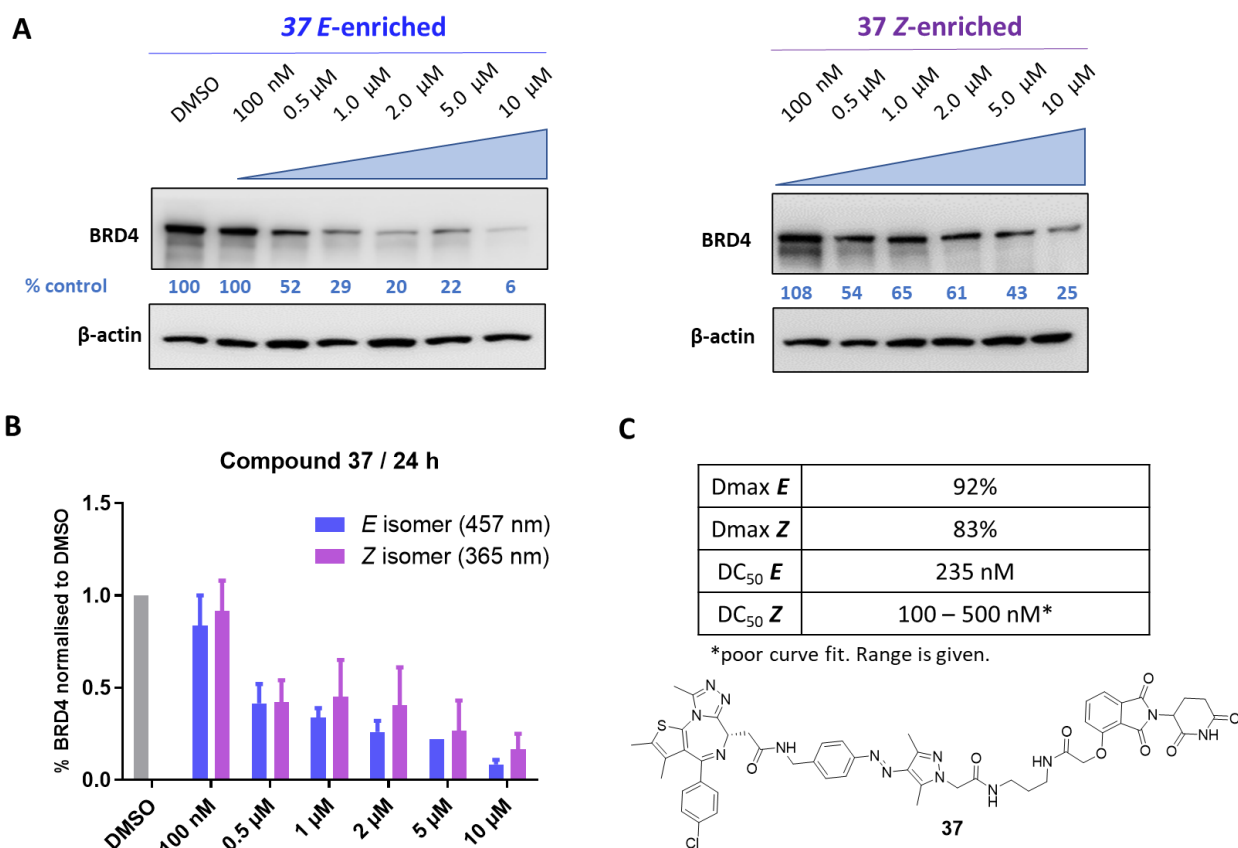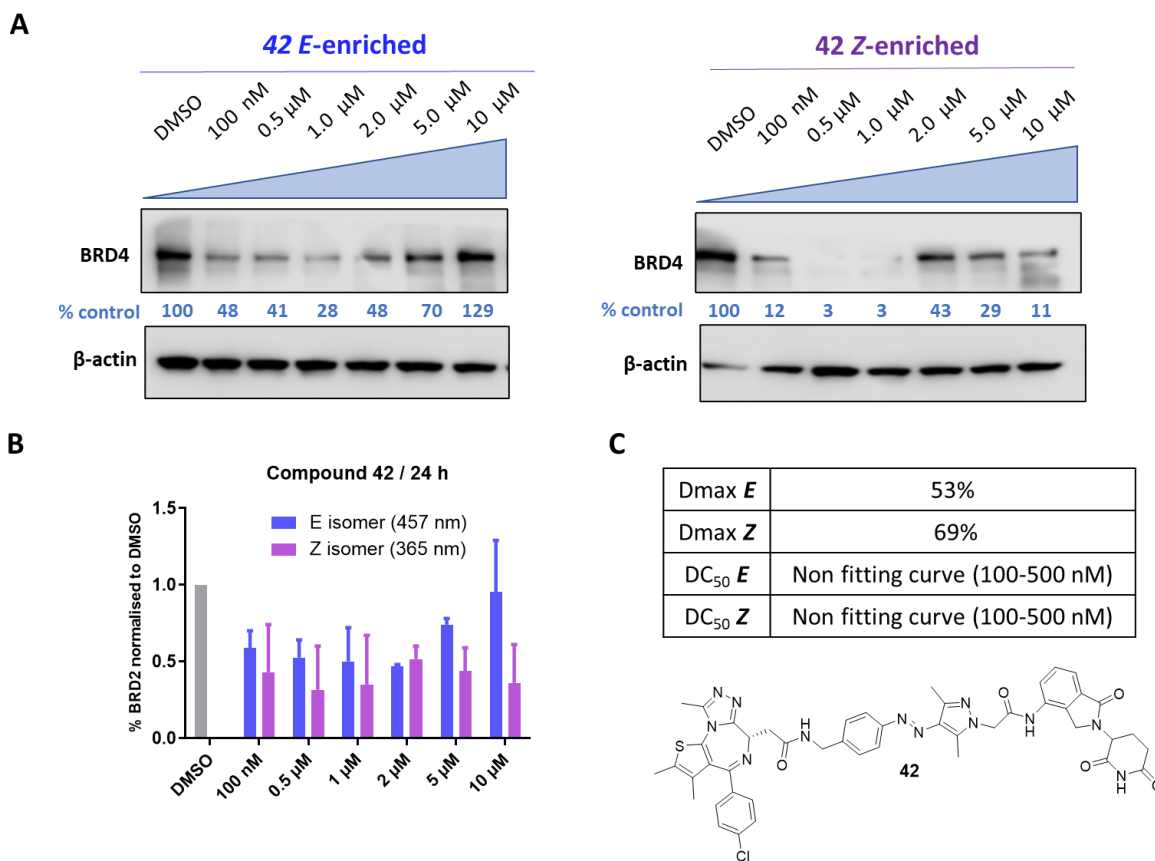
Figure 3.17 *In vitro* testing of photoswitchable PROTAC **42.** (A) Immunoblots and (B) quantification of BRD4 in HeLa cells after 24 h treatment with DMSO control and **42** irradiated with 457 nm (E-enriched) or 365 nm (Z-enriched) wavelength. (C) Extracted Dmax and DC50 values from triplicates experiments obtained by plotting BRD4 band intensities.

Pleasingly, the four compounds we have designed and synthesized (8 isomers in total) all achieved degradation of BRD4, and with a level of potency close to what is reported for known BRD4 degraders. This emphasizes the fact that the rigid arylazopyrazole linker was well tolerated and allowed ternary complex formation. Nonetheless, a clear superiority of one isomer versus the other was not evident under the conditions tested. Another positive point was that each of the three E3 ligands (VHL, thalidomide and lenalidomide) attached to the photoswitch, proved to be effective in recruiting their respective E3 ligase to trigger ubiquitination and degradation. In that respect, this system (i.e., combination of an E3 recruiter with the azopyrazole photoswitch) appeared to be versatile. Interestingly, a strong hook effect was detected mainly with **42**. This may reflect more favorable binary than ternary interactions for this compound for which binding studies would be helpful to confirm such observations.

3.2.2.4 Intermittent irradiation and BRD2 selectivity

In our previous experiments which investigated the degradation ability of the two isomers, HeLa cells were treated with pre-irradiated samples and were left to incubate for 24 h at 37˚C. Since reversion of the *Z* isomer to the *E* can occur under incubating temperatures (cf. photocharacterization data at 37˚C, vide supra), we thought to perform our experiments with intermittent irradiation of the cells (as opposed to one-time pre-irradiation only). The purpose of this new protocol was to maintain the highest PSS ratio before the end point of the experiment. When HeLa cells were treated with 100 nM of compound **40** for 8 h with intermittent irradiation (10-second irradiation every 2 h), a distinct degradation profile was reached for each isomer. While the *E*-enriched sample yielded up to 86% BRD4 degradation, only 35% was achieved with the *Z*-enriched sample (**Figure 3.18 A**). The wider gap between the two isomers observed with the new experimental protocol confirmed our hypothesis about the retention of the PSS ratios throughout the duration of the experiment.

More strikingly, another BRD isoform, BRD2, was left untouched by the *Z*-enriched sample while the *E*-enriched resulted in 75% degradation of BRD2 (**Figure 3.18 B**).
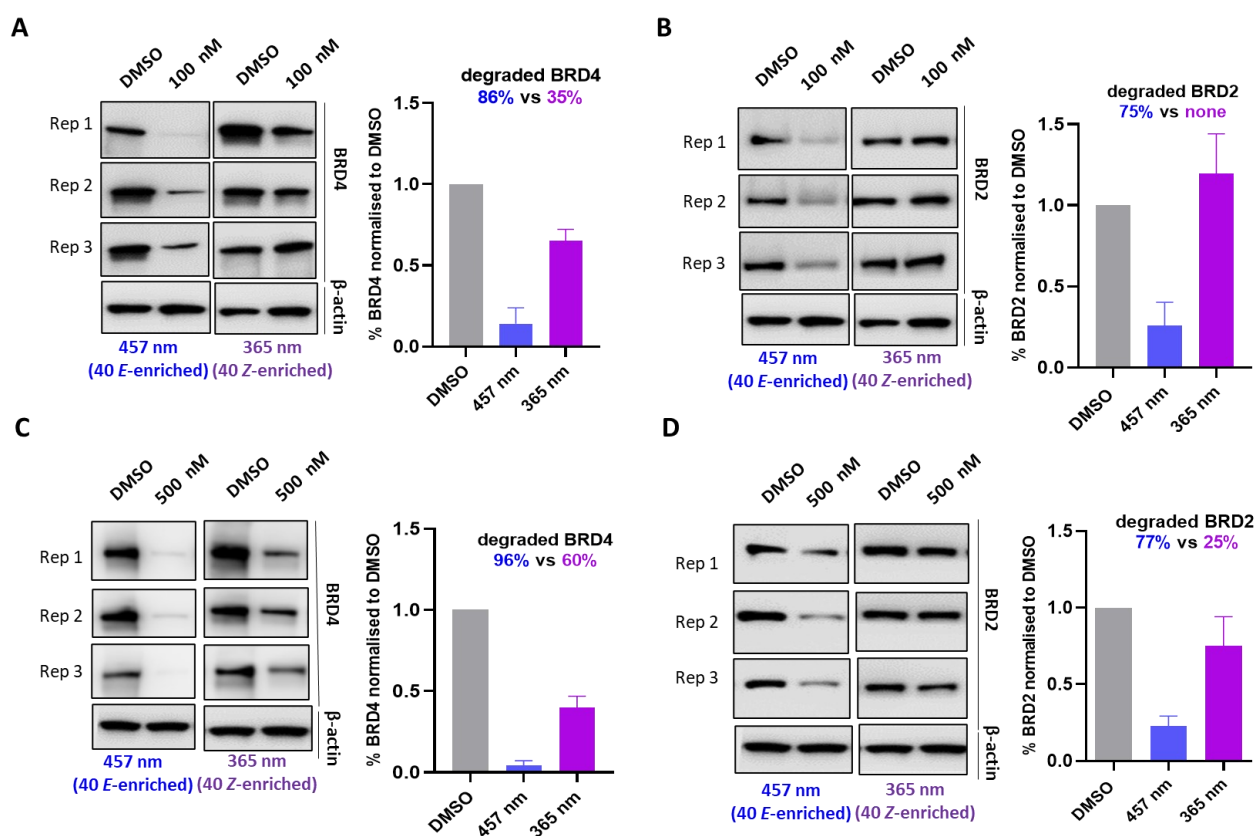
Figure 3.18 *In vitro* testing of photoswitchable PROTAC **40** with intermittent irradiation. (A) Immunoblots and quantification of BRD4 and (B) BRD2 in HeLa cells after 8 h treatment with DMSO control or 100 nM **40**. Cells were irradiated with 457 nm (*E*-enriched) or 365 nm (*Z*-enriched) wavelength for 10 seconds every 2 h. (C) and (D) same experiment as (A) and (B) with 500 nM **40**.

At the higher concentration of 500 nM, the degradation window between the two isomers was reduced, although the *E*-enriched sample significantly outperformed the *Z*-enriched with 96% degradation against 60%, respectively (**Figure 3.18 C**). For BRD2, the same level of degradation (77%) was maintained at 500 nM for the *E*-isomer while the Z-isomer achieved only 25% BRD2 depletion (**Figure 3.18 D**). The manifest difference between the two isomers is an extremely encouraging result since it comes towards our goal of realizing on/off switching of protein degradation with a single molecule. In addition, the data generated for BRD2 adds another benefit to the photoswitchable degrader approach by demonstrating partial isoform selectivity with superior degradation of BRD4 versus BRD2. The PROTAC **MZ1** has also shown in previous reports a preferential degradation for BRD4 over BRD2 and BRD3.[28] We can postulate that further alterations of the arylazopyrazole photoswitch (e.g., with various substituents or by altering the linker length) could be a path forward to fine-tune the selectivity profile towards one of the BRD proteins. Intermittent irradiation was also applied to compounds **37** and **42** incubated in HeLa cells at a concentration of 500 nM. In both cases, the *E* isomer achieved more than 90% degradation of BRD4 while the *Z* isomer could reach up to 65% (**37**) and 72% (**42**) degradation although it remained less potent (**Figure 3.19 A and B**). Unfortunately, BRD2 was not assessed for those two compounds to make a comparison with BRD4, neither was a lower concentration (e.g., 100 nM) tested.
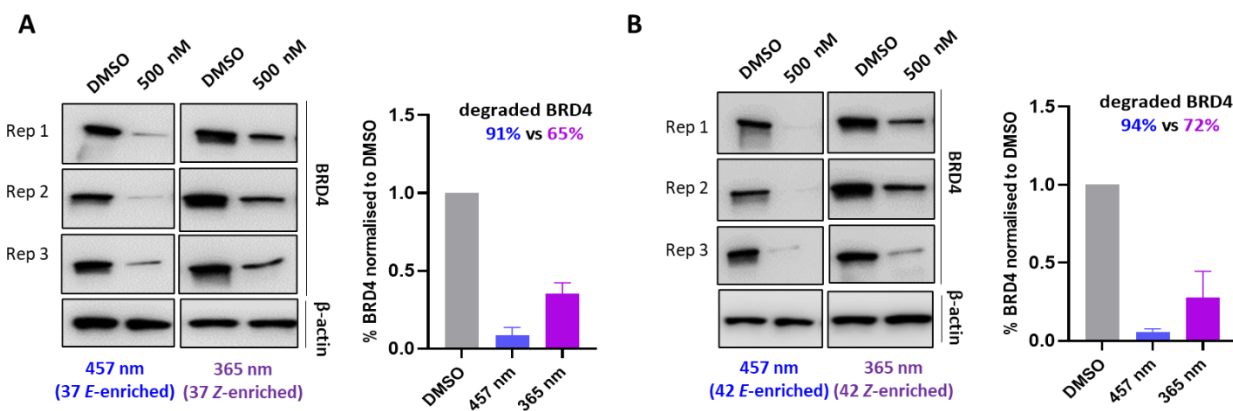
Figure 3.19 *In vitro* testing of photoswitchable PROTAC **37** and **42** with intermittent irradiation. (A) Immunoblots and quantification of BRD4 in HeLa cells after 8 h treatment with DMSO control or 500 nM **37** or (B) **42**. Cells were irradiated with 457 nm (*E*-enriched) or 365 nm (*Z*-enriched) wavelength for 10 seconds every 2 h.

Overall, by irradiating the cells intermittently to maintain a constant *E* to *Z* ratio, a prominent difference was captured between the two isomers of degrader **40**. Such profile was not obtained with the first protocol where stock solutions were pre-irradiated before treating the cells for 24 h. It is worth noting that during this period of time, thermal reversion of the *Z* isomer could occur along with BRD4 resynthesis. In our second protocol, by ending the experiment at a shorter time point (8 h instead of 24 h), differences in degradation profile could also be better detected.

3.2.2.5 Experiments with mCherry BRD4

In parallel to western blot analysis, an alternative readout was developed to monitor BRD4 levels and further distinguish the activity of each isomer. It consisted of an engineered HEK293 cell line expressing a mCherry BRD4 (mchBRD4) construct which was under the control of a tetracycline promoter. The Incucyte® S3 described in the previous chapter allowed us to follow over time the ratio between the signal from mchBRD4 (red fluorescence channel) and the area occupied by the HEK293 cells (phase channel) after incubation with the photoswitchable compounds.

For compound **40**, the faster degradation ability of the *E*-enriched sample (observed in our timecourse experiment) was also confirmed in this cellular assay. Six hours following the start of the incubation, about 75% mchBRD4 degradation was obtained for the *E* isomer while the *Z* isomer attained 43% mchBRD4 depletion (**Figure 3.20 A and C**). The initial decrease of the mchBRD4 signal could be fit into a one phase exponential decay equation and kinetic constants could be compared. It resulted that at 50 nM, the *E* isomer was about three times faster to degrade mchBRD4 than the *Z* isomer. However, at the higher concentration of 500 nM, the amplitude of degradation was higher for both isomers (Dmax>90%) along with faster individual degradation rate (**Figure 3.20 B and D).** This translated into a reduced window and differentiation between the two isomers. Faster kinetics of degradation were also observed for the *E*-enriched sample of compound **42** (**Appendix 3.7**).

	Parameter	500 nM	50 nM
E	K (hr⁻¹)	0.6466	0.4381
	R squared	0.9648	0.9837
Z	K (hr⁻¹))	0.3735	0.1418
	R squared	0.9704	0.9814
E/Z	K ratio	1.731191	3.089563
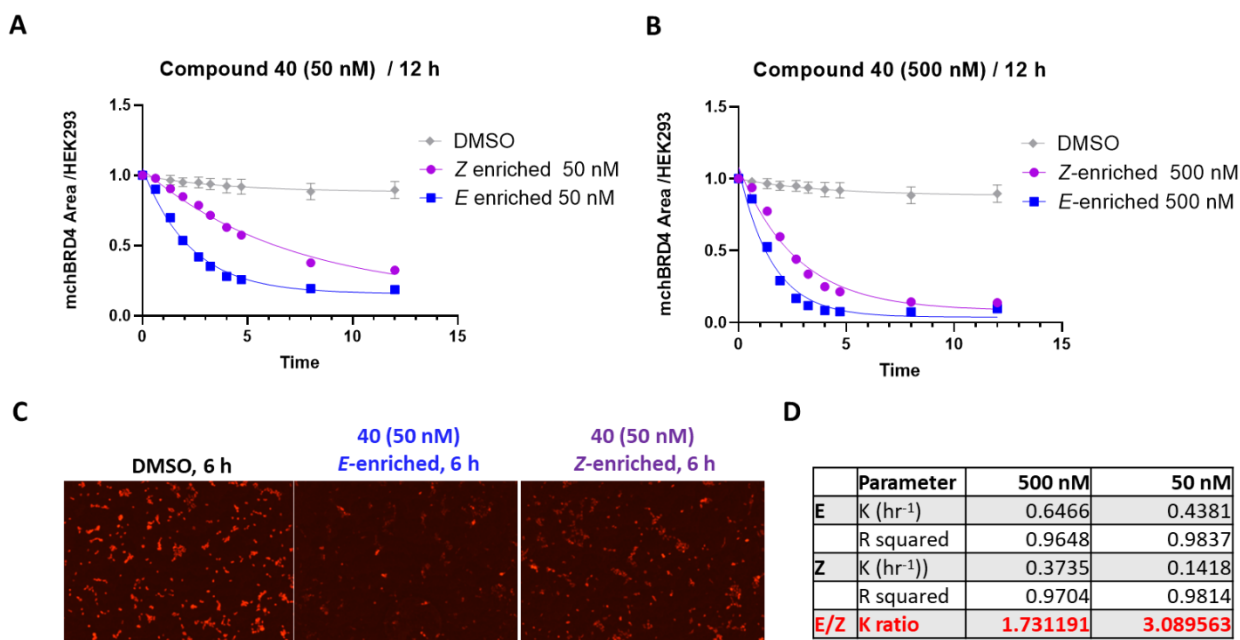
Figure 3.20 *In vitro* testing of photoswitchable PROTAC **40** by live-cell fluorescence imaging. (A) Effect of 50 nM PROTAC **40** and (B) 500nM on mchBRD4 levels after irradiation with 457 nm (*E*-enriched) or 365 nm (*Z*-enriched) wavelength. Red fluorescence area over phase area is plotted on the y axis. (C) Screenshot from Incucyte® S3 of wells containing HeLa cells treated with DMSO, or **40** (*E*-enriched or *Z*-enriched). (D) kinetics parameters obtained from fitting mchBRD4 depletion curve into one phase exponential decay equation.

For practical reasons linked to the Incucyte® S3 mode of operation, intermittent irradiation has not been investigated but one-time pre-irradiation only. If technically feasible, by maintaining a constant PSS ratio via short multiple exposure to 365 nm wavelength in the Incucyte® S3, further distinction in the behavior of the two isomers of our compounds could have been discerned. Nonetheless, *in vitro* assessments of the photoswitchable degrader **40** by western blot and via the Incucyte® S3 are complementary. Although the *Z*-enriched sample also led to BRD4 degradation, its diminished activity at lower concentrations may suggest a weaker binary binding affinity (for BRD4 or the E3 ligase) or a less productive ternary complex characterized by a slower rate of ubiquitination. The limited set of CETSA experiments conducted to explore the binding affinity of **40** for BRD4 were inconclusive. It was confirmed that **40** behave as a bona fide PROTAC as proteasomal inhibition hampered its activity (*E* and *Z* included, **Appendix 3.8)**.

3.2.3 BTK photoswitchable degrader

Bruton's tyrosine kinase (BTK) is a multidomain protein harboring a tyrosine kinase activity which is involved in the maturation of B lymphocytes and their associated signal transduction pathway.[309] Genetic alterations affecting BTK are accompanied with immunodeficiencies, and overactivation of the B-cell receptor pathway often leads to hematological malignances.[310] Hence, BTK has been a widely pursued drug target for which multiple inhibitors have already been developed against.[311] Notably, Ibrutinib is a covalent drug designed to irreversibly binds to cysteine 481 and inactivate BTK.[312] Ibrutinib is currently prescribed for the treatment of several B-cell cancers such as mantle cell lymphoma or chronic lymphocytic leukemia.[313] A major mechanism of resistance in blood malignancies involving BTK is a cysteine to serine mutation, C481S, which annihilates covalent binding of Ibrutinib to BTK.[314] Targeted protein degradation has been proposed as an innovative way to mitigate such resistance since tight binding between the warhead and the POI is not required to produce degradation. Although a mutation may prevent covalent binding, reversible binding could still occur and be harnessed to trigger protein destruction.
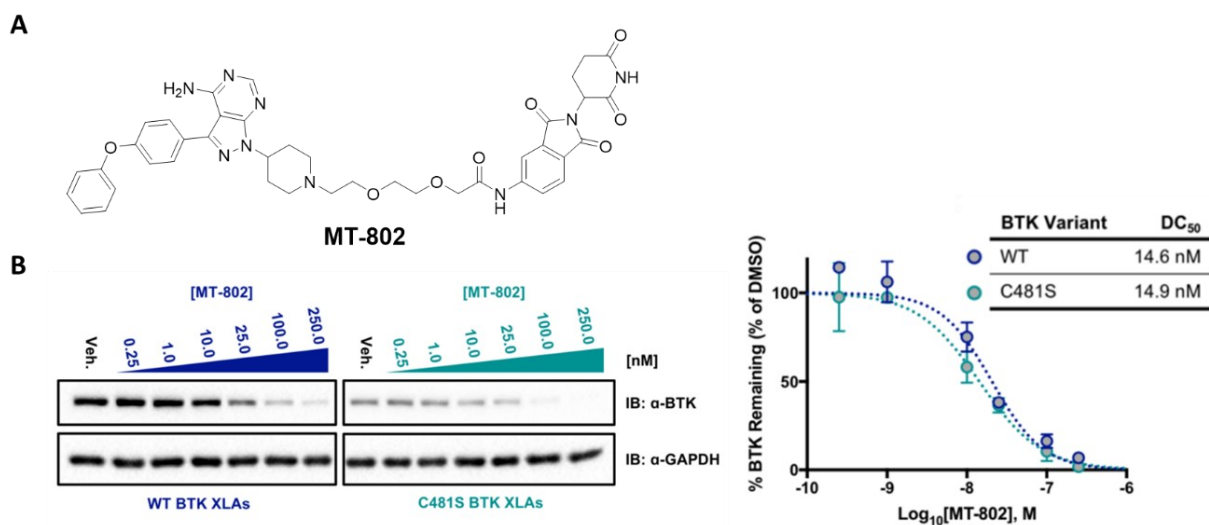
Figure 3.21 BTK degrader **MT-802**. (A) structure of BTK degrader **MT-802**. (B) Immunoblots and DC_{50} quantification of BTK in XLA cells expressing wild type (WT) or mutant (C481S) BTK

Crew's lab ingeniously investigated this approach and demonstrated that the degrader **MT-802**, a bifunctional molecule made of a cereblon recruiter and a non-covalent analogue of Ibrutinib, was able to knockdown BTK and its mutated form (C481S)[315] (**Figure 3.21**).

Following Crew's publication, several other BTK targeting degraders have been developed with reversible non-covalent[316], reversible covalent and irreversible covalent motifs[317]. With the goal of validating the photoswitchable PROTAC concept with a diverse set of targets, we turned to BTK.

3.2.3.1 Design and chemistry

Two molecules were considered for our initial design of a BTK photoswitchable degrader. The Ibrutinib-like warhead could be attached either on the pyrazole or the benzylamine moiety of our azopyrazole linker (**Figure 3.22**). Hydroxythalidomide or lenalidomide could then be incorporated on either end. Compound **43** was selected as the initial design to synthesize although the number of steps to get the second degrader **44** would remain the same. Since for our BRD4 photoswitchable degraders the E3 ligand was always incorporated on the pyrazole moiety, we decided to investigate the alternate design as in molecule **43**.
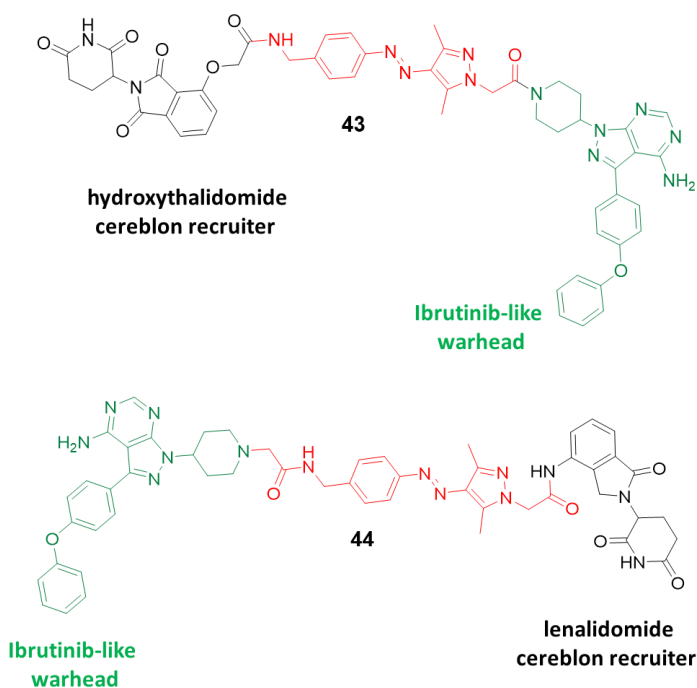
Figure 3.22 Photoswitchable BTK degrader design

The synthesis of our bifunctional molecule is described in **Scheme 3.10**. Commercially available pyrazolo-aminopyrimidine **45** was alkylated on its pyrazole ring via a Mitsunobu coupling with

N-Boc-4-hydroxypiperidine to give the adduct **46**. A subsequent amide coupling with the azopyrazole linker **32** yielded the intermediate **47**. Final Fmoc deprotection and amide coupling with the TFA-deprotected hydroxythalidomide **2** allowed us to obtain the bifunctional molecule **43**. As **MT-802** was not in our possession at the start of our investigation, a positive control **50** with a classical PEG linker was also synthesized according to **Scheme 3.10**.
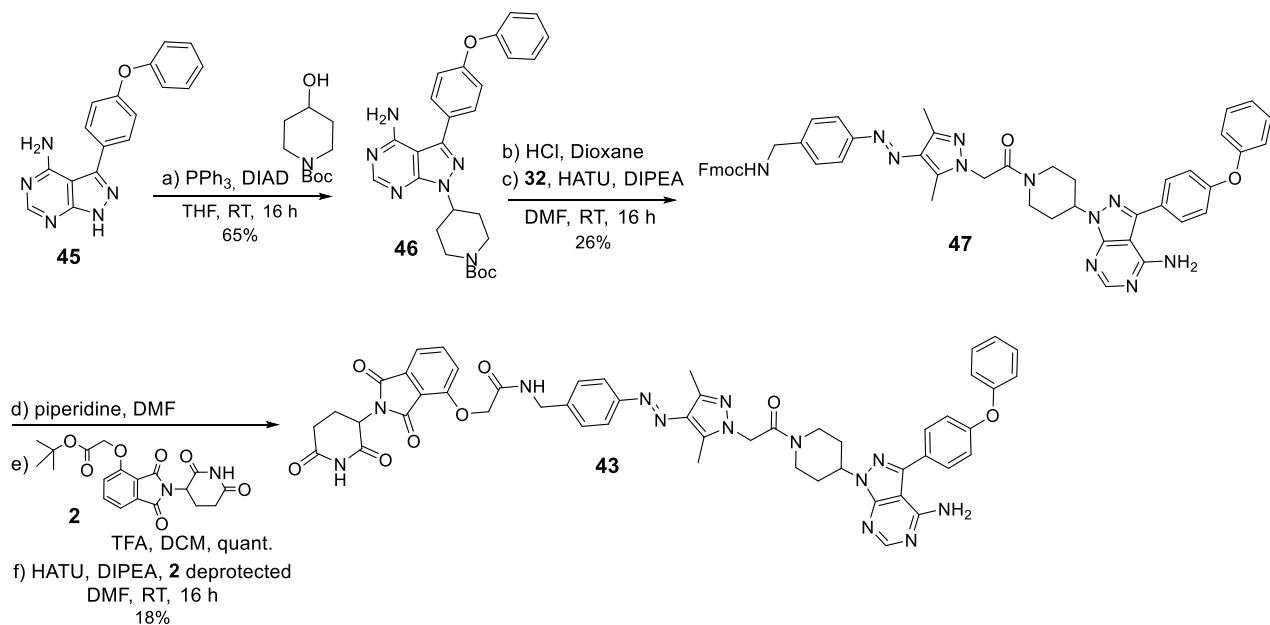
Scheme 3.10 Synthesis of BTK photoswitchable PROTAC **43**
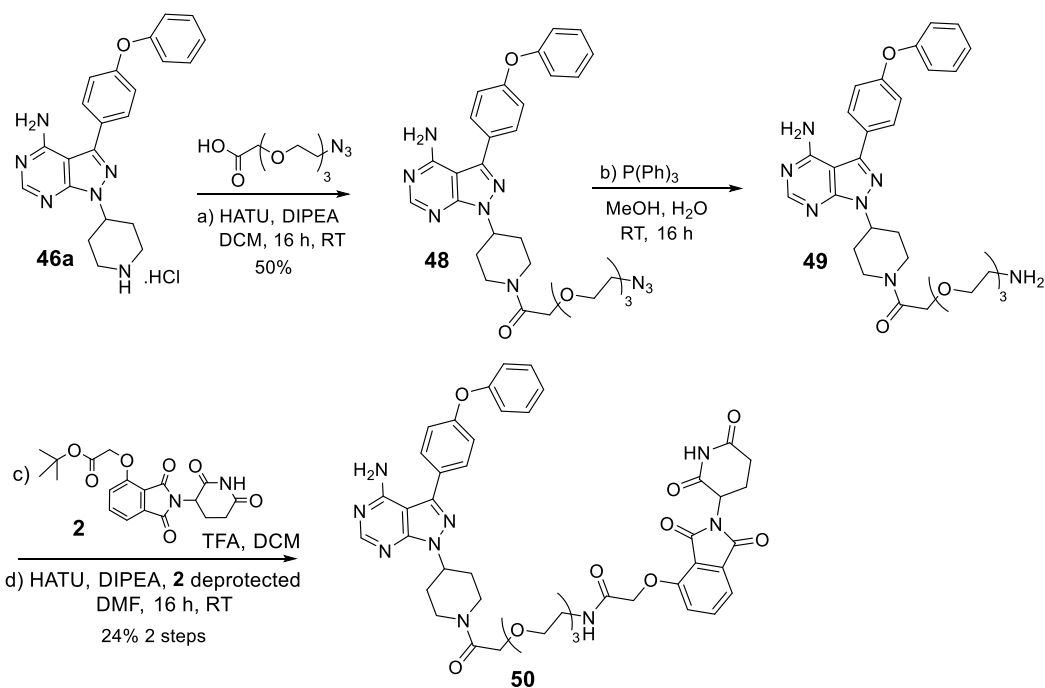
Scheme 3.11 Synthesis of BTK PROTAC **50** as a positive control

3.2.3.2 Photochemistry

The photochemical properties of **43** were assessed by LC-MS and UV-vis (**Figure 3.23 A and B**). Similarly to the BRD4 photoswitchable compounds, a smooth conversion between the *E* and *Z* isomer could be achieved at 365 nm and 457 nm. Up to 76% of the *E* isomer and 87% of the *Z* isomer were observed by LC-MS. In addition, the *Z* isomer of **43** offered a robust stability both at room temperature and at 37˚C (**Figure 3.23 C**). It was confirmed that exposure of the Z isomer to ambient light led to fast reversion to the *E* isomer. On the contrary, keeping the sample in the dark leads to a half-life of at least 18 h (**Figure 3.23 D**).

Figure 3.23 Photocharacterization of **43**. (A) UV-Vis spectrum (100 μM in ACN) after irradiation for 3 min at 365 nm or 457 nm. (B) LC-MS chromatogram (100 μM solution) in ACN/water (1 : 1) after irradiation for 1 min at 365 nm or 457 nm. (C) UV-Vis spectrum after keeping the sample for 24 h at room temperature or at 37˚C in the dark following irradiation at 365 nm for 3 mins. (D) LC-MS chromatogram (100 μM solution) in ACN/water (1 : 1) after keeping the sample for 18 h protected from light (left) or for 30 mins on the bench (right) following 1 min irradiation at 365 nm.

3.2.3.3 Experiments with mCherry BTK

Alongside the mCherry BRD4 cell line generated in the Tate lab for our previous study of BRD4 degraders, a mCherry BTK (mchBTK) cell line was also developed by Dr Maria M. Shchepinova and Dr Daniel Conole. This allowed live-cell monitoring of mchBTK levels over time upon treatment with the photoswitchable compounds. The plots in **Figure 3.24** represents the ratio between the fluorescence from mchBTK (red channel) and the area occupied by HEK293 cells (phase channel) normalized to the time of addition of our tool compounds **43**, **50** and **MT-802**.
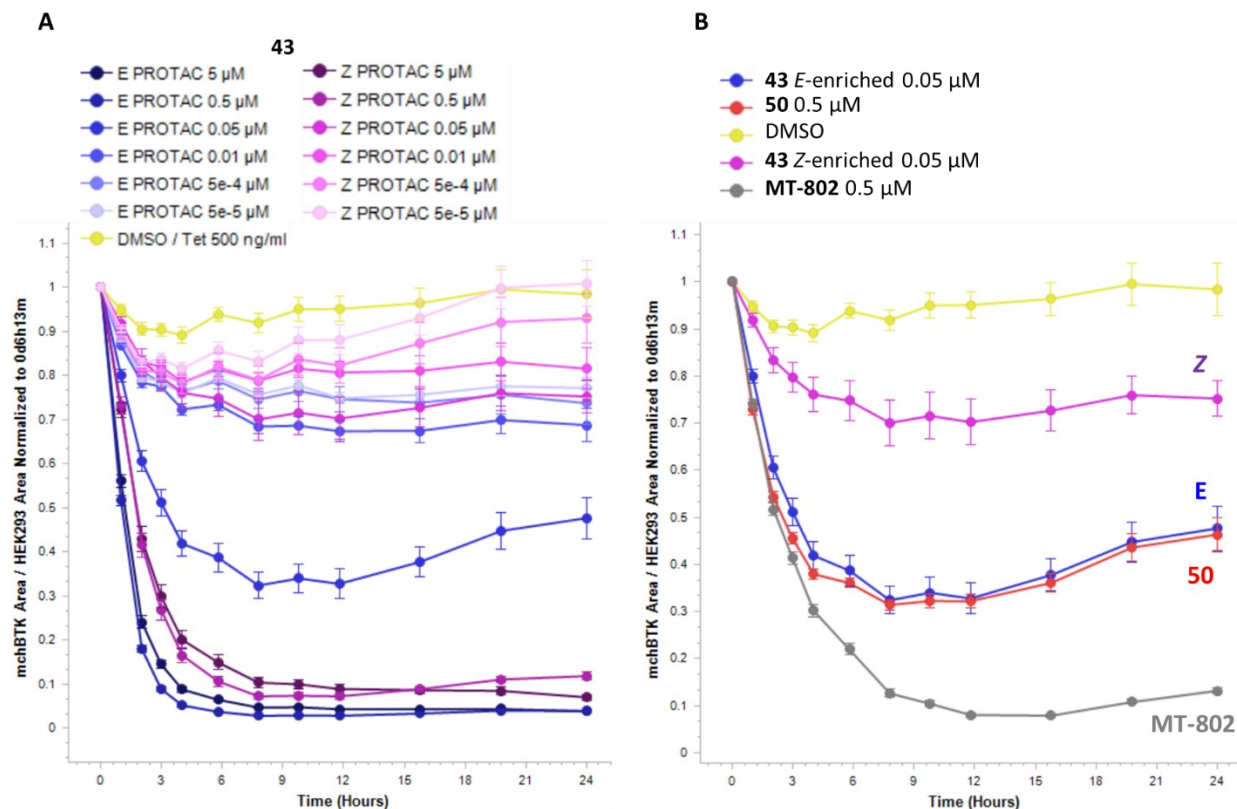
Figure 3.24 *In vitro* testing of photoswitchable PROTAC **43** by live-cell fluorescence imaging

The positive control **MT-802** (tested at 0.5 μM) proved to be extremely efficient at depleting mchBTK in this cellular assay with a Dmax value close to 95% (after 12 h) and a sustained degradation for up to 24 h (**Figure 3.24 B)**. Our designed control **50** (tested at the same concentration of 0.5 μM) was less efficient and achieved a Dmax of 70% (after 8 h) which was not maintained beyond 12 h after incubation. For compound **43**, a dose-dependent decrease in fluorescence over time as compared with the DMSO control was observed, including at concentrations as low as 5 nM (**Figure 3.24 A)**. Interestingly, while at most concentrations tested, the *E* and *Z*-enriched samples where comparable (similar Dmax and degradation rate), at 50 nM, a unique profile was obtained for each isomer of **43**. The *E* isomer reached a Dmax close to 70% while the *Z* isomer attained about 30% maximal degradation of mchBTK after 8 h (**Figure 3.24 B)**. Beyond 12 h, both isomers did not sustain maximal degradation to counteract the slow but continuing mchBTK resynthesis. Those results mirror the profile obtained with the BRD4 photoswitchable compound **40** where between 50-100 nM a distinct behavior for each isomer was recorded. Here again, it is assumed that different binding affinities of **43** (for BTK or cereblon) come into play. Such binary interactions which may be more favorable in the case of the *E* isomer may translate into more productive ternary complex formation. The study of binding interactions between the degrader **43** and its binding partners represents an immense experimental package which would be useful to generate to further explain our findings.

Besides ternary complex formation, evaluation of ubiquitination (rate and extent) for each isomer of **43** would be another important investigation to carry out to clarify our results.

3.3 Other reported photoswitchable degraders

During the same period our research on the caged PROTACs was conducted, protein degradation using photoswitchable units had also been investigated concurrently by several groups (**Figure 3.25**).
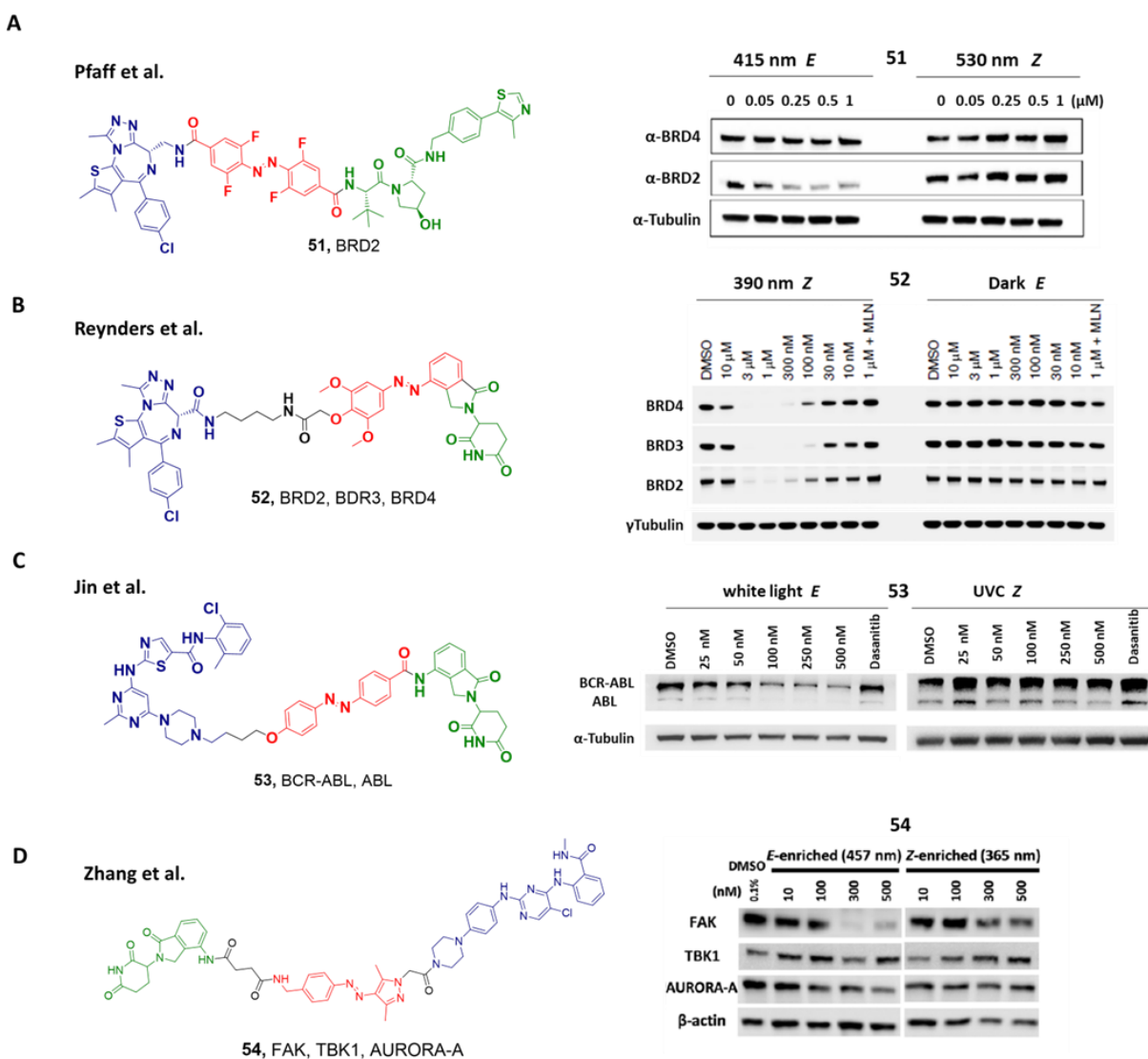
Figure 3.25 Reported photoswitchable degrader design, structures, and activity profiles. Each degrader is made of a warhead (depicted in blue), an E3 ligase recruiter (green), and a photoswitch (red) (A) Structure of photoswitchable PROTAC **51** (left) and Immunoblot analysis after treatment of Ramos cells (right). (B) Structure of the photoswitchable PROTAC **52** (left) and immunoblot analysis after treatment of RS4;11 cells (right). (C) Structure of the photoswitchable PROTAC **53** (left) and Immunoblot analysis following treatment of K562 cells (right). (D) Structure of photoswitchable PROTAC **54** (left) and Immunoblot analysis after treatment of MDB-MB-231 cells(right).

Searching for a bistable photoswitchable compound which would not necessitate continuous irradiation (i.e., thermodynamically stable as the *E* isomer and with an extended *Z* thermal half-life), Carreira's lab turned to the *ortho*-tetrafluoroazobenzene motif[226] (**Figure 3.25 A**). PROTAC **51** was the first reported photoswitchable degrader and its two isomers displayed a distinct degradation profile towards BRD2 (*E* active degrader from 50 nM and *Z* inactive) while leaving BRD4 untouched. The reasons given to explain this selectivity included the presence of the reverse amide bond present on the **JQ1** warhead and the rigidity of the bifunctional molecule which may have led to loss of affinity for BRD4. It is worth noting that at 37°C, thermal isomerization from the *Z* to the *E* isomer of **51** was not observed until after several days. In parallel, Trauner's lab conducted a larger investigation with the azobenzene group synthesizing a total of 19 photoswitchable compounds (coined PHOTACs, Photochemically targeting chimeras) targeting both BRD4 and prolyl isomerase FKBP12.[225] Compound **52** which integrated the phenyl ring of the E3 ligand lenalidomide as part of the photoswitchable linker was the highlight of the exhaustive study. The *Z* isomer of **52** was able to degrade all BRDs (BRD2, BRD3 and BRD4) while the *E* isomer was completely ineffective to deplete the levels of the same proteins (**Figure 3.25 B**). Finally, Jian's lab engineered a BCR-ABL photoswitchable degrader **53** based on an azobenzene linker. In their study, only the *E* isomer achieved degradation of BCR-ABL while the Z remains inactive[318] (**Figure 3.25 C**). It must be noted that the degraders **51**, **52** and **53** could either initiate or reverse proteolysis upon photoisomerization. This on/off switch capability done with a small molecule only, represents an important milestone in the spatiotemporal control of protein stability. Further details about the chemistry and photochemistry of those molecules are given in our previously published perspective.[249] A summary of the element of design and photochemical properties of **51**, **52** and **53** is given in **Table 3.3** along with the properties of compound **40**.

Table 3.3 Characteristics of the reported photoswitchable compounds

Characteristics	51	52	53	40
Photoswitch type	*ortho*-F$_4$-azobenzene	azobenzene	azobenzene	azopyrazole
Activity profile obtained	**E active** / Z inactive	**Z active** / E inactive	**E active** / Z inactive	**E active** / Z less active
E3 ligand / E3 recruited	VH032 / VHL	lenalidomide / cereblon	lenalidomide / cereblon	thalidomide/cereblon
Warhead / Protein degraded	JQ1 / BRD2	JQ1 / BRD4	Dasatinib / BCR-ABL	JQ1 / BRD4 & BRD2
Isoform degradation profile	BRD4 not degraded	BRD4, BRD3 > BRD2	ABL degraded	BRD4 > BRD2
Main irradiation mode[a]	Single initial irradiation	Continuous pulse irradiation	Single initial irradiation	Intermittent irradiation (every 2 h)
λ *E* to *Z* / PSS[b]	530 nm / 68% *Z*	390 nm / >90% *Z*	UVC[c]	365 nm / 85% *Z*
λ *Z* to *E* / PSS[b]	415 nm / 95% *E*	>450 nm / >70% *E*	White light[c]	457 nm / 78% *E*
Z half-life / thermal relaxation[d]	several days (37°C, DMSO)	8.8 h (37°C, DMSO)	10.3 h (25°C)	at least 5 h[e] (37°C)
photoswitch resistance	---	multiple cycles tested	5 cycles tested	multiple cycles tested
In-cell reversible degradation	achieved	achieved	achieved	not tested
Stability towards GSH reduction	stable	---	stable	not tested

[a] Different light sources have been used. Readers should refer to the original publication for details [b] PSS = photostationary state, reported as percentage of Z at equilibrium after irradiation at λ.[c] Wavelength not specified, no PSS data [d] In absence of light [e] Based on early timepoints collected via LC-MS. Compound CK1-280 has showed a half-life of > 48 h at 25°C.

The preliminary work with the azopyrazole photoswitch has been further expanded. In collaboration with the Fuchter lab, PhD student Qisi Zhang connected the azopyrazole photoswitch to a promiscuous kinase degrader (able to bind to 235 kinases) and to lenalidomide[227] (**Figure 3.25 D**). Treatment of breast cancer cell line MDA-MB-231 with the *E*-enriched sample or PROTAC **54** led to the selective depletion of 4 kinases only while the *Z*-enriched sample did not affect the level of any of the kinases monitored. The work by Zhang is the first example of light-mediated degradation of a specific set of kinases starting from a pan-kinase inhibitor.

3.4 Conclusion and future directions

Our investigation of photoswitchable degraders revealed that the same molecule can affect in a different manner the stability of a protein by using specific wavelengths of light. The *E* isomer of our degrader **40** proved to be a better degrader than its *Z* counterpart. Nonetheless, the design of such tools to consistently achieve the desired outcome (i.e., on/off capability) is still empirical and multiple iterations were needed to identify a suitable compound for the studied protein BRD4. Pleasingly, isoform selectivity between BRD2 and BRD4 was also observed for **40** and this feature may bring an advantage when studying proteins pertaining to the same family.

Explanation of the structure-activity relationship has yet to be given at a molecular level and would benefit from binding studies to better understand ternary complex formation for each isomeric pair. It is believed that in silico modelling tools can also provide some help in that respect, not only by means of retrospective analysis but also early in the design of new photoswitchable compounds.
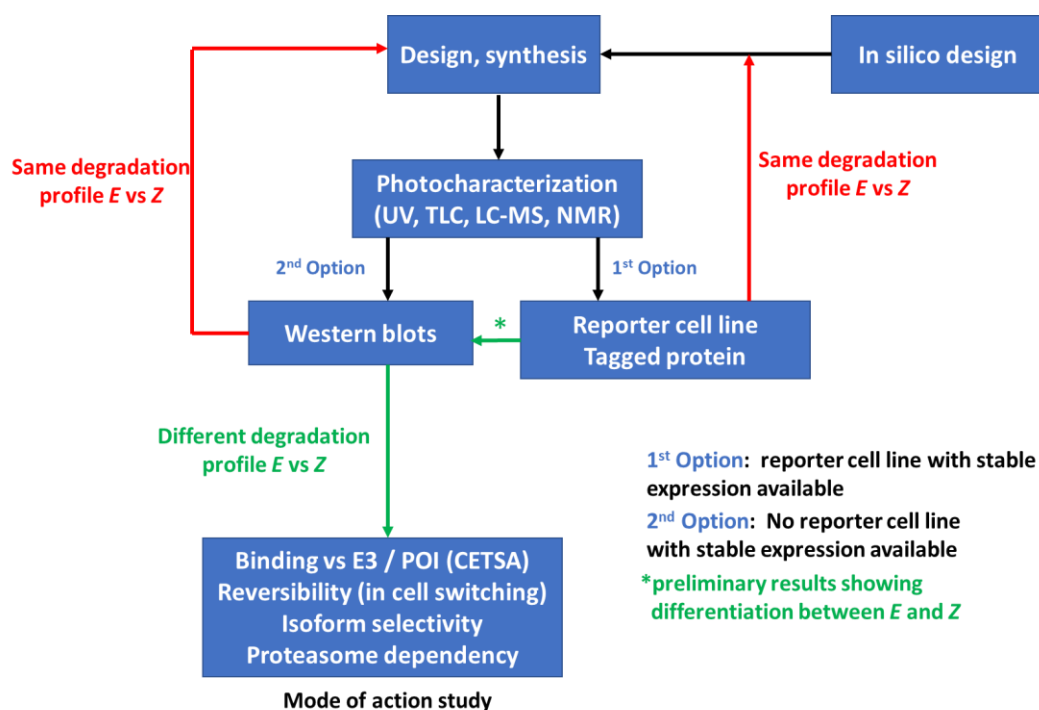
Figure 3.26 Flowchart guide to develop photoswitchable degraders.

The multiple syntheses and *in vitro* testing cycles applied in the course of this work led us to derive a flowchart to guide the discovery and study of future photoswitchable degraders. An emphasis is put here in the development of a reporter cell line expressing the protein of interest to facilitate *in vitro* testing. Such tool was made available to us at a late stage in our research investigation and could have accelerated our search for a set of isomers with unique degradation profile. Overall, efficient synthesis of a library of degraders coupled to an assay with a high throughput (cell reporter assay) is proposed to facilitate the identification of isomers worth a full characterization. Western blot analysis (which is time consuming) would then come at a later stage as a secondary orthogonal assay to confirm preliminary results obtained from the reporter cell line. A full mode of action study would then be triggered only after obtention of robust data by western blot.

Finally, the set of targets to which the photoswitchable approach has been applied remains limited and it is hoped that the results published by our group and others will inspire further work in this field. As with caged degraders, the development of redshifted photoswitches[319,320] is a necessary path to consider a wider use of those tool compounds *in vivo*.

Chapter 4 | Hypoxia-activated degraders

4.1 Oxygen sensing in cells

Hypoxia defined as a low oxygen partial pressure in tissue can be the result of various internal factors such as a diseased state (e.g., pulmonary disease, reduced tissue perfusion, anemia) or external conditions like high altitude. Substantial decrease in oxygen levels in eukaryotic cells provokes profound changes in gene expression allowing cells to adapt to the new hypoxic environment. The research work from Gregg Semenza, William Kaelin, and Peter Ratcliffe (2019 Nobel Prize in Physiology or Medicine) identified the mechanism by which cells sense variation in oxygen levels.

There are two essential proteins, hypoxia-inducible factor 1α (HIF1α) and Von Hippel Lindau tumor suppressor (VHL) which are involved in this regulatory pathway. Under normoxic conditions, HIF1α is hydroxylated by prolyl-hydroxylase. This chemical modification increases the binding affinity of HIF1α for VHL which in turn induces the degradation of the former by a ubiquitination-dependent mechanism (**Figure 4.1**).
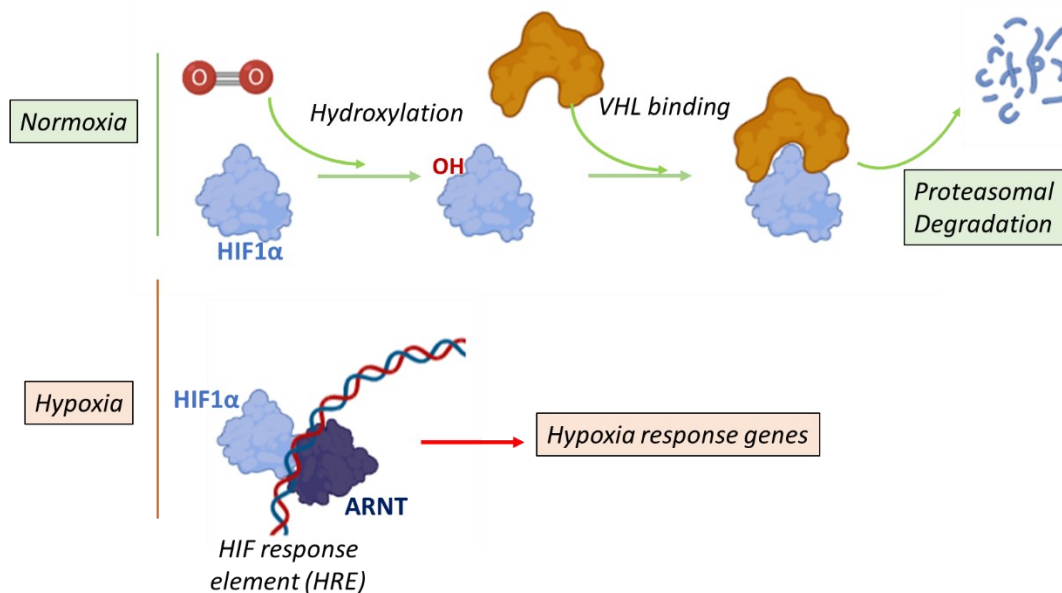
Figure 4.1 Normoxia versus Hypoxia. Hypoxia-inducible factor 1α (HIF1α) is degraded under normoxic conditions but operates as a transcription factor under hypoxic conditions.

In contrast, under hypoxic conditions, HIF1α is not hydroxylated and dimerizes with HIFβ (ARNT). The whole HIF complex then translocate to the nucleus where it binds to hypoxia-responsive element (HRE) in the genome and activates the expression of genes needed for the adaptation to low oxygen levels (oxygen consumption, erythrocyte production and angiogenesis).

4.2 Hypoxia as a target and hypoxia-induced prodrug concept

Hypoxia has been identified as one factor among many that contribute to tumor growth and invasiveness.[222] As cells buried within the tumor mass are less irrigated by blood vessels, those
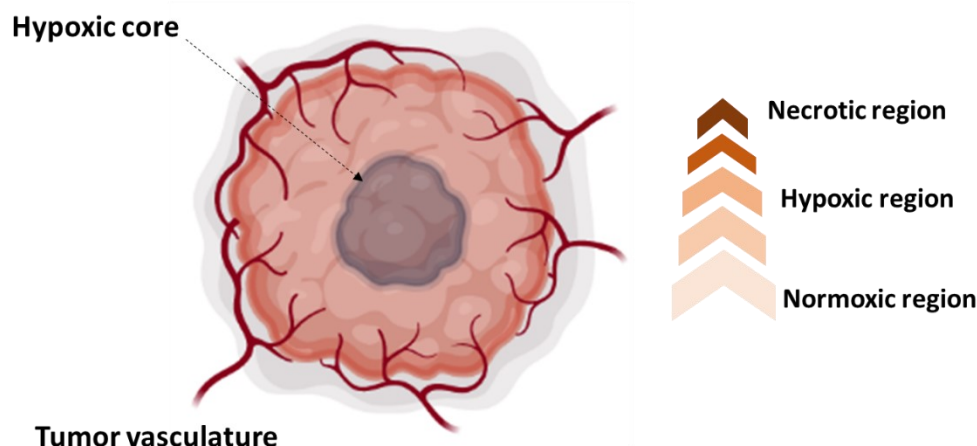
Figure 4.2 Tumor hypoxia and vasculature. Cells away from the main vasculature tend to be more hypoxic. Variability in hypoxic state can be observed within the same tissue and across tissues.[321]

cells tend to be exposed to lower oxygen influx than cells close to the vasculature[322,323] (**Figure 4.2**). One consequence of the hypoxic environment created in those cells is the emergence of resistance towards radiation and chemotherapy.[324] Resistance to radiation therapy is due to the lack of toxic reactive oxygen species generated during the application of the ionizing radiation.[325] The genomic instability and heterogeneity induced by the hypoxic milieu allows cells to resist chemotherapy.[326] It has been hypothesized that the difference in oxygen levels that exists within the solid tumor can be used as a means to kill hypoxic cancer cells while preserving healthy ones. The basis of the selective toxic effect is the redox cycling that occurs in normoxic cells only and not in hypoxic cells upon treatment with a hypoxia-activated prodrug (HAP) bearing a bioreductive moiety[223] (**Figure 4.3**).
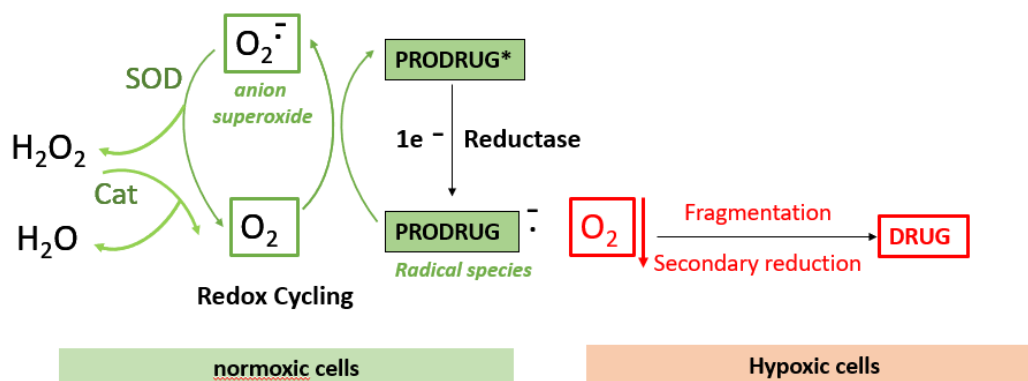
Figure 4.3 Hypoxia-activated prodrug mode of action.

The first step of breakdown of the HAP is the generation of radical species by a reductase enzyme via electron transfer. In presence of oxygen, the radical is quickly oxidized back, and the resulting anion superoxide is dealt with by superoxide dismutase and catalase. Conversely, under hypoxic conditions, the radical can be further fragmented via secondary reduction to release the toxic drug. An example of HAP tested in the clinic for various cancers is evosfosfamide (TH-302).[327] The prodrug contains a nitroimidazole moiety which under hypoxic conditions releases the toxic drug bromoisophosphoramide (Br-IPM), a DNA alkylating agent[328] (**Figure 4.4**). Other bioreductive units incorporated in HAP include quinones, N-oxides and various nitroaromatics derivatives.[329] Although, there is currently no HAP drug approved,[330] the approach has shown positive results i*n vitro* and *in vivo*.[331]
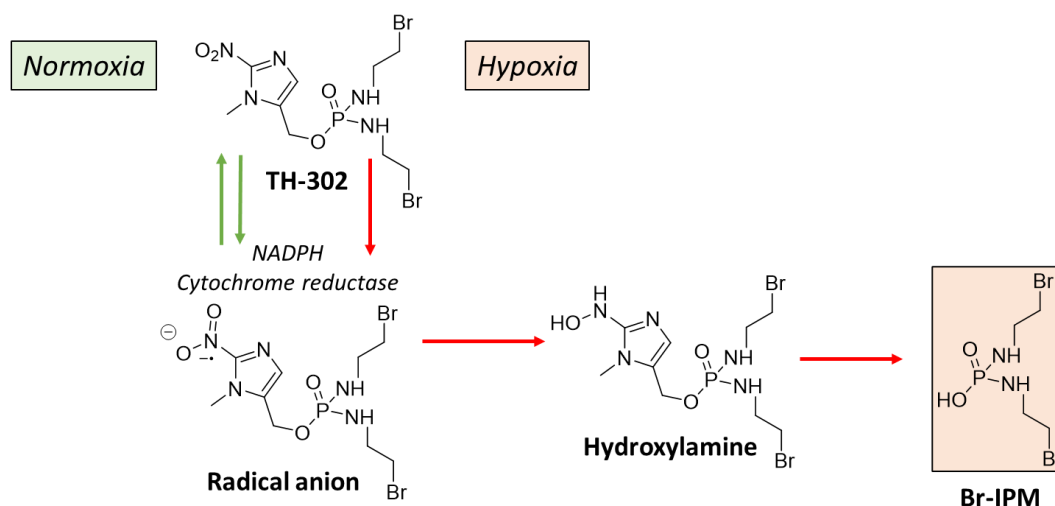
Figure 4.4 TH-302 mode of action.

4.3 Hypoxia induced PROTACs

As part of our investigation towards the conditional control of PROTACs, we decided to apply the HAP approach to a bifunctional degrader. Delivering a PROTAC which can be activated only under hypoxic conditions will achieve the knockdown of a target with high spatiotemporal control only in cells suffering from a lack of oxygen (e.g., cancer cells)

4.3.1 Design, synthesis, and cleavage assessment

Our design of a hypoxia-activated PROTAC relied on the caging of the caging of the VHL hydroxyproline ligand to initially obtain an inactive degrader. Under hypoxic conditions, cleavage of the bioreductive moiety would free up the hydroxyproline to recruit the VHL E3 ligase to our POI (**Figure 4.5**). The *para*-nitrobenzyl group (PNB) was selected as a reductive system as we
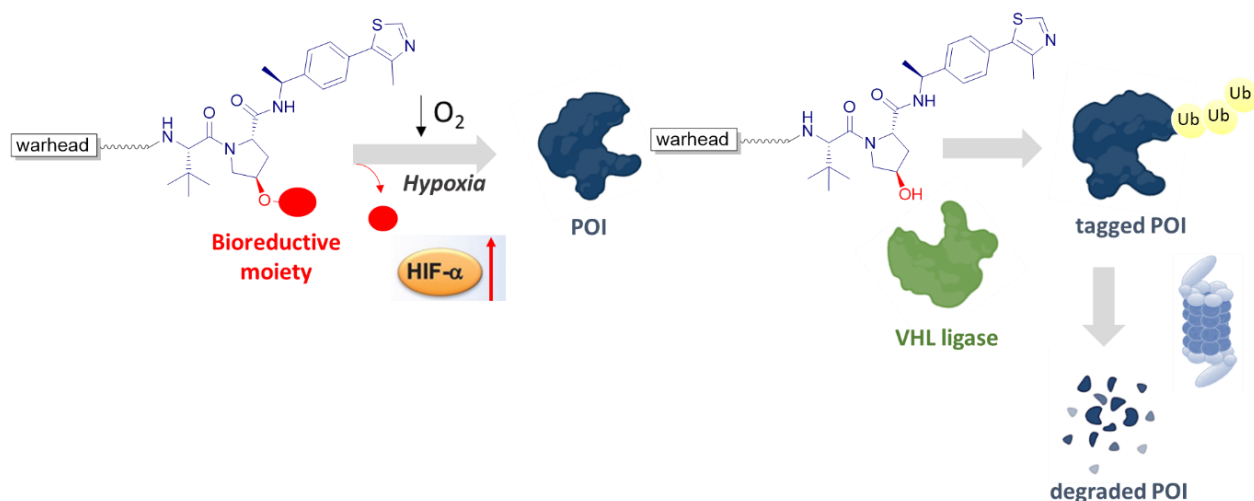
Figure 4.5 Hypoxia-activated PROTAC mode of action.

could leverage on the chemistry already developed with the dimethoxynitrobenzyl group (DMNB) for the light-activated caged PROTACs. Besides, the PNB group has been utilized previously to develop HAPs.[332,333]

At First, the PNB motif was introduced as an ether on the hydroxyproline according to **scheme 4.1**. Using the phase transfer catalysis conditions optimized for the DMNB group, compound **55** could be obtained in a 40% yield. A carbonate analogue **56** was also synthesized by reacting ligand **6** with *para*-nitrobenzyl chloroformate in presence of DMAP.
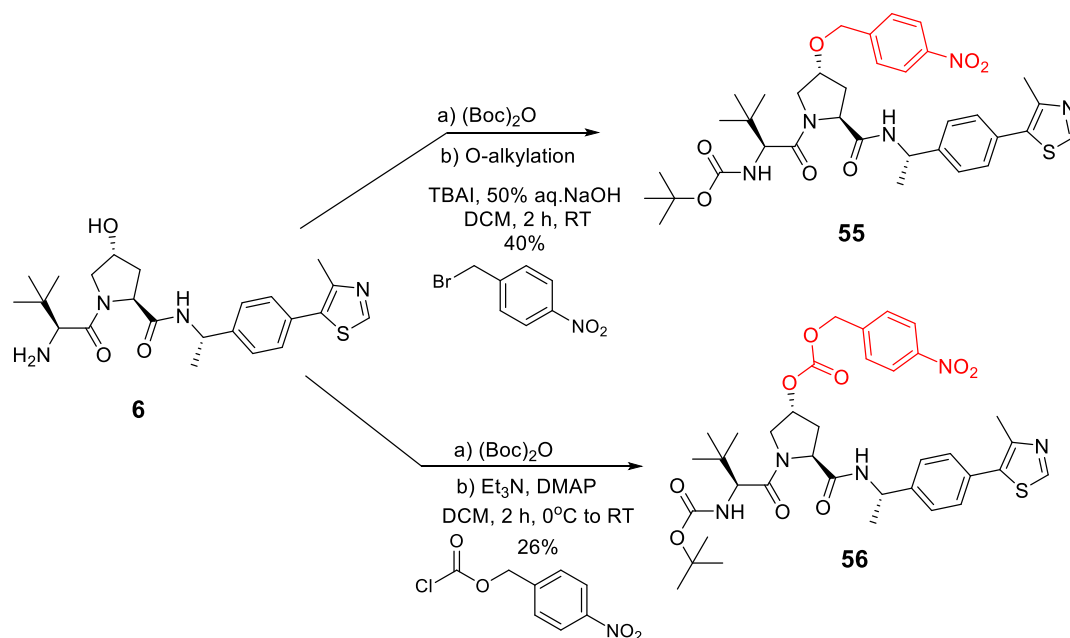
Scheme 4.1 Synthesis of VHL ligand with bioreductive moiety
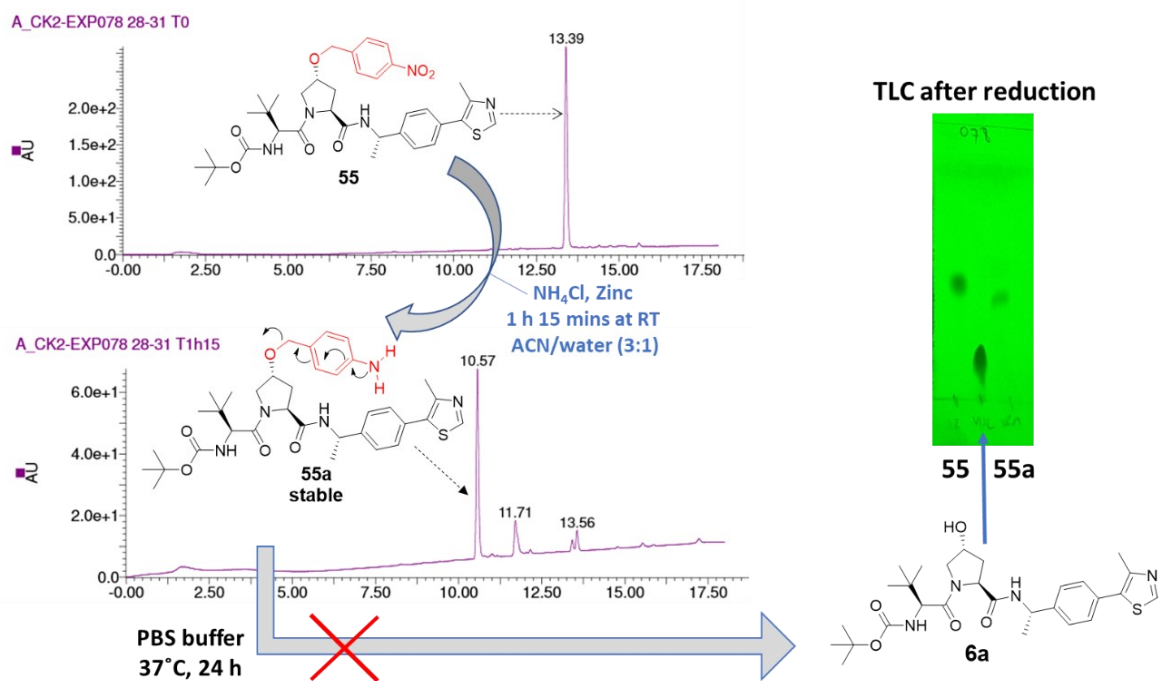
Figure 4.6 Cleavage assessment of compound **55**

We then evaluated the ability of **55** and **56** to release **6** under chemical reduction. A small aliquot of intermediate **55** was incubated in presence of zinc powder and ammonium chloride in acetonitrile/water to reduce the nitro group to the aniline for subsequent fragmentation. Aniline **55a** was observed by LC-MS but did not fragment to the desired intermediate **6a** (**Figure 4.6**).
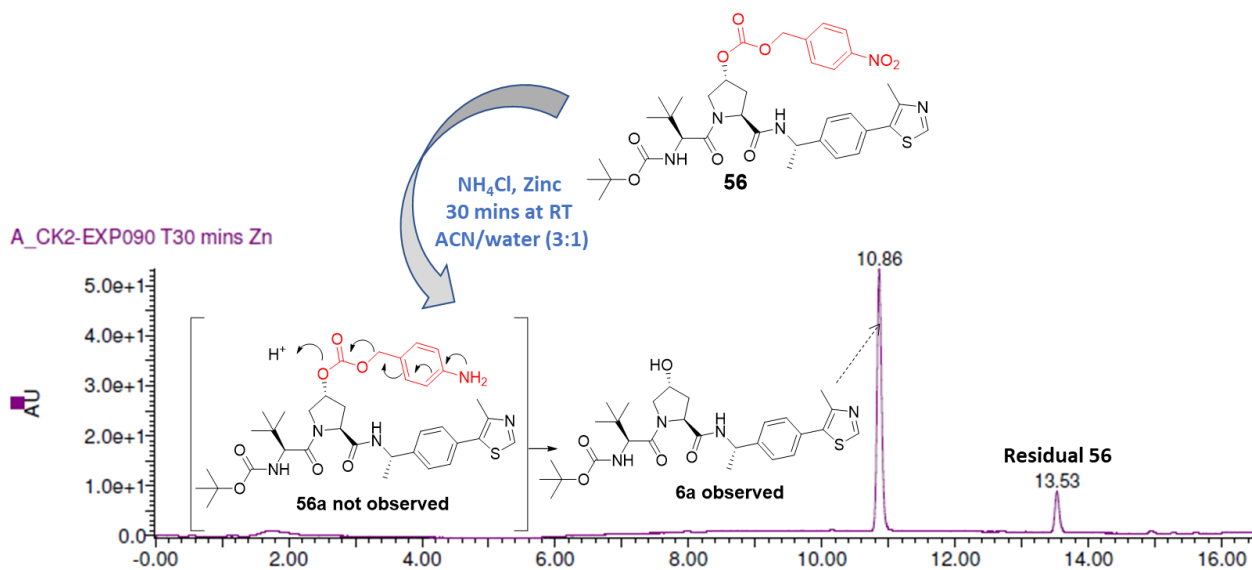
Figure 4.7 Cleavage assessment of compound **56**

At this stage, further incubation of **55a** in PBS buffer at 37°C for 24 h was conducted but it remained stable. On the contrary, reaction between the carbonate **56** and zinc led to the cleaved compound **6a** while **56a** was not observed (**Figure 4.7**).

This result established the carbonate PNB moiety as a suitable reductive group to incorporate in our degrader. Enzymatic cleavage using human nitroreductase (NTR) has been considered to evaluate the cleavage of the caged VHL intermediate **56**, however difficulty in sourcing NTR at a reasonable cost led us to deprioritize this option.

Full PROTAC synthesis was conducted by Boc deprotection of **56** followed by amide coupling with **57** to give the bifunctional BRD4 targeting molecule **58** (**scheme 4.2**).
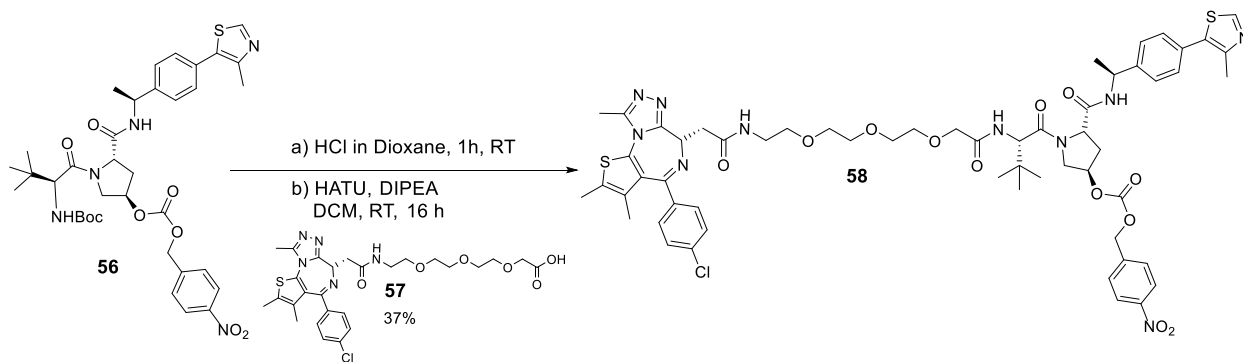
Scheme 4.2 Synthesis of PROTAC **58**

4.3.2 Biological assessment

The testing of compound **58** was done alongside compound **15** using incubators in which the oxygen level had been reduced to 2% to generate hypoxic conditions. In the first attempt, **58** was incubated in HeLa cells for 2 h under normoxia before establishing the hypoxic conditions for a period of 20 h. As anticipated, compound **15** led to degradation of BRD4 irrespective of the oxygen level. However, a similar outcome was obtained for **58** which induced degradation of BRD4 under hypoxia (2% O_2) but also under an oxygen-rich atmosphere (15% O_2) (**Figure 4.8**).
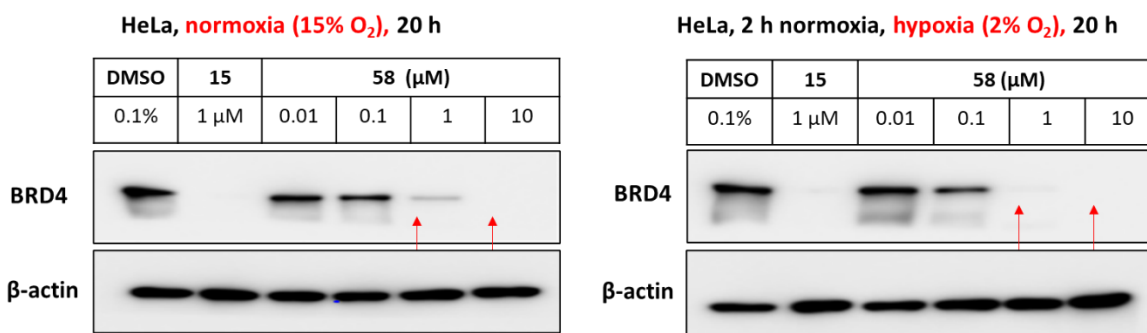
Figure 4.8 Assessment of **58** in HeLa under normoxia and hypoxia. HeLa cells were treated with PROTAC **58** or uncaged PROTAC **15** for 20 h under normoxic (15% O_2) or hypoxic (2% O_2) conditions. Cells were lysed, and lysates collected for Western blot analysis.
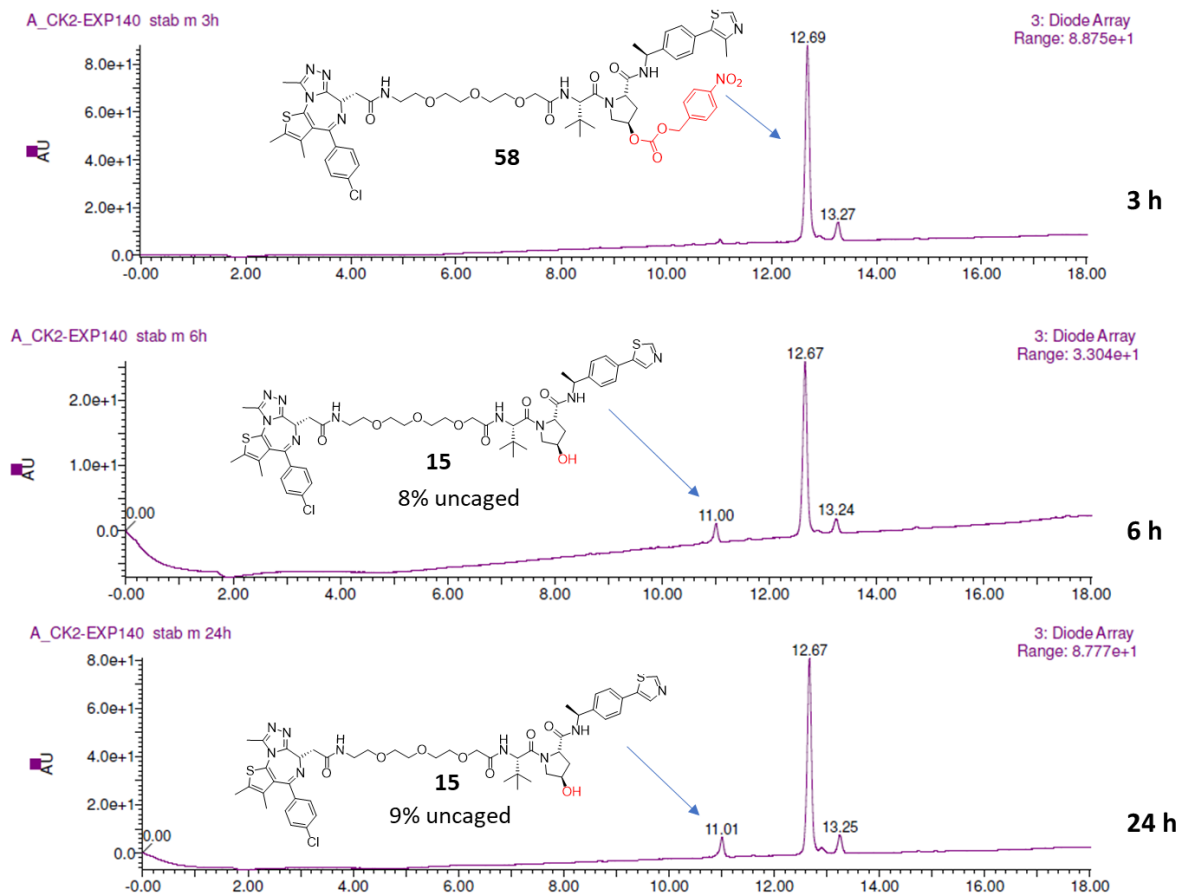
Figure 4.9 Chemical stability of **58** in cell culture. A 50 µM solution of PROTAC **58** in cell culture medium was kept at 37°C for up to 24 h. AUCs was extracted from the chromatogram UV trace.

This result indicated that uncaging of **58** was occurring, hence the carbonate was being cleaved under normoxic conditions either intra-or extracellularly. To examine if **58** suffered from chemical instability, it was incubated at 40°C in cell medium and monitored by LC-MS over 24 h. This led to 9% of uncaged compound **15** after 24 h while no change was observed after 3 h (**Figure 4.9**). Partial release of the parent degrader **15** in the cell culture medium in sufficient amount could explain BRD4 degradation under normoxia, especially considering PROTACs catalytic mode of action. In order to exclude degradation due to hydrolytic cleavage in the media, a shorter incubation was employed for the next in-cell experiments. Despite the reduced incubation time, BRD4 degradation still occurred under normoxic conditions during this shorter timeframe (data not shown). Overall, finding the right balance between cell permeability, compound stability intra-extracellularly and intracellular cleavage under normoxic conditions stood as the key optimization parameter to take into consideration for future designs.

4.4 Reported hypoxia-activated degraders

Shi Shi et al. designed an EFGR degrader **59** by caging the VHL E3 ligand with a nitroimidazole bioreductive moiety[334] (**Figure 4.10 A**). Conditional degradation of EGFR was achieved under hypoxic conditions only. Concurrently, Cheng et al. designed a lenalidomide-based EGFR degrader bearing a PNB group. Although the bifunctional compound had a lower affinity for EGFR than the parent gefitinib warhead, they demonstrated that their caged degrader was activated by nitroreductase *in vitro* and more efficient at degrading EGFR[del19] under hypoxia than normoxia.[335] Finally, Thang Cong do et al. have developed an enzyme-derived clicking PROTACs coined ENCTACs made from the crosslinking of two molecules that degrade BRD4 only under hypoxic conditions.[336] Thalidomide was connected to both a nitroreductase- and GSH-sensitive group (**Figure 4.10 B**). Under hypoxia, cleavage of the PNB followed by glutathione-mediated reduction led to the release of an aminothiol which underwent click reaction with a JQ1-derived benzothiazole. The cascade generated a BRD4 degrader which eventually down regulates HIF1α and associated hypoxia-related response genes.
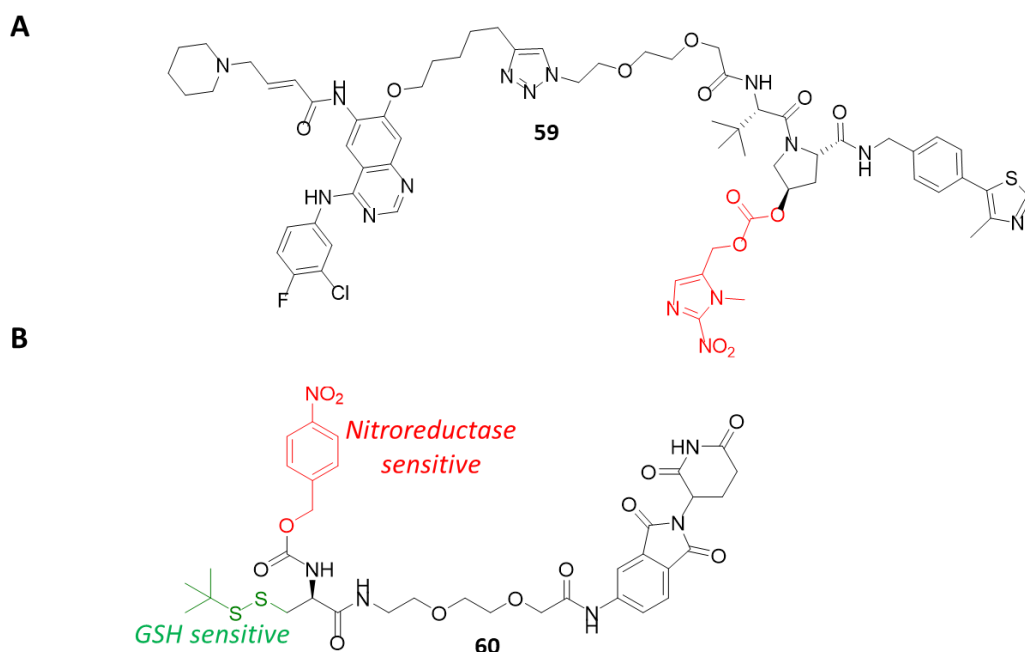
Figure 4.10 Examples of reported Hypoxia-activated degraders

4.5 Conclusion

A novel BRD4 degrader conditional to oxygen level was designed and synthesized. Despite demonstrating that uncaging of the VHL-linked PNB group can occur under chemical reduction, testing of **58** in cells did not show any difference between an oxygen-rich and a hypoxic environment. The reports mentioned above nonetheless validate the approach and add hypoxia-activated degrader as an innovative tool for chemical biology and application in drug discovery.

Chapter 5 | Summary and outlook

The research work described in this thesis investigated the conditional activation of protein degraders with light as an external stimulus and hypoxia as an intracellular trigger. Overall, it was demonstrated that a PROTAC can be rendered inactive by attaching a photoactivatable motif on the VHL ligand. Short exposure with UV light (365 nm) could then irreversibly release the desired degrader. Thanks to the ease of attachment of the caging unit, the developed strategy is potentially applicable to any VHL-based degrader. Beyond the use of caged degraders in chemical biology, their localized activation as phototherapeutics in a tissue or organ could help achieve excellent selectivity, thus delivering a better safety profile versus the parent uncaged degrader. We note that apart from UV light, X-ray radiation has been used recently as an external trigger to activate a PROTAC caged with a phenyl azide motif. The authors named their approach radiotherapy-triggered PROTAC (RT-PROTAC) which also fits into the concept of spatiotemporal degradation.

In the case of photoswitchable degraders, light-mediated isomerization of the incorporated arylazopyrazole unit allowed a distinct BRD4 degradation profile between the *Z* and *E* isomers. In addition, isoform selectivity with greater degradation of BRD4 versus BRD2 was observed with **40**. From a chemical biology perspective, those results suggest that photoswitchable degraders may be used as tools to study the individual role of protein isoforms thanks to selective degradation. This could represent a unique way of modulating a degrader's substrate specificity with the same tool molecule. As with caged degraders, the photoswitchable degraders may also be used as phototherapeutics with high spatiotemporal resolution thanks to an on/off switch mechanism. Identification of a wider set of *E* and *Z* degraders with an opposite degradation profile for various targets would further expand the use of these tools.

Although our hypoxia-sensitive PROTAC **58** did not perform as expected in cells, the release of a degrader under low oxygen level has been achieved, thus validating our proposed hypothesis. It is our belief that incorporation of caging groups which are sensitive to certain intracellular conditions can allow further tissue-specific activation of degraders. For example, a PROTAC caged with an acid labile group may be cleaved preferentially in cells where the cytosol is at low PH (e.g., cancer cells) or in acidic organelles (e.g., lysosomes). Enzymatic activation may also be considered in the case where the overexpression of certain enzymes which drive a "diseased" state can be harnessed as a prompting mechanism (e.g., nitroreductase).

Overall, the research work highlights the various levels of control which can be added to TPD with conditionally activated bifunctional degraders. With those novel tools, protein function may be studied at the resolution of an organ, a tissue or a single cell with external and intracellular stimuli directing the extent, duration, and localization of the degradation event. Besides, with degraders crowding into the clinic with uncertainty about their short- and long-term safety profile, the approaches described here may partly give an answer to address the toxicity flags which may arise.

In order to complement and further enhance the work presented here, we envision three potential future directions. First, besides BRD4, multiple other proteins could be explored to expand the reach and usefulness of light-activation applied to degraders. Secondly, the caging of the degraders and the incorporation of the azopyrazole photoswitch may offer alternative design strategies in which the warhead could be caged or form part of the photoswitch itself to deliver tools with diverse optical properties and differentiated pharmacological response. Finally, the development of light-activated degraders for *in vivo* applications in mammals would increase their impact in both chemical biology and drug discovery.

Chapter 6 | Material and Methods

6.1 Chemistry

6.1.1 General methods

All reagents and solvents were purchased from commercial sources and used as supplied unless otherwise indicated. Pan-bromodomain inhibitor **JQ1** and VHL E3 ligase ligand **6** were provided by GlaxoSmithKline Medicines Research Centre, Stevenage. Reactions were monitored by thin-layer chromatography (TLC) using Merck silica gel 60 F254 plates (0.25 mm). TLC plates were visualized using UV light (254 nm) and / or by using the appropriate TLC stain. Flash column chromatography was performed using silica gel Geduran® Si 60 (40-63 μm) silica gel (Merck). All compounds bearing the photocleavable 4,5-dimethoxy-2-nitrobenzyl (DMNB) group were protected from ambient light during synthesis and purification by turning off the lights of the fume cupboard and were covered with aluminum foil after isolation. Photoswitchable compounds were not protected from light during their synthesis. Irradiation of compounds were conducted using custom-made boxes (by Dr. Charlie Saunders, WaveyTech Ltd) installed with 25 mW LED light bulbs of 365 nm, 405 nm, and 457 nm wavelength. Characteristics of the boxes can be found in **Appendix 2.1**.

Final compound's purity was determined by their LC-MS spectra recorded on a Waters high performance liquid chromatography (HPLC) system, including a 2767 autosampler, 515 pump and a 3100-electrospray ionization (ESI) mass spectrometer, using MassLynx 4.1 software. Compounds were separated on a 4.6 mm × 100 mm analytical Waters XBridge C18 column using the following gradient: 20-98% over 12 min then 98% acetonitrile for 3 mins. UV-Vis spectrum were recorded on a Cary 60 UV vis spectrometer (wavelength range: 190 – 1100 nm, resolution: 1.5 nm, Light source: Xenon Flash Lamp (80 Hz)).

Nuclear magnetic resonance (NMR) spectra were recorded on a Bruker AV-400 (400 Hz) instrument and in deuterated solvents. Chemical shifts (δ) are quoted in ppm (parts per million) to the nearest 0.01 ppm downfield from tetramethylsilane, referenced to residual solvent signals. Coupling constants (J) are given to the nearest 0.1 Hz. The following abbreviations are used to indicate signal multiplicity: s: singlet, d: doublet, dd: doublet of doublet, t: triplet, q: quartet, m: multiplet and br: broad. Spectra were analysed using MestReNova 12 software.

For the photoswitchable compounds bearing an arylazopyrazole, the ^{1}H NMR signals reported are those of the most stable *E* isomer. In case the *Z* isomer is also seen, the chemical shifts of its signals are also given. Efforts have been made to assign most of the protons observed for each compound.

High-resolution mass spectrometry (HRMS) data were acquired by the Imperial Mass Spectrometry service; m/z values are reported in Daltons (Da) to the nearest 0.0001 Da.

6.1.2 Chemical synthesis

1
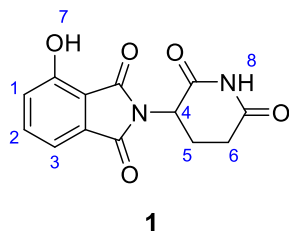
2-(2,6-dioxopiperidin-3-yl)-4-hydroxyisoindoline-1,3-dione (1)

In a 100 ml round bottom flask was added 4-hydroxyisobenzofuran-1,3-dione **1** (2 g, 12 mmol) and 3-aminopiperidine-2,6-dione hydrochloride (2.17 g, 13,2 mmol) along with sodium acetate (2.95 g, 36 mmol). After addition of acetic acid (30 ml), the solution obtained was stirred at reflux for 16 h. The resulting brown slurry was partitioned between ethyl acetate (50 ml) and water (50 ml) . The organic layer was washed with an aqueous solution of sodium bicarbonate (50%) three times (3 x 30 ml) and brine (30 ml). It was then dried over sodium sulfate, filtered, and concentrated in vacuo to give a beige solid (1.0 g). Additionally, a beige precipitate was recovered from the aqueous layer (1.43 g); it was combined to the previously recovered material (2.43 g, 74 %) and was used without further purification. Rf = 0.30 (3% MeOH in DCM).

^{1}H NMR (400 MHz, DMSO-d6) δ 11.20 (s, 1H, 7), 11.11 (s, 1H, 8), 7.69 – 7.63 (m, 1H, 2), 7.33 (d, J = 7.2 Hz, 1H, 3), 7.26 (d, J = 8.3 Hz, 1H, 1), 5.08 (dd, J = 12.8, 5.4 Hz, 1H, 4), 2.96 –2.82 (m, 1H, 5a), 2.65 – 2.53 (m, 2H, 6), 2.02 (d, J = 10.5 Hz, 1H, 5b). This compound is known. ^{1}H NMR data is consistent with previous reports.[337]

2
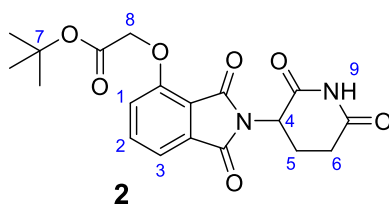
Tert-butyl 2-((2-(2,6-dioxopiperidin-3-yl)-1,3-dioxoisoindolin-4-yl)oxy)acetate (2)

4-hydroxythalidomide **1** (1.43 g, 5.21 mmol) was dissolved in DMF (20 ml) and was added potassium carbonate (1.08 g, 7,82 mmol). After addition of tert-butyl bromoacetate (0.847 ml, 5.73 mmol), the solution obtained was stirred at 50˚C for 4 h. The completion of the reaction was monitored by TLC; the crude was then partitioned between water (30 ml) and ethyl acetate (30 ml). The aqueous layer was further extracted with ethyl acetate thrice (3 x 10 ml). The combined organic layer was washed three times with water (3 x 20 ml) and brine (20 ml). It was then dried over sodium sulfate, filtered, and concentrated in vacuo to give a sticky colorless solid. Trituration

in DCM/n-hexane (50:50) gave a white solid which was further dried under vacuum (1.96 g, 97%). Rf = 0.40 (3% MeOH in DCM).

¹H NMR (400 MHz, DMSO-d_6) δ 11.13 (s, 1H, 9), 7.85 – 7.74 (m, 1H, 2), 7.49 (d, J = 7.2 Hz, 1H, 3), 7.39 (d, J = 8.5 Hz, 1H, 1), 5.11 (dd, J = 12.8, 5.4 Hz, 1H, 4), 4.98 (s, 2H, 8), 3.15 – 3.03 (m, 1H, 6a), 2.96 – 2.80 (m, 1H, 6b), 2.65 – 2.54 (m, 1H, 5a), 2.08 – 2.00 (m, 1H, 5b), 1.43 (s, 9H, 7). **¹³C NMR** (101 MHz, DMSO-d_6) δ 173.26, 170.37, 167.60, 167.18, 165.59, 155.49, 137.23, 133.71, 120.41, 116.89, 116.36, 82.38, 65.95, 49.26, 31.42, 28.14, 22.43. **HRMS** (ESI) m/z: calculated for C19H20N2O7$^+$, 388.2620; found 406.1615 (NH4 adduct). This compound is known. ¹H NMR data is consistent with previous reports.[337]

3
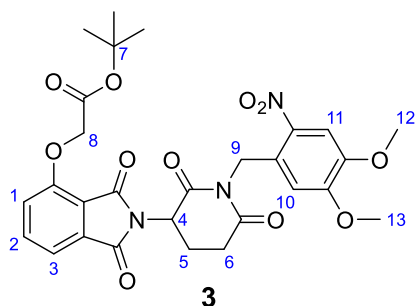
Tert-butyl 2-((2-(1-(4,5-dimethoxy-2-nitrobenzyl)-2,6-dioxopiperidin-3-yl)-1,3-dioxoisoindolin-4-yl)oxy)acetate (3)

In a pre-dried round bottom flask, intermediate **2** (295 mg, 0.76 mmol) was added followed by sodium hydride (60% dispersion) (45.6 mg, 1.14 mmol). The flask was capped with a septum and placed under nitrogen. Anhydrous DMF was added (10 ml) under Argon. After 30 mins, a solution of 4,5-dimethoxy-2-nitrobenzyl methanesulfonate (243 mg, 0.836 mmol) in anhydrous DMF was added. The mixture was stirred at 75°C for 3 h30. The reaction mixture was diluted with water (10 ml) and extracted with ethyl acetate (15 ml). The aqueous layer was further extracted with ethyl acetate thrice (3 x 10 ml).The combined organic layer was washed with water (3 x 10 ml) and brine (15 ml), dried over Na2SO4, filtered, and concentrated in vacuo. The residue recovered was purified by flash chromatography on silica gel (cyclohexane: ethyl acetate = 9:1 to 1:9) to afford **3** as a beige solid (120 mg, 27%). Rf = 0.5 (ethyl acetate: cyclohexane 8:1).

¹H NMR (400 MHz, DMSO-d_6) δ 7.81 (t, J = 7.9 Hz, 1H, 2), 7.66 (s, 1H, 11), 7.49 (d, J = 7.2 Hz, 1H, 3), 7.39 (d, J = 8.5 Hz, 1H, 1), 6.74 (s, 1H, 10), 5.34 (dd, J = 12.9, 5.5 Hz, 1H, 4), 5.24 – 5.08 (m, 2H, 8), 4.97 (s, 2H, 9), 4.01 (s, 3H, 13), 3.87 (s, 3H, 12), 3.35 (s, 1H), 3.14 – 3.01 (m, 1H, 6a), 2.92 – 2.83 (m, 1H, 6b), 2.66 (qd, J = 13.4, 4.5 Hz, 1H, 5a), 2.22 – 2.13 (m, 1H, 5b), 1.43 (s, 9H, 7). **¹³C NMR** (101 MHz, DMSO-d_6) δ 172.27, 170.39, 167.54, 167.16, 165.61, 155.54, 153.92, 147.82, 140.54, 137.34, 133.63, 127.29, 120.54, 116.82, 116.47, 109.21, 108.63, 82.38, 66.00, 56.66, 49.84, 31.57, 28.13, 21.66. **HRMS** (ESI) m/z: calculated for C28H29N3O11$^+$, 583.1800; found 601.2106 (NH4 adduct).
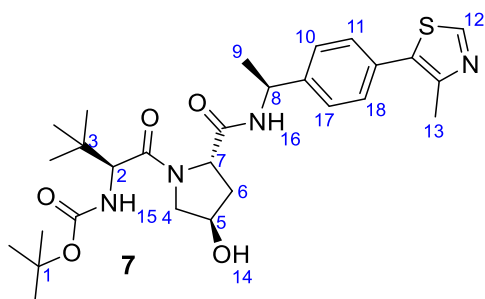
***tert-butyl((S)-1-((2S,4R)-4-hydroxy-2-(((S)-1-(4-(4-methylthiazol-5
yl)phenyl)ethyl)carbamoyl)pyrrolidin-1-yl)-3,3-dimethyl-1-oxobutan-2-yl)carbamate (7)***

Amine **6** (hydrochloride salt, 400 mg, 0.90 mmol, 1.0 eq) was dissolved in DCM (5 ml) and triethylamine (0.57 ml, 4.04 mmol, 4.5 eq) was added. A solution of di-*tert*-butyl dicarbonate (340 mg, 1.56 mmol, 1.75 eq) in DCM (5 ml) was then slowly added to the amine and the mixture was stirred at room temperature for 16 h. The crude mixture was subsequently washed with water (3 x 3 ml). The recovered organic layer was dried over sodium sulfate, filtered, and concentrated in vacuo to afford **7** as a white solid (377 mg, 77%). Rf = 0.3 (100% ethyl acetate)

^{1}H NMR (400 MHz, DMSO-d_6) δ 8.98 (s, 1H, 12), 8.40 (d, J = 7.7 Hz, 1H, NH16), 7.43 (d, J = 8.4 Hz, 2H, 11, 18), 7.37 (d, J = 8.4 Hz, 2H, 10, 17), 6.40 (d, J = 9.3 Hz, 1H, 8), 5.11 (d, J = 3.6 Hz, 1H), 4.90 (t, J = 7.2 Hz, 1H, 7), 4.45 (t, J = 8.1 Hz, 1H, 5), 4.28 (br.s, 1H, 14), 4.14 (d, J = 9.3 Hz, 1H, 2), 3.66 – 3.49 (m, 2H, 4), 2.45 (s, 3H, 13), 2.03 (ddd, J = 11.5, 8.0, 3.0 Hz, 1H, 6a), 1.84 – 1.72 (m, 1H, 6b), 1.44 – 1.31 (m, 12H, 1 and 9), 0.93 (s, 9H, 3). **^{13}C NMR** (101 MHz, DMSO-d_6) δ 171.05, 170.15, 155.79, 151.93, 148.21, 145.21, 131.58, 130.13, 129.28, 126.79, 78.56, 69.25, 58.99, 58.88, 56.74, 48.20, 40.63, 38.18, 35.83, 28.66, 27.82, 26.80, 26.69, 22.96, 16.46. **MS** (ESI) *m/z* 545 (M+H)$^+$. **HRMS** (ESI) m/z: calculated for C28H41N4O5S$^+$, 545.2798; found 545.2798.

9
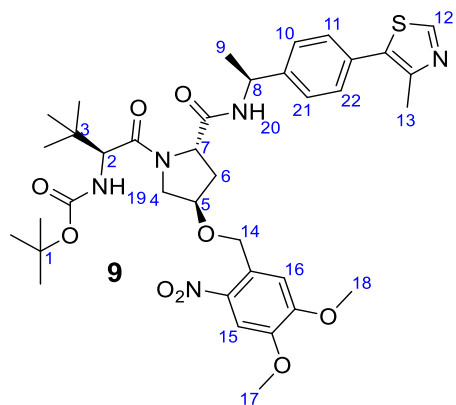
tert-butyl((S)-1-((2S,4R)-4-((4,5-dimethoxy-2-nitrobenzyl)oxy)-2-(((S)-1-(4-(4-methylthiazol-5 yl)phenyl)ethyl)carbamoyl) pyrrolidin-1-yl)-3,3-dimethyl-1-oxobutan-2-yl)carbamate (9).

Intermediate **7** (160 mg, 0.29 mmol, 1.0 eq) and tetrabutylammonium iodide (22 mg, 0.059 mmol, 0.2 eq) were dissolved in DCM (8 ml). 4,5-Dimethoxy-2-nitrobenzyl bromide (89 mg, 0.32 mmol, 1.1 eq) was then added followed by aqueous sodium hydroxide 50% (2 ml). The biphasic mixture was stirred at room temperature and was protected from ambient light (fume cupboard lights off). Completion of the reaction was monitored by TLC. After 2 h, the aqueous layer (bottom layer) was removed with a pipette and the remaining organic layer was washed with water (5 x 6 ml). The recovered organic layer was dried over sodium sulfate, filtered, and concentrated in vacuo. The residue recovered was then purified by silica gel flash chromatography (40-80% ethyl acetate in n-hexane) to afford **9** as a pale-yellow solid (116 mg, 53%). Rf = 0.5 (100% ethyl acetate).

¹H NMR (400 MHz, Chloroform-*d*) δ 8.69 (s, 1H, 12), 7.69 (s, 1H, 15), 7.45 – 7.34 (m, 4H, 10, 11, 21, 22), 7.18 (s, 1H, 16), 5.23 (d, *J* = 9.8 Hz, 1H, 8), 5.10 – 5.02 (m, 1H, 7), 4.94 (s, 2H, 14), 4.76 (dd, *J* = 8.2, 6.0 Hz, 1H, 5), 4.44 (t, *J* = 4.5 Hz, 1H), 4.34 (d, *J* = 9.7 Hz, 1H, 2), 4.27 – 4.21 (m, 1H), 4.13 (dd, *J* = 11.2, 3.4 Hz, 1H), 3.97 (s, 3H, 17), 3.94 (s, 3H, 18), 3.75 (dd, *J* = 11.0, 4.9 Hz, 1H), 3.71 – 3.66 (m, 1H), 3.64 (s, 1H), 2.71 (dt, *J* = 13.1, 5.5 Hz, 1H), 2.53 (s, 3H, 13), 2.16 (ddd, *J* = 12.9, 8.2, 4.4 Hz, 1H), 1.78 (br.s, 2H), 1.67 – 1.51 (m, 1H), 1.47 (d, *J* = 6.8 Hz, 3H, 9), 1.33 (s, 9H, 1), 1.29 – 1.23 (m, 1H), 1.03 (s, 9H, 3). **¹³C NMR** (101 MHz, Chloroform-*d*) δ 172.86, 169.30, 155.55, 153.75, 150.34, 147.62, 143.07, 139.04, 130.91, 130.23, 129.61, 126.46, 109.38, 107.88, 79.73, 76.72, 70.55, 69.35, 67.94, 63.04, 58.62, 58.53, 56.48, 56.37, 53.17, 48.98, 47.19, 35.71, 32.55, 31.73, 29.58, 28.19, 26.39, 25.45, 22.64, 22.21, 16.06, 13.97, 11.81. **MS** (ESI) *m/z* 740 (M+H)⁺. **HRMS** (ESI) m/z: calculated for C37H50N5O9S⁺, 740.3329; found 740.3329.

10
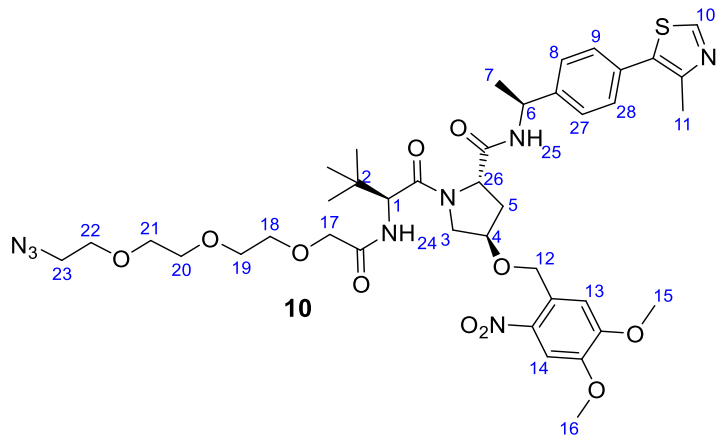
(2S,4R)-1-((S)-14-azido-2-(tert-butyl)-4-oxo-6,9,12-trioxa-3-azatetradecanoyl)-4-((4,5-dimethoxy-2-nitrobenzyl)oxy)-N-((S)-1-(4-(4-methylthiazol-5-yl)phenyl)ethyl)pyrrolidine-2-carboxamide (10)

2-(2-(2-(2-azidoethoxy)ethoxy)ethoxy)acetic acid (10 mg, 0.043 mmol, 1.2 eq) was dissolved in DCM (3 ml) along with HATU (17 mg, 0.044 mmol, 1.3 eq) and DIPEA (0.17 mmol, 29 μl, 5.0 eq). The Boc deprotected **9** (hydrochloride salt, 25 mg, 0.034 mmol, 1.0 eq) was then added and the solution obtained was stirred at room temperature for 16 h (fume cupboard lights off). The reaction mixture was subsequently washed twice with water (2 x 3 ml). The recovered organic layer was dried over sodium sulfate, filtered, and concentrated in vacuo. The residue was purified by silica gel flash chromatography (30-90% ethyl acetate in n-hexane) to afford **10** as a beige solid (12 mg, 41%). R*f* = 0.4 (100% ethyl acetate).

¹H NMR (400 MHz, Chloroform-*d*) δ 8.74 (s, 1H, 10), 7.69 (s, 1H, 14), 7.41 (d, *J* = 8.7 Hz, 2H, 9, 28), 7.37 (d, *J* = 8.3 Hz, 2H, 8, 27), 7.30 (d, *J* = 7.7 Hz, 1H), 7.18 (s, 1H, 13), 5.12 – 5.00 (m, 1H, 26), 4.91 (q, *J* = 13.6 Hz, 2H, 12), 4.77 – 4.67 (m, 2H), 4.45 (t, *J* = 4.4 Hz, 1H), 4.15 (dd, *J* = 10.8, 3.5 Hz, 1H), 4.01 (d, *J* = 15.5 Hz, 1H), 3.97 (s, 3H, 16), 3.94 (s, 3H, 15), 3.88 (d, *J* = 15.5 Hz, 1H), 3.78 (dd, *J* = 11.0, 4.9 Hz, 1H), 3.72 – 3.64 (m, 10H, 18, 19, 20, 21, 22), 3.39 (t, *J* = 3.9 Hz, 2H), 2.80 (s, 2H, 17), 2.71 – 2.60 (m, 1H), 2.54 (s, 3H, 11), 2.17 (ddd, *J* = 11.0, 8.3, 4.3 Hz, 1H), 1.99 – 1.87 (m, 4H), 1.48 (d, *J* = 7.5 Hz, 3H, 7), 1.06 (s, 9H, 2). **¹³C NMR** (101 MHz, Chloroform-*d*) δ 171.71, 169.56, 169.42, 153.76, 150.60, 147.68, 143.25, 139.14, 130.01, 129.60, 126.50, 109.74, 107.92, 71.07, 70.67, 70.47, 70.30, 70.02, 68.07, 58.63, 56.56, 56.50, 56.37, 53.28, 50.68, 48.96, 38.63, 35.68, 32.63, 26.45, 22.16, 15.89. **MS** (ESI) *m/z* 855 (M+H)⁺. **HRMS** (ESI) m/z: calculated for $C_{40}H_{54}N_8O_{11}NaS^+$ (Na adduct), 877.3530; found 877.3550.
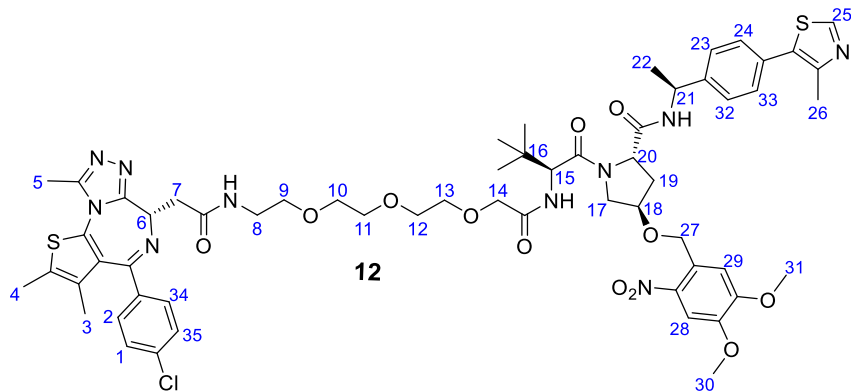
12

(2S,4R)-1-((S)-2-(tert-butyl)-17-((S)-4-(4-chlorophenyl)-2,3,9-trimethyl-6H-thieno[3,2-f][1,2,4]triazolo[4,3-a][1,4]diazepin-6-yl)-4,16-dioxo-6,9,12-trioxa-3,15-diazaheptadecanoyl)-4-((4,5-dimethoxy-2-nitrobenzyl)oxy)-N-((S)-1-(4-(4-methylthiazol-5-yl)phenyl)ethyl)pyrrolidine-2-carboxamide (12)

Intermediate **10** (10 mg, 0.012 mmol, 1.0 eq) was dissolved in MeOH (2 ml) and triphenylphosphine (4 mg, 0.015 mmol, 1.25 eq) was added. The solution obtained was stirred at 50°C for 8 h under N_2. The crude mixture was then concentrated in vacuo and the residue redissolved in DCM (3 ml) along with HATU (6 mg, 0.016 mmol, 1.3 eq) and DIPEA (0.024 mmol, 4.2 μl, 2.0 eq). JQ1-COOH (5 mg, 0.012 mmol, 1.0 eq) was then added and the solution obtained was stirred at room temperature for 16 h (fume cupboard lights off). The reaction mixture was subsequently washed twice with water (2 x 3 ml). The recovered organic layer was dried over sodium sulfate, filtered, and concentrated in vacuo. The residue was purified by preparative HPLC (20-98% acetonitrile in water with 0.1% formic acid) to afford **12** as a white solid (6 mg, 41% over 2 steps). Rf = 0.45 (5% MeOH in DCM).

¹H NMR (400 MHz, Chloroform-*d*) δ 8.71 (s, 1H, 25), 7.73 – 7.58 (m, 2H, NH?), 7.44 – 7.29 (m, 9H, 1, 2, 23, 24, 28, 32, 33, 34, 35), 7.17 (s, 1H, 29), 5.12 – 5.02 (m, 1H, 20), 4.87 (d, *J* = 1.3 Hz, 2H, 27), 4.84 – 4.78 (m, 1H), 4.72 (d, *J* = 9.4 Hz, 1H), 4.44 – 4.37 (m, 1H), 4.19 (d, *J* = 11.6 Hz, 1H), 4.09 (d, *J* = 15.6 Hz, 1H), 4.00 – 3.94 (m, 4H, includes 30), 3.93 (s, 3H, 31), 3.82 (dd, *J* = 11.0, 4.7 Hz, 1H), 3.75 – 3.63 (m, 8H, 10, 11, 12, 13), 3.61 – 3.55 (m, 2H), 3.51 – 3.41 (m, 4H), 2.66 (s, 3H, 5), 2.52 (s, 4H, includes 26), 2.40 (s, 3H, 4), 2.27 (td, *J* = 10.3, 9.2, 4.9 Hz, 1H), 1.67 (s, 3H, 3), 1.45 (d, *J* = 7.0 Hz, 3H, 22), 1.08 (s, 9H, 16). **¹³C NMR** (101 MHz, Chloroform-*d*) δ 171.37, 170.61, 169.87, 169.82, 155.45, 153.77, 150.35, 149.98, 148.03, 147.62, 143.51, 139.06, 131.23, 130.44, 130.10, 130.04, 129.47, 128.79, 126.50, 109.75, 107.87, 70.90, 70.62, 70.58, 70.42, 70.30, 69.86, 67.94, 58.75, 56.62, 56.56, 56.34, 54.05, 53.49, 48.91, 39.54, 35.62, 33.25, 26.49, 22.15, 15.91, 14.42, 13.14, 11.77. **MS** (ESI) *m/z* 1211 (M+H)⁺. **HRMS** (ESI) m/z: calculated for C59H72N10O12S2Cl⁺, 1211.4461; found 1211.4481.
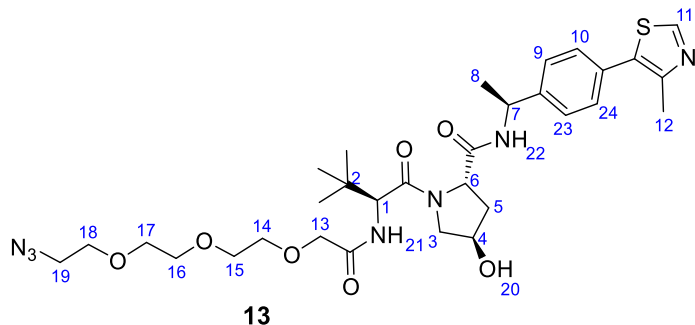
13

(2S,4R)-1-((S)-14-azido-2-(tert-butyl)-4-oxo-6,9,12-trioxa-3-azatetradecanoyl)-4-hydroxy-N-((S)-1-(4-(4-methylthiazol-5-yl)phenyl)ethyl)pyrrolidine-2-carboxamide (13)

2-(2-(2-(2-azidoethoxy)ethoxy)ethoxy)acetic acid (26 mg, 0.112 mmol, 1.0 eq) was dissolved in DCM (3 ml) along with HATU (55 mg, 0.15 mmol, 1.3 eq) and DIPEA (0.45 mmol, 76 µl, 4.0 eq). The amine **6** (hydrochloride salt, 50 mg, 0.11 mmol, 1.0 eq) was then added and the solution obtained was stirred at room temperature for 16 h. The reaction mixture was subsequently washed twice with water (2 x 3 ml). The recovered organic layer was dried over sodium sulfate, filtered, and concentrated in vacuo. The residue was purified by silica gel flash chromatography (2-10% MeOH in DCM) to afford **13** as a white solid (26.5 mg, 36 %). Rf = 0.3 (100% ethyl acetate).

^{1}H NMR (400 MHz, Chloroform-*d*) δ 8.70 (s, 1H, 11), 7.50 (d, *J* = 7.8 Hz, 1H, NH), 7.45 – 7.33 (m, 5H, 9, 10, 23, 24 and NH), 5.13 – 5.07 (m, 1H, 7), 4.76 (t, *J* = 7.8 Hz, 1H, 6), 4.56 (d, *J* = 8.6 Hz, 1H, 1), 4.53 (br.s, 1H, 20), 4.14 – 4.08 (m, 1H, 4), 4.04 (d, *J* = 5.4 Hz, 2H, 13), 3.73 – 3.69 (m, 8H, 14, 15, 16, 17), 3.69 – 3.66 (m, 2H, 3), 3.63 (dd, *J* = 11.3, 3.8 Hz, 1H, 19), 3.40 (dd, *J* = 5.6, 4.5 Hz, 2H, 18), 2.60 – 2.50 (m, 4H, includes 12 and 5), 2.07 (ddt, *J* = 13.5, 8.3, 1.9 Hz, 1H, includes 5), 1.50 (d, *J* = 7.0 Hz, 3H, 8), 1.09 (s, 9H, 2). **^{13}C NMR** (101 MHz, Chloroform-*d*) δ 171.57, 170.56, 169.64, 150.31, 148.45, 143.19, 131.62, 130.85, 129.56, 126.43, 71.17, 70.71, 70.55, 70.35, 70.07, 58.35, 57.20, 56.59, 50.69, 48.87, 35.37, 35.00, 26.49, 22.27, 16.08. **MS** (ESI) *m/z* 660 (M+H)$^+$. **HRMS** (ESI) m/z: calculated for C31H46N7O7S$^+$, 660.3179; found 660.3181.
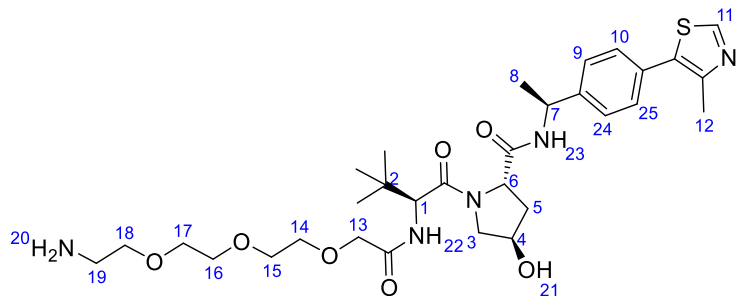
14

(2S,4R)-1-((S)-14-amino-2-(tert-butyl)-4-oxo-6,9,12-trioxa-3-azatetradecanoyl)-4-hydroxy-N-((S)-1-(4-(4-methylthiazol-5-yl)phenyl)ethyl)pyrrolidine-2-carboxamide (14)

The azide **13** (145 mg, 0.22 mmol) was dissolved in ethanol (5 ml) and was added palladium 10% on carbon (14.5 mg, 10% w/w). After 3 cycles of degassing and purging with nitrogen gas, the solution was placed under hydrogen gas for 3 h at room temperature. It was then filtered over celite, and the recovered solution concentrated in vacuo and further dried under high vacuum to give a sticky colorless gum (96 mg, 70%).

^{1}H NMR (400 MHz, Chloroform-*d*) δ 8.70 (s, 1H, 11), 8.57 (d, *J* = 7.9 Hz, 1H, NH), 7.49 – 7.33 (m, 5H, 9, 10, 24, 25, NH), 5.20 – 5.06 (m, 1H, 7), 4.78 (t, *J* = 8.6 Hz, 1H, 6), 4.72 (d, *J* = 9.6 Hz, 1H, 1), 4.43 (s, 1H), 4.21 (d, *J* = 15.6 Hz, 1H, 4), 4.08 – 3.95 (m, 2H, 13), 3.90 – 3.56 (m, 12H, 14, 15, 16, 17, 18, 19), 3.40 – 3.11 (m, 1H), 2.55 (s, 3H, 12), 2.29 (dd, *J* = 13.4, 7.5 Hz, 1H, 5b), 2.08 – 1.92 (m, 1H, 5a), 1.52 (d, *J* = 7.0 Hz, 3H, 8), 1.08 (s, 9H, 2). **^{13}C NMR** (101 MHz, Chloroform-*d*) δ 171.19, 170.46, 170.15, 150.16, 148.36, 143.91, 131.79, 130.47, 129.43, 126.38, 70.59, 70.27, 69.92, 69.84, 69.53, 66.55, 59.09, 57.24, 56.82, 48.84, 39.95, 37.68, 36.08, 26.45, 22.59, 16.11. **MS** (ESI) *m/z* 634 (M+H)$^+$. **HRMS** (ESI) m/z: calculated for C31H48N5O7S$^+$, 634.3274; found 634.3274.
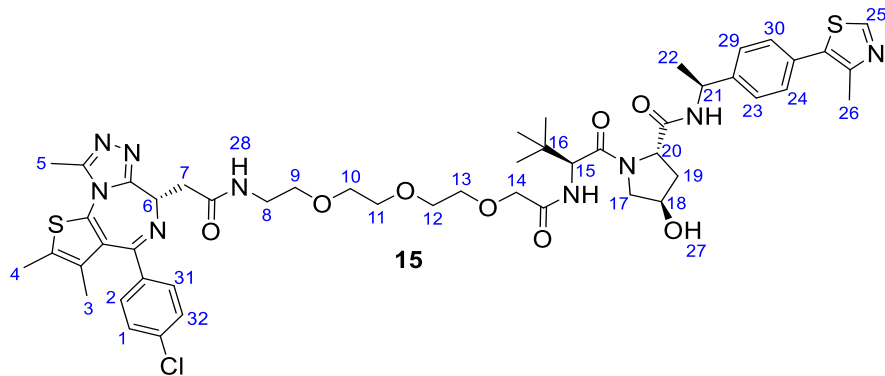
(2S,4R)-1-((S)-2-(tert-butyl)-17-((S)-4-(4-chlorophenyl)-2,3,9-trimethyl-6H-thieno[3,2-f][1,2,4]triazolo[4,3-a][1,4]diazepin-6-yl)-4,16-dioxo-6,9,12-trioxa-3,15-diazaheptadecanoyl)-4-hydroxy-N-((S)-1-(4-(4-methylthiazol-5-yl)phenyl)ethyl)pyrrolidine-2-carboxamide (15)

JQ1 carboxylic acid (JQ1-COOH, 24 mg, 0.06 mmol, 1.0 eq) was dissolved in DCM (4 ml) along with HATU (30 mg, 0.078 mmol, 1.3 eq) and DIPEA (20 μl, 0.12 mmol, 2.0 eq). The amine **14** (38 mg, 0.06 mmol, 1.0 eq) was then added and the solution obtained was stirred at room temperature for 16 h. The reaction mixture was subsequently washed twice with water (2 x 3 ml). The recovered organic layer was dried over sodium sulfate, filtered, and concentrated in vacuo. The residue recovered was purified by silica gel flash chromatography (2-8% MeOH in DCM) to afford 1**5** as a white solid (33 mg, 54%).). R*f* = 0.35 (5% MeOH in DCM).

¹H NMR (500 MHz, Chloroform-*d*) δ 8.68 (s, 1H, 25), 7.97 (t, *J* = 5.6 Hz, 1H, 28), 7.45 (d, *J* = 7.8 Hz, 1H, NH), 7.43 – 7.28 (m, 9H, 1, 2, 23, 24, 29, 30, 31, 32, NH), 5.13 – 5.03 (m, 1H, 20), 4.82 (t, *J* = 7.8 Hz, 1H, 6), 4.73 (d, *J* = 9.3 Hz, 1H, 15), 4.68 (dd, *J* = 8.8, 5.2 Hz, 1H, 21), 4.44 (br.s, 1H), 4.35 (d, *J* = 15.9 Hz, 1H), 4.15 (d, *J* = 15.9 Hz, 1H), 4.11 (br.s, 1H, 27), 3.77 – 3.59 (m, 10H, 9, 10, 11, 12, 13), 3.58 – 3.49 (m, 2H, 8), 3.39 – 3.31 (m, 2H), 2.63 (s, 3H, 5), 2.52 (s, 3H, 4), 2.49 – 2.42 (m, 1H), 2.39 (s, 3H, 26), 2.12 – 2.05 (m, 1H), 1.67 (s, 3H, 3), 1.46 (d, *J* = 6.9 Hz, 3H, 22), 1.07 (s, 9H, 16). **¹³C NMR** (126 MHz, Chloroform-*d*) δ 171.40, 170.94, 170.85, 170.04, 163.81, 162.16, 155.82, 150.29, 149.78, 148.33, 143.34, 136.70, 136.49, 131.80, 131.70, 131.06, 130.92, 130.76, 130.64, 129.97, 129.48, 128.70, 127.90, 126.44, 77.00, 71.72, 70.83, 70.49, 70.30, 70.11, 69.87, 58.62, 56.99, 56.69, 54.10, 48.76, 39.78, 38.05, 35.62, 35.49, 26.48, 22.19, 16.02, 14.43, 13.10, 11.73. **MS** (ESI) *m/z* 1016 (M+H)⁺. **HRMS** (ESI) m/z: calculated for C₅₀H₆₃N₉O₈S₂Cl⁺, 1016.3930; found 1016.3928.
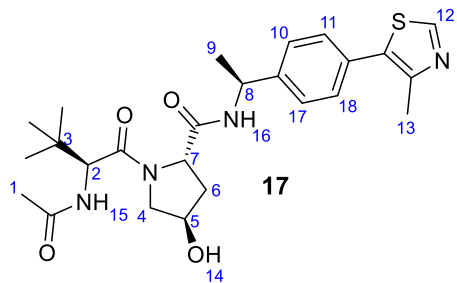
(2S,4R)-1-((S)-2-acetamido-3,3-dimethylbutanoyl)-4-hydroxy-N-((S)-1-(4-(4-methylthiazol-5-yl)phenyl)ethyl)pyrrolidine-2-carboxamide (17). Acetylation was performed according to a reported procedure.[338] Amine **6** (hydrochloride salt, 50 mg, 0.11 mmol, 1.0 eq) was dissolved in DCM (5 ml) and triethylamine (0.063 ml, 0.44 mmol, 4.0 eq) was added followed by acetic anhydride (0.016 ml, 0.17 mmol, 1.5 eq). The mixture was stirred at room temperature for 3 h and was subsequently washed with water (3 x 3 ml). The recovered organic layer was dried over sodium sulfate, filtered, and concentrated in vacuo. The residue obtained was then purified by silica gel flash chromatography (60-90% ethyl acetate in n-hexane) to afford **17** as a white solid (35 mg, 65%). %). Rf = 0.4 (80% ethyl acetate in cyclohexane).

¹H NMR (400 MHz, Chloroform-d) δ 8.71 (s, 1H, 12), 7.49 (d, J = 7.9 Hz, 1H, 15), 7.46 – 7.36 (m, 4H, 10, 11, 17, 18), 6.30 (d, J = 8.8 Hz, 1H, 16), 5.16 – 5.05 (m, 1H, 8), 4.71 (t, J = 8.0 Hz, 1H, 7), 4.57 (d, J = 8.9 Hz, 1H, 2), 4.52 (br.s, 1H, 14), 4.09 (dt, J = 11.5, 1.8 Hz, 1H, 5), 3.62 (dd, J = 11.4, 3.7 Hz, 1H, 4a), 2.55 (s, 3H, 13), 2.48 (ddd, J = 13.0, 7.9, 4.6 Hz, 1H, 6a), 2.09 (ddt, J = 13.5, 8.0, 1.9 Hz, 1H, 6b), 2.00 (s, 3H, 1), 1.50 (d, J = 7.0 Hz, 3H, 9), 1.06 (s, 9H, 3). **¹³C NMR** (101 MHz, Chloroform-d) δ 171.94, 170.85, 169.73, 150.37, 148.41, 143.18, 131.61, 130.87, 129.58, 126.48, 70.00, 58.59, 57.72, 56.78, 48.84, 35.59, 35.09, 26.49, 23.09, 22.17, 16.05. **MS** (ESI) m/z 487 (M+H)$^+$. **HRMS** (ESI) m/z: calculated for C25H35N4O4S$^+$, 487.2379; found 487.2367.   .

27
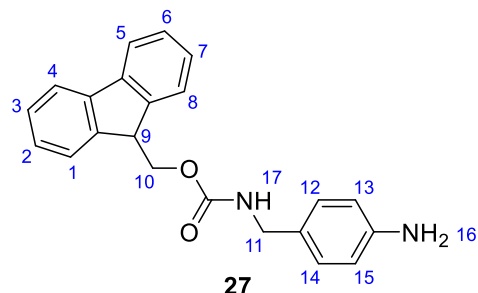
(9H-fluoren-9-yl)methyl (4-aminobenzyl)carbamate (27)

4-(aminomethyl)aniline (1.39 ml, 12,27 mmol) was dissolved in DCM (80 ml) and DIPEA (2.14 ml, 12.27 mmol) was added. The solution was cooled down to 0˚C. A solution of 9-Fluorenylmethyl-succinimidyl carbonate (4,14 g, 12.27 mmol) in DCM (30 ml) was prepared and was slowly added to the amine. A precipitate started forming. Upon completion of the addition of Fmoc-O-Su, the mixture was brought to room temperature and was stirred for 16 h. The resulting milky solution was added water (80 ml). The org layer was recovered and adsorbed onto silica. Purification using a gradient cyclohexane: ethylacetate = 7:3 to 2:8 afforded **27** as a beige solid (3.5 g, 83%).

¹H NMR (400 MHz, Chloroform-*d*) δ 7.76 (d, *J* = 7.5 Hz, 2H, 4, 5), 7.59 (d, *J* = 7.5 Hz, 2H, 1, 8), 7.40 (t, *J* = 7.5 Hz, 2H, 2, 7), 7.31 (t, J = 7.5 Hz, 2H, 3, 6), 7.07 (d, *J* = 7.8 Hz, 2H, 12, 14), 6.65 (d, *J* = 7.8 Hz, 2H, 13, 15), 4.97 (s, 1H, 9), 4.44 (s, 2H, 16), 4.26 (d, *J* = 5.8 Hz, 2H, 10), 3.66 (s, 2H, 11). **¹³C NMR** (101 MHz, Chloroform-*d*) δ 156.32, 145.88, 143.98, 141.33, 128.99, 128.23, 127.66, 127.04, 125.07, 119.98, 115.22, 77.36, 77.04, 76.72, 66.62, 47.31, 44.80. **HRMS** (ESI) m/z: calculated for $C_{22}H_{20}N_2O_2{}^+$, 345.1603; found 345.1590.

28
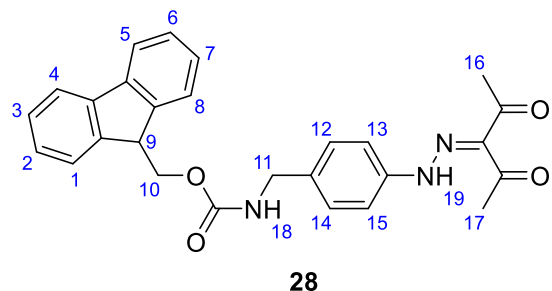
(9H-fluoren-9-yl)methyl (4-(2-(2,4-dioxopentan-3-ylidene)hydrazineyl)benzyl)carbamate (28)

Aniline **27** (500 mg, 1.45 mmol) was dissolved in acetic acid (5 ml) and 1.4 ml of HCl (37%). A solution of sodium nitrite (200 mg, 2.90 mmol) in water (2 ml) was then added at 0˚C to the aniline to form the diazonium salt. The yellow solution obtained was stirred at 0˚C for 1 h. At this stage, in another flask, acetylacetone (0.193 ml, 1.88 mmol) was dissolved in ethanol (5 ml) along with sodium acetate (476 mg, 5.81 mmol). That solution was cooled in an ice bath and was added the diazonium salt. A bright yellow solution was obtained. It was stirred from 0˚C to room temperature for 3 h. The crude solution was added ethyl acetate (20 ml) and was washed with sodium bicarbonate (1M) and brine. A yellow precipitate was recovered from the aqueous layer (25 mg) and was added to the organic layer. The organic layer was dried over Na_2SO_4, filtered, and concentrated in vacuo to yield an orange solid (550 mg, 85%). Rf = 0.7 (80% ethyl acetate in cyclohexane).

¹H NMR (400 MHz, DMSO-d_6) δ 14.11 (s, 1H, 19), 7.93 – 7.81 (m, 3H, 4, 5, 18), 7.70 (d, J = 7.4 Hz, 2H, 1, 8), 7.53 (d, J = 8.2 Hz, 2H, 12, 14), 7.42 (t, J = 7.5 Hz, 2H, 2, 7), 7.33 (t, J = 7.4 Hz, 2H, 3, 6), 7.26 (d, J = 8.2 Hz, 2H, 13, 15), 4.37 (d, J = 6.8 Hz, 2H, 10), 4.23 (t, J = 6.8 Hz, 1H, 9), 4.17 (d, J = 6.1 Hz, 2H, 11), 2.48 (s, 3H, 16), 2.42 (s, 3H, 17). **¹³C NMR** (101 MHz, DMSO-d_6) δ 196.60, 196.23, 156.35, 143.88, 140.78, 140.58, 137.09, 133.18, 128.24, 127.60, 127.05, 125.15, 120.13, 116.30, 65.26, 46.82, 43.29, 31.21, 26.40. **HRMS** (ESI) m/z: calculated for $C_{27}H_{25}N_3O_4^+$, 456.1923; found 456.1919.

30
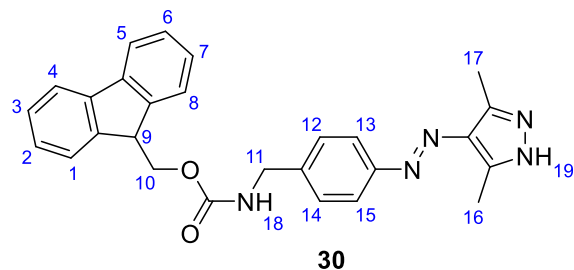
(9H-fluoren-9-yl)methyl (E)-(4-((3,5-dimethyl-1H-pyrazol-4-yl)diazenyl)benzyl)carbamate (30)

The diketone **28** (150 mg, 0.329 mmol) was dissolved in DCM (2.5 ml) and methanol (7.5 ml) in a 50 ml round bottom flask. Hydrazino (0.034 ml, 0.493 mmol) was then added, and the mixture was stirred at 50˚C for 2 h. Completion of the reaction was monitored by TLC. The crude mixture was then partitioned between DCM (5 ml) and aq. HCl (1M) (5 ml). The organic layer was recovered and further washed with aq. HCl (1M) (5 ml). After drying over Na_2SO_4, it was filtered and concentrated in vacuo to yield an orange solid (163 mg, 100%). Rf = 0.4 (80% ethyl acetate in cyclohexane).

^{1}H NMR (500 MHz, Chloroform-d) δ 7.81 – 7.71 (m, 4H, 4, 5, 13, 15), 7.64 – 7.57 (m, 2H, 12, 14), 7.46 – 7.28 (m, 6H, 1, 2, 3, 6, 7, 8), 4.49 (d, J = 6.8 Hz, 2H, 10), 4.45 (d, J = 6.1 Hz, 2H, 11), 4.24 (t, J = 6.8 Hz, 1H, 9), 2.58 (s, 6H, 16, 17). *Only E isomer observed*. **^{13}C NMR** (126 MHz, Chloroform-d) δ 143.87, 141.33, 128.04, 127.68, 127.05, 124.99, 122.16, 119.98, 66.71, 47.30, 44.81, 29.70, 29.32. **HRMS** (ESI) m/z: calculated for $C27H25N5O2^+$, 452.2087; found 452.2069.

31
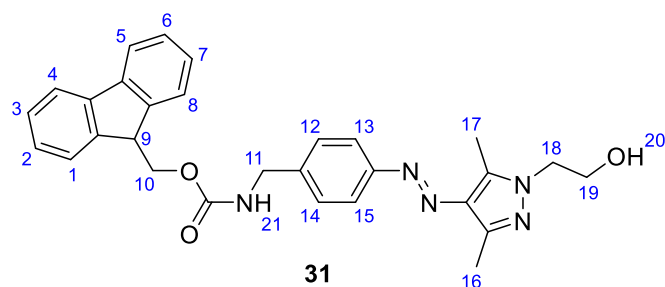
(9H-fluoren-9-yl)methyl (E)-(4-((1-(2-hydroxyethyl)-3,5-dimethyl-1H-pyrazol-4-yl)diazenyl)benzyl)carbamate (31)

The diketone **28** (150 mg, 0.329 mmol) was dissolved in DCM (2.5 ml) and methanol (7.5 ml) in a 50 ml round bottom flask. Hydrazinoethanol (0.034 ml, 0.493 mmol) was then added and the mixture was stirred at 50˚C for 2 h. Completion of the reaction was monitored by TLC. The crude mixture was then partitioned between DCM (5 ml) and aq. HCl (1M) (5 ml). The organic layer was recovered and further washed with aq. HCl (1M) (5 ml). After drying over Na_2SO_4, it was filtered and concentrated in vacuo to yield an orange solid (163 mg, 100%). Rf = 0.4 (90% ethyl acetate in cyclohexane).

1H NMR (400 MHz, Chloroform-*d*) δ 7.85 – 7.72 (m, 4H, 4, 5, 13, 15), 7.63 (d, *J* = 7.5 Hz, 2H, 12, 14), 7.50 – 7.31 (m, 6H, 1, 2, 3, 6, 7, 8), 5.15 (br.s, 1H, 9), 4.51 (d, *J* = 6.8 Hz, 2H, 10), 4.47 (d, *J* = 6.0 Hz, 2H, 11), 4.31 – 4.23 (m, 2H, 18), 4.09 (t, *J* = 4.9 Hz, 2H, 19), 2.65 (s, 3H, 17), 2.58 (s, 3H, 16). *Only E isomer observed.* **13C NMR** (101 MHz, Chloroform-*d*) δ 152.93, 144.01, 141.49, 128.22, 127.85, 127.20, 125.14, 122.40, 120.15, 61.44, 50.30, 47.46, 44.95, 30.73, 19.25, 13.88, 10.01. **MS** (ESI) *m/z* 496 (M+H)$^+$. **HRMS** (ESI) m/z: calculated for C29H29N5O3$^+$, 496.2349; found 496.234.

32
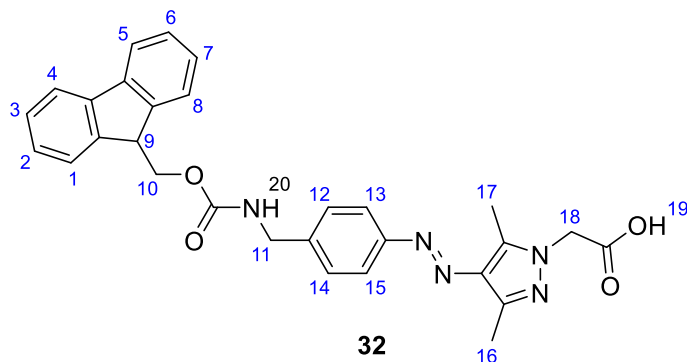
(E)-2-(4-((4-(((((9H-fluoren-9-yl)methoxy)carbonyl)amino)methyl)phenyl)diazenyl)-3,5-dimethyl-1H-pyrazol-1-yl)acetic acid (32)

The alcohol **31** (150 mg, 0.3 mmol) was dissolved in DMSO (4 ml) and was added Dess Martin reagent (381 mg, 0.9 mmol). The solution was stirred for 16 h at room temperature. A mixture of aldehyde and carboxylic acid was obtained at this stage; the cloudy mixture was added water (5 ml) and ethyl acetate (5 ml). The biphasic mixture was then filtered to remove the DMP by-product, and the organic layer was recovered. The aqueous layer was further extracted with ethyl acetate (5 ml). The combined organic layer was dried over Na2SO4, filtered, and concentrated in vacuo to yield an orange solid (73 mg of a mixture 2:1 aldehyde/carboxylic acid) which was re-dissolved in acetonitrile and water (2 ml each). Sodium chlorite (50 mg, 0.559 mmol), 2-methylbut-2-ene (0.1 ml, 0.93 mmol) and NaH2PO4 (55 mg, 0.93 mmol) were added. The solution was stirred for 16 h at room temperature. The crude was partitioned between water (5 ml) and ethyl acetate (5 ml). The aqueous layer was further extracted with ethyl acetate (5 ml). The combined organic layer was dried over Na2SO4, filtered, and concentrated in vacuo to yield an orange solid (60 mg, 40%). ^{1}H NMR (400 MHz, DMSO-*d$_6$*).

1H NMR (400 MHz, DMSO-*d$_6$*) δ 7.99 – 7.85 (m, 4H, 4, 5, 13, 15), 7.74 – 7.65 (m, 4H, 1, 8, 12, 14), 7.50 – 7.39 (m, 2H, 7, 2), 7.38 – 7.29 (m, 2H, 3, 6), 7.25 – 7.13 (m, *Z* isomer) 4.84 (s, 2H, 18), 4.81 (s, *Z* isomer, 18), 4.37 (d, *J* = 6.8 Hz, 2H, 10), 4.27 – 4.20 (m, 3H, 11, 9), 2.54 (s, 3H, 17) *partly under DMSO peak*, 2.37 (s, 3H, 16) *Ratio of 9:1 E vs Z isomer observed.* **13C NMR** (101 MHz, DMSO-*d$_6$*) δ 156.86, 152.49, 144.34, 141.75, 141.23, 140.78, 134.97, 132.49, 130.32, 128.54, 128.22, 128.08, 127.53, 125.63, 121.84, 120.59, 65.80, 51.65, 47.27, 43.98, 14.32, 9.92. **MS** (ESI) *m/z* 510 (M+H)$^+$. **HRMS** (ESI) m/z: calculated for C29H27N5O4$^+$, 510.2141; found 510.2128.

33
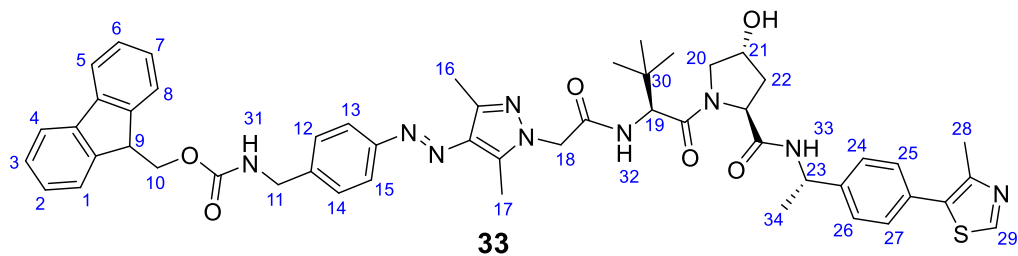
(9H-fluoren-9-yl)methyl (4-((E)-1-(2-(((S)-1-((2S,4R)-4-hydroxy-2-(((S)-1-(4-(4-methylthiazol-5-yl)phenyl)ethyl)carbamoyl)pyrrolidin-1-yl)-3,3-dimethyl-1-oxobutan-2-yl)amino)-2-oxoethyl)-3,5-dimethyl-1H-pyrazol-4-yl)diazenyl)benzyl)carbamate (33)

Carboxylic acid **32** (25 mg, 0.049 mmol, 1.0 eq) was dissolved in DCM (4 ml) along with HATU (24 mg, 0.063 mmol, 1.3 eq) and DIPEA (17 μl, 0.098 mmol, 2.0 eq). The amine **6** (hydrochloride salt, 23.5 mg, 0.049 mmol, 1.0 eq) was then added and the solution obtained was stirred at room temperature for 16 h. The reaction mixture was subsequently washed twice with water (2 x 3 ml). The recovered organic layer was dried over sodium sulfate, filtered, and concentrated in vacuo. The residue recovered was purified by silica gel flash chromatography (2-8% MeOH in DCM) to afford **33** as an orange solid (17 mg, 35%). Rf = 0.6 (5% MeOH in DCM).

^{1}H NMR (400 MHz, Chloroform-d) δ 8.66 (s, Z isomer, 29), 8.64 (s, 1H, 29), 7.81 – 7.70 (m, 4H, 4, 5, 13, 15), 7.60 (d, J = 7.5 Hz, 2H, 12, 14), 7.52 – 7.28 (m, 11H, 1, 2, 3, 6, 7, 8, 24, 25, 26, 27, 32), 5.06 (q, J = 7.3 Hz, 2H), 4.74 (d, J = 5.6 Hz, 2H, 10), 4.47 (d, J = 5.9 Hz, 2H, 11), 4.43 (d, Z isomer, 11), 4.27 – 4.19 (m, 1H), 4.04 (d, J = 11.4 Hz, 1H), 3.60 (dd, J = 11.3, 3.7 Hz, 1H), 2.58 (s, 3H, 17), 2.51 (s, 3H, 16), 2.49 (s, 3H, 28), 2.13 – 2.03 (m, 2H), 2.02 – 1.86 (m, 4H, 22), 1.45 (d, J = 6.9 Hz, 3H, 34), 1.29 – 1.22 (m, 1H), 1.14 (s, 2H), 0.99 (s, 9H, 30). *Ratio of 7:3 E vs Z isomer observed.* **^{13}C NMR** (101 MHz, Chloroform-d) δ 171.13, 169.67, 167.29, 150.33, 141.35, 129.55, 127.71, 127.07, 126.41, 125.01, 122.21, 120.01, 70.13, 66.70, 58.42, 58.03, 56.63, 48.92, 47.32, 35.63, 35.08, 26.39, 22.25, 16.07, 14.01, 9.84. **MS** (ESI) *m/z* 937 (M+H)$^+$. **HRMS** (ESI) m/z: calculated for C$_{52}$H$_{57}$N$_9$O$_6$S$^+$, 936.4231; found 936.4197.

34
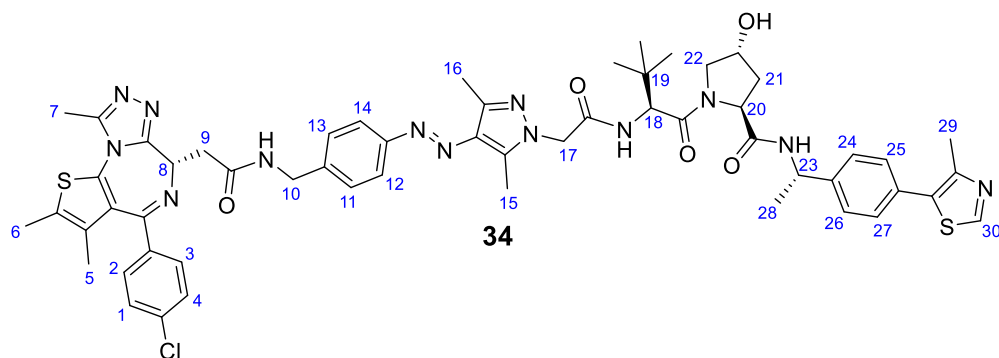
(2S,4R)-1-((S)-2-(2-(4-((E)-(4-((2-((S)-4-(4-chlorophenyl)-2,3,9-trimethyl-6H-thieno[3,2-f][1,2,4]triazolo[4,3-a][1,4]diazepin-6-yl)acetamido)methyl)phenyl)diazenyl)-3,5-dimethyl-1H-pyrazol-1-yl)acetamido)-3,3-dimethylbutanoyl)-4-hydroxy-N-((S)-1-(4-(4-methylthiazol-5-yl)phenyl)ethyl)pyrrolidine-2-carboxamide (34)

The intermediate **33** (74 mg, 0.067 mmol) was re-dissolved in DMF (2 ml) and was added piperidine (0.134 ml, 0.138 mmol). The solution was stirred at room temperature for 16 h. HATU (25 mg, 0.067 mmol) and DIPEA (0.059 ml, 0.335 mmol) were added followed by JQ1-COOH (32 mg, 0.080 mmol) and the mixture was stirred for another 16 h. The crude was partitioned between water (4 ml) and ethyl acetate (4 ml). The aqueous layer was further extracted with ethyl acetate (4 ml). The combined organic layer was dried over Na_2SO_4, filtered, and concentrated in vacuo. Purification by flash column chromatography using a gradient of methanol in DCM (1% to 4%) afforded **34** as a yellow solid (12.5 mg, 16%). Rf = 0.35 (5% MeOH in DCM).

^{1}H NMR (500 MHz, Chloroform-d) δ 8.70 (s, 1H, 30), 8.69 (s, Z isomer), 7.76 (s, 1H, NH), 7.74 (s, 1H, NH), 7.48 – 7.40 (m, 4H, 2, 3, 14, 12), 7.39 – 7.30 (m, 8H, 1, 4, 13, 11, 24, 25, 26, 27), 5.11 – 5.03 (m, 2H), 4.81 – 4.76 (m, 1H), 4.76 – 4.72 (m, 3H), 4.71 – 4.66 (m, 2H), 4.59 – 4.53 (m, 2H), 4.48 (d, J = 8.0 Hz, 1H), 4.45 – 4.39 (m, 2H), 4.12 (br.s, 1H), 4.09 (br.s, 1H), 3.64 – 3.62 (m, 1H), 3.61 – 3.57 (m, 2H), 3.48 (dd, J = 14.3, 7.0 Hz, 1H), 2.69 (s, 3H, 15), 2.60 (s, 3H, 16), 2.55 (s, 3H, 5), 2.52 (s, 4H, 6 +?), 2.43 (s, 3H, 7), 2.13 – 2.03 (m, 2H), 1.87 (d, J = 3.2 Hz, 1H), 1.47 (d, J = 6.8 Hz, 3H, 28), 1.29 – 1.26 (m, 2H), 1.01 (s, 9H, 19). *Ratio of 9:1 E vs Z isomer observed.* **^{13}C NMR** (126 MHz, Chloroform-d) δ 171.25, 170.55, 167.37, 164.08, 155.61, 150.31, 148.49, 140.41, 140.18, 136.80, 136.52, 129.82, 129.56, 128.72, 128.34, 126.41, 122.18, 70.15, 58.06, 56.52, 54.49, 51.54, 48.91, 43.31, 39.32, 35.28, 34.88, 26.38, 22.24, 16.08, 14.42, 14.02, 13.13, 11.86, 9.84. **MS** (ESI) m/z 1097 (M+H)$^+$. **HRMS** (ESI) m/z: calculated for C56H62ClN13O5S2$^+$, 1096.4205; found 1096.4242.

35
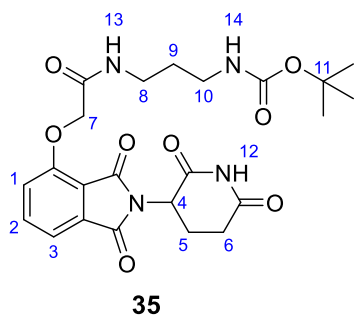
tert-butyl (3-(2-((2-(2,6-dioxopiperidin-3-yl)-1,3-dioxoisoindolin-4 yl)oxy)acetamido)propyl)carbamate (35)

After deprotection of **2** with TFA, the resulting acid (200 mg, 0.60 mmol) was re-dissolved in DMF (4 ml) and was added HATU (296 mg, 0.78 mmol) and DIPEA (0.312 ml, 1.80 mmol) were added followed by tert-butyl-(3-aminopropyl)carbamate (115 mg, 0.66 mmol) and the mixture was stirred for another 16 h. The crude was partitioned between water (4 ml) and ethyl acetate (4 ml). The aqueous layer was further extracted with ethyl acetate (4 ml). The combined organic layer was dried over Na_2SO_4, filtered, and concentrated in vacuo. Purification by flash column chromatography using a gradient of methanol in DCM (1% to 4%) afforded **35** as a beige gum (208 mg, 71%). R*f* = 0.40 (3% MeOH in DCM).

¹H NMR (400 MHz, Chloroform-*d*) δ 8.48 (s, 1H, 12), 7.75 (t, *J* = 8.4, 7.3 Hz, 1H, 2), 7.66 (br.s, 1H, 13), 7.56 (d, *J* = 7.3 Hz, 1H, 3), 7.23 (d, *J* = 8.4 Hz, 1H, 1), 6.47 (br.s, 1H, 14), 5.07 – 4.87 (m, 3H, 7, 4), 4.74 – 4.55 (m, 2H, 10), 3.50 – 3.34 (m, 2H, 8), 3.29 – 3.21 (m, 2H, 9), 3.20 – 3.10 (m, 2H, 6), 2.23 – 2.12 (m, 1H, 5a), 1.87 – 1.67 (m, 2H, 5b), 1.42 (d, *J* = 3.2 Hz, 9H, 11). **¹³C NMR** (101 MHz, Chloroform-*d*) δ 170.81, 167.18, 161.88, 154.79, 137.15, 133.51, 120.30, 117.67, 79.87, 68.62, 55.69, 49.36, 43.64, 42.22, 39.93, 38.61, 37.60, 36.31, 31.38, 30.22, 28.41, 22.67. **MS** (ESI) m/z 489 (M+H)⁺.

36
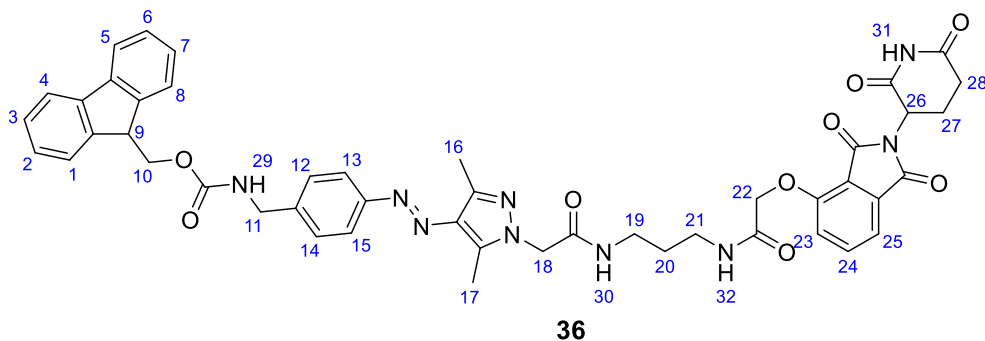
(9H-fluoren-9-yl)methyl (E)-(4-((1-(2-((3-(2-((2-(2,6-dioxopiperidin-3-yl)-1,3-dioxoisoindolin-4-yl)oxy)acetamido)propyl)amino)-2-oxoethyl)-3,5-dimethyl-1H-pyrazol-4-yl)diazenyl)benzyl)carbamate (36)

Carboxylic acid **32** (38 mg, 0.074 mmol, 1.0 eq) was dissolved in DCM (4 ml) along with HATU (42 mg, 0.111 mmol, 1.3 eq) and DIPEA (0.052 ml, 0.296 mmol, 2.0 eq). The amine **35** which was deprotected with HCl (hydrochloride salt, 35 mg, 0.082 mmol, 1.0 eq) was then added and the solution obtained was stirred at room temperature for 16 h. The reaction mixture was subsequently washed twice with water (2 x 3 ml). The recovered organic layer was dried over sodium sulfate, filtered, and concentrated in vacuo. The residue recovered was purified by silica gel flash chromatography (2-8% MeOH in DCM) to afford **36** as an orange solid (15 mg, 23%). Rf = 0.60 (5% MeOH in DCM).

¹H NMR (400 MHz, Chloroform-*d*) δ 8.36 (s, 1H, 31), 7.81 – 7.72 (m, 2H, 4, 5), 7.68 – 7.60 (m, 2H, 13, 15), 7.45 – 7.38 (m, 4H, 12, 14, 1, 8), 7.38 – 7.30 (m, 3H, 23, 24, 25), 7.23 – 7.07 (m, 4H, 2, 3, 6, 7), 5.74 (s, 2H, 18), 5.29 (t, *J* = 6.4 Hz, 1H, 9), 5.10 – 5.02 (m, 1H, 26), 4.99 (s, 2H, 22), 4.75 (d, *J* = 13.6 Hz, 1H), 4.51 (d, *J* = 6.8 Hz, 2H, 10), 4.44 (d, *J* = 6.0 Hz, 2H, 11), 4.26 (t, *J* = 6.8 Hz, 1H), 4.21 – 4.13 (m, 1H), 3.40 (d, *J* = 12.6 Hz, 2H, 19), 2.97 (t, *J* = 12.7 Hz, 2H, 21), 2.62 (s, 3H, 17), 2.52 (s, 3H, 16), 2.43 – 2.26 (m, 2H, 28), 2.18 – 2.08 (m, 2H, 27). *Only E isomer observed.* **¹³C NMR** (101 MHz, Chloroform-*d*) δ 164.36, 158.52, 157.89, 156.48, 156.33, 155.66, 153.89, 153.07, 143.89, 143.08, 141.34, 140.88, 139.59, 135.43, 130.00, 129.94, 128.05, 127.07, 125.03, 124.08, 122.14, 119.99, 119.53, 119.16, 98.60, 66.69, 53.55, 51.08, 47.33, 44.84, 44.37, 41.67, 31.52, 30.91, 14.11, 10.15. **MS** (ESI) m/z 880 (M+H)⁺. **HRMS** (ESI) m/z: calculated for C47H45N9O9⁺, 878.3891; found 878.3907.

37
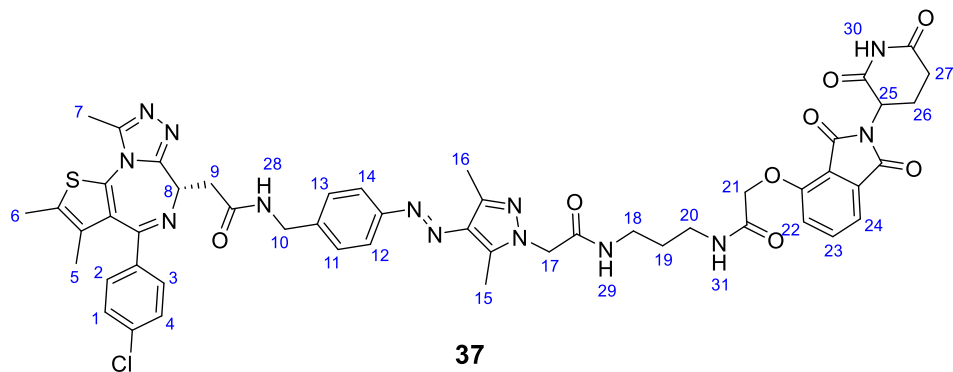
2-((S)-4-(4-chlorophenyl)-2,3,9-trimethyl-6H-thieno[3,2-f][1,2,4]triazolo[4,3-a][1,4]diazepin-6-yl)-N-(4-((E)-(1-(2-((3-(2-((2-(2,6-dioxopiperidin-3-yl)-1,3-dioxoisoindolin-4-yl)oxy)acetamido)propyl)amino)-2-oxoethyl)-3,5-dimethyl-1H-pyrazol-4-yl)diazenyl)benzyl)acetamide (37)

The intermediate **36** (15 mg, 0.017 mmol) was re-dissolved in DMF (2 ml) and was added piperidine (0.033 ml, 0.034 mmol). The solution was stirred at room temperature for 16 h. HATU (8. 5 mg, 0.022 mmol) and DIPEA (0.006 ml, 0.034 mmol) were added followed by JQ1-COOH (7 mg, 0.017 mmol) and the mixture was stirred for another 16 h. The crude was partitioned between water (4 ml) and ethyl acetate (4 ml). The aqueous layer was further extracted with ethyl acetate (4 ml). The combined organic layer was dried over Na_2SO_4, filtered, and concentrated in vacuo. Purification by flash column chromatography using a gradient of methanol in DCM (1% to 4%) afforded **37** as a yellow solid (6 mg, 34%). Rf = 0.50 (5% MeOH in DCM).

^{1}H NMR (500 MHz, DMSO-d_6) δ 11.12 (s, 1H, 30), 8.85 (t, J = 6.1 Hz, 1H, 28) 8.78 (t, J = 6.1 Hz, Z isomer, 28), 8.21 (t, J = 5.6 Hz, 1H, 29), 8.02 (t, J = 5.8 Hz, 1H, 31), 7.79 (dd, J = 8.5, 7.3 Hz, 1H, 23), 7.70 (d, J = 8.4 Hz, 1H, 24), 7.51 – 7.45 (m, 2H, 1, 4), 7.43 – 7.31 (m, 3H, 2, 3, 22), 5.11 (dd, J = 12.8, 5.5 Hz, 1H, 8), 4.77 (d, J = 9.7 Hz, 4H), 4.58 – 4.46 (m, 2H), 4.33 (dd, J = 15.4, 5.6 Hz, 2H), 3.26 – 3.07 (m, 6H), 2.93 – 2.83 (m, 1H), 2.60 (s, 3H, 15), 2.54 (s, 1H), 2.52 (s, 6H, 16, 6), 2.40 (s, 3H, 5), 2.37 (s, 3H, 7), 2.06 – 1.99 (m, 1H), 1.66 – 1.55 (m, 5H, 19, 26). *Ratio of 8:2 E vs Z isomer observed.* **^{13}C NMR** (126 MHz, DMSO-d_6) δ 173.25, 170.35, 167.19, 166.62, 165.92, 155.55, 152.40, 150.33, 141.80, 137.40, 135.66, 133.50, 130.61, 128.52, 121.79, 117.25, 116.49, 68.09, 54.49, 49.25, 36.95, 31.40, 29.49, 22.45, 14.51, 13.14, 11.78. **MS** (ESI) m/z 1041 (M+H)[+]. **HRMS** (ESI) m/z: calculated for C47H45N9O9[+], 1040.3393; found 1040.3412.

38
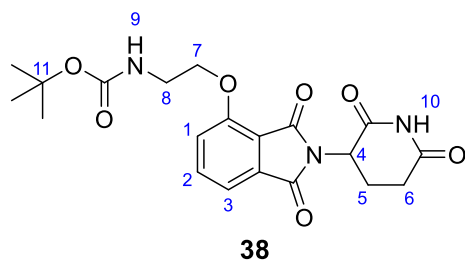
tert-butyl (2-((2-(2,6-dioxopiperidin-3-yl)-1,3-dioxoisoindolin-4-yl)oxy)ethyl)carbamate (38)
4-hydroxythalidomide (150 mg, 0.55 mmol) was dissolved in DMF (4 ml) and was added potassium carbonate (75 mg, 0.55 mmol) followed by tert-butyl (2-bromoethyl)carbamate (112 mg, 0.5 mmol). The solution was stirred for 16 h at room temperature. A mixture of mono and bis-alkylated material was observed by LC-MS. The crude mixture was partitioned between water (5 ml) and ethyl acetate (5 ml). The aqueous layer was further extracted with ethyl acetate (5 ml). The combined organic layer was washed with water (3 x 4 ml), then dried over Na_2SO_4, filtered, and concentrated in vacuo. The residue recovered was purified by silica gel flash chromatography (2-8% MeOH in DCM) to afford **38** as a pale-yellow oil (96 mg, 42%, contains 20% of bis alkylated material). Rf = 0.45 (3% MeOH in DCM).
¹H NMR (400 MHz, Chloroform-*d*) δ 8.29 (s, 1H, 10), 7.75 – 7.66 (m, 1H, 2), 7.53 – 7.45 (m, 1H, 1), 7.25 (dd, *J* = 8.4, 2.3 Hz, 1H, 3), 5.33 (s, 1H, 9), 5.05 – 4.94 (m, 1H, 4), 4.25 (t, *J* = 5.0 Hz, 2H, 7), 4.08 – 3.94 (m, 1H), 3.67 – 3.58 (m, 8H, 8 plus bis alkylated, 3.04 – 2.63 (m, 4H, 5, 6), 1.81 (s, 3H, bis alkylated), 1.46 (s, 9H, 11).
¹³C NMR (101 MHz, Chloroform-*d*) δ 171.26, 170.95, 169.03, 168.10, 166.92, 165.80, 156.26, 136.71, 133.73, 119.27, 116.38, 116.31, 79.71, 68.89, 60.42, 49.82, 49.16, 40.38, 39.82, 38.90, 31.83, 31.41, 28.39, 22.63, 22.07, 21.07, 14.21.

39
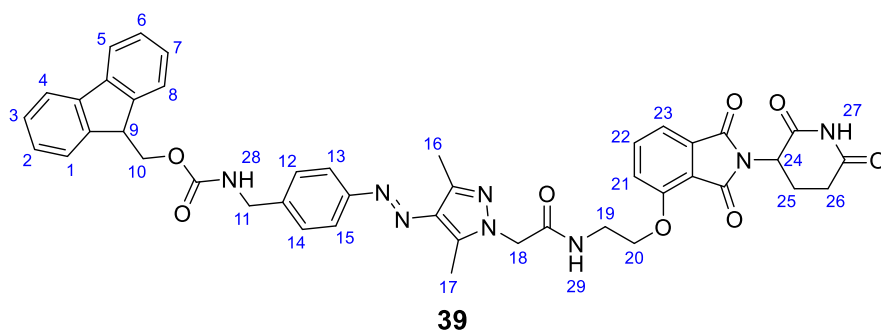
(9H-fluoren-9-yl)methyl (E)-(4-((1-(2-((2-((2-(2,6-dioxopiperidin-3-yl)-1,3-dioxoisoindolin-4-yl)oxy)ethyl)amino)-2-oxoethyl)-3,5-dimethyl-1H-pyrazol-4-yl)diazenyl)benzyl)carbamate (39)

Carboxylic acid **32** (25 mg, 0.049 mmol, 1.0 eq) was dissolved in DCM (4 ml) along with HATU (24 mg, 0.063 mmol, 1.3 eq) and DIPEA (0.017 ml, 0.098 mmol, 2.0 eq). The amine **38** which was deprotected with HCl (hydrochloride salt, 17 mg, 0.049 mmol, 1.0 eq) was then added and the solution obtained was stirred at room temperature for 16 h. The reaction mixture was subsequently washed twice with water (2 x 3 ml). The recovered organic layer was dried over sodium sulfate, filtered, and concentrated in vacuo. The residue recovered was purified by silica gel flash chromatography (2-8% MeOH in DCM) to afford **39** as an orange solid (10 mg, 25%). R*f* = 0.65 (5% MeOH in DCM).

^{1}H NMR (400 MHz, Chloroform-*d*) δ 8.28 (s, 1H, 27), 7.81 – 7.69 (m, 4H, 4, 5, 13, 15), 7.69 – 7.54 (m, 4H, 1, 8, 12, 14), 7.48 – 7.36 (m, 3H, 21, 22, 23), 7.36 – 7.27 (m, 4H, 2, 3, 6, 7), 7.18 (d, *J* = 8.3 Hz, 1H), 7.08 – 6.97 (m, 1H), 6.94 (d, *J* = 5.5 Hz, 1H), 5.48 (t, *J* = 6.0 Hz, 1H), 4.77 (s, 2H, 18), 4.74 – 4.61 (m, 1H), 4.51 – 4.45 (m, 4H, 10, 11), 4.45 – 4.36 (m, 2H), 4.27 – 4.15 (m, 4H), 3.90 – 3.75 (m, 2H, 20), 3.73 – 3.59 (m, 2H, 19), 2.72 – 2.59 (m, 2H), 2.55 (s, 3H, 17), 2.47 (s, 3H, 16), 2.45 – 2.40 (m, 2H, 25). *Only E isomer observed.* **^{13}C NMR** (101 MHz, Chloroform-*d*) δ 171.18, 167.24, 143.91, 141.34, 136.73, 133.66, 128.27, 127.70, 127.06, 125.07, 122.07, 119.99, 119.53, 116.70, 68.00, 66.70, 52.08, 47.31, 44.75, 38.70, 31.03, 22.49, 14.08, 9.89. **MS** (ESI) m/z 810 (M+H)$^+$. **HRMS** (ESI) m/z: calculated for C44H40N8O8$^+$, 809.3047; found 809.3051.
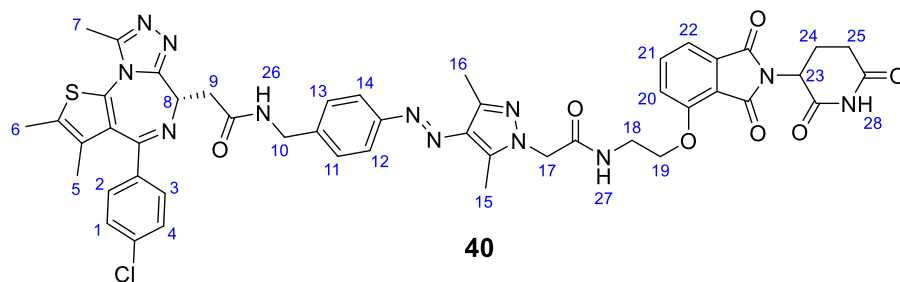
40

2-((S)-4-(4-chlorophenyl)-2,3,9-trimethyl-6H-thieno[3,2-f][1,2,4]triazolo[4,3-a][1,4]diazepin-6-yl)-N-(4-((E)-(1-(2-((2-((2-(2,6-dioxopiperidin-3-yl)-1,3-dioxoisoindolin-4-yl)oxy)ethyl)amino)-2-oxoethyl)-3,5-dimethyl-1H-pyrazol-4-yl)diazenyl)benzyl)acetamide (40)

The intermediate **39** (10 mg, 0.017 mmol) was re-dissolved in DMF (2 ml) and was added piperidine (0.003 ml, 0.034 mmol). The solution was stirred at room temperature for 16 h. HATU (8.5 mg, 0.022 mmol) and DIPEA (0.006 ml, 0.034 mmol) were added followed by JQ1-COOH (7 mg, 0.017 mmol) and the mixture was stirred for another 16 h. The crude was partitioned between water (4 ml) and ethyl acetate (4 ml). The aqueous layer was further extracted with ethyl acetate (4 ml). The combined organic layer was dried over Na_2SO_4, filtered, and concentrated in vacuo. The organic layer was dried over sodium sulfate, filtered, and concentrated in vacuo. The residue was purified by preparative HPLC (20–98% acetonitrile in water with 0.1% formic acid) to afford **40** (3 mg, 17%). R*f* = 0.35 (5% MeOH in DCM).

¹H NMR (500 MHz, DMSO-d_6) δ 12.85 (s, 1H, HCOOH), 11.11 (s, 1H, 28), 8.83 (t, *J* = 6.1 Hz, 1H, 26), 8.48 (t, *J* = 5.0 Hz, 1H, 27), 7.81 (dd, *J* = 8.5, 7.3 Hz, 2H, 14, 12), 7.71 – 7.64 (m, 2H, 2, 3), 7.56 (d, *J* = 8.6 Hz, 1H, 21), 7.50 – 7.43 (m, 2H, 1, 4), 7.43 – 7.39 (m, 2H, 13, 11), 7.37 – 7.30 (m, 2H, 22, 20), 6.89 (s, 2H, 17), 5.08 (dd, *J* = 12.7, 5.4 Hz, 1H, 8), 4.80 (s, 2H, 10), 4.54 (ddd, *J* = 9.1, 5.4, 1.7 Hz, 1H, 23), 4.48 (dd, *J* = 15.5, 6.4 Hz, 1H), 4.36 – 4.23 (m, 2H, 19), 3.56 – 3.49 (m, 1H), 2.92 – 2.83 (m, 1H, 25b), 2.59 (s, 3H, 15), 2.51 (s, 3H, 16), 2.39 (s, 3H, 7), 2.36 (s, 3H, 6), 2.05 – 1.98 (m, 1H, 24a), 1.59 (s, 3H, 5). *Ratio of 8:2 E vs Z isomer observed.* **¹³C NMR** (126 MHz, DMSO-d_6) δ 172.77, 169.91, 169.70, 166.76, 165.23, 163.08, 155.62, 155.05, 151.93, 149.83, 137.06, 136.68, 132.28, 130.69, 130.13, 129.78, 129.54, 128.33, 128.04, 121.31, 67.36, 54.01, 48.74, 41.75, 37.69, 30.93, 14.03, 13.91, 12.66, 11.30. **MS** (ESI) m/z 970 (M+H)⁺. **HRMS** (ESI) m/z: calculated for $C_{48}H_{45}ClN_{12}O_7S^+$, 969.3022; found 969.3033.
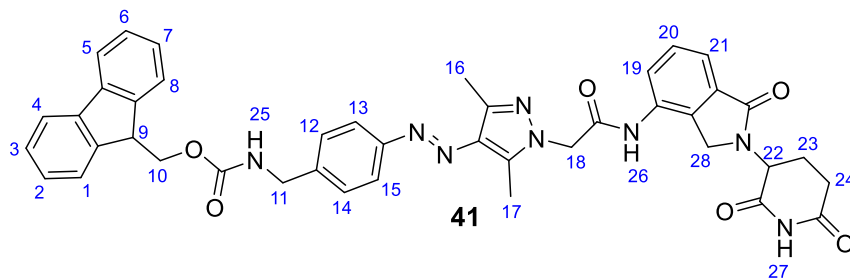
(9H-fluoren-9-yl)methyl (E)-(4-((1-(2-((2-(2,6-dioxopiperidin-3-yl)-1-oxoisoindolin-4-yl)amino)-2-oxoethyl)-3,5-dimethyl-1H-pyrazol-4-yl)diazenyl)benzyl)carbamate (41)

Carboxylic acid **32** (35 mg, 0.068 mmol, 1.0 eq) was dissolved in DCM (4 ml) along with HATU (34 mg, 0.089 mmol, 1.3 eq) and DIPEA (0.024 ml, 0.134 mmol, 2.0 eq). Lenalidomide (18 mg, 0.068 mmol, 1.0 eq) was then added and the solution obtained was stirred at room temperature for 16 h. The reaction mixture was subsequently washed twice with water (2 x 3 ml). The recovered organic layer was dried over sodium sulfate, filtered, and concentrated in vacuo. The residue recovered was purified by silica gel flash chromatography (2-8% MeOH in DCM) to afford **41** as an orange solid (13 mg, 25%). R*f* = 0.55 (5% MeOH in DCM).

¹H NMR (400 MHz, DMSO-d_6) δ 11.05 (s, 1H, 27), 11.04 (s, Z isomer. 27), 10.30 (s, 1H, 26), 8.00 – 7.83 (m, 4H, 4, 5, 13, 15), 7.71 (dd, *J* = 7.9, 3.6 Hz, 2H, 12, 14), 7.63 – 7.49 (m, 4H, 8, 1, 19, 20), 7.43 (t, *J* = 7.5 Hz, 2H, 2, 7), 7.39 – 7.30 (m, 2H, 6, 3), 7.29 – 7.14 (m, 1H, 21), 5.18 (dd, *J* = 13.3, 5.0 Hz, 1H, 22), 5.10 (s, 2H, 18), 4.50 (t, *J* = 7.9 Hz, 1H, 9), 4.44 (d, *J* = 12.1 Hz, 1H, 10), 4.39 (d, *J* = 6.8 Hz, 2H, 11), 4.25 (s, 2H, 28), 2.94 (ddd, *J* = 16.5, 13.4, 5.1 Hz, 2H), 2.65 (d, *J* = 2.8 Hz, 1H, 24b), 2.59 (s, 3H, 17), 2.46 – 2.31 (m, 4H, 16, 24a), 2.07 (dd, *J* = 11.9, 6.2 Hz, 2H, 23). *Ratio of 9:1 E vs Z isomer observed.* **¹³C NMR** (101 MHz, DMSO-d_6) δ 173.35, 171.55, 168.19, 165.83, 156.86, 152.46, 144.34, 141.86, 141.66, 135.01, 134.08, 133.52, 133.28, 131.69, 129.33, 128.23, 128.08, 127.53, 125.62, 121.88, 120.60, 120.00, 65.81, 52.29, 52.06, 47.28, 46.89, 43.98, 31.70, 23.14, 14.38, 10.11. **MS** (ESI) m/z 750 (M+H)⁺. HRMS (ESI) m/z: calculated for C42H38N8O6⁺, 749.2836; found 749.2850.
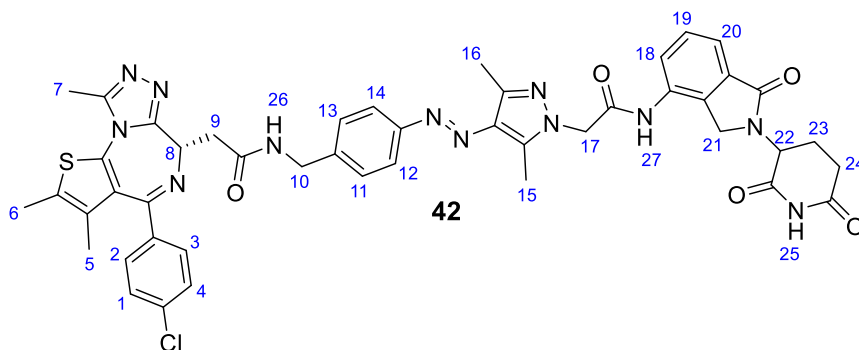
42

2-((S)-4-(4-chlorophenyl)-2,3,9-trimethyl-6H-thieno[3,2-f][1,2,4]triazolo[4,3-a][1,4]diazepin-6-yl)-N-(4-((E)-(1-(2-((2-(2,6-dioxopiperidin-3-yl)-1-oxoisoindolin-4-yl)amino)-2-oxoethyl)-3,5-dimethyl-1H-pyrazol-4-yl)diazenyl)benzyl)acetamide (42)

The intermediate **41** (10 mg, 0.013 mmol) was re-dissolved in DMF (2 ml) and was added piperidine (0.002 ml, 0.02 mmol). The solution was stirred at room temperature for 16 h. HATU (6.4 mg, 0.0169 mmol) and DIPEA (0.004 ml, 0.026 mmol) were added followed by JQ1-COOH (5 mg, 0.013 mmol) and the mixture was stirred for another 16 h. The crude was partitioned between water (2 ml) and ethyl acetate (2 ml). The aqueous layer was further extracted with ethyl acetate (2 ml). The combined organic layer was dried over Na_2SO_4, filtered, and concentrated in vacuo. The organic layer was dried over sodium sulfate, filtered, and concentrated in vacuo. The residue was purified by preparative HPLC (20–98% acetonitrile in water with 0.1% formic acid) to afford 42 (3 mg, 24%). Rf = 0.35 (5% MeOH in DCM).

**^{1}H NMR** (500 MHz, DMSO-d_6) δ 11.04 (s, 1H, 25), 10.29 (s, 1H, 27), 8.85 (t, J = 6.1 Hz, 1H, 26), 8.77 (t, J = 5.9 Hz, Z isomer, 26), 7.87 (dd, J = 7.5, 1.3 Hz, 2H, 14, 12), 7.75 – 7.66 (m, 2H, 2, 3), 7.58 – 7.31 (m, 8H, 1, 4, 13, 11, 18, 19, 20, 26), 7.08 – 6.97 (m, 1H), 5.16 (dd, J = 13.2, 5.1 Hz, 1H, 8), 5.09 (s, 2H, 17), 4.58 – 4.50 (m, 1H, 22), 4.49 – 4.36 (m, 2H, 21), 4.36 – 4.26 (m, 2H, 10), 2.97 – 2.86 (m, 1H), 2.68 – 2.62 (m, 1H), 2.63 – 2.54 (m, 6H, 15, 6), 2.42 – 2.38 (m, 4H, 16), 2.38 – 2.33 (m, 1H), 2.09 – 2.02 (m, 1H), 1.60 (s, 3H, 5), 1.47 – 1.37 (m, 2H, 23). *Ratio of 7:3 E vs Z isomer observed.* **^{13}C NMR** (126 MHz, DMSO-d_6) δ 172.86, 171.08, 167.70, 165.35, 155.12, 155.06, 151.92, 149.85, 136.70, 133.61, 133.07, 132.82, 130.15, 128.85, 128.07, 125.14, 121.37, 119.51, 54.02, 51.58, 46.41, 44.38, 31.22, 25.41, 22.67, 14.05, 12.67, 11.31, 9.65. **MS** (ESI) m/z 912 (M+H)$^+$. **HRMS** (ESI) m/z: calculated for $C_{46}H_{43}ClN_{12}O_5S^+$, 911.2967; found 911.2954.
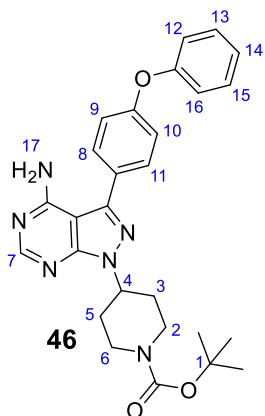
***tert*-butyl 4-(4-amino-3-(4-phenoxyphenyl)-1H-pyrazolo[3,4-d]pyrimidin-1-yl)piperidine-1-carboxylate (46)**

The amine **45** (1000 mg, 3.30 mmol) was dissolved in THF (15 ml) along with *tert*-butyl 4-hydroxypiperidine-1-carboxylate (663 mg, 3.30 mmol). After the solution was cooled down to 0°C, triphenylphosphine (864 mg, 3.30 mmol) and DIAD (0.71 ml, 3.63 mmol) were added.
The mixture was then stirred from 0°C to room temperature over the course of 12 h. The crude mixture was concentrated in vacuo. The residue obtained was then purified by silica gel flash chromatography (60-90% ethyl acetate in n-hexane) to afford **46** as a beige solid (1040 mg, 65%), The samples contained 5% of triphenylphosphine oxide (Ph₃PO). R*f* = 0.55 (90% ethyl acetate in cyclohexane).
¹H NMR (400 MHz, Chloroform-*d*) δ 8.38 (s, 1H, 7), 7.74 – 7.64 (m, 3H, 8, 11, Ph₃PO), 7.60 – 7.53 (m, 1H, Ph₃PO), 7.51 – 7.45 (m, 1H, Ph₃PO), 7.45 – 7.35 (m, 2H, 13, 15), 7.23 – 7.14 (m, 3H, 9, 10, 14), 7.13 – 7.06 (m, 2H, 12, 16), 5.76 (s, 2H, 17), 4.95 (tt, *J* = 11.6, 4.1 Hz, 1H, 4), 4.33 (s, 2H, 6a, 2a), 3.12 – 2.82 (m, 2H, 6b, 2b), 2.30 (qd, *J* = 12.4, 4.4 Hz, 2H, 5a, 3a), 2.02 (d, *J* = 12.7 Hz, 2H, 5b, 3b), 1.50 (s, 9H, 1). **¹³C NMR** (101 MHz, Chloroform-*d*) δ 158.47, 157.80, 156.37, 155.43, 154.53, 153.76, 143.71, 132.15, 132.06, 131.93, 128.57, 128.45, 127.85, 124.02, 119.51, 119.17, 79.73, 54.28, 31.33, 28.47. **MS** (ESI) m/z 487 (M+H)⁺.

43
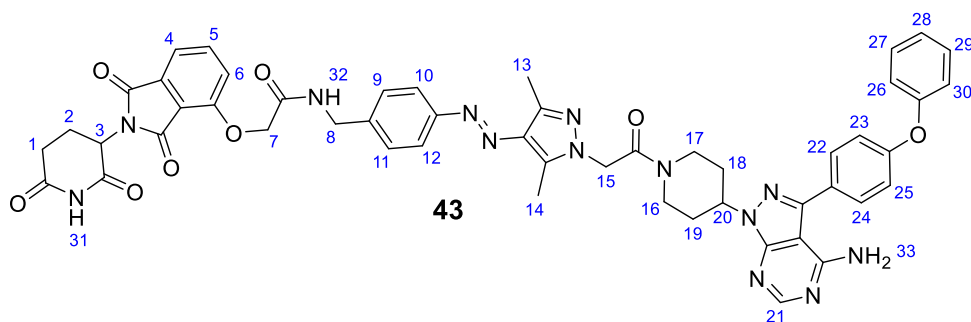
(E)-N-(4-((1-(2-(4-(4-amino-3-(4-phenoxyphenyl)-1H-pyrazolo[3,4-d]pyrimidin-1-yl)piperidin-1-yl)-2-oxoethyl)-3,5-dimethyl-1H-pyrazol-4-yl)diazenyl)benzyl)-2-((2-(2,6-dioxopiperidin-3-yl)-1,3-dioxoisoindolin-4-yl)oxy)acetamide (43)

Carboxylic acid **32** (16 mg, 0.030 mmol) was dissolved in DCM (4 ml) along with HATU (15 mg, 0.039 mmol) and DIPEA (0.026 ml, 0.15 mmol). The amine **46a** (14 mg, 0.036 mmol) resulting from the deprotection of **46** with HCl was then added and the solution obtained was stirred at room temperature for 16 h. The reaction mixture was subsequently washed twice with water (2 x 3 ml). The recovered organic layer was dried over sodium sulfate, filtered, and concentrated in vacuo. The residue recovered **47** (7 mg, 26%) was used as it is in the next step without purification. The intermediate **47** (5 mg, 0.005 mmol) was re-dissolved in DMF (2 ml) and was added piperidine (0.0015 ml, 0.01 mmol). The solution was stirred at room temperature for 3 h. Then HATU (2.5 mg, 0.0065 mmol) and DIPEA (0.0086 ml, 0.05 mmol) were added followed by deprotected **2** (2 mg, 0.0075 mmol) and the mixture was stirred for another 16 h. The crude was partitioned between water (2 ml) and ethyl acetate (2 ml). The aqueous layer was further extracted with ethyl acetate (2 ml). The combined organic layer was dried over Na_2SO_4, filtered, and concentrated in vacuo. The residue was purified by preparative HPLC (20–98% acetonitrile in water with 0.1% formic acid) to afford **43** (1 mg, 18%). Rf = 0.45 (5% MeOH in DCM). There was no sufficient material for a full ^{13}C NMR characterization.

^{1}H NMR (400 MHz, Chloroform-*d*) δ 8.84 (s, 1H, 31), 8.40 (s, 1H, 21), 8.12 (s, 1H, 32), 7.83–7.72 (m, 3H, 10, 12, 5), 7.69 – 7.62 (m, 2H, 9, 11), 7.58 (dd, *J* = 5.4, 4.0 Hz, 1H), 7.46 – 7.38 (m, 3H, 26, 20, 28), 7.26 – 7.14 (m, 5H, 22, 24, 27, 29), 7.13 – 7.08 (m, 2H, 23, 25), 5.11 – 4.85 (m, 5H, 15, 8), 4.81 – 4.54 (m, 5H, 7), 4.23 – 4.12 (m, 2H), 3.48 – 3.25 (m, 1H, 20), 2.99 – 2.85 (m, 2H), 2.66 (d, *J* = 10.5 Hz, 3H), 2.51 (s, 6H, 13, 14), 2.19 – 2.04 (m, 3H), 1.36 – 1.23 (m, 2H). *Isomer ratio not clearly visible*. MS (ESI) m/z 971(M+H)$^+$. **HRMS** (ESI) m/z: calculated for $C_{46}H_{43}ClN_{12}O_5S^+$, 970.3749; found 970.3737.
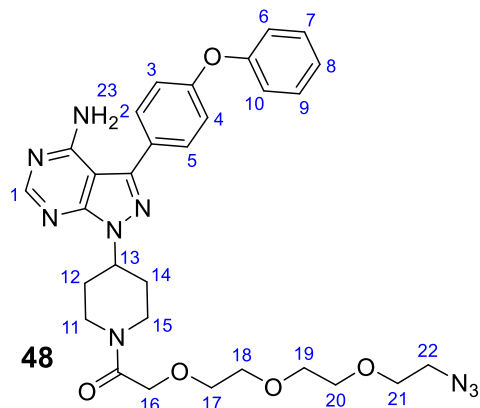
1-(4-(4-amino-3-(4-phenoxyphenyl)-1H-pyrazolo[3,4-d]pyrimidin-1-yl)piperidin-1-yl)-2-(2-(2-(2-azidoethoxy)ethoxy)ethoxy)ethan-1-one (48)

2-(2-(2-(2-azidoethoxy)ethoxy)ethoxy)acetic acid (22 mg, 0.094 mmol) was dissolved in DCM (3 ml) along with HATU (46 mg, 0.122 mmol) and DIPEA (0.081 ml, 0.47 mmol). The amine **46a** (40 mg, 0.094 mmol) resulting from the deprotection of **46** with HCl was then added and the solution obtained was stirred at room temperature for 16 h. The reaction mixture was subsequently washed twice with water (2 x 3 ml). The recovered organic layer was dried over sodium sulfate, filtered, and concentrated in vacuo. The residue was purified by silica gel flash chromatography (2-10% MeOH in DCM) to afford **48** as a white solid (28 mg, 50 %). Rf = 0.60 (90% ethyl acetate in cyclohexane).

^{1}H NMR (400 MHz, Chloroform-*d*) δ 8.36 (s, 1H, 1), 7.63 (d, *J* = 8.6 Hz, 2H, 2, 5), 7.38 (dd, *J* = 8.6, 7.4 Hz, 2H, 7, 9), 7.20 – 7.12 (m, 3H, 3, 4, 8), 7.10 – 7.04 (m, 2H, 6, 10), 5.64 (s, 2H, 23), 5.01 (tt, *J* = 11.4, 4.2 Hz, 1H, 13), 4.73 (d, *J* = 13.5 Hz, 1H, 11a), 4.26 (s, 2H, 16), 4.12 (d, *J* = 13.6 Hz, 1H, 15a), 3.78 – 3.59 (m, 10H, 17, 18, 19, 20, 21), 3.37 (t, *J* = 5.6 Hz, 2H, 11b, 15b), 3.26 (t, *J* = 12.8 Hz, 1H, 12b) 2.87 (t, *J* = 12.7, 11.9 Hz, 1H, 14b), 2.40 – 2.19 (m, 2H, 12a, 14a), 2.13 – 2.04 (m, 2H, 22). **^{13}C NMR** (101 MHz, Chloroform-*d*) δ 167.69, 158.53, 157.85, 156.31, 155.71, 153.88, 143.75, 129.98, 127.76, 124.07, 119.55, 119.11, 98.60, 70.62, 70.53, 69.96, 53.84, 50.64, 44.11, 41.20, 31.70, 31.11, 29.72. **MS** (ESI) m/z 602 (M+H)$^{+}$.

50
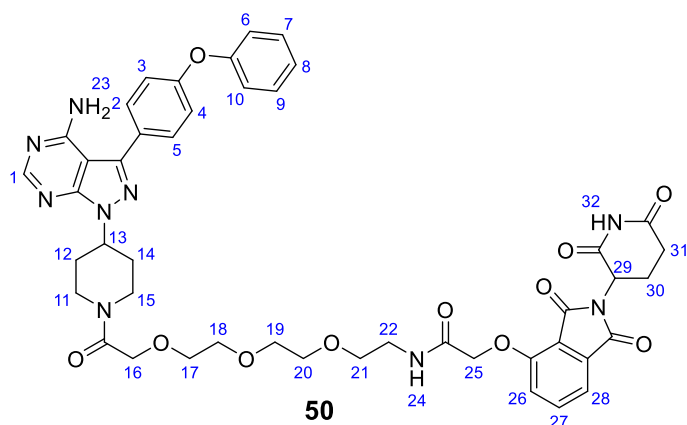
N-(2-(2-(2-(2-(4-(4-amino-3-(4-phenoxyphenyl)-1H-pyrazolo[3,4-d]pyrimidin-1-yl)piperidin-1-yl)-2-oxoethoxy)ethoxy)ethoxy)ethyl)-2-((2-(2,6-dioxopiperidin-3-yl)-1,3-dioxoisoindolin-4-yl)oxy)acetamide (50)

The azide **48** (10 mg, 0.016 mmol) was dissolved in MeOH (2 ml) and triphenylphosphine (6 mg, 0.02 mmol) was added. The solution obtained was stirred at 50˚C for 8 h under N_2. The crude mixture was then concentrated in vacuo and the residue redissolved in DCM (3 ml) along with HATU (6 mg, 0.0208 mmol) and DIPEA (0.006 ml 0.032 mmol). JQ1-COOH (6.4 mg, 0.016 mmol) was then added and the solution obtained was stirred at room temperature for 16 h. The reaction mixture was subsequently washed twice with water (2 x 3 ml). The recovered organic layer was dried over sodium sulfate, filtered, and concentrated in vacuo. The residue was purified by preparative HPLC (20-98% acetonitrile in water with 0.1% formic acid) to afford **50** as a white solid (4 mg, 24% over 2 steps). R*f* = 0.40 (5% MeOH in DCM)

¹H NMR (500 MHz, Chloroform-*d*) δ 10.25 (s, 1H, 32), 10.11 (s, 1H, 24), 8.40 (s, 1H, 1), 7.75 (t, *J* = 7.9 Hz, 1H, 8), 7.65 (d, *J* = 8.3 Hz, 2H, 2, 5), 7.57 (d, *J* = 7.3 Hz, 1H, 28), 7.41 (dd, *J* = 8.6, 7.4 Hz, 2H, 7, 9), 7.23 – 7.14 (m, 5H, 3, 4, 26, 27), 7.13 – 7.05 (m, 2H, 6, 10), 5.68 (s, 2H, 23), 5.07 – 4.92 (m, 2H, 25), 4.74 (d, *J* = 13.7 Hz, 1H, 29), 4.67 (s, 2H, 16), 4.39 – 4.19 (m, 2H), 4.09 (d, *J* = 13.8 Hz, 1H), 3.84 – 3.52 (m, 11H, 17, 18, 19, 20, 21), 3.26 (q, *J* = 12.2, 11.7 Hz, 1H), 2.98 – 2.71 (m, 5H), 2.48 – 2.24 (m, 2H), 2.23 – 2.07 (m, 2H, 30).

¹³C NMR (126 MHz, Chloroform-*d*) δ 168.44, 167.81, 166.86, 165.85, 157.82, 156.32, 155.55, 154.46, 153.85, 143.73, 136.91, 133.71, 129.98, 129.94, 127.70, 124.06, 119.54, 119.12, 118.01, 117.25, 70.36, 69.48, 67.89, 49.35, 44.14, 41.24, 39.06, 31.53, 30.93, 22.71. **MS** (ESI) m/z 890 (M+H)⁺. **HRMS** (ESI) m/z: calculated for C45H47N9O11⁺, 890.3473; found 890.3490.
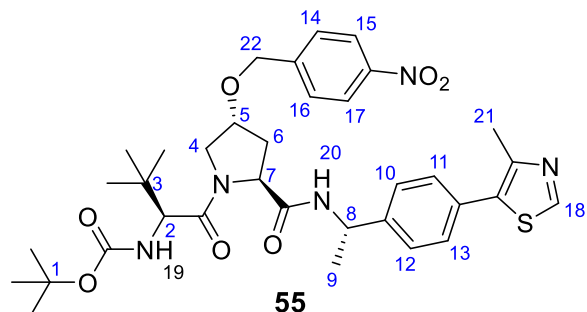
55

tert-butyl ((S)-3,3-dimethyl-1-((2S,4R)-2-(((S)-1-(4-(4-methylthiazol-5-yl)phenyl)ethyl)carbamoyl)-4-((4-nitrobenzyl)oxy)pyrrolidin-1-yl)-1-oxobutan-2-yl)carbamate (55)

Intermediate **7** (90 mg, 0.165 mmol) and tetrabutylammonium iodide (30 mg, 0.0826 mmol) were dissolved in DCM (6 ml). 4-nitrobenzyl bromide (39 mg, 0.181 mmol) was then added followed by aqueous sodium hydroxide 50% (1 ml). The biphasic mixture was stirred at room temperature for 2 h. Completion of the reaction was monitored by TLC. After 2 h, the aqueous layer (bottom layer) was removed with a pipette and the remaining organic layer was washed with water (3 x 5 ml). The recovered organic layer was dried over sodium sulfate, filtered, and concentrated in vacuo. The residue recovered was then purified by silica gel flash chromatography (40-80% ethyl acetate in n-hexane) to afford **55** as a pale-yellow solid (44 mg, 40%). R*f* = 0.60 (90% ethyl acetate in cyclohexane).

1H NMR (400 MHz, Chloroform-*d*) δ 8.70 (s, 1H, 18), 8.20 (d, *J* = 8.3 Hz, 2H, 15, 17), 7.50 (d, *J* = 8.3 Hz, 2H, 11, 13), 7.43 (d, *J* = 8.1 Hz, 2H, 14, 16), 7.38 (d, *J* = 8.0 Hz, 2H, 10, 12), 5.27 (d, *J* = 9.8 Hz, 1H, 8), 5.08 (p, *J* = 7.1 Hz, 1H, 5), 4.79 (t, *J* = 7.3 Hz, 1H, 7), 4.73 (d, *J* = 12.8 Hz, 1H, 2), 4.58 (d, *J* = 12.8 Hz, 1H), 4.38 (d, *J* = 10.1 Hz, 2H, 22), 4.19 (d, *J* = 11.1 Hz, 1H, 4a), 3.67 (dd, *J* = 11.2, 4.5 Hz, 1H, 4b), 2.73 (dt, *J* = 12.5, 5.8 Hz, 1H, 6b), 2.55 (s, 3H, 21), 2.22 – 2.09 (m, 1H, 6a), 1.49 (d, *J* = 6.9 Hz, 3H, 9), 1.39 (s, 9H, 1), 1.06 (s, 9H, 3).

13C NMR (101 MHz, Chloroform-*d*) δ 172.77, 169.28, 155.77, 150.32, 148.52, 147.37, 145.30, 143.01, 130.98, 127.66, 126.42, 123.61, 79.88, 69.72, 58.62, 58.39, 52.67, 49.00, 35.57, 32.71, 28.25, 26.38, 22.26, 16.11. **MS** (ESI) m/z 680 (M+H)$^{+}$.
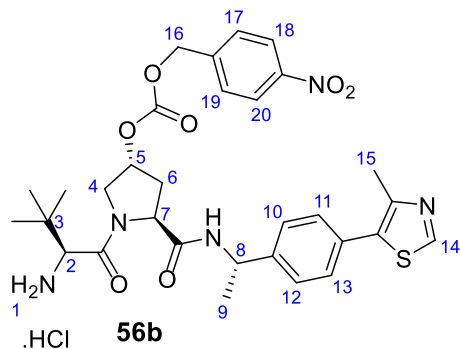
***tert*-butyl ((S)-3,3-dimethyl-1-((2S,4R)-2-(((S)-1-(4-(4-methylthiazol-5-yl)phenyl)ethyl)carbamoyl)-4-((((4-nitrobenzyl)oxy)carbonyl)oxy)pyrrolidin-1-yl)-1-oxobutan-2-yl)carbamate (56b)**

In a pre-dried round bottom flask, intermediate **7** (100 mg, 0.184 mmol) and DMAP (22 mg, 0.184 mmol) were dissolved in DCM (6 ml) and the solution was cooled down to 0˚C using an ice bath. A solution of *p*-nitrobenzyl chloroformate (51 mg, 0.239 mmol) in DCM (2 ml) was then added dropwise followed by DIPEA (0.064 ml, 0.367 mmol). The solution was brought to room temperature and stirred for 2 h. The reaction was washed with water (2 x 5 ml) and the recovered organic layer was dried over sodium sulfate, filtered, and concentrated in vacuo before being purified by flash chromatography on silica gel (cyclohexane: ethyl acetate = 9:1 to 1:9) to afford **56** (41 mg, 36%). Compound **56** was directly deprotected using HCl (4 M in Dioxane) (0.82 ml, 3,29 mmol) in 3 ml of DCM. The progress of the reaction was checked by TLC and after 2 h, it was stopped. The crude was concentrated in vacuo and evaporated a few times with DCM to give **56b** as a beige solid (22 mg, 26%, over 2 steps)

^{1}H NMR (400 MHz, Methanol-d_4) δ 9.10 (s, 1H, 14), 8.26 (d, J = 8.3 Hz, 2H, 18, 20), 7.64 (d, J = 8.4 Hz, 2H, 11, 13), 7.45 (q, J = 8.2 Hz, 4H, 17, 19, 10, 12), 5.38 – 5.25 (m, 3H, 16, 5), 5.00 (q, J = 6.9 Hz, 1H, 8), 4.68 (t, J = 8.8 Hz, 1H, 7), 4.14 (d, J = 12.3 Hz, 1H, 4a), 4.09 (s, 1H, 2), 3.85 (dd, J = 12.2, 3.7 Hz, 1H, 4b), 2.58 – 2.53 (m, 1H, 6a), 2.50 (s, 3H, 15), 2.18 – 2.08 (m, 1H, 6b), 1.51 (d, J = 7.0 Hz, 3H, 9), 1.15 (s, 9H, 3). **^{13}C NMR** (101 MHz, Methanol-d_4) δ 170.62, 167.06, 154.08, 152.23, 147.89, 146.40, 144.52, 142.75, 129.51, 129.16, 128.44, 126.30, 123.31, 77.20, 67.94, 59.22, 59.04, 54.07, 34.75, 34.44, 25.25, 21.02, 13.86. **MS** (ESI) m/z 624 (M+H)$^+$.
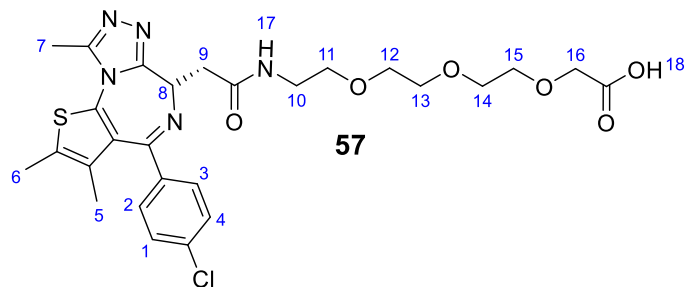
***(S)-1-(4-(4-chlorophenyl)-2,3,9-trimethyl-6H-thieno[3,2-f][1,2,4]triazolo[4,3-a][1,4]diazepin-6-yl)-
2-oxo-6,9,12-trioxa-3-azatetradecan-14-oic acid (57)***

2-(2-(2-(2-aminoethoxy)ethoxy)ethoxy)acetic acid (30 mg, 0.075 mmol) was dissolved in DCM
(3 ml) along with HATU (28 mg, 0.075 mmol) and DIPEA (0.033 ml 0.1875 mmol). Then JQ1-
COOH (30 mg, 0.075 mmol) was then added, and the solution obtained was stirred at room
temperature for 16 h. The reaction mixture was subsequently washed twice with water (2 x 3 ml).
The recovered organic layer was dried over sodium sulfate, filtered, and concentrated in vacuo.
The residue was purified by silica gel flash chromatography (2-10% MeOH in DCM) to afford **57**
as a light-yellow solid (26.5 mg, 36 %).

^{1}H NMR (400 MHz, Methanol-d_4) δ 8.49 (s, 1H, 17), 7.46 (d, J = 8.6 Hz, 2H, 2, 3), 7.41 (d, J =
8.4 Hz, 2H, 1, 4), 4.64 (dd, J = 8.6, 5.5 Hz, 1H, 8), 3.99 (s, 2H, 16), 3.74 – 3.56 (m, 10H, 11, 12,
13, 14, 15), 3.52 – 3.39 (m, 2H, 10), 2.78 – 2.72 (m, 1H, 9a), 2.70 (s, 3H, 6), 2.45 (s, 3H, 7), 2.38
– 2.29 (m, 1H, 9b), 1.70 (s, 3H, 5). **^{13}C NMR** (101 MHz, Methanol-d_4) δ 164.79, 136.71, 136.57,
131.85, 130.61, 130.56, 129.95, 128.39, 69.91, 69.81, 69.64, 69.45, 53.79, 39.05, 37.37, 13.03,
11.53, 10.22. **MS** (ESI) m/z 591 (M+H)$^+$.

58
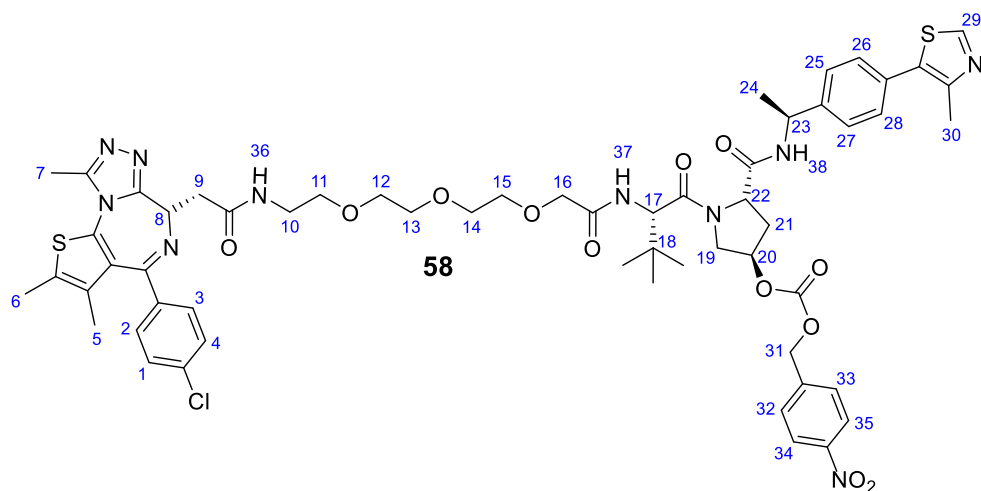
(3R,5S)-1-((S)-2-(tert-butyl)-17-((S)-4-(4-chlorophenyl)-2,3,9-trimethyl-6H-thieno[3,2-f][1,2,4]triazolo[4,3-a][1,4]diazepin-6-yl)-4,16-dioxo-6,9,12-trioxa-3,15-diazaheptadecanoyl)-5-(((S)-1-(4-(4-methylthiazol-5-yl)phenyl)ethyl)carbamoyl)pyrrolidin-3-yl (4-nitrobenzyl) carbonate (58)

Carboxylic acid **57** (10 mg, 0.017 mmol was dissolved in DCM (3 ml) along with HATU (8 mg, 0.022 mmol) and DIPEA (0.006 ml, 0.034 mmol). Then amine **56b** (11 mg, 0.017 mmol) was added, and the solution obtained was stirred at room temperature for 16 h. The reaction mixture was subsequently washed twice with water (2 x 3 ml). The recovered organic layer was dried over sodium sulfate, filtered, and concentrated in vacuo. The residue was purified by silica gel flash chromatography (2-10% MeOH in DCM) to afford **58** as a pale solid (6 mg, 36 %). R*f* = 0.55 (5% MeOH in DCM)

¹H NMR (500 MHz, Chloroform-*d*) δ 10.10 (s, 1H, 29), 8.67 (d, *J* = 6.6 Hz, 2H, 34, 35), 8.26 – 8.22 (m, 2H, 26, 28), 8.20 (d, *J* = 8.8 Hz, 2H, 2, 3), 7.81 (d, *J* = 7.8 Hz, 1H, NH), 7.56 – 7.50 (m, 3H, 32, 33), 7.43 – 7.38 (m, 2H, 1, 4), 7.38 – 7.33 (m, 2H, 25, 27), 7.32 – 7.27 (m, 2H), 6.96 (d, *J* = 7.7 Hz, 1H), 5.54 (d, *J* = 5.9 Hz, 1H), 5.35 (t, *J* = 4.0 Hz, 1H), 5.30 – 5.27 (m, 2H, 31), 5.26 (d, *J* = 2.8 Hz, 1H), 5.23 (s, 2H), 5.07 (p, *J* = 7.1 Hz, 2H), 4.92 (t, *J* = 7.7 Hz, 1H), 4.69 – 4.62 (m, 2H), 4.57 (d, *J* = 9.1 Hz, 1H), 4.32 (d, *J* = 12.0 Hz, 1H), 4.15 – 4.08 (m, 2H), 3.99 (d, *J* = 15.6 Hz, 1H), 3.85 (dd, *J* = 12.0, 4.4 Hz, 1H), 3.75 – 3.65 (m, 6H, 12, 13, 14), 3.65 – 3.55 (m, 2H, 15), 3.51 (dd, *J* = 14.8, 6.4 Hz, 2H), 3.46 – 3.36 (m, 1H), 2.89 (s, 2H), 2.67 – 2.62 (m, 1H), 2.61 (s, 3H), 2.53 (s, 3H, 6), 2.51 (s, 3H, 7), 2.39 (s, 3H, 30), 2.29 (dd, *J* = 14.1, 8.5 Hz, 1H), 1.49 (d, *J* = 6.9 Hz, 2H), 1.45 (d, *J* = 7.0 Hz, 3H, 24), 1.25 (s, 3H, 5), 1.12 (s, 3H), 1.06 (s, 9H, 18). **¹³C NMR** (126 MHz, Chloroform-*d*) δ 171.03, 170.80, 170.15, 169.49, 168.86, 168.66, 163.63, 161.91, 155.74, 154.18, 153.65, 150.33, 150.22, 149.78, 148.54, 148.44, 147.82, 143.22, 142.68, 142.21, 136.67, 136.59, 131.95, 131.59, 131.11, 130.80, 130.72, 130.57, 129.84, 129.61, 129.44, 128.82, 128.67, 128.52, 126.45, 126.36, 123.95, 123.80, 70.84, 70.57, 70.44, 70.07, 68.56, 68.16, 63.48, 58.74, 58.35, 56.78, 54.25, 53.73, 49.15, 48.90, 39.52, 38.80, 36.65, 35.28, 33.00, 29.69, 26.46, 22.08, 16.09, 14.41, 13.08, 11.74. **HRMS** (ESI) m/z: calculated for $C_{45}H_{47}N_9O_{11}^+$, 1195.4148; found 1195.4166.

6.1.3 General Photocharacterization methods

PSS ratio determination by LC-MS

An initial stock solution of photoswitchable PROTACs in DMSO (10 mM) were used to prepared samples in acetonitrile: water (1:1) at a final concentration of 80 μM. The solutions were irradiated at 365 nm or 457 nm for 3 mins (previous experiments indicated that at such concentration, longer irradiation times did not affect the E:Z ratio). Samples were injected into the LC-MS straight after being irradiated with limited exposure to ambient light. The integration of the peaks from the chromatogram was computed to obtain the PSS ratio values.

_Z_ isomer half-life determination at 37˚C

100 μM solutions of photoswitchable PROTACs in acetonitrile: water (1:1) were prepared and irradiated at 365 nm for 3 mins. 5 timepoints were selected (T= 0 h, T= 1 h, T = 3 h, T = 5 h, T = 24 h) and the samples were kept wrapped up with foil at 37˚C. At each timepoint, the sample were removed from the heat source and submitted for LC-MS analysis.

UV-vis spectra recording

Concentrated samples of photoswitchable PROTACs (100 μM) in acetonitrile were prepared and measured at room temperature in Polystyrene semi-micro cuvettes (1.5 mL, 1 cm) from 200 to 800 nm. The data was analyzed using WinUV software. In the case of assessment of the _Z_ isomer stability at 37˚C and at room temperature, a sample was first irradiated at 365 nm for 3 mins then kept protected from light for 24 h before recording the spectrum.
N.B. The high concentrations used led to absorbance greater than 1 (i.e., saturated signals in the spectrum). Diluted samples should be used for future experiments.

NMR photoswitching

3 mg of material was dissolved in deuterated chloroform. The solution was irradiated at 365 nm or 457 nm for 3 mins then covered with aluminium foil before recording the ^{1}H NMR spectrum. Sample recording was done as quickly as possible after the initial irradiation in deuterated solvent to limit back switching. The _Z_ to _E_ ratio was calculated based the differential peaks observed before and after irradiation. We note that the suboptimal protection from ambient light and a short irradiation time relative to the concentration of the sample (i.e., the PSS was not reached) may account for inaccurate ratios observed.

6.2 Biology

6.2.1 General methods

Reagents

All reagents were purchased from commercial sources and used as supplied unless otherwise indicated. Reagents for the radio immunoprecipitation assay buffer (RIPA lysis buffer) were purchased from Sigma Aldrich and include sodium deoxycholate, Triton X-100 and SDS 10%. Tris base and sodium chloride were purchased from VWR. DMEM media and heat deactivated fetal bovine serum (FBS) were purchased from Merck and Gibco, Life Technologies respectively. Complete Mini EDTA free Protease inhibitor cocktail was purchased from Sigma. Benzonase Nuclease was purchased from Sigma Aldrich.

Lysis buffer composition (20 ml final volume)

NaCl (2 ml, 750 mM, final concentration 75 mM), sodium deoxycholate (1 ml, 5%, final concentration 0.25%), Triton X-100 (100 µl, final concentration 0.5%), SDS 10% (100 µl, final concentration 0.05%), 16.8 ml of Milli-Q purified water. Benzonase (4 µl, 250 units per µl).

Cell culture

HeLa cells and HEK293 cells were cultured in low-glucose Dulbecco's Modified Medium (DMEM, Merck) supplemented with 10% heat-inactivated fetal bovine serum (FBS, Gibco). All cells were maintained in a humidified incubator at 37°C and 5% CO_2. Cells were seeded on plates at least 24 h before experiment.

Western blot analysis

After cell treatment, the media was aspirated, and the tissue layer washed with 0.5 ml of PBS. The cells were then added 150 µl of cold RIPA-buffer containing protease inhibitor cocktail and were detached using a cell scraper. After collection of the lysates on ice, centrifugation at 4 °C (12,000 g, 15 mins) allowed the recovery of supernatant. The protein concentration was measured with a Bio-Rad *DC* Protein Assay. 15-20 µg of protein extracts were fractionated by SDS-PAGE and transferred to PVDF membranes which were then blocked with 5% skim milk in Tris-buffered saline with 0.1 % Tween-20 (TBS-T). Subsequent incubation with primary antibodies Anti-BRD4 (Cell Signaling, (E2A7X) Rabbit mAb #13440), Anti-c-myc (Abcam, ab32072) and Anti-beta Actin (Abcam, (ab8227)) was conducted overnight at 4 °C. After washes with TBS-T (3 x 10 mins), the appropriate secondary antibodies (Goat Anti-Rabbit IgG H&L (HRP) (ab205718)) was incubated for 1 h. Finally, the bands were detected by western fluorescent detection reagent (Merck™ Luminata™ Western HRP Chemiluminescence) and imaged within the ImageQuant LAS 4000 series.

6.2.2 Protocols for caged degraders

Testing of PROTAC 15 and 16

HeLa cells were seeded in 6-well plates with a density of 0.6 x 10^6 cells per well in 2.0 ml growth medium (low-glucose DMEM). 24 h after settling, 2 ml solutions of PROTAC **15** and **16** in growth medium were prepared in serial dilution (10 μM to 10 nM) from 10 mM DMSO stocks. After aspiration of the media, cells were treated with PROTACs for 24 h in the incubator (37 °C, 5% CO2). Cells were lysed according to the protocol described above.

Testing of PROTAC 12, 15 and 16 (with irradiation at 365 nm or 405 nm)

HeLa cells were seeded in 6-well plates with a density of 0.6 x 10^6 cells per well in 2.0 ml growth medium (low-glucose DMEM). 24 h after settling, 2 ml solutions of PROTAC **12** in growth medium were prepared in serial dilution (1 μM to 10 nM) from a 10 mM DMSO stock.
PROTAC **15** and **16** were tested at 1 μM. After aspiration of the media, cells were treated with PROTACs for 2 h in the incubator (37 °C, 5% CO2) prior to irradiation for 60 seconds at 80 mm from a 25 mW 365 nm LED. Cells were further kept in the incubator for 22 h and were finally lysed according to the protocol described in the general methods.

Timecourse experiment with PROTAC 12, 15 and 16

Cells were seeded and treated as above. For PROTAC **15** and **16** (1 μM) , the time course started immediately after incubation with the compounds. For PROTAC **12** (1 μM), the time course started after irradiation for 60 seconds at 365 nm. Cells were lysed at 60 min intervals to evaluate onset of BRD4 degradation.

VHL-dependency experiment

HeLa cells were seeded in 6-well plates with a density of 0.6 x 10^6 cells per well in 2.0 ml growth medium (low-glucose DMEM). 24 h after settling, cells were treated with rising concentrations of VHL ligand **17** (0.1 to 10 μM) for 2 h then were treated with DMSO vehicle 0.1% (v/v), PROTAC **12**, **15** or **16** (1 μM) for 2 h before irradiation for 60 seconds at 365 nm. Cells were further kept in the incubator (37 °C, 5% CO2) for another 20 h before lysis.

Proteasome-dependency experiment

HeLa cells were seeded in 6-well plates with a density of 0.6 x 10^6 cells per well in 2.0 ml growth medium (low-glucose DMEM). 24 h after settling, cells were treated with proteasome inhibitor bortezomib (BTZ**,** 10 μM) for 2 h then were treated with DMSO vehicle 0.1% (v/v), PROTAC **12**, **15** or **16** (1 μM) for 2 h prior to irradiation for 60 seconds at 365 nm. Cells were further kept in the incubator (37 °C, 5% CO2) for another 20 h before lysis.

Washout experiment

HeLa cells were seeded in 6-well plates with a density of 0.6 x 10^6 cells per well in 2.0 ml growth medium (low-glucose DMEM). 24 h after settling, cells were treated with PROTAC **12, 15** or **16** (1 μM) for 2 h then cells were washed with PBS (3 x 0.5 ml) prior to irradiation for 60 seconds at 365 nm. Cells were further kept in the incubator for 6 h and were finally lysed according to the protocol described above.

Cell proliferation experiment

HeLa cells were seeded in 96-well plates with a density of 0.5 x 10^4 cells per well in 0.2 ml growth medium (low-glucose DMEM). 24 h after settling, cells were treated with DMSO, JQ1, PROTAC **12, 15** or **16** for 1 h 30 mins then cells were irradiated for 60 seconds at 365 nm. Cell proliferation was monitored over 6 days via live-cell microscopy using the IncuCyte S3. Values were normalized to cell count at T0, and fold changes were plotted.

CETSA experiment

Tm determination: HeLa cells were seeded in a T75 flask (triplicate). After reaching about 90% confluency, cells were collected (detachment with trypsin) and pelleted by centrifugation. The pellet was washed with PBS twice then resuspended in PBS containing a protease inhibitor cocktail. The sample obtained was divided into twelve aliquots of 100 µl each and individual aliquots were heated for 3 mins within a PCR tube in a thermo cycler following a temperature gradient (12 temperatures from 37.6°C to 66,9°C). After cooling, the samples were subjected to a freeze-thaw cycle (3 times) to lyse the cells. A centrifugation step allowed the recovery of the supernatant from the cell debris. The lysates were subsequently analysed by Western Blot. Gel quantification with ImageJ yielded the melting temperature Tm = 44.3°C.

Isothermal dose response CETSA: HeLa cells were seeded in 6-well plates with a density of 0.6 x 10^6 cells per well in 2.0 ml growth medium (low-glucose DMEM). 24 h after settling, cells were treated with PROTAC **12** or JQ1 for 18 h. Cells were detached as per above, and the resulting aliquots were heated at 44.3°C. Following lysis and centrifugation, the soluble fractions obtained were analyzed by Western blot.

Generation of pEGFP-BRD4-C1 plasmid

The BRD4 gene was cut out from NanoLuc®-BRD4 plasmid (pFN31K-BRD4, kind gift from Promega, UK) using SalI, XhoI, ClaI and SpeI restriction enzymes and isolated by agarose gel purification. The pEGFP-C1 vector (kind gift from Dr Cory Antonio Ocasio (Francis Crick Institute, London, UK) was linearized by PCR using primers with the following sequences: tacccgggggatcctctagag*tcgac*GCCATACCACATTTGTAGAGG (forward, overlaps with SalI restriction site) and agacatggcgatcgcgccg*ctcgaggctct*CTTGTACAGCTCGTCCATGC (reverse, overlaps with XhoI restriction site). The N-terminally tagged GFP-BRD4 fusion sequence was assembled with NEBuilder® HIFI DNA Assembly Master Mix (New England Biolabs, MA).

Live-cell fluorescence imaging and quantification

HEK293 cells were seeded into 12-well plate coverslips (Mattek, P12G-1.5-14-F) and incubated overnight in DMEM (Gibco) (with 10% FCS). Cells were then transfected with 100 ng of pEGFP-BRD4-C1 plasmid (see above) per well with 300 ng of empty vector and 1.2 µL of Lipofectamine 2000 (Invitrogen) in Opti-MEM® (Gibco) following the manufacturer's protocol. After 2 h post-transfection, medium was removed and replaced with fresh DMEM (with 10% FCS). After 24 h post-transfection, cells were treated with PROTACs at various concentrations and immediately imaged using a Nikon Eclipse Ti2 inverted microscope (Nikon, Tokyo, Japan) equipped with 20x 0.75NA Ph2 objective and controlled with Micro-Manager v2.0 software (Open-Imaging). For uncaging, cells were incubated with PROTAC **12** or DMSO for 1 h, imaged at 0 time point, irradiated with a UV light box at 365 nm for 60 seconds and then imaged after irradiation every 20 min. GFP fluorescence was monitored using LED GFP 470/24 (excitation) and ET525_50m (emission) standard filters over 6 hours with 20 min interval between image captures. Image processing, analysis and quantification was performed using ImageJ (NIH) and GraphPad Prism.

Upon background subtraction, a group of cells was selected, and snapshots generated at given time intervals. For quantification, a fluorescence intensity of 10 individual cells was measured over time and divided by fluorescence intensity for each cell at 0 time. The mean fluorescence intensity with SEM was plotted on a graph at given time points.

Testing of PROTAC 12 and 15 with ^{18}FDG

HeLa cells were seeded in 6-well plates with a density of 0.6 x 10^6 cells per well in 2.0 ml growth medium (low-glucose DMEM). 24 h after settling, ^{18}FDG (20 µCi/well) was added and the cells were incubated for 1 h after which 2 ml solutions of PROTAC **12** or **15** were added to the growth medium (1 µM). Cells were further kept in the incubator for 12 h and were finally lysed for western blot analysis according to the protocol described in the general methods.

Uncaging of PROTAC 12 with ^{32}P

A solution of ^{32}P-labelled sodium orthophosphate in water (from 50 µCi to 500 µCi) was added to a 100 µM solution (0.5 ml) of caged degrader **12**. The samples were kept at room temperature for 24 h and protected from light. Extraction with ethyl acetate (0.6 ml) was performed to recover material derived from the caged degrader while the orthophosphate was washed away in the aqueous layer. Extracted samples were then submitted for LC-MS analysis.

Uncaging of PROTAC 12 with ^{90}Y

The photocaged PROTAC **12** was provided as a 100 µM solution in acetonitrile water (1:1) to the Department of Nuclear medicine at Imperial College London. In total, 6 safe glass microwave vials (with 1 ml of PROTAC **12** solution) were prepared and equipped with a rubber septum for ease of ^{90}Y delivery via a syringe. A 10 mCi dose of ^{90}Y was added in triplicate into the 3 vials and water into the other 3 vials (as a control). The samples were kept at room temperature protected from light for 3 months. The cold samples once recovered were then submitted for LC-MS analysis.

6.2.3 Protocols for photoswitchable degraders

General method for in-cell testing of photoswitchable compounds (one time irradiation)

HeLa cells were seeded in 6-well plates with a density of 0.6 x 10^6 cells per well in 2.0 ml growth medium (low-glucose DMEM). 24 h after settling, 2 ml solutions of PROTAC **15** and **16** in growth medium were prepared in serial dilution (10 µM to 10 nM) from 10 mM DMSO stocks. The solutions of photoswitchable compounds were then irradiated at 365 nm or 457 nm for 3 mins before treating the cells for the desired length of time. Cells were lysed according to the protocol described above.

General method for in-cell testing of photoswitchable compounds (intermittent irradiation)
The same protocol as above was applied except that cells were removed from the incubator every two hours for a 1-min irradiation before being placed back into the incubator.

General method for in-cell testing of photoswitchable compounds with mchBDR4 or mchBTK HEK cell lines.
On the first day, the cells (HEK293 mchBRD4 or mchBTK) are plated (5000-7500 cells /well) in a 96-well plate using Glutamax® medium supplemented with blasticidin and hygromycin (both 1:500 dilution). After an overnight incubation, tetracycline is added to induce mchBRD4 or mchBTK expression for 18 h. Cells are then treated with pre-irradiated solutions of PROTAC **12** (serial diluted). Red fluorescence and cell growth are then recorded over time in the Incucyte S3.

6.2.4 Protocols for hypoxia-activated degraders

Chemical uncaging of 56

56 (2 mg, 0.003 mmol) was dissolved in ACN (1 ml) and water (0.5 ml). The solution was added 0.15 ml of ammonium chloride (10%) and zinc powder (5 mg, 0.076 mmol). After being stirred at room temperature for 30 mins, an aliquot was filtered over celite and submitted for LC-MS analysis.

General method for in-cell testing of the hypoxia-activated degrader

HeLa cells were seeded in 6-well plates with a density of 0.6 x 10^6 cells per well in 2.0 ml growth medium (low-glucose DMEM). 24 h after settling, PROTAC **58** (0.01 to 10 μM) or **15** (1 μM) were added to the growth medium under normoxic conditions (15% O_2) for a 2 h-incubation before being placed under hypoxic conditions (2% O2). Cells were further kept in the incubator (37 °C, 5% CO2) for another 20 h before lysis and western blot analysis.

References

1   C. Hetz and L. H. Glimcher, *Curr Opin Cell Biol*, 2011, **23**, 123.

2   L. Clausen, A. B. Abildgaard, S. K. Gersing, A. Stein, K. Lindorff-Larsen and R. Hartmann-Petersen, *Adv Protein Chem Struct Biol*, 2019, **114**, 61–83.

3   J. W. Yewdell, *Trends Cell Biol*, 2001, **11**, 294–297.

4   A. Ciechanover, *Nat Rev Mol Cell Biol*, 2015, **16**, 322–324.

5   M. P. Liebl and T. Hoppe, *Am J Physiol Cell Physiol*, 2016, **311**, 166–178.

6   K. D. Wilkinson, *Proc Natl Acad Sci U S A*, 2005, **102**, 15280–15282.

7   C. M. Pickart and M. J. Eddins, *Biochimica et Biophysica Acta (BBA) - Molecular Cell Research*, 2004, **1695**, 55–72.

8   M. Scheffner, U. Nuber and J. M. Huibregtse, *Nature*, 1995, **373**, 81–83.

9   Q. Yang, J. Zhao, D. Chen and Y. Wang, *Molecular Biomedicine 2021 2:1*, 2021, **2**, 1–17.

10   M. Maneiro, E. de Vita, D. Conole, C. S. Kounde, Q. Zhang and E. W. Tate, *Prog Med Chem*, 2021, **60**, 67–190.

11   F. E. Morreale and H. Walden, *Cell*, 2016, **165**, 248-248.e1.

12   M. J. Clague, S. Urbé and D. Komander, *Nat Rev Mol Cell Biol*, 2019, 20, 338–352.

13   M. J. Clague and S. Urbé, *Cell*, 2010, **143**, 682–685.

14   K. Tanaka, *Proc Jpn Acad Ser B Phys Biol Sci*, 2009, **85**, 12–36.

15   A. Cichanover, *Cell Death & Differentiation 2005 12:9*, 2005, **12**, 1178–1190.

16   L. D. Harris, S. Jasem and J. D. F. Licchesi, *Adv Exp Med Biol*, 2020, **1233**, 195–221.

17   H. Walden and M. M. K. Muqit, *Biochemical Journal*, 2017, **474**, 1439.

18   D. H. Wolf and R. Menssen, *FEBS Lett*, 2018, **592**, 2515–2524.

19   G. Nalepa, M. Rolfe and J. W. Harper, *Nat Rev Drug Discov*, 2006, **5**, 596–613.

20   P. M. Cromm and C. M. Crews, *ACS Cent Sci*, 2017, **3**, 830–838.

21   US6306663B1 - Controlling protein levels in eucaryotic organisms - Google Patents, https://patents.google.com/patent/US6306663B1/en, (accessed 29 January 2023).

22   M. M. Gosink and R. D. Vierstra, *Proc Natl Acad Sci U S A*, 1995, **92**, 9117–9121.

23   K. M. Sakamoto, K. B. Kim, A. Kumagai, F. Mercurio, C. M. Crews and R. J. Deshaies, *Protacs: Chimeric molecules that target proteins to the Skp1-Cullin-F box complex for ubiquitination and degradation*, 2001.

24   J. S. Schneekloth, F. N. Fonseca, M. Koldobskiy, A. Mandal, R. Deshaies, K. Sakamoto and C. M. Crews, *J Am Chem Soc*, 2004, **126**, 3748–3754.

25   A. R. Schneekloth, M. Pucheault, H. S. Tae and C. M. Crews, *Bioorg Med Chem Lett*, 2008, **18**, 5904–5908.

26   T. Ito, H. Ando, T. Suzuki, T. Ogura, K. Hotta, Y. Imamura, Y. Yamaguchi and H. Handa, *Science (1979)*, 2010, **327**, 1345–1350.

27   D. L. Buckley, J. L. Gustafson, I. Van-Molle, A. G. Roth, H. S. Tae, P. C. Gareiss, W. L. Jorgensen, A. Ciulli and C. M. Crews, *Angewandte Chemie - International Edition*, 2012, **51**, 11463–11467.

28   M. Zengerle, K. H. Chan and A. Ciulli, *ACS Chem Biol*, 2015, **10**, 1770–1777.

29   G. E. Winter, D. L. Buckley, J. Paulk, J. M. Roberts, A. Souza, S. Dhe-Paganon and J. E. Bradner, *Science (1979)*, 2015, **348**, 1376–1381.

30   X. Sun, H. Gao, Y. Yang, M. He, Y. Wu, Y. Song, Y. Tong and Y. Rao, *Signal Transduct Target Ther*, 2019, **4**, 1–33.

31   Arvinas, *Press Release*, 2020, 1–6.

32   A. Mullard, *Nat Rev Drug Discov*, 2019, **18**, 895.

33   M. Pettersson and C. M. Crews, *Drug Discov Today Technol*, 2019, **31**, 15–27.

34   G. M. Burslem and C. M. Crews, *Cell*, 2020, **181**, 102–114.

35   A. C. Lai and C. M. Crews, *Nat Rev Drug Discov*, 2017, **16**, 101–114.

36   M. Toure and C. M. Crews, *Angewandte Chemie - International Edition*, 2016, **55**, 1966–1973.

37   J. Popow, H. Arnhof, G. Bader, H. Berger, A. Ciulli, D. Covini, C. Dank, T. Gmaschitz, P. Greb, J. Karolyi-Özguer, M. Koegl, D. B. McConnell, M. Pearson, M. Rieger, J. Rinnenthal, V. Roessler, A. Schrenk, M. Spina, S. Steurer, N. Trainor, E. Traxler, C. Wieshofer, A. Zoephel and P. Ettmayer, *J Med Chem*, 2019, **62**, 2508–2520.

38   P. M. Cromm, K. T. G. Samarasinghe, J. Hines and C. M. Crews, *J Am Chem Soc*, 2018, **140**, 17019–17026.

39   I. Churcher, *J Med Chem*, 2018, **61**, 444–452.

40   D. P. Bondeson, A. Mares, I. E. D. Smith, E. Ko, S. Campos, A. H. Miah, K. E. Mulholland, N. Routly, D. L. Buckley, J. L. Gustafson, N. Zinn, P. Grandi, S. Shimamura, G. Bergamini, M. Faelth-Savitski, M. Bantscheff, C. Cox, D. A. Gordon, R. R. Willard, J. J. Flanagan, L. N. Casillas, B. J. Votta, W. den Besten, K. Famm, L. Kruidenier, P. S. Carter, J. D. Harling, I. Churcher, C. M. Crews, W. Den Besten, K. Famm, L. Kruidenier, P. S. Carter, J. D. Harling, I. Churcher, C. M. Crews, D. P. Bondeson, A. Mares, I. E. D. Smith, E. Ko, S. Campos, A. H. Miah, K. E. Mulholland, N. Routly, D. L. Buckley, L. Jeffrey, N. Zinn, P. Grandi, S. Shimamura, G. Bergamini, M. Bantscheff, C. Cox, D. A. Gordon, R. R. Willard, J. J. Flanagan, L. N. Casillas, B. J. Votta, W. Den Besten, L. Kruidenier, P. S. Carter, J. D. Harling, I. Churcher and M. Craig, *Nat Chem Biol*, 2015, **617**, 611–617.

41   P. Ottis and C. M. Crews, *ACS Chem Biol*, 2017, **12**, 892–898.

42   J. Salami and C. M. Crews, *Science (1979)*, 2017, **355**, 1163–1167.

43   R. D. Roy, C. Rosenmund and M. I. Stefan, *BMC Syst Biol*, 2017, **11**, 1–10.

44   A. Mares, A. H. Miah, I. E. D. Smith, M. Rackham, A. R. Thawani, J. Cryan, P. A. Haile, B. J. Votta, A. M. Beal, C. Capriotti, M. A. Reilly, D. T. Fisher, N. Zinn, M. Bantscheff, T. T. MacDonald, A. Vossenkamper, P. Dace, I. Churcher, A. B. Benowitz, G. Watt, J. Denyer, P. Scott-Stevens and J. D. Harling, *Commun Biol*, 2020, **3**, 1–13.

45   C. M. Crews, *Chem Biol*, 2010, 17, 551–555.

46   S. Moon and B. H. Lee, *Mol Cells*, 2018, 41, 933–942.

47   D. P. Bondeson, B. E. Smith, G. M. Burslem, A. D. Buhimschi, J. Hines, S. Jaime-Figueroa, J. Wang, B. D. Hamman, A. Ishchenko and C. M. Crews, *Cell Chem Biol*, 2018, **25**, 78-87.e5.

48   H. T. Huang, D. Dobrovolsky, J. Paulk, G. Yang, E. L. Weisberg, Z. M. Doctor, D. L. Buckley, J. H. Cho, E. Ko, J. Jang, K. Shi, H. G. Choi, J. D. Griffin, Y. Li, S. P. Treon, E. S. Fischer, J. E. Bradner, L. Tan and N. S. Gray, *Cell Chem Biol*, 2018, **25**, 88-99.e6.

49   B. E. Smith, S. L. Wang, S. Jaime-Figueroa, A. Harbin, J. Wang, B. D. Hamman and C. M. Crews, *Nat Commun*, 2019, **10**, 1–13.

50   W. Farnaby and M. Koegl, *Nat Chem Biol*, 2019, **15**, 672–680.

51   T. Ishida and A. Ciulli, *SLAS Discov*, 2021, **26**, 484–502.

52   Y. Demizu, N. Shibata, T. Hattori, N. Ohoka, H. Motoi, T. Misawa, T. Shoda, M. Naito and M. Kurihara, *Bioorg Med Chem Lett*, 2016, **26**, 4865–4869.

53   N. Ohoka, K. Nagai, N. Shibata, T. Hattori, H. Nara, N. Cho and M. Naito, *Cancer Sci*, 2017, **108**, 1032–1041.

54   Y. Itoh, M. Ishikawa, R. Kitaguchi, S. Sato, M. Naito and Y. Hashimoto, *Bioorg Med Chem*, 2011, **19**, 3229–3241.

55   B. Wang, S. Wu, J. Liu, K. Yang, H. Xie and W. Tang, *Eur J Med Chem*, 2019, **176**, 476–491.

56   J. Hines, S. Lartigue, H. Dong, Y. Qian and C. M. Crews, *Cancer Res*, 2019, **79**, 251–262.

57   R. I. Troup, C. Fallan and M. G. J. Baud, *Explor Target Antitumor Ther*, 2020, **1**, 273–312.

58   K. Cyrus, M. Wehenkel, E.-Y. Y. Choi, H.-J. J. Han, H. Lee, H. Swanson and K.-B. B. Kim, *Mol Biosyst*, 2011, **7**, 359–364.

59   M. A. Troy Bemis, J. J. La Clair and M. D. Burkart, , DOI:10.1021/acs.jmedchem.1c00482.

60   C. Donoghue, M. Cubillos-Rojas, N. Gutierrez-Prat, C. Sanchez-Zarzalejo, X. Verdaguer, A. Riera and A. R. Nebreda, *Eur J Med Chem*, 2020, **201**, 112451.

61   Y. Li, J. Yang, A. Aguilar, D. McEachern, S. Przybranowski, L. Liu, C. Y. Yang, M. Wang, X. Han and S. Wang, *J Med Chem*, 2019, **62**, 448–466.

62   X. Han, C. Wang, C. Qin, W. Xiang, E. Fernandez-Salas, C. Y. Yang, M. Wang, L. Zhao, T. Xu, K. Chinnaswamy, J. Delproposto, J. Stuckey and S. Wang, *J Med Chem*, 2019, **62**, 941–964.

63   L. W. Xia, M. Y. Ba, W. Liu, W. Cheng, C. P. Hu, Q. Zhao, Y. F. Yao, M. R. Sun and Y. T. Duan, *https://doi.org/10.4155/fmc-2019-0159*, 2019, **11**, 2919–2973.

64   A. Zorba, C. Nguyen, Y. Xu, J. Starr, K. Borzilleri, J. Smith, H. Zhu, K. A. Farley, W. D. Ding, J. Schiemer, X. Feng, J. S. Chang, D. P. Uccello, J. A. Young, C. N. Garcia-Irrizary, L. Czabaniuk, B. Schuff, R. Oliver, J. Montgomery, M. M. Hayward, J. Coe, J. Chen, M. Niosi, S. Luthra, J. C. Shah, A. El-Kattan, X. Qiu, G. M. West, M. C. Noe, V. Shanmugasundaram, A. M. Gilbert, M. F. Brown and M. F. Calabrese, *Proc Natl Acad Sci U S A*, 2018, **115**, E7285–E7292.

65   M. S. Gadd, A. Testa, X. Lucas, K. H. Chan, W. Chen, D. J. Lamont, M. Zengerle and A. Ciulli, *Nat Chem Biol*, 2017, **13**, 514–521.

66   C. W. Chung, H. Dai, E. Fernandez, C. P. Tinworth, I. Churcher, J. Cryan, J. Denyer, J. D. Harling, A. Konopacka, M. A. Queisser, C. J. Tame, G. Watt, F. Jiang, D. Qian and A. B. Benowitz, *ACS Chem Biol*, 2020, **15**, 2316–2323.

67   T. M. Leissing, L. M. Luh and P. M. Cromm, *Drug Discov Today Technol*, 2020, **37**, 73–82.

68   D. Zaidman, J. Prilusky and N. London, *J Chem Inf Model*, 2020, **60**, 4894–4903.

69   D. L. Daniels, K. M. Riching and M. Urh, *Drug Discov Today Technol*, 2019, 31, 61–68.

70   K. M. Riching, S. Mahan, C. R. Corona, M. McDougall, J. D. Vasta, M. B. Robers, M. Urh and D. L. Daniels, *ACS Chem Biol*, 2018, **13**, 2758–2770.

71   W. den Besten and J. R. Lipford, *Nat Chem Biol*, 2020, 16, 1157–1158.

72   S. L. Schreiber, *Cell*, 2021, **184**, 3–9.

73   E. J. Hanan, J. Liang, X. Wang, R. Blake, N. Blaquiere, S. T. Staben and R. A. Blake, *J Med Chem*, 2020, **63**, 11330–11361.

74   G. Dong, Y. Ding, S. He and C. Sheng, *J Med Chem*, 2021, **64**, 10606–10620.

75   T. Ito and H. Handa, *Proc Jpn Acad Ser B Phys Biol Sci*, 2020, **96**, 189.

76   S. Gao, S. Wang and Y. Song, *Biomark Res*, 2020, **8**, 1–8.

77   M. Ishoey, S. Chorn, N. Singh, M. G. Jaeger, M. Brand, J. Paulk, S. Bauer, M. A. Erb, K. Parapatics, A. C. Müller, K. L. Bennett, G. F. Ecker, J. E. Bradner and G. E. Winter, *ACS Chem Biol*, 2018, **13**, 553–560.

78   X. Tan, L. A. Irina Calderon-Villalobos, M. Sharon, C. Zheng, C. V Robinson, M. Estelle and N. Zheng, *Nature*, 2007, **446**, 640–5.

79   D. E. Bussiere, L. Xie, H. Srinivas, W. Shu, A. Burke, C. Be, J. Zhao, A. Godbole, D. King, R. G. Karki, V. Hornak, F. Xu, J. Cobb, N. Carte, A. O. Frank, A. Frommlet, P. Graff, M. Knapp, A. Fazal, B. Okram, S. Jiang, P. Y. Michellys, R. Beckwith, H. Voshol, C. Wiesmann, J. M. Solomon and J. Paulk, *Nat Chem Biol*, 2020, **16**, 15–23.

80   C. Mayor-Ruiz, S. Bauer, M. Brand, Z. Kozicka, M. Siklos, H. Imrichova, I. H. Kaltheuner, E. Hahn, K. Seiler, A. Koren, G. Petzold, M. Fellner, C. Bock, A. C. Müller, J. Zuber, M. Geyer, N. H. Thomä, S. Kubicek and G. E. Winter, *Nat Chem Biol*, 2020, **16**, 1199–1207.

81   Z. Li, Y. Lin, H. Song, X. Qin, Z. Yu, Z. Zhang, G. Dong, X. Li, X. Shi, L. Du, W. Zhao and M. Li, *Acta Pharm Sin B*, 2020, **10**, 1669–1679.

82   H. Lee, D. Puppala, E. Y. Choi, H. Swanson and K. B. Kim, *ChemBioChem*, 2007, **8**, 2058–2062.

83   I. You, E. C. Erickson, K. A. Donovan, N. A. Eleuteri, E. S. Fischer, N. S. Gray and A. Toker, *Cell Chem Biol*, 2020, **27**, 66–73.e7.

84   C. Zhang, X. R. Han, X. Yang, B. Jiang, J. Liu, Y. Xiong and J. Jin, *Eur J Med Chem*, 2018, **151**, 304–314.

85   C. E. Powell, Y. Gao, L. Tan, K. A. Donovan, R. P. Nowak, A. Loehr, M. Bahcall, E. S. Fischer, P. A. Jänne, R. E. George and N. S. Gray, *J Med Chem*, 2018, **61**, 4249–4255.

86   C. H. Kang, D. H. Lee, C. O. Lee, J. Du Ha, C. H. Park and J. Y. Hwang, *Biochem Biophys Res Commun*, 2018, **505**, 542–547.

87   J. Salami, S. Alabi, R. R. Willard, N. J. Vitale, J. Wang, H. Dong, M. Jin, D. P. McDonnell, A. P. Crew, T. K. Neklesa and C. M. Crews, *Commun Biol*, 2018, **1**, 100.

88   X. Han, C. Wang, C. Qin, W. Xiang, E. Fernandez-Salas, C. Y. Yang, M. Wang, L. Zhao, T. Xu, K. Chinnaswamy, J. Delproposto, J. Stuckey and S. Wang, *J Med Chem*, 2019, **62**, 941–964.

89   N. Shibata, K. Nagai, Y. Morita, O. Ujikawa, N. Ohoka, T. Hattori, R. Koyama, O. Sano, Y. Imaeda, H. Nara, N. Cho and M. Naito, *J Med Chem*, 2018, **61**, 543–575.

90   X. Han, L. Zhao, W. Xiang, C. Qin, B. Miao, T. Xu, M. Wang, C. Y. Yang, K. Chinnaswamy, J. Stuckey and S. Wang, *J Med Chem*, 2019, **62**, 11218–11231.

91   R. Wang, A. Abdelbaki, C. Ascanelli, A. Fung, T. Rasmusson, K. Roberts and C. Lindon, *bioRxiv 2020.07.22.215814*, , DOI:https://doi.org/10.1101/2020.07.22.215814.

92   Z. Wang, N. He, Z. Guo, C. Niu, T. Song, Y. Guo, K. Cao, A. Wang, J. Zhu, X. Zhang and Z. Zhang, *J Med Chem*, 2019, **62**, 8152–8163.

93   W. McCoull, T. Cheung, E. Anderson, P. Barton, J. Burgess, K. Byth, Q. Cao, M. P. Castaldi, H. Chen, E. Chiarparin, R. J. Carbajo, E. Code, S. Cowan, P. R. Davey, A. D. Ferguson, S. Fillery, N. O. Fuller, N. Gao, D. Hargreaves, M. R. Howard, J. Hu, A. Kawatkar, P. D. Kemmitt, E. Leo, D. M. Molina, N. O'Connell, P. Petteruti, T. Rasmusson, P. Raubo, P. B. Rawlins, P. Ricchiuto, G. R. Robb, M. Schenone, M. J. Waring, M. Zinda, S. Fawell and D. M. Wilson, *ACS Chem Biol*, 2018, **13**, 3131–3141.

94   S. Khan, X. Zhang, D. Lv, Q. Zhang, Y. He, P. Zhang, X. Liu, D. Thummuri, Y. Yuan, J. S. Wiegand, J. Pei, W. Zhang, A. Sharma, C. R. McCurdy, V. M. Kuruvilla, N. Baran, A. A. Ferrando, Y. mi Kim, A. Rogojina, P. J. Houghton, G. Huang, R. Hromas, M. Konopleva, G. Zheng and D. Zhou, *Nat Med*, 2019, **25**, 1938–1947.

95   N. Shibata, K. Shimokawa, K. Nagai, N. Ohoka, T. Hattori, N. Miyamoto, O. Ujikawa, T. Sameshima, H. Nara, N. Cho and M. Naito, *Sci Rep*, 2018, **8**, 13549.

96   G. M. Burslem, A. R. Schultz, D. P. Bondeson, C. A. Eide, S. L. S. Stevens, B. J. Druker and C. M. Crews, *Cancer Res*, 2019, **79**, 4744–4753.

97   Ashton Lai, T. Momar, D. Hellerschmieda, J. Salamia, S. J.-F. E. Ko, J. Hinesa, C. M. Crewsa, A. C. Lai, M. Toure, D. Hellerschmied, J. Salami, S. Jaime-Figueroa, E. Ko, J. Hines, C. M. Crews, Ashton Lai, T. Momar, D. Hellerschmieda, J. Salamia, S. J.-F. E. Ko, J. Hinesa, C. M. Crewsa, A. C. Lai, M. Toure, D. Hellerschmied, J. Salami, S. Jaime-Figueroa, E. Ko, J. Hines and C. M. Crews, *Angewandte Chemie International Edition*, 2016, **55**, 807–810.

98   G. Xue, J. Chen, L. Liu, D. Zhou, Y. Zuo, T. Fu and Z. Pan, *Chemical Communications*, 2020, **56**, 1521–1524.

99   H. Chen, F. Chen, S. Pei and S. Gou, *Bioorg Chem*, 2019, **87**, 191–199.

100   X. R. Han, L. Chen, Y. Wei, W. Yu, Y. Chen, C. Zhang, B. Jiao, T. Shi, L. Sun, C. Zhang, Y. Xu, M. R. Lee, Y. Luo, M. B. Plewe and J. Wang, *J Med Chem*, 2020, **63**, 4069–4080.

101   G. E. Winter, D. L. Buckley, J. Paulk, J. M. Roberts, A. Souza, S. Dhe-Paganon and J. E. Bradner, *Science (1979)*, 2015, **348**, 1376–1381.

102   J. Lu, Y. Qian, M. Altieri, H. Dong, J. Wang, K. Raina, J. Hines, J. D. Winkler, A. P. Crew, K. Coleman and C. M. Crews, *Chem Biol*, 2015, **22**, 755–763.

103   J. Hines, S. Lartigue, H. Dong, Y. Qian and C. M. Crews, *Cancer Res*, 2019, **79**, 251–262.

104   T. H. Pillow, P. Adhikari, R. A. Blake, J. Chen, G. Del Rosario, G. Deshmukh, I. Figueroa, K. E. Gascoigne, A. V. Kamath, S. Kaufman, T. Kleinheinz, K. R. Kozak, B. Latifi, D. D. Leipold, C. Sing Li, R. Li, M. M. Mulvihill, A. O'Donohue, R. K. Rowntree, J. D. Sadowsky, J. Wai, X. Wang, C. Wu, Z. Xu, H. Yao, S. F. Yu, D. Zhang, R. Zang, H. Zhang, H. Zhou, X. Zhu and P. S. Dragovich, *ChemMedChem*, 2020, **15**, 17–25.

105   M. Zengerle, K. H. Chan and A. Ciulli, *ACS Chem Biol*, 2015, **10**, 1770–1777.

106   V. Zoppi, S. J. Hughes, C. Maniaci, A. Testa, T. Gmaschitz, C. Wieshofer, M. Koegl, K. M. Riching, D. L. Daniels, A. Spallarossa and A. Ciulli, *J Med Chem*, 2019, **62**, 699–726.

107   D. Remillard, D. L. Buckley, J. Paulk, G. L. Brien, M. Sonnett, H.-S. Seo, S. Dastjerdi, M. Wühr, S. Dhe-Paganon, S. A. Armstrong and J. E. Bradner, *Angew Chem Int Ed Engl*, 2017, **56**, 5738–5743.

108   A. D. Buhimschi, H. A. Armstrong, M. Toure, S. Jaime-Figueroa, T. L. Chen, A. M. Lehman, J. A. Woyach, A. J. Johnson, J. C. Byrd and C. M. Crews, *Biochemistry*, 2018, **57**, 3564–3575.

109   C. P. Tinworth, H. Lithgow, L. Dittus, Z. I. Bassi, S. E. Hughes, M. Muelbaier, H. Dai, I. E. D. Smith, W. J. Kerr, G. A. Burley, M. Bantscheff and J. D. Harling, *ACS Chem Biol*, 2019, **14**, 342–347.

110   J. (Jack) Chi, H. Li, Z. Zhou, J. Izquierdo-Ferrer, Y. Xue, C. M. Wavelet, G. E. Schiltz, B. Zhang, M. Cristofanilli, X. Lu, I. Bahar and Y. Wan, *EBioMedicine*, 2019, **49**, 40–54.

111   F. Zhou, L. Chen, C. Cao, J. Yu, X. Luo, P. Zhou, L. Zhao, W. Du, J. Cheng, Y. Xie and Y. Chen, *Eur J Med Chem*, 2020, **187**, 111952.

112   M. Teng, J. Jiang, Z. He, N. P. Kwiatkowski, K. A. Donovan, C. E. Mills, C. Victor, J. M. Hatcher, E. S. Fischer, P. K. Sorger, T. Zhang and N. S. Gray, *Angewandte Chemie - International Edition*, 2020, **59**, 13865–13870.

113   B. Jiang, E. S. Wang, K. A. Donovan, Y. Liang, E. S. Fischer, T. Zhang and N. S. Gray, *Angewandte Chemie - International Edition*, 2019, **58**, 6321–6326.

114   B. Jiang, E. S. Wang, K. A. Donovan, Y. Liang, E. S. Fischer, T. Zhang and N. S. Gray, *Angewandte Chemie - International Edition*, 2019, **58**, 6321–6326.

115   J. M. Hatcher, E. S. Wang, L. Johannessen, N. Kwiatkowski, T. Sim and N. S. Gray, *ACS Med Chem Lett*, 2018, **9**, 540–545.

116   J. Bian, J. Ren, Y. Li, J. Wang, X. Xu, Y. Feng, H. Tang, Y. Wang and Z. Li, *Bioorg Chem*, 2018, **81**, 373–381.

117   Y. Itoh, M. Ishikawa, R. Kitaguchi, K. Okuhira, M. Naito and Y. Hashimoto, *Bioorg Med Chem Lett*, 2012, **22**, 4453–4457.

118   H. Chen, F. Chen, N. Liu, X. Wang and S. Gou, *Bioorg Chem*, 2018, **81**, 536–544.

119   K. Okuhira, T. Shoda, R. Omura, N. Ohoka, T. Hattori, N. Shibata, Y. Demizu, R. Sugihara, A. Ichino, H. Kawahara, Y. Itoh, M. Ishikawa, Y. Hashimoto, M. Kurihara, S. Itoh, H. Saito and M. Naito, *Mol Pharmacol*, 2017, **91**, 159–166.

120   C. Steinebach, S. Lindner, N. D. Udeshi, D. C. Mani, H. Kehm, S. Köpff, S. A. Carr, M. Gütschow and J. Krönke, *ACS Chem Biol*, 2018, **13**, 2771–2782.

121   M. Girardini, C. Maniaci, S. J. Hughes, A. Testa and A. Ciulli, *Bioorg Med Chem*, 2019, **27**, 2466–2479.

122   C. Steinebach, H. Kehm, S. Lindner, L. P. Vu, S. Köpff, Á. López Mármol, C. Weiler, K. G. Wagner, M. Reichenzeller, J. Krönke and M. Gütschow, *Chemical Communications*, 2019, **55**, 1821–1824.

123   D. Ma, Y. Zou, Y. Chu, Z. Liu, G. Liu, J. Chu, M. Li, J. Wang, S. Y. Sun and Z. Chang, *Theranostics*, 2020, **10**, 3708–3721.

124   J. H. R. Hsu, T. Rasmusson, J. Robinson, F. Pachl, J. Read, S. Kawatkar, D. H. O' Donovan, S. Bagal, E. Code, P. Rawlins, A. Argyrou, R. Tomlinson, N. Gao, X. Zhu, E. Chiarparin, K. Jacques, M. Shen, H. Woods, E. Bednarski, D. M. Wilson, L. Drew, M. P. Castaldi, S. Fawell and A. Bloecher, *Cell Chem Biol*, 2020, **27**, 41–46.e17.

125   F. Potjewyd, A. M. W. Turner, J. Beri, J. M. Rectenwald, J. L. Norris-Drouin, S. H. Cholensky, D. M. Margolis, K. H. Pearce, L. E. Herring and L. I. James, *Cell Chem Biol*, 2020, **27**, 47–56.e15.

126   G. M. Burslem, B. E. Smith, A. C. Lai, S. Jaime-Figueroa, D. C. McQuaid, D. P. Bondeson, M. Toure, H. Dong, Y. Qian, J. Wang, A. P. Crew, J. Hines and C. M. Crews, *Cell Chem Biol*, 2018, **25**, 67–77.e3.

127   X. Zhang, F. Xu, L. Tong, T. Zhang, H. Xie, X. Lu, X. Ren and K. Ding, *Eur J Med Chem*, 2020, **192**, 112199.

128   J. Jang, C. To, D. J. H. De Clercq, E. Park, C. M. Ponthier, B. H. Shin, M. Mushajiang, R. P. Nowak, E. S. Fischer, M. J. Eck, P. A. Jänne and N. S. Gray, *Angewandte Chemie - International Edition*, 2020, **59**, 14481–14489.

129   J. Hu, B. Hu, M. Wang, F. Xu, B. Miao, C. Y. Yang, M. Wang, Z. Liu, D. F. Hayes, K. Chinnaswamy, J. Delproposto, J. Stuckey and S. Wang, *J Med Chem*, 2019, **62**, 1420–1442.

130   B. L. Roberts, Z. X. Ma, A. Gao, E. D. Leisten, D. Yin, W. Xu and W. Tang, *ACS Chem Biol*, 2020, **15**, 1487–1496.

131   N. Ohoka, K. Okuhira, M. Ito, K. Nagai, N. Shibata, T. Hattori, O. Ujikawa, K. Shimokawa, O. Sano, R. Koyama, H. Fujita, M. Teratani, H. Matsumoto, Y. Imaeda, H. Nara, N. Cho and M. Naito, *Journal of Biological Chemistry*, 2017, **292**, 4556–4570.

132   H. Lebraud, D. J. Wright, C. N. Johnson and T. D. Heightman, *ACS Cent Sci*, 2016, **2**, 927–934.

133   L. Peng, Z. Zhang, C. Lei, S. Li, Z. Zhang, X. Ren, Y. Chang, Y. Zhang, Y. Xu and K. Ding, *ACS Med Chem Lett*, 2019, **10**, 767–772.

134   D. P. Bondeson, A. Mares, I. E. D Smith, E. Ko, S. Campos, A. H. Miah, K. E. Mulholland, N. Routly, D. L. Buckley, J. L. Gustafson, N. Zinn, P. Grandi, S. Shimamura, G. Bergamini, M. Faelth-Savitski, M. Bantscheff, C. Cox, D. A. Gordon, R. R. Willard, J. J. Flanagan, L. N. Casillas, B. J. Votta, W. Den Besten, K. Famm, L. Kruidenier, P. S. Carter, J. D. Harling, I. Churcher, C. M. Crews, I. E. D. Smith, E. Ko, S. Campos, A. H. Miah, K. E. Mulholland, N. Routly, D. L. Buckley, J. L. Gustafson, N. Zinn, P. Grandi, S. Shimamura, G. Bergamini, M. Faelth-Savitski, M. Bantscheff, C. Cox, D. A. Gordon, R. R. Willard, J. J. Flanagan, L. N. Casillas, B. J. Votta, W. Den Besten, K. Famm, L. Kruidenier, P. S. Carter, J. D. Harling, I. Churcher and C. M. Crews, *Nat Chem Biol*, 2015, **11**, 611–617.

135   J. Popow, H. Arnhof, G. Bader, H. Berger, A. Ciulli, D. Covini, C. Dank, T. Gmaschitz, P. Greb, J. Karolyi-Özguer, M. Koegl, D. B. McConnell, M. Pearson, M. Rieger, J. Rinnenthal, V. Roessler, A. Schrenk, M. Spina, S. Steurer, N. Trainor, E. Traxler, C. Wieshofer, A. Zoephel and P. Ettmayer, *J Med Chem*, 2019, **62**, 2508–2520.

136   P. M. Cromm, K. T. G. Samarasinghe, J. Hines and C. M. Crews, *J Am Chem Soc*, 2018, **140**, 17019–17026.

137   H. T. Huang, D. Dobrovolsky, J. Paulk, G. Yang, E. L. Weisberg, Z. M. Doctor, D. L. Buckley, J. H. Cho, E. Ko, J. Jang, K. Shi, H. G. Choi, J. D. Griffin, Y. Li, S. P. Treon, E. S. Fischer, J. E. Bradner, L. Tan and N. S. Gray, *Cell Chem Biol*, 2018, **25**, 88-99.e6.

138   X. Sun, J. Wang, X. Yao, W. Zheng, Y. Mao, T. Lan, L. Wang, Y. Sun, X. Zhang, Q. Zhao, J. Zhao, R. P. Xiao, X. Zhang, G. Ji and Y. Rao, *Cell Discov*, 2019, **5**, 1–13.

139   X. Zhang, V. M. Crowley, T. G. Wucherpfennig, M. M. Dix and B. F. Cravatt, *Nat Chem Biol*, 2019, **15**, 737–746.

140   G. M. Burslem, J. Song, X. Chen, J. Hines and C. M. Crews, *J Am Chem Soc*, 2018, **140**, 16428–16432.

141   J. Hines, J. D. Gough, T. W. Corson and C. M. Crews, *Proc Natl Acad Sci U S A*, 2013, **110**, 8942–8947.

142   M. Ishoey, S. Chorn, N. Singh, M. G. Jaeger, M. Brand, J. Paulk, S. Bauer, M. A. Erb, K. Parapatics, A. C. Müller, K. L. Bennett, G. F. Ecker, J. E. Bradner and G. E. Winter, *ACS Chem Biol*, 2018, **13**, 553–560.

143   M. E. Matyskiela, G. Lu, T. Ito, B. Pagarigan, C.-C. Lu, K. Miller, W. Fang, N.-Y. Wang, D. Nguyen, J. Houston, G. Carmel, T. Tran, M. Riley, L. ' Al Nosaka, G. C. Lander, S. Gaidarova, S. Xu, A. L. Ruchelman, H. Handa, J. Carmichael, T. O. Daniel, B. E. Cathers, A. Lopez-Girona and P. P. Chamberlain, *Nature*, 2016, **535**, 252–257.

144   J. P. Smalley, G. E. Adams, C. J. Millard, Y. Song, J. K. S. Norris, J. W. R. Schwabe, S. M. Cowley and J. T. Hodgkinson, *Chemical Communications*, 2020, **56**, 4476–4479.

145   K. Yang, H. Wu, Z. Zhang, E. D. Leisten, X. Nie, B. Liu, Z. Wen, J. Zhang, M. D. Cunningham and W. Tang, *ACS Med Chem Lett*, 2020, **11**, 575–581.

146   H. Wu, K. Yang, Z. Zhang, E. D. Leisten, Z. Li, H. Xie, J. Liu, K. A. Smith, Z. Novakova, C. Barinka and W. Tang, *J Med Chem*, 2019, **62**, 7042–7057.

147   M. X. Li, Y. Yang, Q. Zhao, Y. Wu, L. Song, H. Yang, M. He, H. Gao, B. L. Song, J. Luo and Y. Rao, *J Med Chem*, 2020, **63**, 4908–4928.

148   S. Tomoshige, S. Nomura, K. Ohgane, Y. Hashimoto and M. Ishikawa, *Angewandte Chemie*, 2017, **129**, 11688–11691.

149   J. Nunes, G. A. McGonagle, J. Eden, G. Kiritharan, M. Touzet, X. Lewell, J. Emery, H. Eidam, J. D. Harling and N. A. Anderson, *ACS Med Chem Lett*, 2019, **10**, 1081–1085.

150   R. R. Shah, J. M. Redmond, A. Mihut, M. Menon, J. P. Evans, J. A. Murphy, M. A. Bartholomew and D. M. Coe, *Bioorg Med Chem*, 2020, **28**, 115326.

151   M. J. Bond, L. Chu, D. A. Nalawansha, K. Li and C. M. Crews, *ACS Cent Sci*, 2020, **6**, 1367–1375.

152   R. B. Kargbo, *ACS Med Chem Lett*, 2020, 11, 2070–2071.

153   C. Donoghue, M. Cubillos-Rojas, N. Gutierrez-Prat, C. Sanchez-Zarzalejo, X. Verdaguer, A. Riera and A. R. Nebreda, *Eur J Med Chem*, 2020, **201**, 112451.

154   B. E. Smith, S. L. Wang, S. Jaime-Figueroa, A. Harbin, J. Wang, B. D. Hamman and C. M. Crews, *Nat Commun*, 2019, **10**, 1–13.

155   Y. Li, J. Yang, A. Aguilar, D. McEachern, S. Przybranowski, L. Liu, C. Y. Yang, M. Wang, X. Han and S. Wang, *J Med Chem*, 2019, **62**, 448–466.

156   B. Wang, S. Wu, J. Liu, K. Yang, H. Xie and W. Tang, *Eur J Med Chem*, 2019, **176**, 476–491.

157   K. M. Sakamoto, K. B. Kim, A. Kumagai, F. Mercurio, C. M. Crews and R. J. Deshaies, *Proc Natl Acad Sci U S A*, 2001, **98**, 8554–8559.

158   M. de Wispelaere, G. Du, K. A. Donovan, T. Zhang, N. A. Eleuteri, J. C. Yuan, J. Kalabathula, R. P. Nowak, E. S. Fischer, N. S. Gray and P. L. Yang, *Nat Commun*, 2019, **10**, 3468.

159   Q. Zhao, T. Lan, S. Su and Y. Rao, *Chemical Communications*, 2019, **55**, 369–372.

160   S. Wang, L. Han, J. Han, P. Li, Q. Ding, Q. J. Zhang, Z. P. Liu, C. Chen and Y. Yu, *Nat Chem Biol*, 2019, **15**, 1223–1231.

161   Z. I. Bassi, M. C. Fillmore, A. H. Miah, T. D. Chapman, C. Maller, E. J. Roberts, L. C. Davis, D. E. Lewis, N. W. Galwey, K. E. Waddington, V. Parravicini, A. L. Macmillan-Jones, C. Gongora, P. G. Humphreys, I. Churcher, R. K. Prinjha and D. F. Tough, *ACS Chem Biol*, 2018, **13**, 2862–2867.

162   W. Li, C. Gao, L. Zhao, Z. Yuan, Y. Chen and Y. Jiang, *Eur J Med Chem*, 2018, **151**, 237–247.

163   N. E. A. Chessum, S. Y. Sharp, J. J. Caldwell, A. E. Pasqua, B. Wilding, G. Colombano, I. Collins, B. Ozer, M. Richards, M. Rowlands, M. Stubbs, R. Burke, P. C. McAndrew, P. A. Clarke, P. Workman, M. D. Cheeseman and K. Jones, *J Med Chem*, 2018, **61**, 918–933.

164   X. Mu, L. Bai, Y. Xu, J. Wang and H. Lu, *Biochem Biophys Res Commun*, 2020, **521**, 833–839.

165   Y. Itoh, R. Kitaguchi, M. Ishikawa, M. Naito and Y. Hashimoto, *Bioorg Med Chem*, 2011, **19**, 6768–6778.

166   Y. Song, P. M. C. Park, L. Wu, A. Ray, S. Picaud, D. Li, V. K. Wimalasena, T. Du, P. Filippakopoulos, K. C. Anderson, J. Qi and D. Chauhan, *Leukemia*, 2019, **33**, 2685–2694.

167   H. Tovell, A. Testa, H. Zhou, N. Shpiro, C. Crafter, A. Ciulli and D. R. Alessi, *ACS Chem Biol*, 2019, **14**, 2024–2034.

168   M. Wang, J. Lu, M. Wang, C. Y. Yang and S. Wang, *J Med Chem*, 2020, **63**, 7510–7528.

169   M. Schiedel, D. Herp, S. Hammelmann, S. Swyter, A. Lehotzky, D. Robaa, J. Oláh, J. Ovádi, W. Sippl and M. Jung, *J Med Chem*, 2018, **61**, 482–491.

170   A. Bensimon, M. D. Pizzagalli, F. Kartnig, V. Dvorak, P. Essletzbichler, G. E. Winter and G. Superti-Furga, *Cell Chem Biol*, 2020, **27**, 728–739.e9.

171   X. Wang, S. Feng, J. Fan, X. Li, Q. Wen and N. Luo, *Biochem Pharmacol*, 2016, **116**, 200–209.

172   W. Farnaby, M. Koegl, M. J. Roy, C. Whitworth, E. Diers, N. Trainor, D. Zollman, S. Steurer, J. Karolyi-Oezguer, C. Riedmueller, T. Gmaschitz, J. Wachter, C. Dank, M. Galant, B. Sharps, K. Rumpel, E. Traxler, T. Gerstberger, R. Schnitzer, O. Petermann, P. Greb, H. Weinstabl, G. Bader, A. Zoephel, A. Weiss-Puxbaum, K. Ehrenhöfer-Wölfer, S. Wöhrle, G. Boehmelt, J. Rinnenthal, H.

Arnhof, N. Wiechens, M. Y. Wu, T. Owen-Hughes, P. Ettmayer, M. Pearson, D. B. McConnell and A. Ciulli, *Nat Chem Biol*, 2019, **15**, 672–680.

173   R. B. Kargbo, *ACS Med Chem Lett*, 2020, **11**, 1086–1087.

174   H. Zhou, L. Bai, R. Xu, Y. Zhao, J. Chen, D. McEachern, K. Chinnaswamy, B. Wen, L. Dai, P. Kumar, C. Y. Yang, Z. Liu, M. Wang, L. Liu, J. L. Meagher, H. Yi, D. Sun, J. A. Stuckey and S. Wang, *J Med Chem*, 2019, **62**, 11280–11300.

175   N. Ohoka, K. Nagai, N. Shibata, T. Hattori, H. Nara, N. Cho and M. Naito, *Cancer Sci*, 2017, **108**, 1032–1041.

176   M. C. Silva, F. M. Ferguson, Q. Cai, K. A. Donovan, G. Nandi, D. Patnaik, T. Zhang, H. T. Huang, D. E. Lucente, B. C. Dickerson, T. J. Mitchison, E. S. Fischer, N. S. Gray and S. J. Haggarty, *Elife*, 2019, **8**, e45457.

177   A. P. Crew, K. Raina, H. Dong, Y. Qian, J. Wang, D. Vigil, Y. V. Serebrenik, B. D. Hamman, A. Morgan, C. Ferraro, K. Siu, T. K. Neklesa, J. D. Winkler, K. G. Coleman and C. M. Crews, *J Med Chem*, 2018, **61**, 583–598.

178   L. N. Gechijian, D. L. Buckley, M. A. Lawlor, J. M. Reyes, J. Paulk, C. J. Ott, G. E. Winter, M. A. Erb, T. G. Scott, M. Xu, H. S. Seo, S. Dhe-Paganon, N. P. Kwiatkowski, J. A. Perry, J. Qi, N. S. Gray and J. E. Bradner, *Nat Chem Biol*, 2018, **14**, 405–412.

179   B. Zhao and K. Burgess, *Mol Pharm*, 2019, **16**, 4313–4318.

180   C. Maniaci, S. J. Hughes, A. Testa, W. Chen, D. J. Lamont, S. Rocha, D. R. Alessi, R. Romeo and A. Ciulli, *Nat Commun*, 2017, **8**, 830.

181   Z. Li, B. J. Pinch, C. M. Olson, K. A. Donovan, R. P. Nowak, C. E. Mills, D. A. Scott, Z. M. Doctor, N. A. Eleuteri, M. Chung, P. K. Sorger, E. S. Fischer and N. S. Gray, *Cell Chem Biol*, 2020, **27**, 57–65.e9.

182   K. Montrose and G. W. Krissansen, *Biochem Biophys Res Commun*, 2014, **453**, 735–740.

183   X. Li and Y. Song, *J Hematol Oncol*, 2020, 13, 50.

184   J. Nunes, G. A. McGonagle, J. Eden, G. Kiritharan, M. Touzet, X. Lewell, J. Emery, H. Eidam, J. D. Harling and N. A. Anderson, *ACS Med Chem Lett*, 2019, **10**, 1081–1085.

185   C. C. Ward, J. I. Kleinman, S. M. Brittain, P. S. Lee, C. Y. S. Chung, K. Kim, Y. Petri, J. R. Thomas, J. A. Tallarico, J. M. McKenna, M. Schirle and D. K. Nomura, *ACS Chem Biol*, 2019, **14**, 2430–2440.

186   B. Tong, J. N. Spradlin, L. F. T. Novaes, E. Zhang, X. Hu, M. Moeller, S. M. Brittain, L. M. McGregor, J. M. McKenna, J. A. Tallarico, M. Schirle, T. J. Maimone and D. K. Nomura, *ACS Chem Biol*, 2020, **15**, 1788–1794.

187   X. Zhang, V. M. Crowley, T. G. Wucherpfennig, M. M. Dix and B. F. Cravatt, *Nat Chem Biol*, 2019, **15**, 737–746.

188   S. M. Banik, K. Pedram, S. Wisnovsky, G. Ahn, N. M. Riley and C. R. Bertozzi, *Nature*, 2020, **584**, 291–297.

189   D. Takahashi and H. Arimoto, *Autophagy*, 2020, **16**, 765–766.

190   D. Takahashi, J. Moriyama, T. Nakamura, E. Miki, E. Takahashi, A. Sato, T. Akaike, K. Itto-Nakama and H. Arimoto, *Mol Cell*, 2019, **76**, 797–810.e10.

191   Z. Li, C. Zhu, Y. Ding, Y. Fei and B. Lu, *Autophagy*, 2020, **16**, 185–187.

192   S. U. Siriwardena, D. N. P. Munkanatta Godage, V. M. Shoba, S. Lai, M. Shi, P. Wu, S. K. Chaudhary, S. L. Schreiber and A. Choudhary, *J Am Chem Soc*, 2020, **142**, 14052–14057.

193   N. J. Henning, L. Boike, J. N. Spradlin, C. C. Ward, G. Liu, E. Zhang, B. P. Belcher, S. M. Brittain, M. J. Hesse, D. Dovala, L. M. McGregor, R. Valdez Misiolek, L. W. Plasschaert, D. J. Rowlands, F. Wang, A. O. Frank, D. Fuller, A. R. Estes, K. L. Randal, A. Panidapu, J. M. McKenna, J. A. Tallarico, M. Schirle and D. K. Nomura, *Nat Chem Biol*, , DOI:10.1038/s41589-022-00971-2.

194   S. Yamazoe, J. Tom, Y. Fu, W. Wu, L. Zeng, C. Sun, Q. Liu, J. Lin, K. Lin, W. J. Fairbrother and S. T. Staben, *J Med Chem*, 2020, **63**, 2807–2813.

195   S. D. Edmondson, B. Yang and C. Fallan, *Bioorg Med Chem Lett*, 2019, 29, 1555–1564.

196   A. Pike, B. Williamson, S. Harlfinger, S. Martin and D. F. McGinnity, *Drug Discov Today*, 2020, 25, 1793–1800.

197   C. Cantrill, P. Chaturvedi, C. Rynn, J. Petrig Schaffland, I. Walter and M. B. Wittwer, *Drug Discov Today*, 2020, **25**, 969–982.

198   D. W. Bartlett and A. M. Gilbert, *Chem Soc Rev*, 2022, **51**, 3477–3486.

199   J. Jang, C. To, D. J. H. De Clercq, E. Park, C. M. Ponthier, B. H. Shin, M. Mushajiang, R. P. Nowak, E. S. Fischer, M. J. Eck, P. A. Jänne and N. S. Gray, *Angewandte Chemie - International Edition*, 2020, **59**, 14481–14489.

200   X. Zhang, F. Xu, L. Tong, T. Zhang, H. Xie, X. Lu, X. Ren and K. Ding, *Eur J Med Chem*, 2020, **192**, 112199.

201   Y. Sun, N. Ding, Y. Song, Z. Yang, W. Liu, J. Zhu and Y. Rao, *Leukemia*, 2019, 33, 2105–2110.

202   N. Bery, A. Miller and T. Rabbitts, *Nat Commun*, , DOI:10.1038/s41467-020-17022-w.

203   S. Alabi, S. Jaime-Figueroa, Z. Yao, Y. Gao, J. Hines, K. T. G. Samarasinghe, L. Vogt, N. Rosen and C. M. Crews, *bioRxiv*, , DOI:10.1101/2020.08.10.245159.

204   Y. Sun, X. Zhao, N. Ding, H. Gao, Y. Wu, Y. Yang, M. Zhao, J. Hwang, Y. Song, W. Liu and Y. Rao, *Cell Res*, 2018, **28**, 779–781.

205   L. Zhang, B. Riley-Gillis, P. Vijay and Y. Shen, *Mol Cancer Ther*, 2019, **18**, 1302–1311.

206   P. Ottis, C. Palladino, P. Thienger, A. Britschgi, C. Heichinger, M. Berrera, A. Julien-Laferriere, F. Roudnicky, T. Kam-Thong, J. R. Bischoff, B. Martoglio and P. Pettazzoni, *ACS Chem. Biol.*, 2019, **14**, 2215–2223.

207   A. M. Kurimchak, C. Herrera-Montávez, S. Montserrat-Sangrà, D. Araiza-Olivera, J. Hu, R. Neumann-Domer, M. Kuruvilla, A. Bellacosa, J. R. Testa, J. Jin and J. S. Duncan, *Sci Signal*, 2022, **15**, eabn2707.

208   K. Moreau, M. Coen, A. X. Zhang, F. Pachl, M. P. Castaldi, G. Dahl, H. Boyd, C. Scott and P. Newham, *Br J Pharmacol*, 2020, **177**, 1709–1718.

209   K. A. Donovan, J. An, R. P. Nowak, J. C. Yuan, E. C. Fink, B. C. Berry, B. L. Ebert and E. S. Fischer, *Elife*, 2018, **7**, 1–25.

210   X. Liu, Y. Zhang, L. D. Ward, Q. Yan, T. Bohnuud, R. Hernandez, S. Lao, J. Yuan and F. Fan, *Scientific Reports 2021 11:1*, 2021, **11**, 1–11.

211   K. Moreau, M. Coen, A. X. Zhang, F. Pachl, M. P. Castaldi, G. Dahl, H. Boyd, C. Scott and P. Newham, *Br J Pharmacol*, 2020, **177**, 1709.

212   T. H. Pillow, P. Adhikari, R. A. Blake, J. Chen, G. del Rosario, G. Deshmukh, I. Figueroa, K. E. Gascoigne, A. v. Kamath, S. Kaufman, T. Kleinheinz, K. R. Kozak, B. Latifi, D. D. Leipold, C. Sing Li, R. Li, M. M. Mulvihill, A. O'Donohue, R. K. Rowntree, J. D. Sadowsky, J. Wai, X. Wang, C. Wu, Z. Xu, H. Yao, S. F. Yu, D. Zhang, R. Zang, H. Zhang, H. Zhou, X. Zhu and P. S. Dragovich, *ChemMedChem*, 2020, **15**, 17–25.

213   M. Maneiro, N. Forte, M. M. Shchepinova, C. S. Kounde, V. Chudasama, J. R. Baker and E. W. Tate, *ACS Chem Biol*, 2020, **15**, 1306–1312.

214   H. Chen, J. Liu, H. Ü. Kaniskan, W. Wei and J. Jin, *J Med Chem*, 2021, **64**, 12273–12285.

215   J. Liu, H. Chen, Y. Liu, Y. Shen, F. Meng, H. Ü. Kaniskan, J. Jin and W. Wei, *J Am Chem Soc*, 2021, **143**, 7380.

216   N. Ankenbruck, T. Courtney, Y. Naro and A. Deiters, *Angew Chem Int Ed Engl*, 2018, **57**, 2768.

217   I. Ahmed and L. Fruk, *Mol Biosyst*, 2013, **9**, 565–570.

218   J. Broichhagen, J. A. Frank and D. Trauner, *Acc Chem Res*, 2015, **48**, 1947–1960.

219   K. Hüll, J. Morstein and D. Trauner, *Chem Rev*, 2018, **118**, 10710–10747.

220   D. Hanahan, *Cancer Discov*, 2022, **12**, 31–46.

221   N. D. Amoêdo, J. P. Valencia, M. F. Rodrigues, A. Galina and F. D. Rumjanek, *Biosci Rep*, 2013, **33**, 865–873.

222   B. Muz, P. de la Puente, F. Azab and A. K. Azab, *Hypoxia*, 2015, **3**, 83.

223   F. W. Hunter, B. G. Wouters and W. R. Wilson, *Br J Cancer*, 2016, **114**, 1071–1077.

224   Y. H. Jin, M. C. Lu, Y. Wang, W. X. Shan, X. Y. Wang, Q. D. You and Z. Y. Jiang, *J Med Chem*, 2020, **63**, 4644–4654.

225   M. Reynders, B. S. Matsuura, M. Bérouti, D. Simoneschi, A. Marzio, M. Pagano and D. Trauner, *Sci Adv*, 2020, **6**, eaay5064.

226   P. Pfaff, K. T. G. Samarasinghe, C. M. Crews and E. M. Carreira, *ACS Cent Sci*, 2019, **5**, 1682–1690.

227   Qisi Zhang, C. S. Kounde, Milon Mondal, J. L. Greenfield, J. R. Baker, Sergei Kotelnikov, Mikhail Ignatov, C. P. Tinworth, Leran Zhang, Daniel Conole, E. D. Vita, Dima Kozakov, Adam McCluskey, J. D. Harling, M. J. Fuchter and E. W. Tate, *Chemical Communications*, , DOI:10.1039/D2CC03092F.

228   G. Xue, K. Wang, D. Zhou, H. Zhong and Z. Pan, *J Am Chem Soc*, 2019, **141**, 18370–18374.

229   J. Liu, H. Chen, L. Ma, Z. He, D. Wang, Y. Liu, Q. Lin, T. Zhang, N. Gray, H. Ü. Kaniskan, J. Jin and W. Wei, *Sci. Adv*, 2020, **6**, eaay5154.

230   S. Konermann, M. D. Brigham, A. E. Trevino, P. D. Hsu, M. Heidenreich, L. Cong, R. J. Platt, D. A. Scott, G. M. Church and F. Zhang, *Nature*, 2013, **500**, 472.

231   T. Courtney and A. Deiters, *Curr Opin Chem Biol*, 2018, **46**, 99–107.

232   L. de Mena, P. Rizk and D. E. Rincon-Limas, *Front Genet*, 2018, **9**, 518.

233   D. Hartmann, J. M. Smith, G. Mazzotti, R. Chowdhry and M. J. Booth, *Biochem Soc Trans*, 2020, **48**, 1645–1659.

234   X. X. Zhou, H. K. Chung, A. J. Lam and M. Z. Lin, *Science*, 2012, **338**, 810.

235   A. S. Baker and A. Deiters, *ACS Chem Biol*, 2014, **9**, 1398–1407.

236   J. M. Christie, M. Salomon, K. Nozue, M. Wada and W. R. Briggs, *Proc Natl Acad Sci U S A*, 1999, **96**, 8779–8783.

237   J. T. M. Kennis, I. H. M. van Stokkum, S. Crosson, M. Gauden, K. Moffat and R. van Grondelle, *J Am Chem Soc*, 2004, **126**, 4512–4513.

238   C. Renicke, D. Schuster, S. Usherenko, L. O. Essen and C. Taxis, *Chem Biol*, 2013, **20**, 619–626.

239   K. M. Bonger, R. Rakhit, A. Y. Payumo, J. K. Chen and T. J. Wandless, *ACS Chem Biol*, 2014, **9**, 111–115.

240   Q. Delacour, C. Li, M. A. Plamont, E. Billon-Denis, I. Aujard, T. le Saux, L. Jullien and A. Gautier, *ACS Chem Biol*, 2015, **10**, 1643–1647.

241   E. S. Fischer, K. Böhm, J. R. Lydeard, H. Yang, M. B. Stadler, S. Cavadini, J. Nagel, F. Serluca, V. Acker, G. M. Lingaraju, R. B. Tichkule, M. Schebesta, W. C. Forrester, M. Schirle, U. Hassiepen, J. Ottl, M. Hild, R. E. J. Beckwith, J. W. Harper, J. L. Jenkins and N. H. Thomä, *Nature*, 2014, **512**, 49–53.

242   C. Galdeano, M. S. Gadd, P. Soares, S. Scaffidi, I. Van Molle, I. Birced, S. Hewitt, D. M. Dias and A. Ciulli, *J Med Chem*, 2014, **57**, 17.

243   A. A. Akuffo, A. Y. Alontaga, R. Metcalf, M. S. Beatty, A. Becker, J. M. McDaniel, R. S. Hesterberg, W. E. Goodheart, S. Gunawan, M. Ayaz, Y. Yang, M. Rezaul Karim, M. E. Orobello, K. Daniel, W. Guida, J. A. Yoder, A. M. Rajadhyaksha, E. Schönbrunn, H. R. Lawrence, N. J. Lawrence and P. K. Epling-Burnette, *J Biol Chem*, 2018, **293**, 6187.

244   D. L. Buckley, I. van Molle, P. C. Gareiss, H. S. Tae, J. Michel, D. J. Noblin, W. L. Jorgensen, A. Ciulli and C. M. Crews, *J Am Chem Soc*, 2012, **134**, 4465–4468.

245   M. E. Matyskiela, G. Lu, T. Ito, B. Pagarigan, C. C. Lu, K. Miller, W. Fang, N. Y. Wang, D. Nguyen, J. Houston, G. Carmel, T. Tran, M. Riley, L. Nosaka, G. C. Lander, S. Gaidarova, S. Xu, A. L. Ruchelman, H. Handa, J. Carmichael, T. O. Daniel, B. E. Cathers, A. Lopez-Girona and P. P. Chamberlain, *Nature*, 2016, **535**, 252–257.

246   P. Klán, T. Šolomek, C. G. Bochet, A. Blanc, R. Givens, M. Rubina, V. Popik, A. Kostikov and J. Wirz, *Chem Rev*, 2013, 113, 119–191.

247   G. C. R. Ellis-Davies, *Nat Methods*, 2007, 4, 619–628.

248   Y. v. Il'ichev, M. A. Schwörer and J. Wirz, *J Am Chem Soc*, 2004, **126**, 4581–4595.

249   C. S. Kounde and E. W. Tate, *J Med Chem*, 2020, **63**, 15483–15493.

250   B. N. Devaiah, C. Case-Borden, A. Gegonne, C. H. Hsu, Q. Chen, D. Meerzaman, A. Dey, K. Ozato and D. S. Singer, *Nature Structural & Molecular Biology 2016 23:6*, 2016, **23**, 540–548.

251   H. A. Ali, Y. Li, A. H. M. Bilal, T. Qin, Z. Yuan and W. Zhao, *Front Pharmacol*, 2022, **13**, 366.

252   B. N. Devaiah, J. Mu, B. Akman, S. Uppal, J. D. Weissman, D. Cheng, L. Baranello, Z. Nie, D. Levens and D. S. Singer, *Proc Natl Acad Sci U S A*, 2020, **117**, 13457–13467.

253   T. Shimamura, Z. Chen, M. Soucheray, J. Carretero, E. Kikuchi, J. H. Tchaicha, Y. Gao, K. A. Cheng, T. J. Cohoon, J. Qi, E. Akbay, A. C. Kimmelman, A. L. Kung, J. E. Bradner and K. K. Wong, *Clin Cancer Res*, 2013, **19**, 6183–6192.

254   A. G. Cochran, A. R. Conery and R. J. Sims, *Nat Rev Drug Discov*, 2019, **18**, 609–628.

255   B. Donati, E. Lorenzini and A. Ciarrocchi, *Mol Cancer*, , DOI:10.1186/S12943-018-0915-9.

256   J. Lu, Y. Qian, M. Altieri, H. Dong, J. Wang, K. Raina, J. Hines, J. D. Winkler, A. P. Crew, K. Coleman and C. M. Crews, *Chem Biol*, 2015, **22**, 755–763.

257   J. Lu, Y. Qian, K. Raina, M. Altieri, H. Dong, J. Wang, X. Chen, A. Crew, K. Coleman, C. Crews and J. Winkler, *Blood*, 2015, **126**, 2050–2050.

258   F. C. Lam, Y. W. Kong, Q. Huang, T. L. Vu Han, A. D. Maffa, E. M. Kasper and M. B. Yaffe, *Nat Commun*, , DOI:10.1038/S41467-020-17503-Y.

259   A. Alqahtani, K. Choucair, M. Ashraf, D. M. Hammouda, A. Alloghbi, T. Khan, N. Senzer and J. Nemunaitis, *Future Sci OA*, , DOI:10.4155/FSOA-2018-0115/ASSET/IMAGES/LARGE/FIGURE1.JPEG.

260   B. Nabet, J. M. Roberts, D. L. Buckley, J. Paulk, S. Dastjerdi, A. Yang, A. L. Leggett, M. A. Erb, M. A. Lawlor, A. Souza, T. G. Scott, S. Vittori, J. A. Perry, J. Qi, G. E. Winter, K. K. Wong, N. S. Gray and J. E. Bradner, *Nat Chem Biol*, 2018, **14**, 431–441.

261   M. Maneiro, N. Forte, M. M. Shchepinova, C. S. Kounde, V. Chudasama, J. R. Baker and E. W. Tate, *ACS Chem Biol*, 2020, **15**, 1306–1312.

262 M. Luo, J. Spradlin, S. Brittain, J. McKenna, J. Tallarico, M. Schirle, T. Maimone and D. Nomura, , DOI:10.1101/2020.07.12.198150.

263 C. C. Ward, J. I. Kleinman, S. M. Brittain, P. S. Lee, C. Y. S. Chung, K. Kim, Y. Petri, J. R. Thomas, J. A. Tallarico, J. M. McKenna, M. Schirle and D. K. Nomura, *ACS Chem Biol*, 2019, **14**, 2430–2440.

264 X. Zhang, V. M. Crowley, T. G. Wucherpfennig, M. M. Dix and B. F. Cravatt, *Nat Chem Biol*, 2019, **15**, 737–746.

265 H. Lusic and A. Deiters, *ChemInform*, , DOI:10.1002/CHIN.200645122.

266 WO2008022006A2 - Arylalkoxyl hepatitis c virus protease inhibitors - Google Patents, https://patents.google.com/patent/WO2008022006A2/en, (accessed 30 January 2023).

267 J. Lu, Y. Qian, M. Altieri, H. Dong, J. Wang, K. Raina, J. Hines, J. D. Winkler, A. P. Crew, K. Coleman and C. M. Crews, *Chem Biol*, 2015, **22**, 755–763.

268 P. P. Chamberlain and L. G. Hamann, *Nat Chem Biol*, 2019, **15**, 937–944.

269 D. Martinez Molina and P. Nordlund, *Annu Rev Pharmacol Toxicol*, 2016, **56**, 141–161.

270 Y. Naro, K. Darrah and A. Deiters, *J Am Chem Soc*, 2020, **142**, 2193–2197.

271 et al. Agostinis P, Berg K, Cengel K., *Ca Cancer J Clin*, 2017, **61**, 250–281.

272 K. Kunzi-Rapp, *Photonics Lasers Med*, 2015, **4**, 378–379.

273 C. M. Moore, D. Pendse and M. Emberton, *Nat Clin Pract Urol*, 2009, **6**, 18–30.

274 G. Gunaydin, M. E. Gedik and S. Ayan, *Front Chem*, 2021, **9**, 400.

275 J. Wang, G. Liu, K. Leung, R. Loffroy, P.-X. Lu and Y. J. Wáng, *Curr Pharm Des*, 2015, **21**, 5401–5416.

276 Z.-Q. Wang, D. Zhang and C. Bao, , DOI:10.1002/ange.201800713.

277 D. L. Pettit, S. S. H. Wang, K. R. Gee and G. J. Augustine, *Neuron*, 1997, **19**, 465–471.

278 M. C. Pirrung, W. H. Pieper, K. P. Kaliappan and M. R. Dhananjeyan, *Proc Natl Acad Sci U S A*, 2003, **100**, 12548–12553.

279 M. Klausen and M. Blanchard-Desce, *Journal of Photochemistry and Photobiology C: Photochemistry Reviews*, 2021, **48**, 100423.

280 X. Zhu, J. Zhang, J. Liu and Y. Zhang, *Advanced Science*, , DOI:10.1002/ADVS.201901358.

281 G. Chen, H. Qiu, P. N. Prasad and X. Chen, *Chem Rev*, 2014, **114**, 5161–5214.

282 Y. Yang, Q. Shao, R. Deng, C. Wang, X. Teng, K. Cheng, Z. Cheng, L. Huang, Z. Liu, X. Liu and B. Xing, *Angew Chem Int Ed Engl*, 2012, **51**, 3125–3129.

283 C. Ran, Z. Zhang, J. Hooker and A. Moore, *Mol Imaging Biol*, 2012, **14**, 156–162.

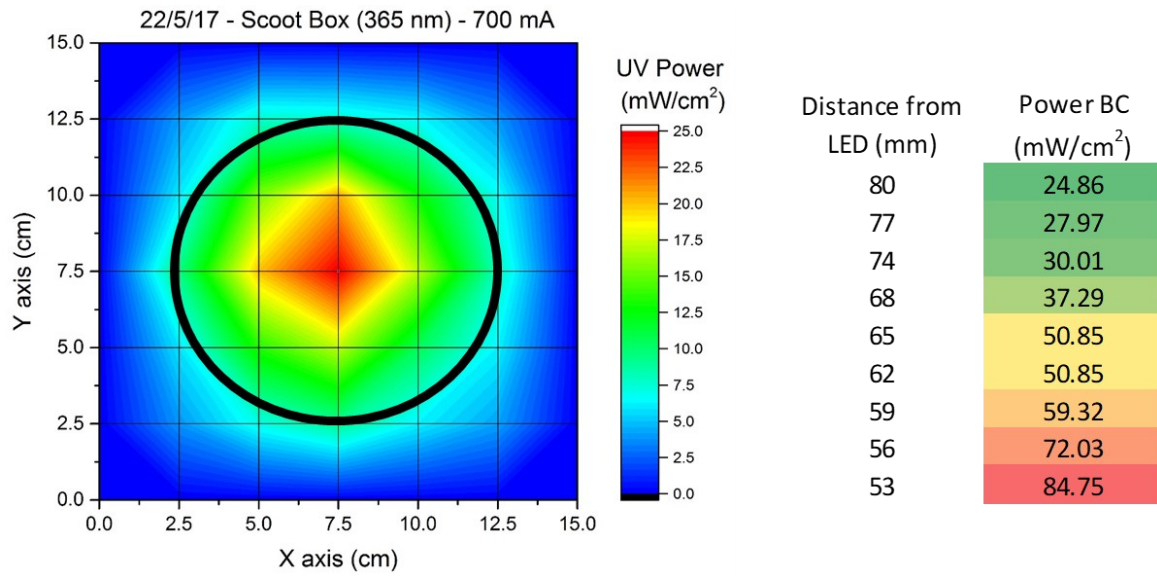284 J. v. Jelley, *Photochemical and Photobiological Reviews*, 1983, 275–318.

285   N. Kotagiri, M. L. Cooper, M. Rettig, C. Egbulefu, J. Prior, G. Cui, P. Karmakar, M. Zhou, X. Yang, G. Sudlow, L. Marsala, C. Chanswangphuwana, L. Lu, L. M. Habimana-Griffin, M. Shokeen, X. Xu, K. Weilbaecher, M. Tomasson, G. Lanza, J. F. Dipersio and S. Achilefu, *Nat Commun*, , DOI:10.1038/S41467-017-02758-9.

286   E. K. J. Pauwels, M. J. Ribeiro, J. H. M. B. Stoot, V. R. McCready, M. Bourguignon and B. Mazière, *Nucl Med Biol*, 1998, **25**, 317–322.

287   A. Almuhaideb, N. Papathanasiou and J. Bomanji, *Ann Saudi Med*, 2011, **31**, 3.

288   A. N. H. Creager, *Stud Hist Philos Biol Biomed Sci*, 2009, **40**, 29.

289   Y. Cheng, A. P. Kiess, J. M. Herman, M. G. Pomper, S. J. Meltzer and J. M. Abraham, *PLoS One*, , DOI:10.1371/JOURNAL.PONE.0128152.

290   B. A. Hartl, H. Hirschberg, L. Marcu and S. R. Cherry, , DOI:10.1615/JEnvironPatholToxicolOncol.

291   R. S. Stubbs and S. K. Wickremesekera, *HPB (Oxford)*, 2004, **6**, 133.

292   C. S. Kounde, M. M. Shchepinova, C. N. Saunders, M. Muelbaier, M. D. Rackham, J. D. Harling and E. W. Tate, *Chemical Communications*, 2020, **56**, 5532–5535.

293   W. Szymański, J. M. Beierle, H. A. V. Kistemaker, W. A. Velema and B. L. Feringa, *Chem Rev*, 2013, 113, 6114–6178.

294   M. J. Fuchter, *J Med Chem*, 2020, 63, 11436–11447.

295   M. Borowiak, W. Nahaboo, M. Reynders, K. Nekolla, P. Jalinot, J. Hasserodt, M. Rehberg, M. Delattre, S. Zahler, A. Vollmar, D. Trauner and O. Thorn-Seshold, *Cell*, 2015, **162**, 403–411.

296   A. A. Beharry and G. A. Woolley, *Chem Soc Rev*, 2011, **40**, 4422–4437.

297   F. A. Jerca, V. V. Jerca and R. Hoogenboom, *Nature Reviews Chemistry 2021 6:1*, 2021, **6**, 51–69.

298   A. Polosukhina, J. Litt, I. Tochitsky, J. Nemargut, Y. Sychev, I. de Kouchkovsky, T. Huang, K. Borges, D. Trauner, R. N. van Gelder and R. H. Kramer, *Neuron*, 2012, **75**, 271–282.

299   O. Sadovski, A. A. Beharry, F. Zhang and G. A. Woolley, *Angew Chem Int Ed Engl*, 2009, **48**, 1484–1486.

300   K. Wu, J. Sun, Y. Ma, D. Wei, O. Lee, H. Luo and H. Fan, *J Mater Chem B*, 2020, **8**, 9212–9226.

301   C. E. Weston, R. D. Richardson, P. J. Haycock, A. J. P. White and M. J. Fuchter, *Arylazopyrazoles: Azoheteroarene photoswitches offering quantitative isomerization and long thermal half-lives. Supplementary Information*, .

302   J. Calbo, C. E. Weston, A. J. P. White, H. S. Rzepa, J. Contreras-García and M. J. Fuchter, *J Am Chem Soc*, 2017, **139**, 1261–1274.

303   C. E. Weston, R. D. Richardson, P. R. Haycock, A. J. P. White and M. J. Fuchter, *J Am Chem Soc*, 2014, **136**, 11878–11881.

304   D. Bléger, J. Schwarz, A. M. Brouwer and S. Hecht, *J Am Chem Soc*, 2012, **134**, 20597–20600.

305   J. Volarić, W. Szymanski, N. A. Simeth and B. L. Feringa, *Chem Soc Rev*, 2021, **50**, 12377–12449.

306   C. E. Weston, A. Krämer, F. Colin, Ö. Yildiz, M. G. J. Baud, F. J. Meyer-Almes and M. J. Fuchter, *ACS Infect Dis*, 2016, **3**, 152–161.

307   P. Y. Lam, A. R. Thawani, E. Balderas, A. J. P. White, D. Chaudhuri, M. J. Fuchter and R. T. Peterson, *J Am Chem Soc*, 2020, **142**, 17457–17468.

308   J. L. Greenfield, M. A. Gerkman, R. S. L. Gibson, G. G. D. Han and M. J. Fuchter, *J Am Chem Soc*, 2021, **143**, 15250–15257.

309   A. J. Mohamed, L. Yu, C. M. Bäckesjö, L. Vargas, R. Faryal, A. Aints, B. Christensson, A. Berglöf, M. Vihinen, B. F. Nore and C. I. Edvard Smith, *Immunol Rev*, 2009, **228**, 58–73.

310   S. Middendorp, G. M. Dingjan, A. Maas, K. Dahlenborg and R. W. Hendriks, *J Immunol*, 2003, **171**, 5988–5996.

311   T. Wen, J. Wang, Y. Shi, H. Qian and P. Liu, *Leukemia 2020 35:2*, 2020, **35**, 312–332.

312   J. A. Burger and J. J. Buggy, *Leuk Lymphoma*, 2013, **54**, 2385–2391.

313   S. Pal Singh, F. Dammeijer and R. W. Hendriks, *Molecular Cancer 2018 17:1*, 2018, **17**, 1–23.

314   J. A. Woyach, A. S. Ruppert, D. Guinn, A. Lehman, J. S. Blachly, A. Lozanski, N. A. Heerema, W. Zhao, J. Coleman, D. Jones, L. Abruzzo, A. Gordon, R. Mantel, L. L. Smith, S. McWhorter, M. Davis, T. J. Doong, F. Ny, M. Lucas, W. Chase, J. A. Jones, J. M. Flynn, K. Maddocks, K. Rogers, S. Jaglowski, L. A. Andritsos, F. T. Awan, K. A. Blum, M. R. Grever, G. Lozanski, A. J. Johnson and J. C. Byrd, *Journal of Clinical Oncology*, 2017, **35**, 1437.

315   A. D. Buhimschi, H. A. Armstrong, M. Toure, S. Jaime-Figueroa, T. L. Chen, A. M. Lehman, J. A. Woyach, A. J. Johnson, J. C. Byrd and C. M. Crews, *Biochemistry*, 2018, **57**, 3564–3575.

316   C. P. Tinworth, H. Lithgow, L. Dittus, Z. I. Bassi, S. E. Hughes, M. Muelbaier, H. Dai, I. E. D. Smith, W. J. Kerr, G. A. Burley, M. Bantscheff and J. D. Harling, *ACS Chem Biol*, 2019, **14**, 342–347.

317   R. Gabizon, A. Shraga, P. Gehrtz, E. Livnah, Y. Shorer, N. Gurwicz, L. Avram, T. Unger, H. Aharoni, S. Albeck, A. Brandis, Z. Shulman, B.-Z. Z. Katz, Y. Herishanu and N. London, *JACS*, 2020, **10**, 11734–11742.

318   Y.-H. Y. Jin, M.-C. M. M.-C. Lu, Y. Wang, W.-X. W. Shan, X.-Y. X. X.-Y. Wang, Q.-D. You and Z.-Y. Z. Jiang, *J Med Chem*, 2020, **63**, 4644–4654.

319   S. Samanta, A. A. Beharry, O. Sadovski, T. M. McCormick, A. Babalhavaeji, V. Tropepe and G. A. Woolley, *J Am Chem Soc*, 2013, **135**, 9777–9784.

320   M. Dong, A. Babalhavaeji, S. Samanta, A. A. Beharry and G. A. Woolley, *Acc Chem Res*, 2015, **48**, 2662–2670.

321   A. Carreau, B. El Hafny-Rahbi, A. Matejuk, C. Grillon and C. Kieda, *J Cell Mol Med*, 2011, **15**, 1239–1253.

322   D. M. Gilkes, G. L. Semenza and D. Wirtz, *Nat Rev Cancer*, 2014, **14**, 430–439.

323   N. Campillo, B. Falcones, J. Otero, R. Colina, D. Gozal, D. Navajas, R. Farré and I. Almendros, *Front Oncol*, 2019, **9**, 43.

324   P. Vaupel and L. Harrison, , DOI:10.1634/theoncologist.9-90005-4.

325   B. S. Sørensen and M. R. Horsman, *Front Oncol*, 2020, **10**, 562.

326   L. M. Minassian, T. Cotechini, E. Huitema and C. H. Graham, *Adv Exp Med Biol*, 2019, **1136**, 123–139.

327   Y. Li, L. Zhao and X. F. Li, *Front Pharmacol*, 2021, **12**, 524.

328   G. J. Weiss, J. R. Infante, E. G. Chiorean, M. J. Borad, J. C. Bendell, J. R. Molina, R. Tibes, R. K. Ramanathan, K. Lewandowski, S. F. Jones, M. E. Lacouture, V. K. Langmuir, H. Lee, S. Kroll and H. A. Burris, *Clinical Cancer Research*, 2011, **17**, 2997–3004.

329   F. W. Hunter, B. G. Wouters and W. R. Wilson, *British Journal of Cancer 2016 114:10*, 2016, **114**, 1071–1077.

330   L. Spiegelberg, R. Houben, R. Niemans, D. de Ruysscher, A. Yaromina, J. Theys, C. P. Guise, J. B. Smaill, A. v. Patterson, P. Lambin and L. J. Dubois, *Clin Transl Radiat Oncol*, 2019, **15**, 62.

331   J. Benito, Y. Shi, B. Szymanska, H. Carol, I. Boehm, H. Lu, S. Konoplev, W. Fang, P. A. Zweidler-McKay, D. Campana, G. Borthakur, C. Bueso-Ramos, E. Shpall, D. A. Thomas, C. T. Jordan, H. Kantarjian, W. R. Wilson, R. Lock, M. Andreeff and M. Konopleva, *PLoS One*, 2011, **6**, e23108.

332   W. A. Denny, *http://dx.doi.org/10.2217/fon.10.1*, 2010, **6**, 419–428.

333   C. Cazares-Körner, I. M. Pires, I. D. Swallow, S. C. Grayer, L. J. O'Connor, M. M. Olcina, M. Christlieb, S. J. Conway and E. M. Hammond, *ACS Chem Biol*, 2013, **8**, 1451–1459.

334   S. Shi, Y. Du, Y. Zou, J. Niu, Z. Cai, X. Wang, F. Qiu, Y. Ding, G. Yang, Y. Wu, Y. Xu and Q. Zhu, *J Med Chem*, 2022, **65**, 5057–5071.

335   W. Cheng, S. Li, X. Wen, S. Han, S. Wang, H. Wei, Z. Song, Y. Wang, X. Tian and X. Zhang, *Chemical Communications*, 2021, **57**, 12852–12855.

336   T. C. Do, J. W. Lau, C. Sun, S. Liu, K. T. Kha, S. T. Lim, Y. Y. Oon, Y. P. Kwan, J. J. Ma, Y. Mu, X. Liu, T. J. Carney, X. Wang and B. Xing, *Sci Adv*, , DOI:10.1126/SCIADV.ABQ2216/SUPPL_FILE/SCIADV.ABQ2216_SM.PDF.

337   G. E. Winter, D. L. Buckley, J. Paulk, J. M. Roberts, A. Souza, S. Dhe-Paganon and J. E. Bradner, *Science (1979)*, 2015, **348**, 1376–1381.

338   J. Frost, C. Galdeano, P. Soares, M. S. Gadd, K. M. Grzes, L. Ellis, O. Epemolu, S. Shimamura, M. Bantscheff, P. Grandi, K. D. Read, D. A. Cantrell, S. Rocha and A. Ciulli, *Nat Commun*, 2016, **7**, 1–12.

Appendices

**Appendix 2.1** Characteristics of the box "Scoot" used to irradiate the caged and photoswitchable degraders

Distance from LED (mm)	Power BC (mW/cm^2)
80	24.86
77	27.97
74	30.01
68	37.29
65	50.85
62	50.85
59	59.32
56	72.03
53	84.75

Appendix 2.2 LC-MS profile after uncaging of PROTAC **12.** A 50 μM solution of PROTAC **12** in acetonitrile-water (1:1) was irradiated for 1 min, 3 mins and 5 mins at 365 nm. AUC was extracted from the chromatogram UV trace.
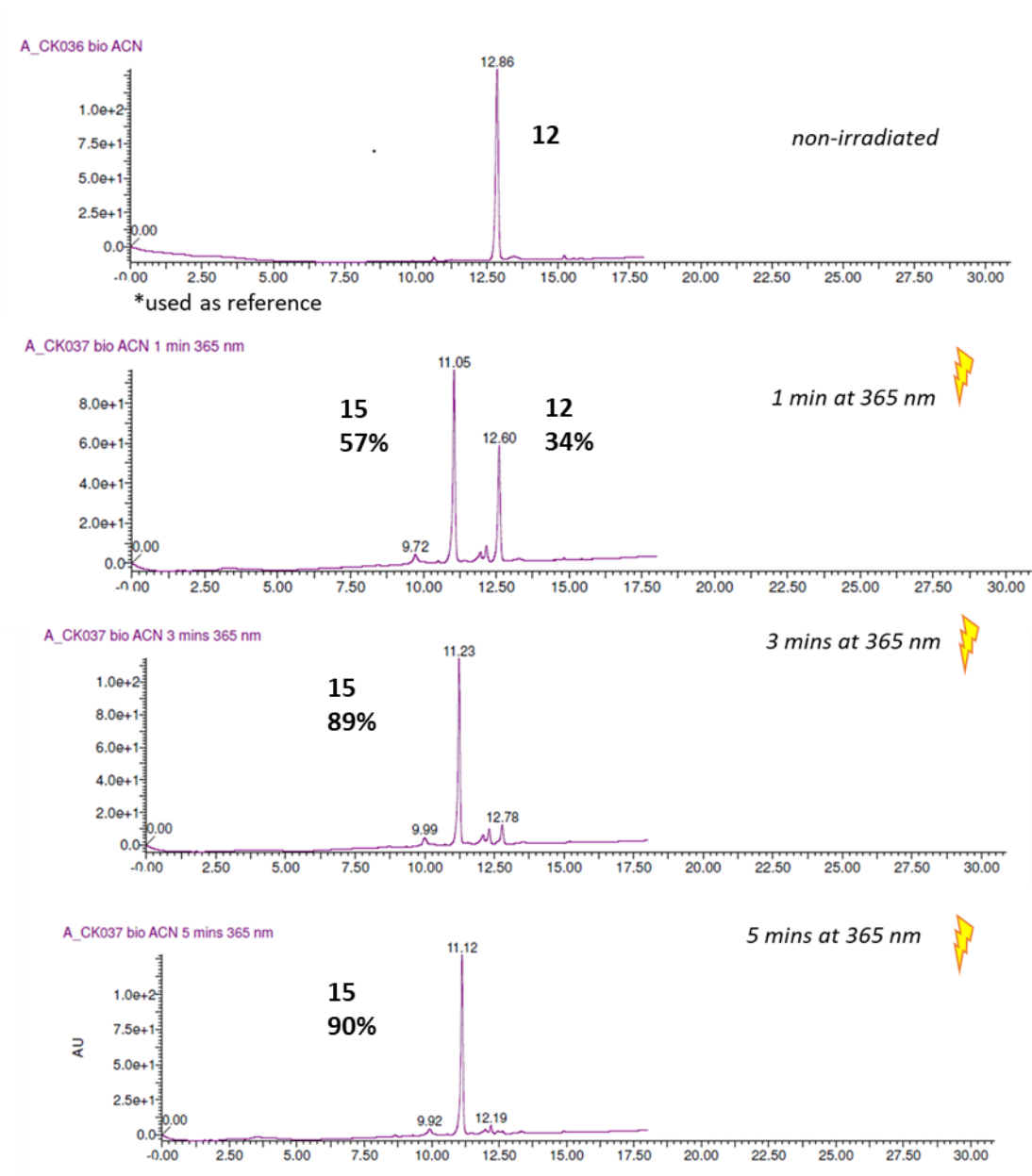
Appendix 2.3 Caged PROTAC **12** stability in DMSO. A fresh solution of PROTAC **12** in DMSO (100 µM) was prepared and analyzed by LC-MS at T0. The solution was kept at room temperature and protected from light. It was re-analyzed after 3 and 5 days. Chromatogram UV trace is represented.
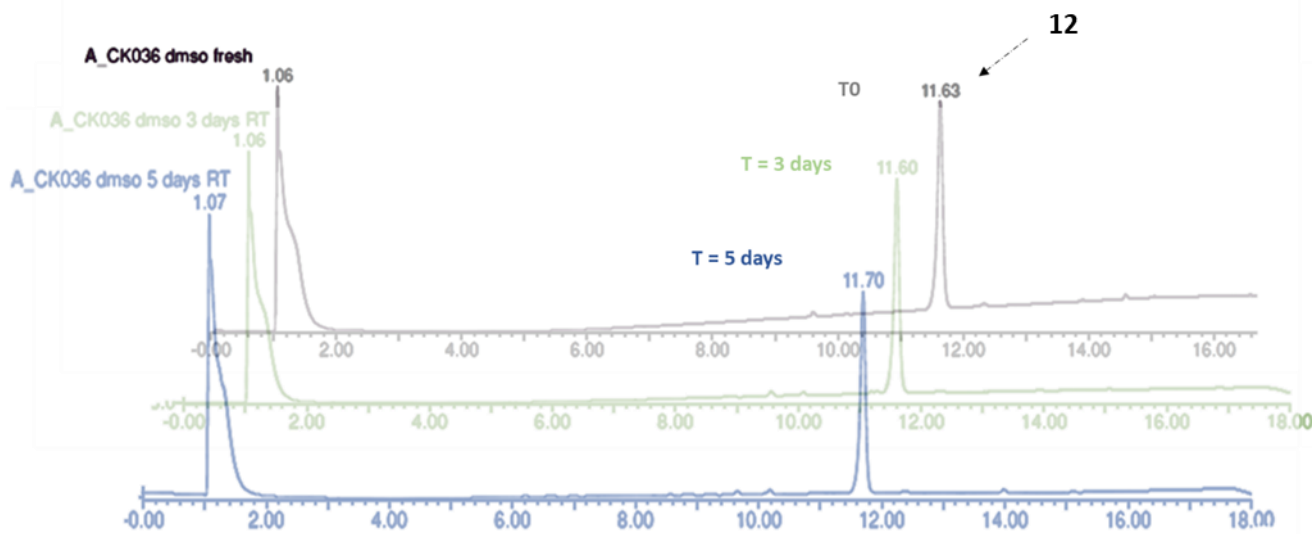
Appendix 2.4 BRD4 Tm determination. Tm = 44.3°C
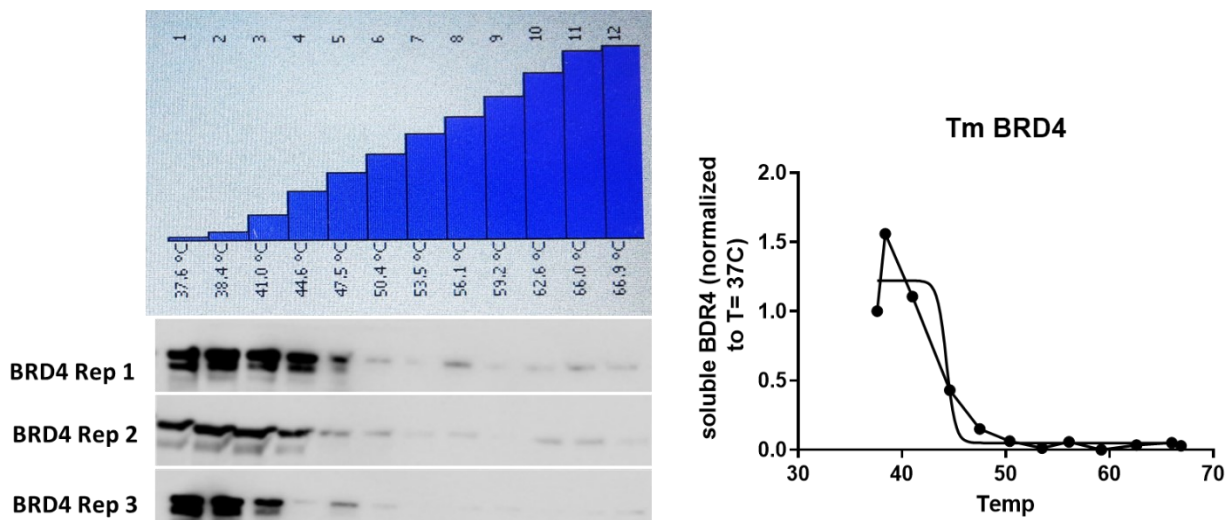
Appendix 2.5 Simulation results of the predicted photon yield per decay in water (in the wavelength range 400–800 nm) as a function of the β-particle endpoint energy for four radionuclides(x)
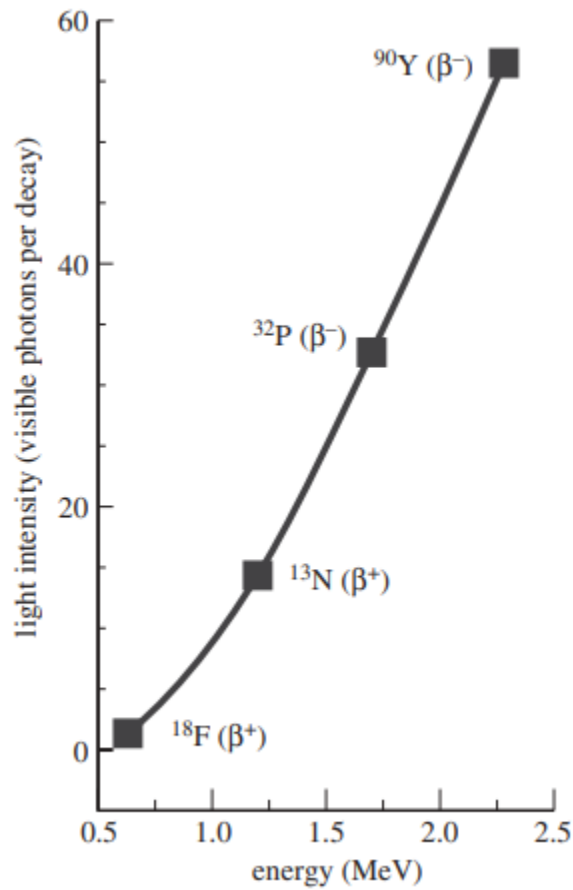
Appendix 2.6 UV chromatogram after incubation of **12** with ^{90}Y spheres (10 mCi) for 60 days in the dark. A new peak could be identified (Rt= 11.15 mins) with the mass corresponding to the uncaged material m/z=1017 (M+1).
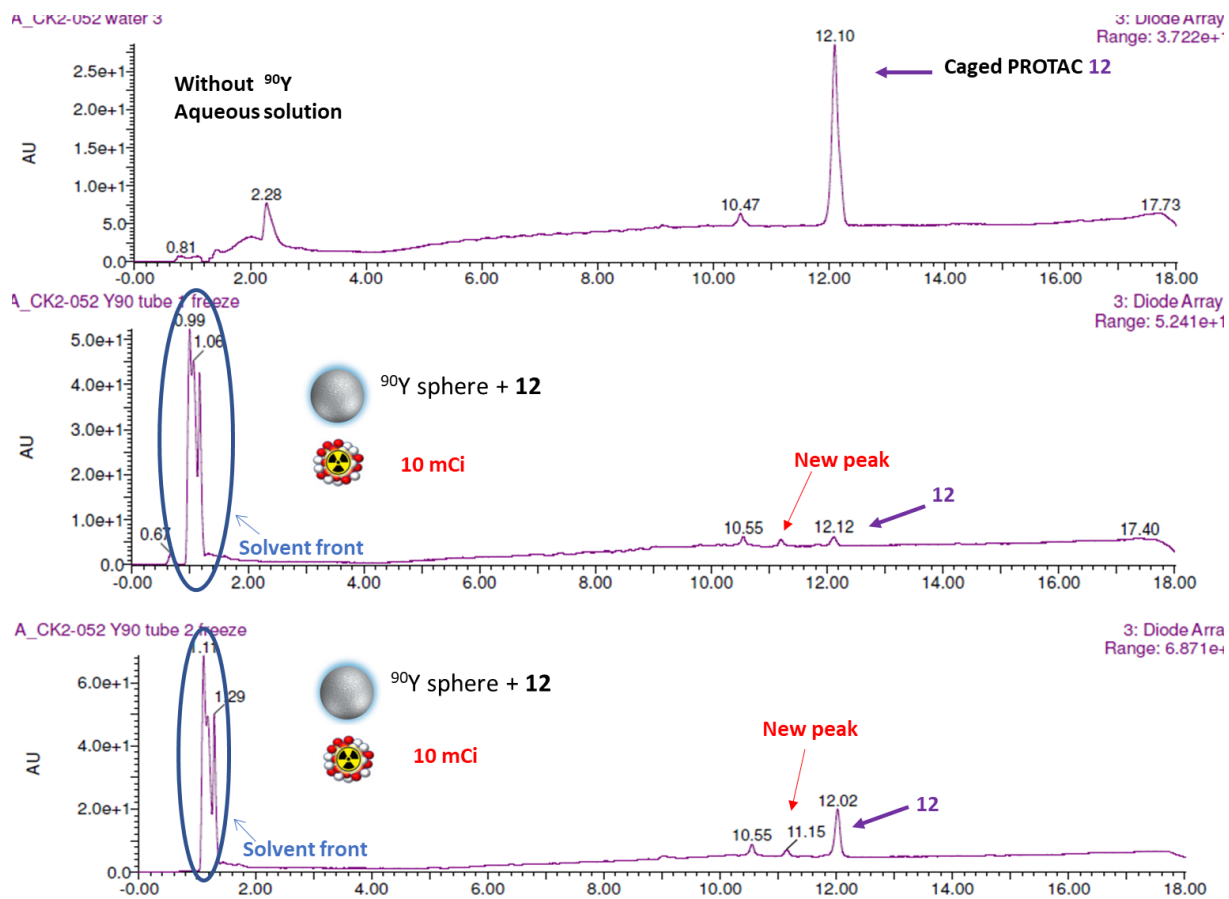
Appendix 2.7 Estimation of the number of photons needed to uncage PROTAC **12** using ^{90}Y

Total energy released by a 365 nm LED light in 60 seconds (E_T)

LED power= 25 mW

Wavelength: 365 nm

Irradiation time: 60 seconds

25 mW = 0.025 Joule / second

E_T= 0.025 × 60 = 1.5 Joule

Energy released by one 365 nm photon (E_p)

Photon energy formula is given by: $E = hc / \lambda$

h= Planck constant=6.626×10^{-34} Js

c= speed of light =3×10^{8} m / s

λ=365 nm

$E_p = (6.626 \times 10^{-34} \times 3 \times 10^{8}) / 365 \times 10^{-9} = 19.878 \times 10^{-26} / 365 \times 10^{-9}$

$E_p = 5.44 \times 10^{-19}$ J

Number of 365 nm photons (n) released in 60 seconds by our LED

n= E_T / E_P

n=$1.5 / 5.44 \times 10^{-19}$

n=2.75×10^{18}

Number of Cherenkov radiation photons (n_{cr}) released by ^{90}Y

Next, we determined the number of photons that can be released from a 10 mCi dose of Yttrium 90 considering an emission of Cherenkov light for the approximate duration of 10 half-lives.

Dose ^{90}Y = 10 mCi (highest dose tested in our experiment)

$T_{1/2}$ = 64.1 h (length of time required for half dose of ^{90}Y to decay = half-life)

10 mCi = 2.22×10^{10} dpm (disintegration per minute) = 3.7×10^{8} dps (disintegration per second)

n_{cr} = $(3.7 \times 10^{\wedge}8)$ dps × 86400 (seconds in 1 day) × 26.7 days (10 half-lives) × 60 (average photons per disintegration of ^{90}Y) = $0.512 \times 10^{\wedge 17}$

The ratio between the number of 365 nm photons (n) released in 60 seconds by the LED and the number of Cherenkov radiation photons (n_{cr}) released by ^{90}Y is as follows:

n/ncr = $2.75 \times 10^{18} / 0.512 \times 10^{\wedge 17}$ = 53.7

Appendix 3.1 LC-MS profile after irradiating PROTAC **31** (50 µM) for 3 mins at 365 nm and leaving the samples at RT, protected from light.
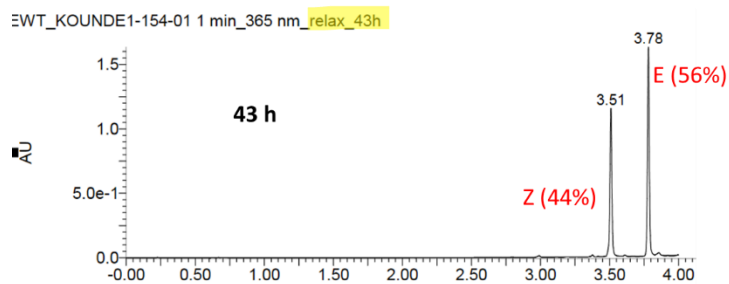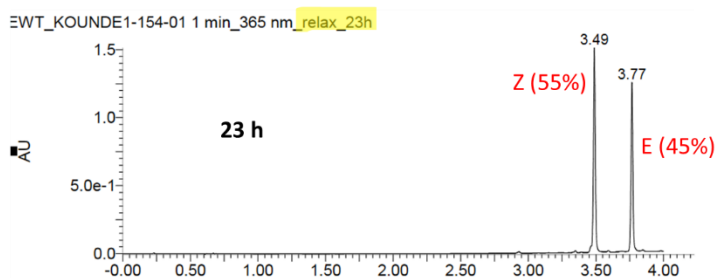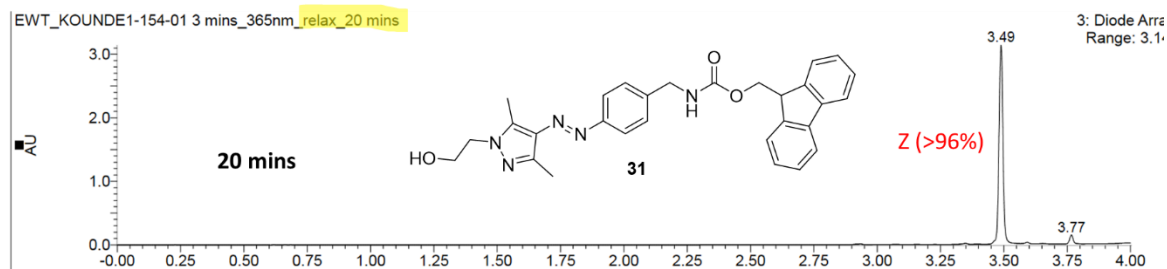
Appendix 3.2 UV-Vis spectrum of **40** (50 µM in ACN) after irradiation for 4 mins at 365 nm versus a non-irradiated sample.
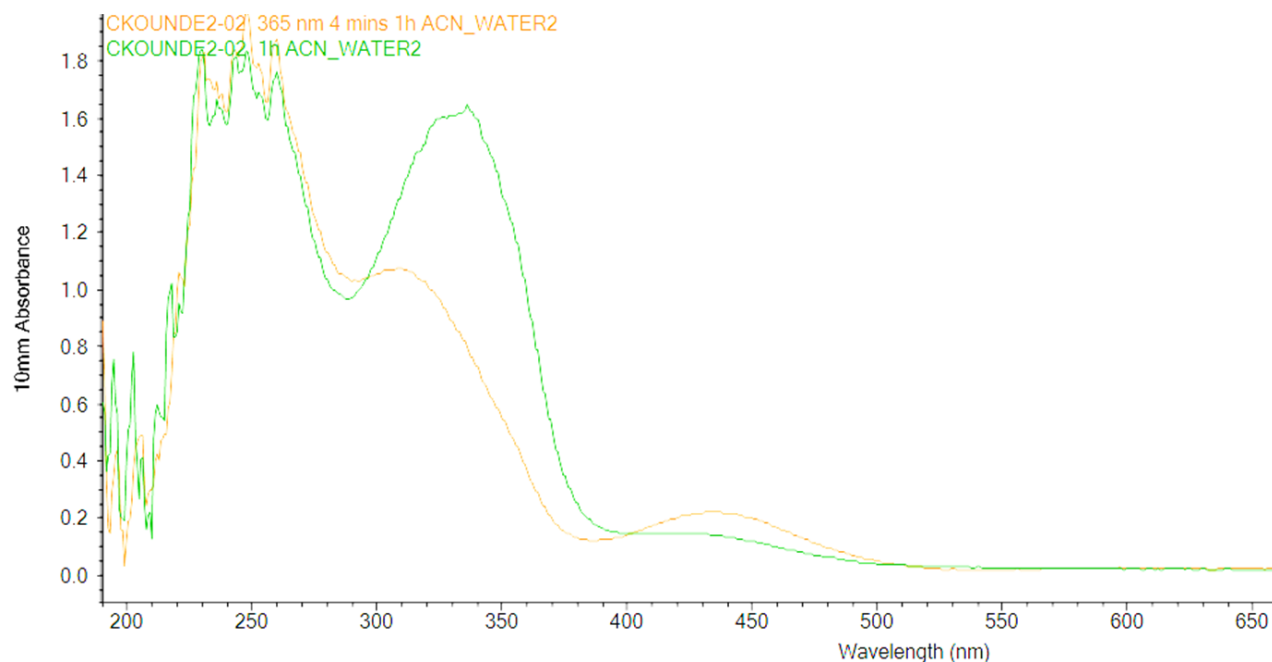
Appendix 3.3 Equation used to calculate the PSS ratio of **40** by UV-vis. Where $a1$ and $a2$ are the PSS ratios of the less stable cis (Z) isomer at wavelength 1 and 2. $Dobsd$ is the observed absorbance, DE is the absorbance of a solution containing only the more stable trans (E) isomer.

$$a_2 = (\frac{\Delta_1}{D_{E1}} - \frac{\Delta_2}{D_{E2}})/(1 + \frac{\Delta_1}{D_{E1}} - n(1 + \frac{\Delta_2}{D_{E2}})$$

$$a_1 = na_2, n = \frac{D_{obsd\,1_{\lambda_{max}}} - D_{E_{\lambda_{max}}}}{D_{obsd\,2_{\lambda_{max}}} - D_{E_{\lambda_{max}}}}$$

$$\Delta = D_{obsd} - D_E$$

190

Appendix 3.4 Timecourse experiments to evaluate the stability of the *Z* isomer of **34** and **42** under physiological conditions (37˚C) after an initial irradiation at 365 nm.
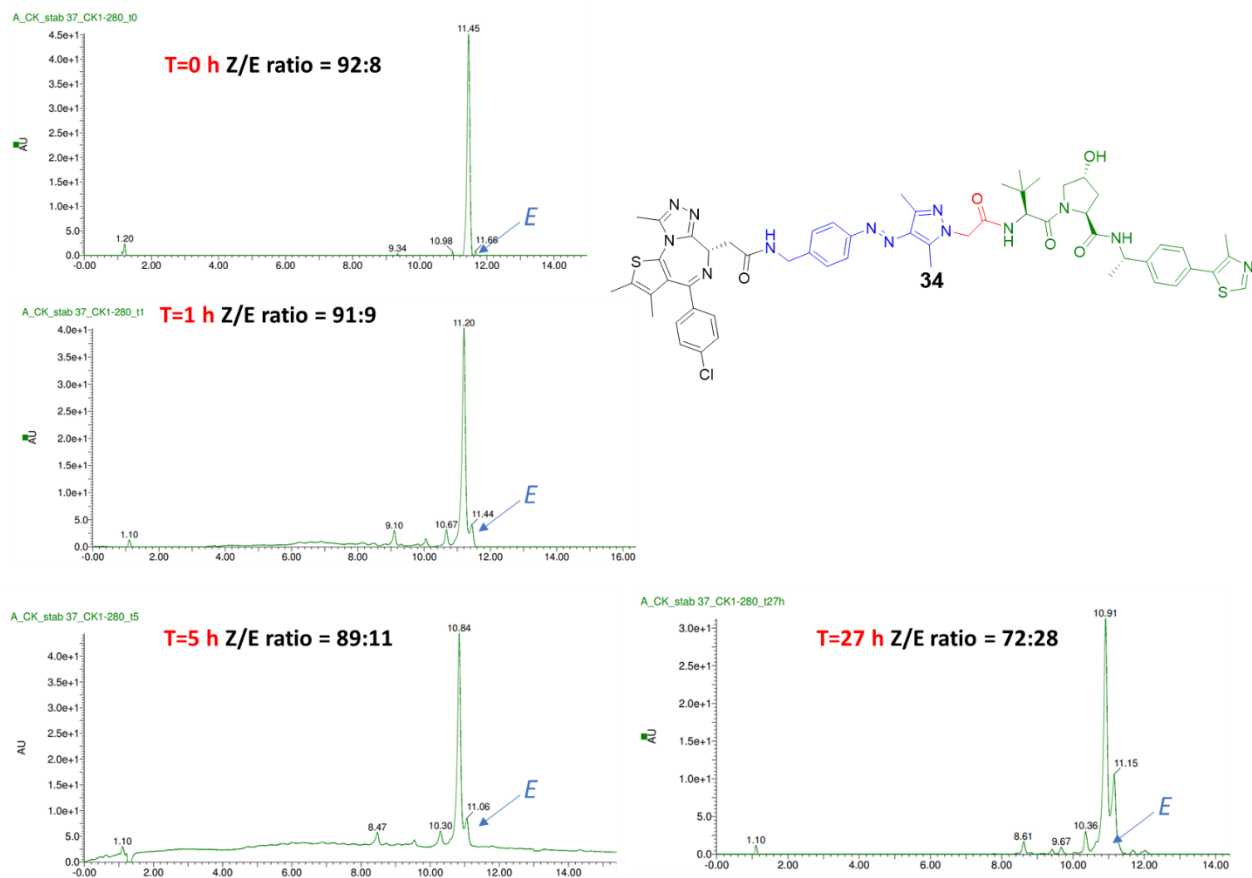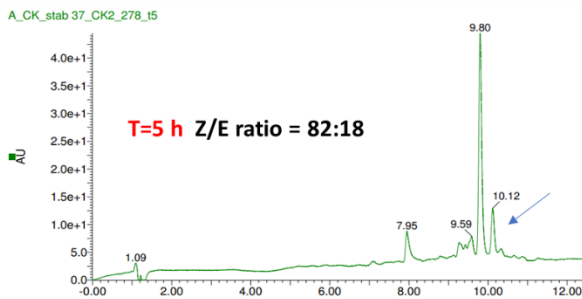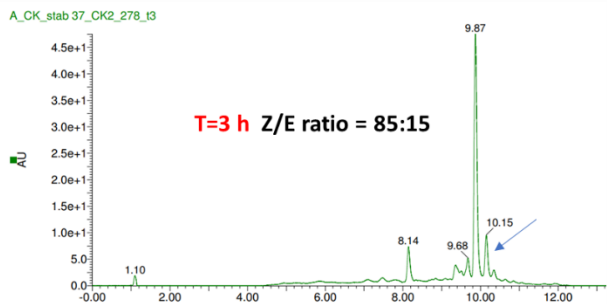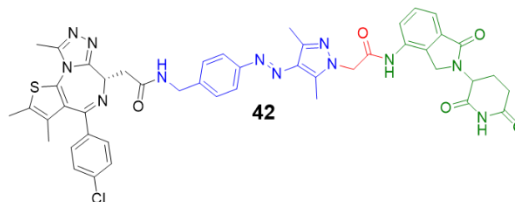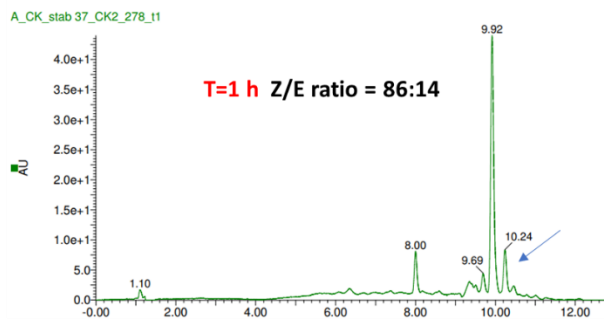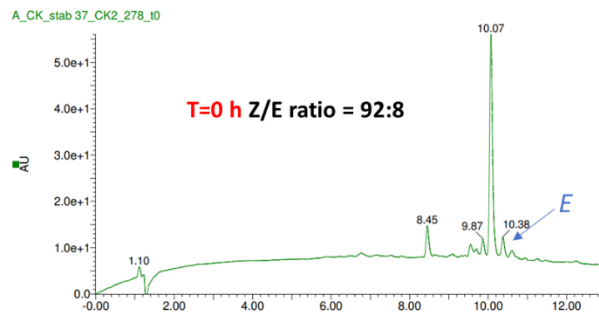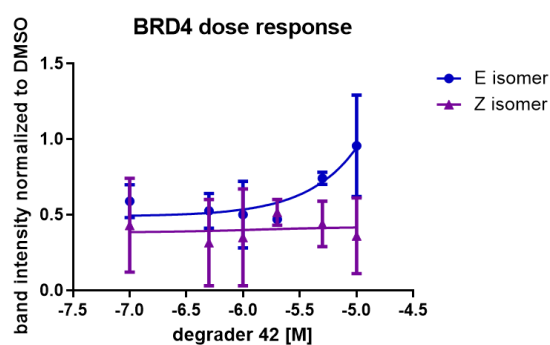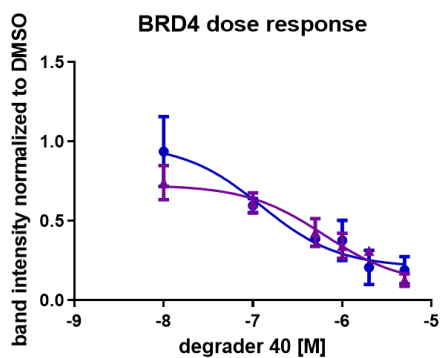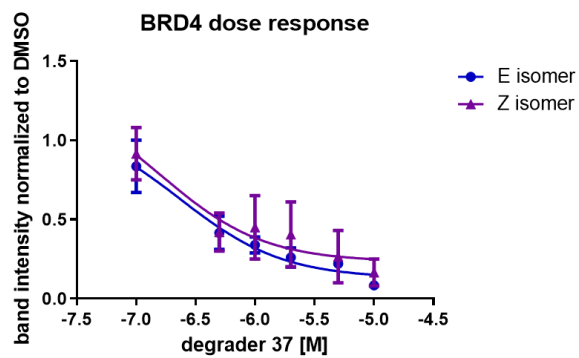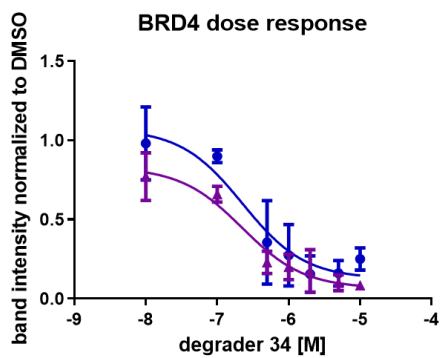
Appendix 3.5 Dose response curves computed from western blots analysis of BRD4 band intensities after treatment of HeLa with the isomer-enriched samples of photoswitchable PROTACs

Appendix 3.6 Immunoblots of BRD4 in HeLa cells after timecourse experiment involving treatment with DMSO control or **40** irradiated with 457 nm (*E*-enriched) or 365 nm (*Z*-enriched) wavelength.
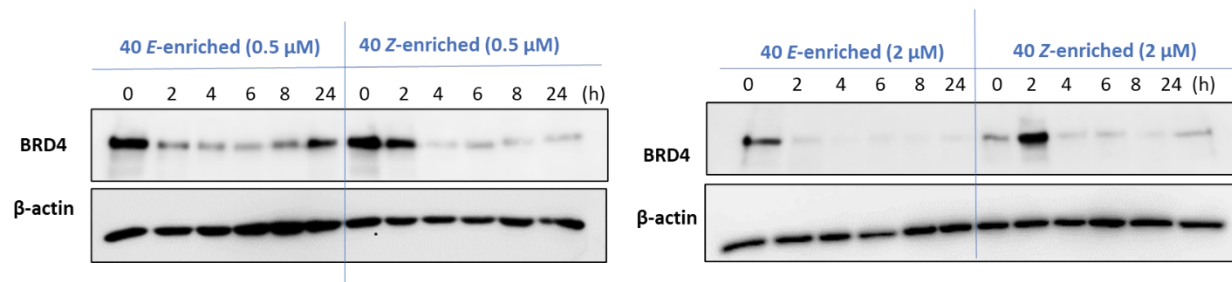
Appendix 3.7 Effect of 50 nM and 500 nM PROTAC **42** on mchBRD4 levels after irradiation with 457 nm (*E*-enriched) or 365 nm (*Z*-enriched) wavelength. Red fluorescence area over phase area is plotted on the y axis.
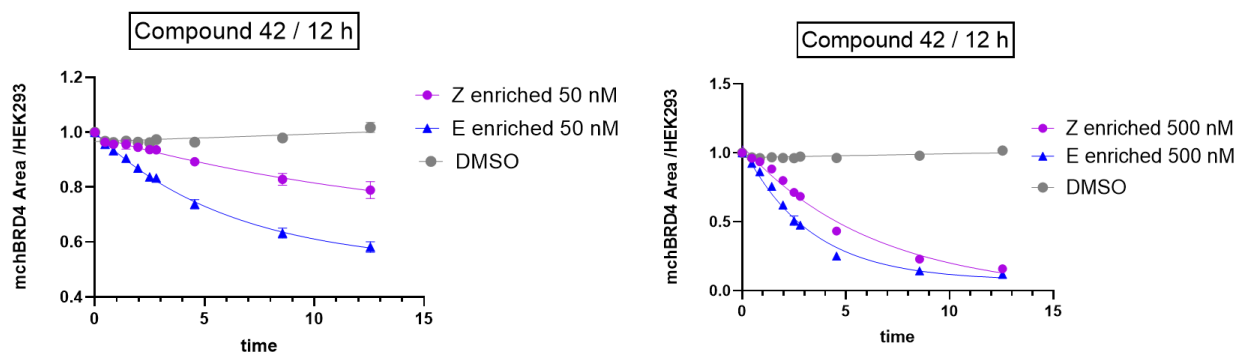
	Parameter	500 nM	50 nM
E	K (hr^{-1})	0.3082	0.1613
	R squared	0.9845	0.993
Z	K (hr^{-1})	0.1586	0.06667
	R squared	0.983	0.9429
E/Z	K ratio	1.943253	2.419379

Appendix 3.8 Proteasome-dependency: HeLa cells were pre-incubated with proteasome inhibitor bortezomib (BTZ, 10 µM) for 2 h, then treated for 4 h with DMSO vehicle 0.1% (v/v) or 500 nM **40** pre-irradiated at 457 nm or 365 nm.